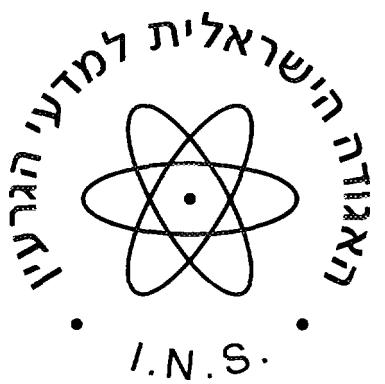

THE 19th CONFERENCE OF THE ISRAEL NUCLEAR SOCIETIES

Program & Book of Abstracts

DAN ACCADIA HOTEL
HERZLIYA
December 9-10, 1996

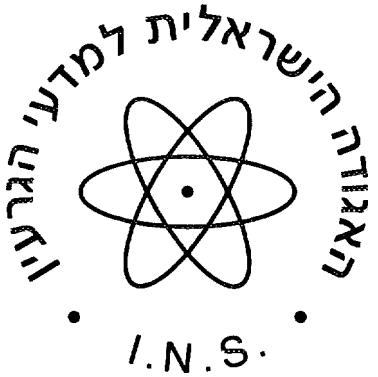

הכינוס הארצי ה-19
של האגודות הגרעיניות בישראל

תכנית וספרי תקצירים

מלון דן-אכדיה, הרצליה
כ"ח-כ"ט בכסלו תשנ"ז
9-10 בדצמבר 1996

האגודה הישראלית למדעי הגרעין

I.N.S.

DAN ACCADIA HOTEL
HERZLIYA
December 9-10, 1996

הכינוס הארצי ה-19
של האגודות הגרעיניות בישראל
מלון דן-אכדיה, הרצליה

חנוכה, כ"ח-כ"ט בכסלו, תשנ"ז
9-10 בדצמבר, 1996

בהשתתפות:

האגודה הישראלית למדעי הגרעין
האגודה הישראלית להגנה מקרינה
האגודה הישראלית לחקר הקרינות
האגודה הישראלית לפיסיקה רפואית
האגודה הישראלית לרפואה גרעינית

ועדה מארגנת:

אבי כתר - יו"ר
אלי אברמוב
שלמה דהן
לואיס טפר
ארנסטו לובין
יעקב סבו
סרג'יו פיירמן
לייב רזניק
עמנואל ריקליס
טוביה שלזינגר
משה שפירא

מזכירות הכינוס:

אורטרא בע"מ
רח' קויפמן 2 (מרכז הטקסטיל)
ת.ד. 50432
תל-אביב 61500
טל.03-5177888
פקס. 03-5174433
E-mail: ortra@trendline.co.il

רשימת מציגים

אופי מדיקל בע"מ
דה האז 24
תל-אביב 62667
טל. 03-5440840
פקס. 03-5441095

אקוספייר
ת.ד. 53006
תל-אביב 61530
טל. 03-6473818
פקס. 03-6496313

לנדסיס
ת.ד. 676
אור-יהודה 60256
טל. 03-5333033
פקס. 03-5333052

נ.י.מ.
ת.ד. 730
אשקלון 78107
טל. 07-6723741
פקס. 07-6751003

פרנקלינס
ת.ד. 37727
תל-אביב 61376
טל. 03-5600724
פקס. 03-5600479

רותם תעשיות בע"מ
ת.ד. 9046
באר-שבע 84190
טל. 07-6567008
פקס. 07-6554502

יום ב', 9 בדצמבר, 1996

09:30–08:30	הרשמה וכיבוד קל	
10:00–09:30	מושב פתיחה:	**אולם נוף–ים**
	ד"ר אבי כתר	– יו"ר הכינוס
	ד"ר לייב רזניק	– סגן נשיא האגודה למדעי הגרעין
	פרופ' שמעון יפתח	– הועדה לאנרגיה אטומית – **25 שנה לאגודה הישראלית למדעי הגרעין**
	ד"ר דני וינר	– סגן מנהל אגף מחקר ופיתוח, חברת החשמל
	מר גדעון פרנק	– מנכ"ל הועדה לאנרגיה אטומית
	ד"ר בני בגין	– שר המדע

מושבים טכניים

10:00-13:00 Plenary Session (P.S) – **אולם נוף־ים**

Chairman: ***A. Keter***

P.S1 Radioactivity and Society - A Journey in the Netherlands
Mr. G. Kupers, ENS President

P.S2 Safety Research for Evolutionary Light Water Reactors
Prof. D.G. Cacuci, KFZ Karlsruhe

P.S3 The Safety of RBMK Reactors 10 years after Chernobyl
Dr. L. Lederman, IAEA

P.S4 Fusion Energy: Status, Technology Gaps and Programs: an Overview
Dr. E. Abramov, NRCN

13:00-14:00 ארוחת צהריים – **אולם אקסודוס**

14:00-15:30 Session 1 (2 אולם נוף־ים) – אולם נוף־ים

Advanced Reactor Physics and Technolgy 1

Chairmen: ***E. Abramov, W. Rothenstein***

1.1 Low Energy Neutron Scattering for Energy Dependent Cross Sections. General Considerations

W. Rothenstein, R. Dagan, *Faculty of Mechnical Engineering, Technion-Israel Institute of Technolgy, Haifa*

1.2 A Comparison of Nodal Methods in Neutron Diffusion Calculations

B. Tavron, *Nuclear Engineering Dept. R&D Division, Israel Electric Corporation*

1.3 The Use of Routine Cell Codes for Evaluating the in-Rod Effective Cross Sections of a Resonance Absorber

M. Segev, *Ben Gurion University, Beer-Sheva*

1.4 Analysis of Fission-Rate-Ratio Measurements in the NIST Iron Sphere Field

R.L. Perel, J.J. Wagschal, Y. Yeivin
Racah, Institute of Physics, The Hebrew University of Jerusalem

1.5 Transport in Stochastic Multi-Dimensional Media

O. Haran, D. Shvarts, *NRC, Negev &* ***R. Thiberger,*** *Ben-Gurion University, Beer-Sheva*

Radiation Protection and Dosimetry 1

Chairmen: *T. Schlesinger, E. Neeman*

2.1 Revised Dose Limits and a New Respiratory Tract Model and Their Implications for the Annual limits of Intake of Radioactive Materials - A Review of Recent ICRP Publications

T. Schlesinger, I. Silverman, M. Shapira,
Soreq NRC, Yavne

2.2 Dose Calculation Due To Electrons Interaction With DNA

***G. Shani, S. Mark, I. Orion**, Dept. of Nuclear Engineering, Ben-Gurion University, Beer Sheva, Soreq NRC, Yavne,*
***B. Laster**, Medical Dept. Brookhaven National Laboratory, N.Y. USA*

2.3 Magnetic Versus Electric fields in RF safety standarts - The Physical origin of difference and the practical implications

M. Margaliot, R. Hareuveny, R. Ruppin and T. Schlesinger, Soreq NRC, Yavne

2.4 Carcinogenic and Other Health Effects of 50/60 Hz Electric and Magnetic Files-Status Report

R. Hareuveny, M. Margaliot, T. Schlesinger,
Radiation Safety Division, Soreq NRC, Yavne

2.5 Radiation Protection Implications Related to Cellular Communications

R. Hareuveny, M. Margaliot, T. Schlesinger,
Radiation Safety Division, Soreq NRC, Yavne

Advanced Reactor Physics and Technology 2

Chairmen: ***S.H. Levine, S. Dahan***

3.1 Calculations of Criticality of the AP600 Reactor with the KENO V.a Code

A. Krumbein, M. Caner, M. Shapira,
Soreq NRC, Yavne

3.2 A Computerized Energy Systems Code and information Library at Soreq

I. Silverman, M. Shapira, M. Caner, D. Saphier,
Soreq NRC, Yavne

3.3 Plasma-Wall Interactions in Controlled Fusion Reactors: an Overview

***E. Abramov**, Ben Gurion University of the Negev, NRC Negev*

3.4 A "Big-Mak"High Converting Water Reactor

***Y. Ronen, Y. Dali**, Dept of Nuclear Engineering, Ben-Gurion University, Beer-Sheva*

Radiation Protection and Dosimetry 2

Chairmen: ***Y. Shamai, E. Levinger***

4.1 Radiation Dose to the Patient in Several Diagnostic X-Ray Examinations Performed with Conventional Radiography Equipment in 3 Major Medical Centers in Israel, A Comparative Study

A. Ben-Shlomo, T. Schlesinger, *Radiation Safty Division, Soreq NRC, Yavne,*
A. Kushilevsky, *Dept. of Biomedical Engineering, Ben-Gurion University, Beer-Sheva*

4.2 An Economic Evaluation of the Rare-Earth Screens to Reduce the Radiation Dose from Diagnostic X-Ray Procedures in Israel

G.M. Ginzburg, *Dept. of Information and Computing, Ministry of Health, Jerusalem,*
T. Schlesinger, A. Ben-Shlomo, *Radiation Safety Division. Soreq NRC, Yavne*

4.3 Neutron Activation Analysis for Environmental Trace Elements Research Determination of Elemental Composition of Sediments in the Sea of Gallilee, Israel

N. Lavi, E. Neeman, S. Brenner, V. Butenko, *Institute for Environmental Research, Tel-Aviv University, Sackler Medical School*

4.4 ^{129}I in Sea-Weeds Determined by AMS

H. Feldstein, D.Berkovits, A. Peled, *Soreq NRC,*
M. Paul, S.Ghelberg, Y.Kashiv, *Racah Institute for Physics, Hebrew University, Jerusalem*

4.5 Enhanced DNA Repair - A New Modality For Improved Radioprotection and Photoprotection

E. Riklis, *EDNAR R&D, NRC, Negev*

09:00-09:45 Plenary Session 5.0 – אולם נוף־ים

Chernobyl: Ten Years After - Sum-up of the Radiological and Health Effects as Reported by IAEA and WHO

J.Koch, D. Ilberg, IAEC

09:45-11:15 Session 5 (בעברית) – אולם נוף־ים

Reactor Safety and Thermohydraulics 1

Chairmen: ***L. Reznik, J. Szabo***

5.1 A New Approach to the Nuclear Power Plant Site Licensing

***A.A. kidron**, Nuclear Project Manager, R&D Division, Israel Electric Corporation*

5.2 Employment of MATLAB in the Analysis of Radionuclide Deposition and Leakage

***L. Reznik, B. Tavron**, Nuclear Engineering Dept. Research and Development Division, Israel Electric Corporation*

5.3 Critical Pressure of Non-Equilibrium Two-Phase Critical Flow

***U. Minzer**, Nuclear Engineering Department, Research & Development Division, Israel Electric Corporation*

5.4 Aerosol Particles Sampling in Sampling and Transport Systems

***T. Kravchik, U. Gherman, Y. Laichter**, NRC, Negev*

5.5 Statistical Criterion for Bubbly-Slug Flow Transition

***J. Zingler*, E. Elias**, Faculty of Mechanical Engineering, Technion, Haifa*

אולם המלך דוד –

Nuclear Instrumentation and Methods 1

Chairmen: *U. German, B. Ben Shachar*

6.1 Operation Program for an Automatic Alpha-Beta Counting System-FAG
U. German, S. Levinson, Y. Shemesh, O. Peled, M. Weinstein, NRC, Negev

6.2 A Manual Low Background Alpha and Beta Counting System
S. Levinson, U. German, O. Peled, S. Turgeman, U. Vangrovitz, D.Tirosh, S. Piestun, H. Assido, NRC, Negev

6.3 A Bar -Code Reader for an Alpha-Beta Automatic Counting System - FAG
S. Levinson, Y. Shemesh, N. Ankry, H. Assido, U. German, O. Peled, NRC, Negev

6.4 Some Dosimetric Properties of the LiF:Mg,Ti Evaluated by the Automatic 6600 Thermoluminescent Reader
B. Ben-Shachar, M. Weinstein, U. German, NRC, Negev

6.5 Computerized Operation of a Multi Detector Spectrometry System
S. Levivson, M. Messing, Y. Gilad, I. Ballon, O.Peled, U. German, NRC, Negev

11:15-11:30 הפסקת קפה

Reactor Safety and Thermohydraulics 2

Chairmen: ***M. Shapira, Y. Barnea***

7.1 A New Thermal-Hydraulic Core Module Based on the Drift-Flux Model for the DSNP

I. Silverman, M. Shapira, D. Saphier,
Soreq NRC, Yavne,
E. Elias, *Dept. of Mechanical Engineering, Technion, Haifa*

7.2 Thermohydraulic Modeling of the Dry Air PCCS Process in the Westinghouse AP-600 ALWR

R. Harari, Y. Weiss, *NRC Negev,*
Y. Barnea, *IAEC Licensing Division, Tel-Aviv*

7.3 Aerosol Filteration by Fibrous and Membrane Filters

T. Kravchik, U. Gherman, Y. Laichter, *NRC, Negev*

7.4 The Importance of Proper Feedback Modelling in HWR

D. Saphier, Z. Gorelik, M. Shapira,
Soreq NRC, Yavne

7.5 Coupling of Conduction with L.aminar Free Convection from a Vertical Flat Plate- An Experimental Study

J.Aharon, C. Lahav, *NRC, Negev,*
H. Kalman, I. Shai, *Pearlstone Center for Aeronautical Engineering Studies, Ben Gurion University, Beer Sheva*

Nuclear Instrumentation and Methods 2

Chairmen: ***Y. Laichter, Y. Kalish***

8.1 "R.I.S-125" ^{125}I Air Monitoring System
I. Belaish, S. Levinson, U. German,O. Pelled, Y. Laichter, U.Wangrovitz, D.Tirosh, D. Barak, *NRC, Negev*

8.2 Limitations of Absolute Activity Determination of I-125 Sources
O. Pelled, U.German, R.Kol, S. Levinson, M. Weinstein, Y. Leichter, *NRC, Negev,* ***Z. Alphassy,*** *Ben Gurion University of the Negev, Beer-Sheva*

8.3 "ASIA" - A Radioactive Aerosols in Air Monitoring System
I. Belaish, O. Pelled, S. Levinson, U. German, Y. Laichter, U. Wangrovitz, E. Gonen, D. Tirosh, D. Barak, *NRC, Negev*

8.4 Locating Gamma Radiation Sources by Self-Collimating BGO Detector System
I. Orion, A. Pernick, D. Ilzycer, H. Zafrir, G. Shani, *Soreq NRC, Yavne, Ben-Gurion University of the Negev, Beer Sheva*

8.5 The Use of Acoustic Resonances to Determine the Mechanical Properties of a Median Layer in a Multi-Layered Structure
F. Tareef, P. Dickstein, *Technion, Haifa*

14:00-15:15 Session 9 – אולם נוף־ים

Advanced Reactor Physics and Technology 3

Chairmen: ***Y. Ronen, M. Segev***

9.1 Thorium Fuel for Light Water Reactors - Reducing Proliferation Potential of Nuclear Power Fuel Cycle

A. Galperin, A. Radkowsky, *Ben-Gurion University of the Negev*

9.2 Improvements in PWR Automatic Optimized Reloading Methods Using Genetic Algorithms

S.H. Levine, K. Ivanov, M. Feltus, *The Pennsylvania State University, USA*

9.3 Whole Core Burnup Calculations Using "MCNP"

O. Haran, Y. Shaham, *NRC, Negev*

9.4 High-Temperature Thermal-Chemical Analysis of Nuclear Fuel Channels

Y. Nekhamkin, V. Rosenband, D. Hasan, E. Hasan E. Elias, E. Wacholder, A. Gany, *Technion, Haifa*

14:00-15:30 אולם המלך דוד

General Assembly of the Israel Radiation Protection Society

15:15-15:30 הפסקת קפה

Radlation Protection and Dosimetry 3

Chairmen: *E. Riklis, A. Eisenberg*

10.1 Monitoring and Radiation Dose Estimation for Internal Contamination of Occupational Workers

R. Kol, Y. Laichter, NRC, Negev

10.2 Acute Internal Exposure to Iodine-125: A Case Study

R. Kol, A. Canfir, N. Dukhan, O. Pelled, D. Brikner, Y. Laicheter, B. Gold, NRC, Negev

10.3 Limitations on the Concentration of Radioactive Substances (natural or enhanced by human activity) in Building Materials-A draft Proposal for Israeli Regulations

T. Schlesinger, R. Hareuveny, M. Margaliot, Radiation Safety Division, Soreq NRC, Yavne

10.4 Occupational Radiation Risks in Conveyance of Bulk Phosphate and Potash

Y. Grof, O. Even, T. Schlesinger, M. Margaliot, Radiation Safety Division, Soreq NRC, Yavne

10.5 The Minimum Measurable Dose (MMD) of CaF_2:Dy Measured via an Improved Heating Profile with an Automatic 6600 Thermoluminescent Detector

B. Ben-Shachar, M. Weinstein, U. German, NRC-Negev

10.6 Radiocesium in Soils of Jerusalem

E. Ne'eman, V. Butenko, S. Brenner, N. Lavi, Sackler Medical School, Tel Aviv University,
J. Kronfeld, Faculty of Exact Sciences, Tel Aviv University,
A. Gilat, Geological Survey of Israel

16:00-17:30 Session 11 (אולם נוף־ים) – אולם נוף־ים

Medical Radiation Physics and Nuclear Medicine

Chairmen: ***S. Faermann, A. Levental***

11.1 Portal Imaging Improvement with a Low Energy Unflattened Beam in High Energy Medical Accelerators

Y. Krutman, S. Faermann, A. Tsechanski, *Ben-Gurion University, Soroka Medical Center, Beer Sheva*

11.2 The Adjoint Monte Carlo - A Viable Option for Efficient Radiotherapy Treatment Planning

M. Goldstein, *NRC, Negev*

11.3 A Retrospective Evaluation of One Year of Cardia Pet Imaging at Hadassah Hospital using Rubidium-82 and the Positron Corporation HZL Pet Scanner

R. Chisin, N. Freedman, R. Marciano, C. Taylor, D. Schechter, *The Hebrew University, Jerusalem*

11.4 ^{99m}Tc High Resolusion Tomographic Imaging in the Thyroid Gland Diseases

A. Reitblat, C. Ben-Horin, *Barzilai Medical Center, Ashkelon*

11.5 The Involement of Oxyradicals in Biostimulation

R. Lubart, H. Friedmann, H. Reuveni, N. Grossman
Bar-Ilan University, Ramat-Gan,
Soroka Medical Center, Beer Sheva

AUTHOR'S INDEX

ABSTRACTS

RADIOACTIVITY and SOCIETY

A journey in the Netherlands
by
Ger Küpers
European Nuclear Society

The end of last century was not only the beginning of a new century but it marked also many fundamental changes in physics, art, literature or in society. Classical mechanics, since Isaac Newton the driving force for many innovations, got in 1904 a powerful brother when Max Planck discovered the quant, which was the start of a new era in physics. The industrialisation already initiated some decades earlier, became a dominant factor in society and the artists in Berlin, Paris, London and Amsterdam shocked the world with impressionistic and expressionistic paintings showing reality and wild colours, quite different from the romantic views from the nineteenth century. In the middle of this melting pot radiation and radioactivity was born. Konrad Röntgen discovered in 1895 a strange type of radiation, Becquerel discovered in 1896 radioactivity and Madame Marie Curie discovered and produced radium. Since then radiation and radioactivity have been part of society and science.

Like in so many countries radiation and radioactivity have many faces in the Netherlands. Apart from reprocessing all activities with respect to radioactivity or producing radioactivity are present in the Netherlands. For the nuclear energy production fuel cycle installations exist for the enrichment of uranium and other isotopes, energy is produced in two nuclear power stations whereas a facility exists to handle all kind of nuclear radioactive waste. In the field of nuclear medicine more than a half of the total quantity of radioisotopes for nuclear pharmaceuticals used in hospitals throughout Europe is produced in the High Flux Reactor at the site of the Energy Research Foundation in Petten. The pharmaceuticals are used for diagnostic and therapeutic reasons. The Petten facilities are also used for cancer treatments like the Boron Neutron Capture Therapy. The radioactivity journey through the Netherlands visits also many academic and city hospitals where radioactivity plays an important role for diagnostic and therapeutic reasons. Other areas where radioactivity plays an important role concern research and development in many scientific disciplines. Many times a year journals report about the occurrence of serious accidents with the use of food poisoned by bacteria. Food irradiation could save many lives. In the Netherlands already many years of experience exist with food irradiation.

The journey through a modern society shows that radioactivity and radiation are used in many places. Much more places than many people do want to believe. The use of radioactivity and radiation has saved many lives and will do so in the future. Radioactivity and radiation have improved quality of life.

SAFETY RESEARCH FOR EVOLUTIONARY LIGHT WATER REACTORS

D. G. Cacuci
Forschungszentrum and University of Karlsruhe
P.O. Box 3640, 76021 Karlsruhe, Germany

INTRODUCTION

The development of nuclear energy has been characterized by a continuous evolution of the technological and philosophical underpinnings of *reactor safety* to enable operation of the plant without causing harm to either the plant operators or the public. Currently, the safety of a nuclear plant is assured through the combined use of procedures and engineered safety features together with a system of multiple protective barriers against the release of radioactivity. This approach is embodied in the concept of Design-Basis Accidents (DBA), which requires the designers to demonstrate that all credible accidents have been identified and that all safety equipments and procedures perform their functions extremely reliably. Particularly important functions are the automatic protection to shut the reactor down and to remove the decay heat while ensuring the integrity of the containment structure. Within the DBA concept, the so-called *severe accidents* were conveniently defined to be those accidents that lie beyond the DBA envelope; hence, they did not form part of the safety case.

The very large number of safety analyses that have been performed during the last three decades have exposed several inherent weaknesses of the DBA approach; these weaknesses pertain to completeness (i.e., occurence of unforeseen accidents), understanding of postulated sequences, equipment reliability, and adequacy of operator procedures. These analyses have also shown that there is a very small, but nevertheless non-zero, probability (of order 10^{-5} per year and reactor) that a reactor's safety features *can* fail; such a failure would lead to an im-

balance between heat production in the reactor core and heat removal by means of the water coolant -- ultimately leading to core melt-down.

Progression beyond DBA inherently requires a departure from the well-defined geometry and physical/chemical properties of the undisturbed reactor. In particular, the molten fuel can no longer be cooled by normal DBA means; this may lead to severe accidents. In the latest German Probabilistic Risk Study [1], the severe accidents were grouped as follows: (a) core melt-down under low system pressure (e.g., following a loss of coolant accident); included in this category are the so-called steam explosions and the hydrogen deflagration/detonation scenarios; (b) core melt-down under high system pressure (e.g., loss of the reactor's heat sink); (c) bypass accidents; (d) direct containment heating. Even though the occurence probabilities for these severe accidents is of the order of 10^{-7} per year and reactor, their consequences and the resulting risk of population evacuation (defined as the occurence probability multiplied by the damage potential) is of the order of 10^{-3} km^2 per year and reactor. This risk is one order of magnitude larger than that for all other accidents [2].

Since the overall objective of the reactor safety strategy is to protect the public against dangerous releases of radioactive materials and since the population density is very high virtually everywhere in Germany, the German law of July 19, 1994 (coal/nuclear energy) requires that --even in case of a core meltdown -- for future reactors there must be no need to evacuate the population living outside of the plant's perimeter. Furthermore, this requirement must be ensured by deterministic --not probabilistic-- arguments. The immediate consequences of this law are twofold: on the one hand, to continue work towards reducing the probability of core meltdown and, on the other hand, to design a (possibly new) containment that prevents release of radioactivity even if a core meltdown occurs.

Thus, the design requirements for future reactors in Germany can be succintly summarized as follows: their containments must have filters to accomodate leaks

(design basis: max. 1.5 Vol% per day), must not fail as a result of core meltdown consequences, must have a core-catcher to prevent fundament penetration, and must have long-term decay heat dissipation capabilities.

Current reactor safety research in the European Community is aimed at meeting the above design goals mentioned in the foregoing. In particular, the reactor safety program at the Nuclear Research Center in Karlsruhe (FZK), Germany, comprises experiments and code developments in the areas of: hydrogen deflagration/detonation; steam explosions, corium (slug)-structure interaction, core catcher, and heat removal via natural convection. Due to space limitations, only one aspect of this research will be touched upon here, namely FZK´s PREMIX program.

PREMIX: An Experimental Program to Investigate Penetration of Molten Alumina into Water

As has long been known in the foundry and paper-making industries, so-called steam explosions somtimes occur when hot molten material is quenched in a comparable quantity of vaporizable liquid. A reliable explanation of this phenomenon is still lacking despite the large research efforts devoted to its understanding. Taditionally, the steam explosion process is analyzed in four stages (even though these stages are in reality not entirely separate), namely:

1. Coarse mixing: in this stage, the molten core material ("corium") is dispersed in the form of irregular drops of various sizes, surrounded by vapor films, in a metastable configuration in water.
2. Triggering: the coarse mixing metastable state is disturbed by an external or internal pressure pulse. Even though triggering appears to be linked to a local collapse of the vapor film around the corium droplets, the precise nature of triggering is very poorly understood.

3. Propagation: the triggering sets off a self-sustaining wave that propagates through the coarse mixture, causing a fine fragmentation accompanied by extremely rapid coherent heat transfer. Although there is ample experimental evidence for the existence of such a coherent self-propagating fragmentation wave, its underlying physical mechanism is not properly understood.
4. Expansion: the mixture of corium, water, and steam expands rapidly (in- or ex-vessel), generating missiles that could penetrate the containment.

The aim of the experimental program PREMIX [3] is to investigate the coarse mixing stage. Corium is simulated by alumina melt that is generated via the following reaction: $8\ Al + 3\ Fe_2O_4 + xAl_2O_3 \rightarrow (4+x)\ Al_2O_3 + 9\ Fe$. Even though this reaction would theoretically yield a temperature of 3050 K, the measured temperature is about 2600 K due to incompleteness of the reaction and enthalpy losses to the crucible holding the reactants. The alumina and iron reaction products separate during the reaction due to their distinct densities. This separation facilitates the retention of the iron so that only the oxidic melt is released fom the generator into the water pool. The test vessel consists of a cylinder (700 mm diameter and 3000 mm in height) with four venting tubes, mounted at its top, to release the steam generated during the alumina-water interaction. The vessel has glass windows (front, rear, and lateral) for illumination and high-speed photography of the interaction zone. Roughly speaking, the vessel comprises the melt generator (in the upper part) and the water pool (in the lower part); the space between the water surface, melt generator, and vessel walls is filled initially by air. For safety reasons, the PREMIX test vessel is housed in a $220m^3$ container, originally designed as a pressure vessel (design pressure: 1 MPa) for experiments on sodium fires and sodium-concrete interactions. The PREMIX test facility is instrumented extensively with pressure transducers (in water, gas compartment, and venting tubes), vortex flow meters (in the venting tubes), and lances with void probes to determine the development of the interaction zone.

eters: mass of alumina melt (10, resp. 20 kg), melt release nozzles (one, resp. three), melt release form (compact jet, resp. spray), height release above water level (200, resp. 0 mm), water temperature (saturated, resp. 5K subcooled), and depth of water to fragment catcher (1500, 920, resp. 500 mm). The test matrix for a representative selection of tests is presented below:

	PM02	PM04	PM06	PM08	PM09	PM10	PM11
Melt							
Mass kg	9.4	9.2	20.2	9.3	20	20	20
Temperature K	2600	2600	2500	2600	2600	2600	2600
Height above water mm	168	185	195	0	0	0	0
Type of release -	compact	spray	compact	spray	compact	spray	3 jets
Duration of release s	0.45	1.0	0.57	0.43	0.9	0.81	1.0
Water							
Temperature K	372	368	371	373	373	373	373
Depth mm	1500	1500	1500	1500	920	500	500

DISCUSSION

The computerized evaluation of the instrument readings together with the interpretation of the video and high-speed recordings show that the melt stream forms a funnel-shaped interaction zone while undergoing hydrodynamic fragmentation. The interaction zone grows and pushes the liquid water away, thereby limiting the intensity of the coarse mixing process. In the experiments with 50 cm water depth the melt conglomerated into lumps and --in the case of high flow rates-- formed a cake on the bottom of the catcher. This points towards the existence of a physical mechanism that inherently limits the amounts of melt that can coarsely mix with water -- a phenomenon whose occurence has also been con-

jectured by other investigators.

Experiment PM11 has unexpectedly produced a steam explosion that damaged the PREMIX facility. The underlying causes have not been elucidated yet. The facility is now being rebuild while the analysis of the experimental data continues. On the other hand, the numerical post-test simulations using three-dimensional multifield codes have revealed that they underpredict the production of steam, the pressure buildup, the spreading of the mixing zone and the respective rise of the water level. Work continues on improving both the physical models and the numerical solution algorithms. A transfer to reactor conditions of the results obtained so far in the PREMIX program is still in the future.

REFERENCES

[1] Deutsche Risikostudie Kernkraftwerke -Phase B
Gesellschaft für Reaktorsicherheit (GRS), Köln, Germany, 1989.

[2] H.H. Hennies, G. Kessler, and J. Eibl, "Sicherheitskonzept zukünftiger Druckwasserreaktoren", KfK Nachrichten, Jahrgang 25, 1/93, Karlsruhe, Germany, 1993

[3] F. Huber, et. al.: PREMIX, Documentation of the results of Experiments PM01 to PM06, IRS/FZK, FZKA 5756, March 1996, Karlsruhe, Germany, 1996

The Safety of RBMK Reactors 10 Years After Chernobyl

L. Lederman
International Atomic Energy Agency

The development of the boiling water cooled graphite moderated pressure tube reactor system (RBMK) came out of the Soviet uranium-graphite Pu production reactors, the first of which began operation in 1948. In 1954 a demonstration 5 MW(e) reactor began operation in Obninsk and subsequently a series of reactors were developed using the combination of graphite moderation and water cooling in a channel design.

Currently there are 15 RBMK reactors in operation: 11 units in Russia, 2 in Ukraine (Chernobyl unit 2 has been shutdown since 1991 after a major fire collapsed the turbine building roof and damaged safety equipment) and 2 in Lithuania. The connection to the electric power grid of these units took place from 1973 (Leningrad 1) to 1990 (Smolensk 3).

In April 1986 the Unit 4 of Chernobyl NPP was destroyed in the worst accident in the history of commercial nuclear power. Unit 4 started operation in 1983 and was a RBMK type nuclear power plant (NPP).

Over the years, three generations of reactors have emerged which have significant differences, particularly with respect to the safety provisions built into their design. The electric power of the RBMK reactors is 1000 MW(e) except for Ignalina whose power is 1500 MW(e). The development of the Kursk Unit 5, currently under construction, has led to many design changes - hence it can be thought of as a fourth generation.

The first generation units (Leningrad-1 and -2, Kursk-1 and Chernobyl-1 and -2) were designed and built before 1982 when new standards on the design and construction of Nuclear Power Plants (NPPs) OPB-82 were introduced in the Soviet Union. Since then other units have been designed and constructed in accordance to these requirements. The safety standards in the USSR were revised again in 1988 (OPB-88).

Since the Chernobyl accident a considerable amount of work has been carried out by Russian designers and RBMK operators to improve RBMK reactor safety and to eliminate the causes of the accident. As a result, major design modifications and operational changes have been implemented. However, safety concerns remain, particularly related to first generation units.

In the framework of a Programme on RBMK safety initiated by the IAEA in 1992, a total of 58 safety issues related to seven topical areas were identified. The issues related to the six design areas were further ranked according to their perceived impact on plant safety.

Safety issues connected to operational areas, particularly those related to ensuring that a high safety culture is an underlying basis for operation, were considered very important. It was stressed that all efforts should be made to implement the related recommendations along with design modifications.

The direct causes of the Chernobyl accident were related to the reactor core design. Therefore, safety improvements have been initially focused on the core physics shortcomings.

It is recognized that to date considerable work has been completed to decrease the core void reactivity coefficient and to increase the efficiency of the shutdown system. However, the problem of the void reactivity associated with the loss of coolant from the channels of the control and protection system (CPS) and the issue of independent and diverse reactor shutdown - both issues of high safety relevance - have not yet been resolved. The intent of the Russian designers to develop and modernize the RBMK CPS to provide higher safety level is strongly supported by international experts.

The safety significance of the safety issue related to the operational reactivity margin (ORM) is high since the ORM has to be controlled in order to maintain the void reactivity coefficient, the effectiveness of the shutdown system (insertion rate, shutdown subcriticality) and the power distribution within the given safety limits. With the present design it is the responsibility of the operator alone to keep the ORM within these safety limits. It was recommended to automate the shutdown actions when the ORM value falls below the safety limits to reduce the safety significance of the manual ORM control.

The design and safety analysis of the RBMK reactors were performed with the calculational tools available at that time. These tools (e.g. computer codes) generally did not have the capability to adequately model spatial interactions between neutronics and thermohydraulics. Considering that these aspects are very important for RBMK safety analysis and core design, development of 3-D methods for predicting space-time dependent depletion, neutron fields, coolant density and temperature distribution of fuel and graphite should be continued. These methods should be used to confirm results of previous safety analysis and should be used for further studies.

The major concerns are the segregation between the electronic systems and the level of diversity present in the most important systems and equipment. For example, the flux control system shares many common elements with the shutdown system and, although there is considerable resilience in the system due to the high level of redundancy, the two systems would be vulnerable to common mode failure, thus control and protection could be lost simultaneously.

Some primary coolant circuit components and piping are outside of the accident localization system. The guillotine break in 800 mm diameter piping in the first generation of RBMK NPPs can result in damage to civil structures. Application of the leak before break (LBB) concept would reduce risk of primary coolant circuit failures, but the applicability of this concept for RBMK conditions is not fully demonstrated and LBB method and techniques are not in use.

To date there have been three single channel ruptures due to water flow blockage or power-flow imbalance. It was recommended to analyze and to implement, as feasible, the reduction of the number of in-line components, the failure of which can result in a water flow blockage.

The reviews indicate that at some plants operation has continued even though the frequency and the number of examinations required by the national regulations for the reactor pressure boundary are not performed or when the results are not satisfactory. The existing time schedules for implementation of modifications and additional analysis as well as the requirements for record keeping are sometimes not followed. Criteria for limiting plant operation in these cases are not established.

The required high volume of in-service inspection is not fulfilled in practice. It was found that in some cases the required number of fuel channels was not inspected. The approach adopted at RBMK plants to repair identified critical defects differs from the predictive approach adopted for in-service inspection (ISI) elsewhere. Pre-service inspection records and ISI predictive records are not maintained. The equipment and procedures used are inadequate to give repeatable measurements of subcritical defect size.

The scope of analysis of postulated accidents available in the Technical Justification of Safety (TOB) was determined by national regulations effective at the time the TOB was issued. Compared to current practices, it was found to be limited and the related information usually does not provide a clear description of the assumptions used in the analysis. The computer codes used at the time of RBMK design were of limited modeling capability. The lack of an experimental data base on pipe rupture of the primary heat transport system limited the possibility of integral code validation. Presently, more modern Russian codes and some Western codes are being used, but these codes have not been sufficiently validated for modeling RBMKs.

In general it has been found that the high redundancy which exists in several of the front line safety systems is not present to the same extent in the supporting systems such as the service water and intermediate cooling systems. Moreover, the high level of redundancy in the safety systems cannot always be given full credit due to potential common cause failures.

In general, it has been found that the differences between the plants are so important that each recommendation has to be evaluated on a plant specific basis.

Fire risks were not adequately considered in the design phase of RBMK reactors when passive measures could have easily been implemented. However, much work has been done afterwards. Removal of the largest fire load, the plastic floor coating, has started gradually. Improvement of compartmentation has been carried out by upgrading fire doors and penetration sealings. Within the compartments the main improvement effort has been the covering of cables with a fire resistant protective coating.

Manual fire suppression capability is generally very strong at NPPs in the former Soviet Union. This applies to the number and the training of fire brigade personnel. Deficiencies, however, exist in the personal protective equipment, communication equipment and fire fighting equipment, such as fire extinguishers, hoses and nozzles.

Outlook

On the basis of national and multilateral safety reviews the main safety concerns of RBMK NPPs have been identified and the required safety improvements agreed upon. Much work is still required to implement the safety improvements at the individual NPPs.

Despite the work carried out to date, safety concerns remain, particularly those related to the first generation units. Therefore, future IAEA work will focus on assisting in the review of the first generation units and on streamlining efforts to resolve generic safety issues.

Fusion Energy : Status, Technology Gaps and Programs: an Overview

E. Abramov

Ben-Gurion University of the Negev, P.O. Box 653, Beer-Sheva ; and Nuclear Research Centre-Negev, P.O. Box 9001, Beer-Sheva

Fusion energy offers the promise of becoming a safe, economical, abundant, and environmentally acceptable source of power. While the technological challenges of harnessing fusion power are large, significant advances have been and continue to be made. Today, most of the industrialized countries invent a huge amount of resources in order to develop the possibility of commercial utilization of fusion power.

The talk will review the development of fusion technology and the status of the main experimental facilities that being used. Focus will be given to describe the development of the leading technology of magnetic confinement, and mainly to the Tokamak machines. An emphasis will be given to the technology gaps exist especially in materials selection and development.

One of the main milestones in the road to a commercial fusion reactor is the design and construction of ITER (International Thermonuclear Experimental Reactor) to demonstrate a reasonable cost per unit of fusion power. This multi-billion dollar project is being stirred and funded by the United States, the European Community, Russia and Japan. The status of the ITER project and the obstacles to its completion will be discussed. Other independent national program will be mentioned.

Although Israel does not have any formal part in any Fusion program, there are many on-going related activities in Israel. Few ideas to try to initiate such programs in Israel during the years will be described. A proposal to establish an organized future activity in Israel will be suggested.

LOW ENERGY NEUTRON SCATTERING FOR ENERGY DEPENDENT CROSS SECTIONS.

GENERAL CONSIDERATIONS.

W. Rothenstein and R. Dagan
Faculty of Mechanical Engineering
Technion - Israel Institute of Technology
Haifa, 32000, Israel

Introduction

We consider in this paper some aspects related to neutron scattering at low energies by nuclei which are subject to thermal agitation. The scattering is determined by a temperature dependent joint scattering kernel, or the corresponding joint probability density, which is a function of two variables, the neutron energy after scattering, and the cosine of the angle of scattering, for a specified energy and direction of motion of the neutron, before the interaction takes place.

This joint probability density is easy to calculate, when the nucleus which causes the scattering of the neutron is at rest. It can be expressed by a delta function, since there is a one to one correspondence between the neutron energy change, and the cosine of the scattering angle.

If the thermal motion of the target nucleus is taken into account, the calculation is rather more complicated. The delta function relation between the cosine of the angle of scattering and the neutron energy change is now averaged over the spectrum of velocities of the target nucleus, and becomes a joint kernel depending on both these variables. This function has a simple form, if the target nucleus behaves as an ideal gas, which has a scattering cross section independent of energy.

An energy dependent scattering cross section complicates the treatment further. An analytic expression is no longer obtained for the ideal gas temperature dependent joint scattering kernel as a function of the neutron energy after the interaction and the cosine of the scattering angle. Instead the kernel is expressed by an inverse Fourier Transform of a complex integrand, which is averaged over the velocity spectrum of the target nucleus.

In order to make use of this scattering kernel in deterministic and stochastic neutron transport calculations in the low epithermal energy region, in which there are pronounced resonances of the fertile nuclei in reactor fuel, it may well be necessary to replace the kernel by a highly truncated spherical harmonics expansion involving the lowest order Legendre Polynomials of the angle of scattering of the neutron only.

Derivation of the Expression for the Scattering Kernel and its Legendre Moments.

The joint scattering kernel per unit final neutron energy near E' and per unit solid angle near the final direction of motion of the neutron $\vec{\Omega}'$, and its expansion in Legendre Polynomials of the cosine μ_0^{lab} of the angle of scattering in the laboratory frame of reference, is given by:

$$\sigma_s^T(E \rightarrow E', \vec{\Omega} \rightarrow \vec{\Omega}') = \frac{1}{2\pi} \sum_{n=0}^{\infty} \sigma_{sn}^T(E \rightarrow E') P_n(\mu_0^{lab}) \quad , \quad \mu_0^{lab} = (\vec{\Omega} \cdot \vec{\Omega}') \tag{1}$$

where $(\vec{\Omega} \rightarrow \vec{\Omega}') = (\vec{\Omega} \cdot \vec{\Omega}')$ for an isotropic medium. The expansion coefficients are given by:

$$\sigma_{sn}^T(E \rightarrow E') = 2\pi \int_{-1}^{1} \sigma_s^T(E \rightarrow E'; \Omega \rightarrow \Omega') P_n(\mu_0^{lab}) d\mu_0^{lab} \tag{2}$$

and are called the Legendre Moments (of order n) of the two dimensional or joint scattering kernel. Each moment is a one dimensional kernel, i.e. a function of one variable (the final neutron energy) only. The moment of order zero is the integrated joint scattering kernel over all neutron directions of motion after scattering; it is the cumulative scattering kernel.

The characteristics of elastic scattering of a neutron by a moving nucleus must be determined by conserving the total momentum and the total kinetic energy of the two interacting particles. Three frames of reference may be used in the treatment of the scattering process: The laboratory coordinate system, the coordinate system in which the target nucleus is at rest, and the one in which the center of mass of the two particles is at rest.

The simplest problem is of course the one in which the target nucleus is indeed at rest. In this case there is no difference between the first two coordinate systems, and it is a simple matter to calculate the neutron velocity and that of the target relative to the center of mass, so that their total momentum is zero. Momentum conservation is then ensured by merely rotating the line along which the two particles approach one another in a random manner, and, if one lets them separate subsequently along the rotated line without change in the magnitudes of their velocities, their total kinetic energy is also conserved. At low neutron energies the rotation has an isotropic frequency distribition. Transformation back to the laboratory frame of reference then leads to the well known relations between the change of neutron energy E to E' in laboratory coordinates, and the cosines of the scattering angle μ_0^{CM} in the center of mass, and μ_0^{lab} in the laboratory, frames of reference [1] :

$$\begin{aligned}
\frac{E'}{E} &= 1 - \frac{(1-\alpha)}{2}(1-\mu_0^{CM}) = \frac{[\ \mu_0^{lab} + \sqrt{A^2 - 1 + (\mu_0^{lab})^2}\ ]^2}{(A+1)^2} \\
\mu_0^{CM} &= 1 - \frac{2}{(1-\alpha)}(1 - \frac{E'}{E}) = \frac{(\mu_0^{lab})^2 - 1 + \mu_0^{lab}\sqrt{A^2 - 1 + (\mu_0^{lab})^2}}{A} \\
\mu_0^{lab} &= \frac{A+1}{2}\sqrt{\frac{E'}{E}} - \frac{A-1}{2}\sqrt{\frac{E}{E'}} = \frac{1 + A\mu_0^{CM}}{\sqrt{1 + 2A\mu_0^{CM} + A^2}}
\end{aligned} \tag{3}$$

These relations express the one to one correspondence of the changes of energy and direction of motion of the neutron by scattering from a target at rest. Joint probability densities as a function of two of the variables, after the interaction has taken place, are then delta functions, such as:

$$p^T(E \rightarrow E', \Omega \rightarrow \Omega') \qquad \frac{1}{2\pi}\delta(\mu_0^{lab} - \hat{\mu}_0^{lab}) \quad , \quad \hat{\mu}_0^{lab} = \frac{A+1}{2}\sqrt{\frac{E'}{E}} - \frac{A-1}{2}\sqrt{\frac{E}{E'}} \qquad (4)$$

which is zero for almost all final $\vec{\Omega}'$, except the one for which μ_0^{lab} equals $\hat{\mu}_0^{lab}$, the latter quantity being a function of E'/E only.

When the thermal agitation of the target nucleus is taken into account, the expressions given in equation (3) still hold, provided one transforms the initial neutron velocity $\vec{v}$ to its velocity relative to the target at rest, using $\vec{v_r} = \vec{v} - \vec{V}$, where $\vec{V}$ is the target velocity. The averaging process over the spectrum of $\vec{V}$ was described first by Ouisloumen and Sanchez [2]; it referred to the case when the scattering cross section is a function of $E_r = (m/2)v_r^2$. The velocity diagram showing the neutron velocities in the three frames of reference, laboratory, target at rest, and center of mass at rest, is now much more complicated than in the case for which $\vec{V} = 0$, and is given in [3]. It is used to make the transformation from the laboratory to the center of mass coordinate system in order to use the same principle as in the derivation of equations (3): the magnitude of the neutron velocity relative to the center of mass is the same before and after elastic scattering. The resulting equation is :

$$\begin{aligned}
\sigma_{sn}^T(E \rightarrow E') \;=\; & [\beta^{5/2}/(4E)]exp(E/k_BT)\int_0^\infty dt\left\{t\sigma_s^{tab}(E_r,0)\right\}exp(-t^2/A) \\
& [H(t_+ - t)H(t - t_-)\int_{\epsilon_{max}-t}^{t+\epsilon_{min}} dx\ e^{-x^2} + H(t-t_+)\int_{t-\epsilon_{min}}^{t+\epsilon_{min}} dx\ e^{-x^2}] \\
& [(4/\sqrt{\pi})\int_0^{2\pi} d\varphi P(u,\hat{\mu}_0^{CM})P_n(\hat{\mu}_0^{lab})] \qquad (5)
\end{aligned}$$

Here dimensionless variables are being used in the integrations: $t^2 = [m(A+1)/(2k_BT]u^2$, $x^2 = [m(A+1)/(2k_BT]c^2$, with u the neutron speed relative to the center of mass, and c the speed of the center of mass in laboratory coordinates. In addition $\epsilon^2 = (A+1)E/(k_BT)$, with ϵ_{max} and ϵ_{min} referring to the larger and the smaller of E and E'. Finally the definitions $t_+ = (\epsilon_{max} + \epsilon_{min})/2$ and $t_- = (\epsilon_{max} - \epsilon_{min})/2$ are used in the arguments of the Heaviside functions H .

The form of equation (5) is of interest, when one considers the treatment under discussion. It calculates a thermal average involving two basic variables V and $\mu_V = (\vec{v}\cdot\vec{V})/(vV)$, which have been changed by a Jacobian Transformation to t and x , or the speeds u and c as defined in the previous paragraph. In addition the theory refers to two basic variables relating to the scattering process in center of mass coordinates, the cosine μ_0^{CM} of the scattering angle and the difference φ of the azimuth angles, (with respect to the velocity $\vec{c}$ as axis), of the planes in which the two particles approach one another, and then separate again, before and after the interaction. The triple integral on the right hand side of equation (5) accounts for three of these four basic variables, leaving only one, E', to be used as a variable parameter in the

quantity calculated on the left hand side of equation (5), see reference [3] . This aspect of the development of equation (5), as well as its details, lead to the conclusion, that a different physical principle from the one, which merely equates the neutron speeds in center of mass coordinates before and after the collision, is needed in order to calculate the joint scattering kernel as a function of E' and μ_0^{lab} $(= \vec{\Omega} \cdot \vec{\Omega'})$ of equation (1).

The alternative physical principle refers directly to the laboratory coordinate system, as is also used in the quantum mechanical treatment of scattering. The neutron transfers momentum $\vec{q} = \vec{p} - \vec{p'}$ to the target nucleus, which will then have momentum $\vec{P'} = \vec{P} + \vec{q}$. The gain in kinetic energy of the target nucleus is then given by

$$[(P')^2 - P^2]/(2mA) = q^2/(2mA) + (\vec{P} \cdot \vec{q})/(mA)$$

while the energy gain of the neutron is $E' - E$. Energy conservation is then expressed by the delta function :

$$\delta(\beta + \alpha + 2\sqrt{\alpha A}\,\mu_q\,V) \;,\; \beta = \frac{E' - E}{k_B T} \;,\; \alpha = \frac{E + E' - 2\sqrt{EE'}\mu_0^{lab}}{Ak_B T} \tag{6}$$

where $cos^{-1}(\mu_q)$ is the angle between $\vec{P} = (mA\vec{V})$ and $\vec{q}$. In the delta function (6) the variables are dimensionless, so that the target speed V is now a multiple of the standard speed $\sqrt{(2k_BT)/m}$. Transforming the variable β to the Fourier Transform variable τ replaces the delta function by an exponential, so that the thermal average can be calculated before performing the inverse Fourier Transform. The resulting joint scattering kernel may then be written formally as :

$$\sigma_s^T(E \rightarrow E'; \Omega \rightarrow \Omega') =$$

$$\frac{[\frac{A+1}{A}]^2}{4\pi k_B T}\sqrt{\frac{E'}{E}}\frac{1}{2\pi}\int_{-\infty}^{\infty} d\tau\; exp[-i(\beta+\alpha)\tau] < exp(-2i\tau\, V\mu_q\sqrt{A\alpha})\;\; \sigma_s^{tab}(E_r) >_T \tag{7}$$

If the energy dependent scattering cross section is replaced by the constant free atom cross section σ_f, the thermal average is readily calculated for a Maxwellian spectrum, since $\cos^{-1}\mu_q$ is the only angle in the integrand; the average becomes simply $exp(-\alpha\tau^2)$. The remaining inverse Fourier transform then results in the ideal gas scattering kernel [4] :

$$\sigma_s^T(E \rightarrow E'; \Omega \rightarrow \Omega') = \frac{[\frac{A+1}{A}]^2\sigma_f}{4\pi k_B T}\sqrt{\frac{E'}{E}}\;\frac{exp(-\gamma^2)}{2\sqrt{\pi\alpha}} \;,\quad \gamma = \frac{1}{2}(\sqrt{\alpha} + \frac{\beta}{\sqrt{\alpha}}) \tag{8}$$

If, on the other hand, the scattering cross section at temperature 0 K , (usually a tabulated cross section, which can be linearly interpolated), is not constant, the thermal average of an integrand involving an angle additional to $cos^{-1}\mu_q$ must be calculated, since the energy E_r depends on $\vec{r} = (\vec{v} - \vec{V})$, i.e. on the angle between $\vec{v}$ and $\vec{V}$. Consequently the calculation of the joint ideal gas scattering kernel as a function of E' and $\vec{\Omega'}$ by means of equation (7)

is very complicated, since it involves the difficulty just referred to, followed by an inverse Fourier Transform. An alternative would be to relate μ_q to $\mu = (\vec{v} \cdot \vec{V})/(vV)$ by making a suitable spherical harmonics expansion, but that would lead to the Legendre Moments of the joint scattering kernel, which are given by equation (5), and not to the full kernel on the left hand side of equations (1) or (7).

In connection with the alternative just mentioned it is certainly easy to show that the Legendre Moment for $n = 0$ of equation (5) is identical, for constant scattering cross sections, with the cumulative kernel obtained from equation (8), by integrating it over all μ_0^{lab} and azimuth angles, see references [2] and [4].

Use of the Kernels in Resonance Absorption Calculations.

The joint scattering kernel of equation (1), or a number of the Legendre Moments in its truncated expansion with upper limit $n = N$ instead of infinity, can be used in neutron transport calculations, in which there is reason to expect that the use of the broadened kernel at temperature T might lead to results, which are different from those obtained by the use of the asymptotic kernel at $T = 0$. Clearly this is in general not the case at epithermal energies of a few eV, since $k_B T$ is only of the order of about a tenth of an eV at operating temperatures of a reactor. If, however, a neutron of energy near one of the pronounced resonance peaks of a fertile nucleus in the reactor fuel is about to interact with such a nucleus, the energy dependence of $\sigma_s(E_r)$, at 0 K, may be important in equations (5) or (7), since the cumulative kernel of the former equation, or the joint kernel of the latter, may transfer the neutron to another energy within the same resonance, at which the fuel scattering cross section may be very different. In a heterogeneous fuel cell this may influence the energy fine structure of the neutron flux, and therefore the resonance absorption rates, to some extent.

Even in integral transport theory, in which the expansion in equation (1) is truncated at $N = 0$, and the zero order moment is calculated by equation (5), resonance absorption calculations will use the broadened scattering kernel $\sigma_{s0}^T(E \rightarrow E')$ consistently with $\sigma_a^T(E)$, rather than the unbroadened $\sigma_{s0}^0(E \rightarrow E')$ at $T = 0$ K, as is common in many of the standard codes dealing with resonance absorption and its temperature changes. On the other hand, such severe truncations make comparisons of the deterministic resonance absorption calculations with Monte Carlo calculations very desirable [5], provided the latter use the full joint scattering kernel. This will be discussed during the presentation of the Paper.

References

1) Weinberg A.M., Wigner E.P., Neutron Chain Reactors p280, Univ. of Chicago Press 1958.
2) Ouisloumen M., Sanchez R., "A Model for Neutron Scattering Off Heavy Nuclides that accounts for Thermal Agitation Effects", Nucl. Sci. Eng., 107, 189, 1991.
3) Rothenstein W., Dagan R., "Two-Body Kinetics Treatment for Neutron Scattering from a Heavy Maxwellian Gas", Ann. Nucl. Energy Vol. 22, pp. 723-730, 1995.
4) Williams M.M.R., "The Slowing Down and Thermalization of Neutrons, p.26" (North Holland Publishing Co., 1966).
5) MacFarlane R., Prael R., Private Communication, Los Alamos, N.M. 1996.

A Comparison of Nodal Methods in Neutron Diffusion Calculations

Barak Tavron, Nuclear Engineering Department, R&D Division, Israel Electric Corporation

The nuclear engineering department at IEC uses in the reactor analysis three neutron diffusion codes based on nodal methods. The codes, GNOMER[1], ADMARC[2] and NOXER[3] solve the neutron diffusion equation to obtain flux and power distributions in the core. The resulting flux distributions are used for the furl cycle analysis and for fuel reload optimization. This work presents a comparison of the various nodal methods employed in the above codes.

Nodal methods (also called Coarse-mesh methods) have been designed to solve problems that contain relatively coarse areas of homogeneous composition. In the nodal method parts of the equation that present the state in the homogeneous area are solved analytically while, according to various assumptions and continuity requirements, a general solution is sought out. Thus efficiency of the method for this kind of problems, is very high compared with the finite element and finite difference methods. On the other hand, using this method one can get only approximate information about the node vicinity (or coarse-mesh area, usually a fuel assembly of a 20 cm size). These characteristics of the nodal method make it suitable for fuel cycle analysis and reload optimization. This analysis requires many subsequent calculations of the flux and power distributions for the fuel assemblies while there is no need for detailed distribution within the assembly. For obtaining detailed distribution within the assembly methods of power reconstruction may be applied. However homogenization of fuel assembly properties, required for the nodal method, may cause difficulties when applied to fuel assemblies with many absorber rods, due to exciting strong neutron properties heterogeneity within the assembly.

Nodal Method Description

In fuel cycle analysis packages the neutron diffusion equation is solved using nodal methods to obtain the neutron flux distribution, power distribution and criticality parameters. Usually in nodal Green function methods the neutron diffusion equation is first integrated over a node to obtain the nodal equation which transfers the point flux values to node average values (see below). Analytic solution is then possible for parts of the nodal equation and with the use of continuity requirements and numeric iterative techniques the global solution is formed. This process relays on constant neutron properties within the node. The solution gives the values of the average node flux and the criticality factor. The two dimensional neutron diffusion equation is:

$$-D_g \nabla^2 \phi_g + \Sigma_{t,g} \phi_g = f_g$$

$$f_g = \frac{\chi_g}{k_{eff}} \sum_{h=1,2} \nu\Sigma_{f,h} \phi_h + \sum_{h \neq g} \Sigma_{h \to g} \phi_h \qquad (1)$$

$$\phi_g = \phi_g(x,y); f_g = f_g(x,y)$$

(Were the symbols have their usual meanings.) By integration over a node we can get the nodal equations:

$$-D_g \frac{d^2\phi_{x,g}}{dx^2} + \Sigma_{t,g}\phi_{x,g} = f_{x,g} - D_g L_{y,g}$$

$$\phi_g(x) = \phi_{x,g} = \frac{1}{h_y}\int_{h_y} \phi_g(x,y)dy$$

$$L_{y,g}(x) = L_{y,g} = \frac{1}{h_y}\int_{h_y} -\frac{\partial^2}{\partial y^2}\phi_g(x,y)dy = \frac{1}{h_y}\left[\frac{J_g(x,y_i) - J_g(x,y_{i-1})}{D_g}\right] \qquad (2)$$

$$f_g(x) = f_{x,g} = \frac{1}{h_y}\int_{h_y} f_g(x,y)dy$$

In the tranverse leakage formula we have made the use of Fick's law. In some analytic methods, like the NOXER code, the analytic solution is generated for the diffusion equation dirctly (1).

Green function nodal method in the ADMARC code

In the ADMARC code a nodal Green function method is used. The nodal equation (2) is solved by wieghted integration. The wieghting function is the Green function which is the solution of equation (2) for a point source at x_0:

$$-D_g \frac{d^2\psi_g(x_0,x)}{dx^2} + \Sigma_{t,g}\psi_g(x_0,x) = \delta(x - x_0) \qquad (3)$$

Nodal Green function methods differ mainly in the Green function boundary conditions selection. In the ADMARC code, infinite medium boundary conditions are used resulting in a relatively simple Green function:

$$\psi_g(x_0,x) = \frac{1}{2KD}e^{-K(x-x_0)} \quad , \qquad K = \sqrt{\frac{\Sigma_t}{D}} \qquad (4)$$

This Green function is used to solve the nodal equation. Based on flux and current continuity on the node boundaries, a system of equations is constructed presenting the average node flux and currents for a given source term. These equations are solved by common iterative techniques (inner iteration). The node flux is then expanded to a forth order polynom. The polynomials' coefficients are determined by the node average flux and currents and by boundary conditions. The expanded flux is used to update the source term (in equation (1)) and to form the outer iteration.

Green function nodal method in the GNOMER code

The GNOMER code is based on other version of nodal Green function method. The Green function boundary condition is selected as in the boundary element technique, (infinite flux at infinity):

$$\psi_g(x_0,0) = 0 \quad ; \quad \lim_{|x_0 - x| \to \infty} \psi_g(x_0, |x_0 - x|) \to \infty \qquad (5)$$

This selection yields the following Green function:

$$\psi_g(x_0, x) = \frac{1}{2K}\sinh(K|x_0 - x|) \qquad (6)$$

In the same manner as in the ADMARC code, the nodal diffusion equation is solved and using continuity conditions, a system of equations is formed to generate the average flux and current (inner iterations). The average flux is then expanded to a third order Legendre polynomials, with coefficients determined by the sub-regions[1] method and used to update the source term for the next iteration (outer iterations).

The analytic nodal method in the NOXER code:

The nodal method in the NOXER code is based on analytic solution of the diffusion equation (1) by the separation of variables technique. The flux is then used to obtain various average node parameters for coupling equations between the nodes and form the system of equations for the average nodal flux in each direction. With assuming that the transverse leakage is proportional to the average node flux:

$$L_{y,g}(x) = g_y \Phi_{x,g} \qquad (7)$$

Where g is the geometrical buckling. The transverse leakage term is also generated. After obtaining new average nodal flux the above equation is used to update the geometrical buckling for the next iteration. The total node average flux is generated from the average integrated flux in each direction.

Comparison between the nodal methods

Two benchmark problems were selected to compare the above nodal methods: the IAEA2D BSS-11 problem[1] and the BIBLIS PWR problem[1]. The IAEA2D benchmark problem presents relatively strong variation in nuclear properties in some core locations therefore one can test the accuracy of the methods for such extreme conditions. The BIBLIS PWR benchmark problem is a typical core configuration. For the BIBLIS benchmark, a reference solution was generated with the finite difference code CITATION[4]. These benchmarks were executed on out DEC Alpha Station 200 with the UNIX command 'time' to obtain values of execution times. The ADMARC version that we have uses 2 nodes per assembly and have fixed reflector size, so we obtained the IAEA2D benchmark results from the paper[2]. Results for the criticality coefficients and execution time are summarized in table 1. The power distribution results are shown in Fig's 1 and 2 for the IAEA2D benchmark and the BIBLIS PWR benchmark respectively. Power differences are calculated as $(P_x\text{-}P_{ref})/P_{ref}*100$.

Table 1: k_{eff} and execution time results

	IAEA-2D case			BIBLIS PWR case		
	k_{eff}	% diff	cpu time sec	k_{eff}	% diff	cpu time sec
CITATION	1.0295504	0.0	17.346	1.0251933	0.0	18.387
GNOMER	1.0296300	0.0073%	0.1940	1.0251300	-0.0062%	0.2740
ADMARC*	1.0291600	-0.038%	1.7890	na	na	na
NOXER	1.0294800	-0.0068%	0.6910	1.025922	0.0710%	1.0190

*Estimated execution time on DEC Alpha-200, k_{eff} results from[2].

0.7455	1.3099	1.454	1.211	0.6098	0.9353	0.9345	0.7551
-0.11	-0.94	-0.68	-0.78	0.23	-0.19	0.37	0.70
-0.21	-0.22	-0.19	-0.17	-0.10	-0.02	0.07	0.02
-0.79	2.23	2.65	1.87	-1.803	0.05	-0.42	-2.86
1.3099	1.4351	1.4798	1.3149	1.0698	1.0361	0.9503	0.7357
-0.94	-0.59	-0.51	-0.35	-0.41	0.07	0.45	0.99
-0.22	-0.19	-0.18	-0.14	-0.10	0	0.08	0.22
2.22	1.77	1.26	1.30	1.13	-0.21	-1.37	-2.79
1.454	1.4798	1.4693	1.3453	1.1792	1.0705	0.9749	0.692
-0.68	-0.51	-0.44	-0.25	-0.1	0.21	0.13	0.51
-0.19	-0.18	-0.16	-0.13	-0.06	0.02	0.11	0.42
2.65	1.25	0.41	0.72	1.63	-0.47	-2.80	-4.89
1.211	1.3149	1.3453	1.1928	0.967	0.9066	0.8459	
-0.78	-0.35	-0.25	-0.09	-0.21	0.67	1.05	
-0.17	-0.14	-0.13	-0.08	-0.04	0.1	0.27	
1.87	1.31	0.72	0.96	1.09	0.39	-2.14	
0.6098	1.0698	1.1792	0.967	0.4705	0.6856	0.5969	
0.23	-0.41	-0.1	-0.21	0.62	0.28	0.72	
-0.1	-0.1	-0.06	-0.04	0.04	0.16	0.45	
-1.80	1.14	1.63	1.09	-1.98	0.38	-1.73	
0.9353	1.0361	1.0705	0.9066	0.6856	0.585		
-0.19	0.07	0.21	0.67	0.28	0.32		
-0.02	0	0.02	0.1	0.16	0.48		
0.05	-0.21	-0.47	0.39	0.38	-2.18		
0.9345	0.9503	0.9749	0.8459	0.5969			
0.37	0.45	0.13	1.05	0.72			
0.07	0.08	0.11	0.27	0.45			
-0.40	-1.37	-2.80	-2.13	-1.73			
0.7551	0.7357	0.692					
0.70	0.99	0.51					
0.20	0.22	0.42					
-2.86	-2.77	-4.88					

Reference Solution
Gnomer %diff
Admarc %diff
Noxer %diff

Fig 1: Nodal power distribution from IAEA2D Benchmark

The maximum difference in node power from GNOMER code is 1.052%, from ADMARC code is 0.48% and from NOXER code is 4.89%.

1.0609	1.0694	1.2117	1.1918	1.0697	0.9672	1.0842	1.0052
1.81	2.52	1.65	2.10	1.14	1.59	0.93	1.22
2.09	2.55	2.57	2.15	1.36	0.95	0.42	-1.48
1.0696	1.0888	1.1047	1.1983	1.0475	1.0191	1.0613	0.9616
2.49	1.68	2.22	1.37	1.79	0.94	1.13	1.28
2.53	2.30	2.42	2.166	1.30	0.85	1.35	1.03
1.2131	1.1056	1.0992	1.0829	1.1035	0.911	0.9225	0.8169
1.54	2.15	1.32	1.84	1.05	1.51	1.13	1.64
2.46	2.33	1.99	1.78	1.75	0.69	0.89	1.94
1.1944	1.2006	1.0841	1.1438	1.0236	0.9403	0.7569	0.5402
1.88	1.18	1.73	1.00	1.73	1.03	2.02	1.44
1.92	1.98	1.67	1.95	1.60	1.20	0.46	-1.17
1.0734	1.0509	1.1061	1.0247	1.1109	0.9826	0.8658	
0.79	1.47	0.82	1.62	1.04	2.01	1.70	
1.02	0.98	1.51	1.47	1.78	2.36	2.50	
0.972	1.0237	0.9144	0.9425	0.9836	1.1887	0.6779	
1.09	0.48	1.14	0.79	1.91	2.25	1.17	
0.45	0.39	0.32	0.96	2.26	3.75	0.57	
1.0905	1.0672	0.9271	0.7596	0.8674	0.6784		
0.35	0.57	0.63	1.65	1.51	1.10		
-0.15	0.78	0.39	0.10	2.32	0.48		
1.0114	0.9674	0.8214	0.5427				
0.60	0.68	1.08	0.97				
-2.09	0.43	1.38	-1.61				

Citation Reference
Gnomer %diff
Noxer %diff

Fig 2: Nodal power distribution from BIBLIS PWR Benchmark

The maximum difference in node power from GNOMER code is 2.52% and from NOXER code is 3.75%.

Summary

Two Green function nodal methods and one analytic nodal method have been evaluated and compared. In the Green function methods approximations are mainly in the source term to polynomial expansion and the iterative process. In NOXER analytic nodal method separation of variable is performed and the transverse leakage is assumed to be proportional to the total node flux. In the Green function methods the source term is calculated iteratively canceling the coupling between the energy group diffusion equations and therefore simplifying the process. On the other hand this introduce the need for inner and outer iterations. In the analytic method the separation of space variables is assumed while maintaining the energy group coupling. The inner iterations are only performed for each direction.

All the above methods provide very good accuracy in predicting the core multiplication factor. Also the node power shape differences are less then 5%, which is suitable for purposes of fuel cycle optimization. The GNOMER code shows the best results and as described in the reference 1 it can be used for detailed fuel cycle analysis as well as for assembly calculations (with addition of homogenization programs). On general, codes based on nodal methods proved to be more than 10 times faster than codes based on finite difference methods, thus making the method superior for fuel cycle calculations.

References

1. Trkov, M. Najzer and L. Skerget, "Variant of Green's Function Nodal Method for Neutron Diffusin", J. of Nuclear Science and Tech. Vol. 27, No. 8, pp. 766-777, (1990).

2. Moon and S. Levine, "A fundamental Derivation of the Nodal Diffusion Eqution and Its Variation", Nuclear Science and Engineering, Vol. 104, pp. 112-122, (1990)

3. Segev, "Two-Group Diffusion Theory based on separation of variables", Ann. Nucl. Energy, Vol 15., No1, pp.1-16, (1988)

4. Fowler and D. R. Vondy, "Nuclear Reactor Core Analysis Code: CITATION", ORNL-TM-2495, Rev. 1, (1969)

The Use of Routine Cell Codes for Evaluating the In-rod Effective Cross Sections of a Resonance Absorber

M.SEGEV
BEN GURION UNIVERSITY, ISRAEL
OCTOBER 1996

The last three years have witnessed an increasing interest in the in-rod distribution of resonance absorption and of temperature. High burnup, especially beyond the 'clasical' limit of 30 GWd/T, is expected to generate uneven in-rod isotope distributions with consequences for fuel rod integrity and reactor Doppler feedback. There are recent indications that, even for a freshly loaded uranium-oxide rod, proper account of the U238 in-rod absorption rate distribution results in a doppler coefficient some 15% lower in magnitude than its routinely calculated value.

Presently a special form of application is made of the Bogart approach[1]. this approach is based on the fact that, as a fuel rod is filled in from the outside, its resonance capture rate increases monotonically, despite the decreasing effective capture cross section for the thickening annulus. Bogart used this observation to derive a differential equation for the in-rod absorption distribution. Presently we capitalize on the idea in a discrete form.

In the absence of burnup experimental data of the kind that may generate information on the in-rod capture and cross section distribution, Tellier et al.[2] have resorted to Monte-Carlo calculations chosing typical PWR lattice parameters. When the in-rod distributions that come out of these MC 'experiment' are corrected near the rod periphery as suggested by Bogart[3], then the present method yields in-rod distributions that perfectly match the 'experiment'.

The present method is applicable to radially dependent absorber density and temperature. For radially flat density and temperature σ^{eff} for a sub region (r_1,r_2) inside the rod (0,R) is

$$\sigma^{eff}(r_1,r_2) = \frac{I[r_1,R]\left(R^2 - r_1^{\,2}\right) - I[r_2,R]\left(R^2 - r_2^{\,2}\right)}{\left(r_2^{\,2} - r_1^{\,2}\right)} \qquad (1)$$

Where I(r,R) is the resonance integral for the absorber in an annulus extending from r to R.

In order to apply eq. (1), one must know how to calculate the resonance integral for a lattice of (r,R) annular absorbers. A way of achieving this with the aid of cell codes designed for solid cylindrical fuels is to equate

$$I(r,R) = I(s) \qquad (2)$$

where

$$s = \text{radius of a solid cylindrical absorber} \qquad (3)$$

The realization of eq. (2) is enabeled by an 1981 article[4], in which (r,R) resonance integrals are equvalenced to (s) resonance integrals.

The application reported here is in the WIMS code. The Tellier 'benchmark' lattice specifies typical PWR pin and

lattice, with temperatures of $27C^0$ all over. The resonance energy range considered for the MC calculation was 1500 to 2.8 eV. The closest duplication of this range, possible with the WIMS group structure, is 1425 to 4.0 eV. The application yielded, among other, the hystogram of Fig 1. It is to be noted that it well matches the continous curve given by Bogart[3] as his solution for the 'french benchmark'. At the peripheral 10 v/0 the french MC capture rate is 30% lower. Bogart[3] has forwarded an argument as to why the MC rate at the peripheral 10 v/0 is expected to fall 30% short of the correct value.

REFERENCES

2. H. Tellier et al.
Heavy Nucleus Resonant Absorption Calculation Benchmarks
Nucl. Sci. Eng. 113 (p. 20) 1993

1. D. Bogart
Radial Resonance Captures In U238 Metal Rods and Spatial Resonance
Production of Pu239 In Uranium-Oxide Fuels
Nucl. Tech. 112 (p. 9) 1995

3. D. Bogart
Inconsistencies in Widely used Monte carlo methods for Precise calculation
of Radial Resonance Captures in Uranium Fuel Rods
Nucl. Sci. Eng. 123 (p.228) 1996

4. M. Segev
An Equivalence Relation for a Lattice of Annular Absorbers
Nucl. Sci. Eng. 77 (p. 229) 1981

Fig 1. % Resonace Absorption (Accumulative) in U238 Across the Rod of the 'French Benchmark' Lattice

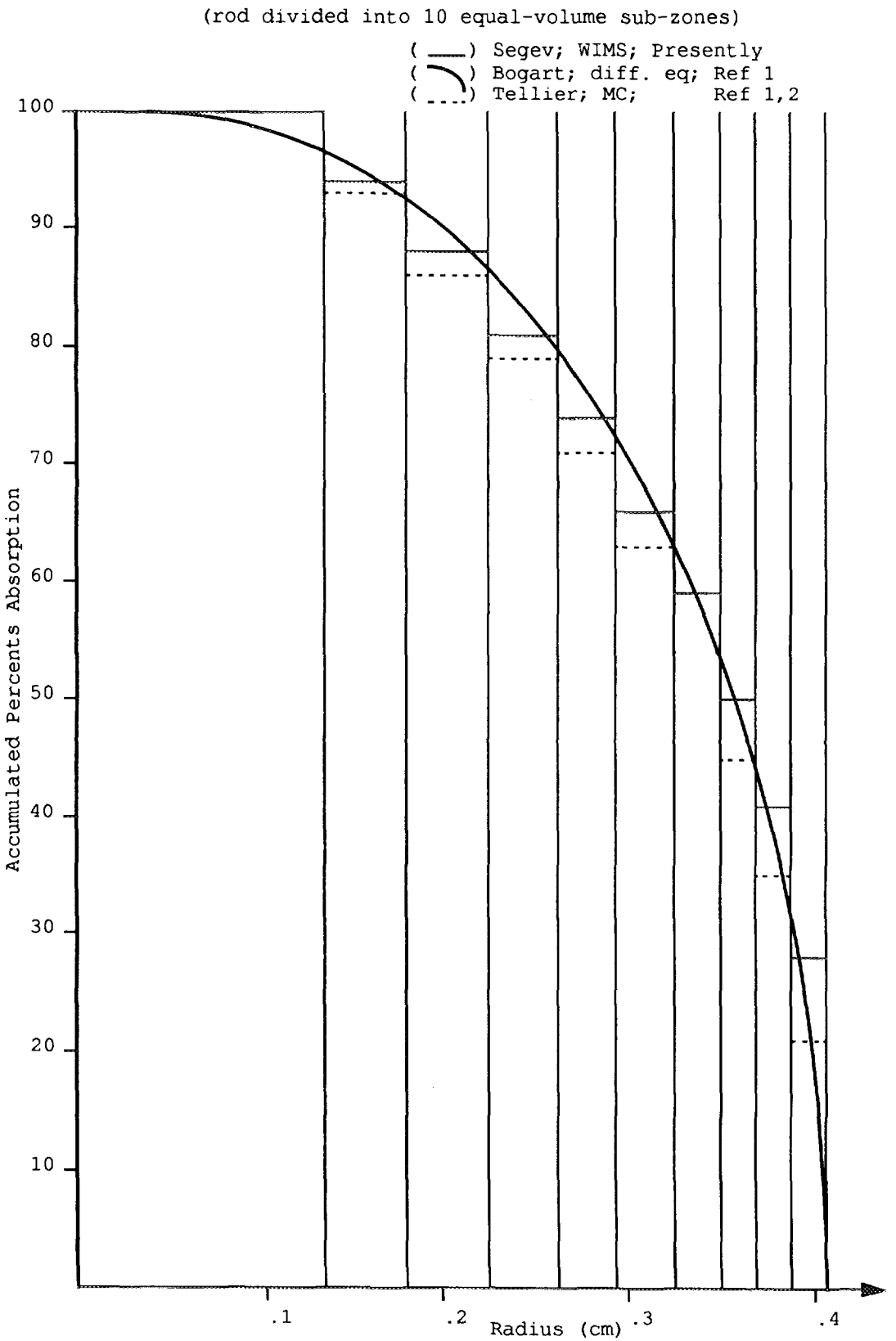

ANALYSIS OF FISSION-RATE-RATIO MEASUREMENTS IN THE NIST IRON SPHERE FIELD

Perel R.L., Wagschal J.J. and Yeivin Y., Racah Institute of Physics,
The Hebrew University of Jerusalem

The evaluation of radiation damage in stainless-steel reactor pressure vessels requires reliable iron cross sections. However, cross sections in general, and those of iron in particular, in even the more recent evaluated-cross-section libraries (e.g. ENDF/B-VI[1]) are not yet reliable enough to satisfy the needs of the dosimetry as well as those of other user communities. Even if the uncertainties due to the approximations involved in the calculational models and numerical schemes are negligible, the uncertainties in calculated responses — due to the uncertainties in the given cross sections — generally are such as to make these responses rather doubtful. Speaking of cross-section (limited) reliability, we refer not only to their nominal values, but also to the uncertainties (collective noun for variance and covariance) in these values. To illustrate the argument about the modest quality of present-day cross-section data, we quote Ref. 1 (p.154): "The ^{56}Fe(n,n') cross section exciting the 0.847 MeV level up to an incident neutron energy of 5 MeV is known to about 5–10%, but an accuracy of 2% is needed for reactor pressure vessel surveillance dosimetry."

In the analysis of any problem, involving the calculation of physical quantities which are functions of certain cross sections, an essential element is the evaluation of the partial derivatives, i.e. the sensitivities of each response to every parameter. The sensitivities are, first of all, necessary to determine the uncertainties in the calculated responses, and for a given response the sensitivities serve to find the "more important" parameters. As the geometry of an assembly becomes even moderately complex, if time-dependent solutions are required, or when point, rather than multi-group, cross sections are called for, then deterministic calculations become unacceptably time consuming.

To overcome these difficulties we turn to MC calculation of the responses and their sensitivities. Then the geometry poses no serious problems, time-dependent problems are as easy to solve as stationary ones and, surprisingly, the differential-operator method, suggested by Hall,[2] reformulated in an elegant paper by Rief,[3] and recently adapted to the evaluation of point-detector sensitivities,[4] facilitates the evaluation of all the sensitivities of all the responses in the one MC run that calculates the responses.

A detailed description of the differential-operator method and the rigorous derivation the actual algorithm for the evaluation, in one MC run, of both the great number of responses and all their sensitivities are given in Ref. 4.

In this work we will present the sensitivities of the recently measured[5] ^{237}Np/^{238}U fission-rate-ratio, in the NIST-Iron-Sphere field, to the ^{56}Fe elastic- and first-level-inelastic-scattering cross sections. The reported measured value of this response is 18.25 and our calculated value, based on ENDF/B-VI data, is 18.65. The respective relative statistical uncertainties are 0.26 and 0.8 percent.

The NIST Iron Sphere has a radius of 25.35 cm, and its density is 7.831 gr/cc. Its isotopic composition is also given. ROSPEC energy-leakage-spectrum measurements at both 1 and 2 meters from the center were performed, as well as fission-rate-ratio measurements at 30 cm from the center, utilizing the NIST back-to-back double-fission chambers[6]. Traditionally, the NIST fission-rate-ratio measurements are very

accurate, and these measurements in the Cf and ISNF standard neutron fields already serve as integral responses in LEPRICON.[7]

It is important to understand the sensitivities of the various fission-rate ratios to the sphere's cross sections, in particular to those of ^{56}Fe. Figure 1 depicts the relative sensitivity of the ^{237}Np/^{238}U fission-rate ratio to the ^{56}Fe elastic- and first-level-inelastic-scattering cross sections. Recall that if R1 is reaction rate of type 1, and R2 reaction rate of type 2, then the relative sensitivity of R1/R2 to a parameter p is

$$\frac{p}{R1/R2}\frac{\partial(R1/R2)}{\partial p} = \frac{p}{R1}\frac{\partial R1}{\partial p} - \frac{p}{R2}\frac{\partial R2}{\partial p};$$

i.e. the difference between the two reaction-rate relative sensitivities. Obviously, the relative sensitivity of this ratio to the first-level-inelastic-scattering cross section vanishes below 847 keV, the energy of the first excited level. One also notices that the sensitivities to the elastic- and inelastic-scattering cross sections are negative at the lower energies up to about 1.5 MeV, and positive at higher energies. The maxima of the relative sensitivities to the elastic- and inelastic-scattering cross sections are at about 1.7 MeV. This energy is slightly higher than the ^{238}U effective fission threshold. An elastic- or inelastic-scattering event at about 1.7 MeV slows the neutron down to below that threshold, diminishes the denominator in our fission-rate ratio and thus increases the response. One has to keep in mind that in an elastic-scattering event the neutron can lose at most $[4A/(A+1)^2]E$ which is 117 keV for a 1.7 MeV neutron elastically scattered on ^{56}Fe. On the other hand, a neutron exciting the first level loses over 850 keV. It is worth noting that due to this the sensitivity to the inelastic-scattering cross section has a much wider maximum than the sensitivity to the elastic-scattering cross section. There is, of course, much more structure in the sensitivities of Fig. 1.

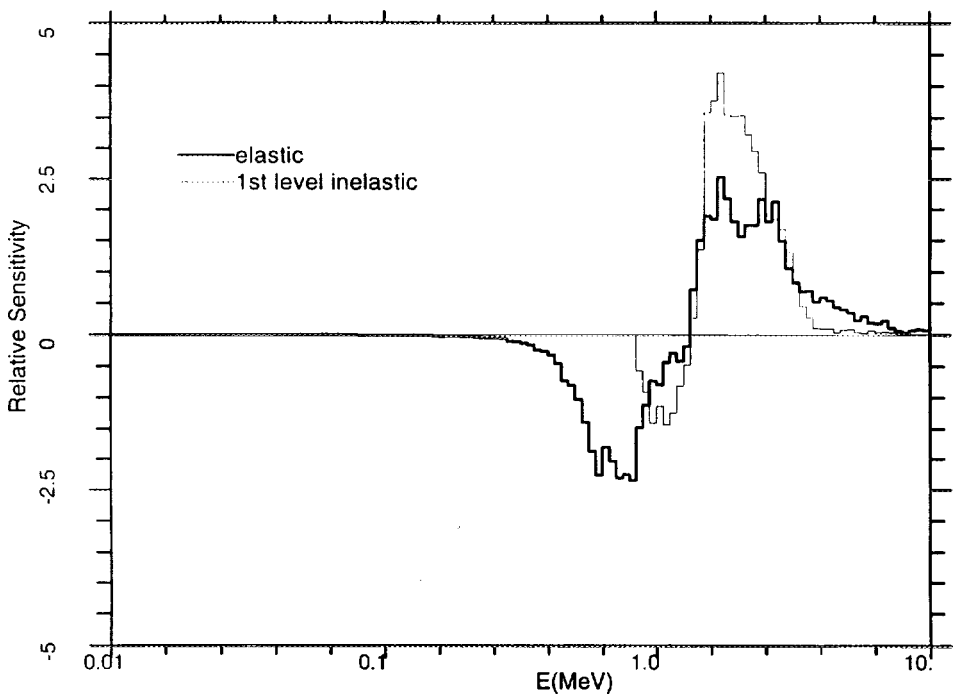

Fig 1: The relative sensitivities of the ^{237}Np/^{238}U fission-rate ratio, at 30 cm from the center of the NIST iron sphere, to the ^{56}Fe elastic- and first-level-inelastic-scattering cross sections

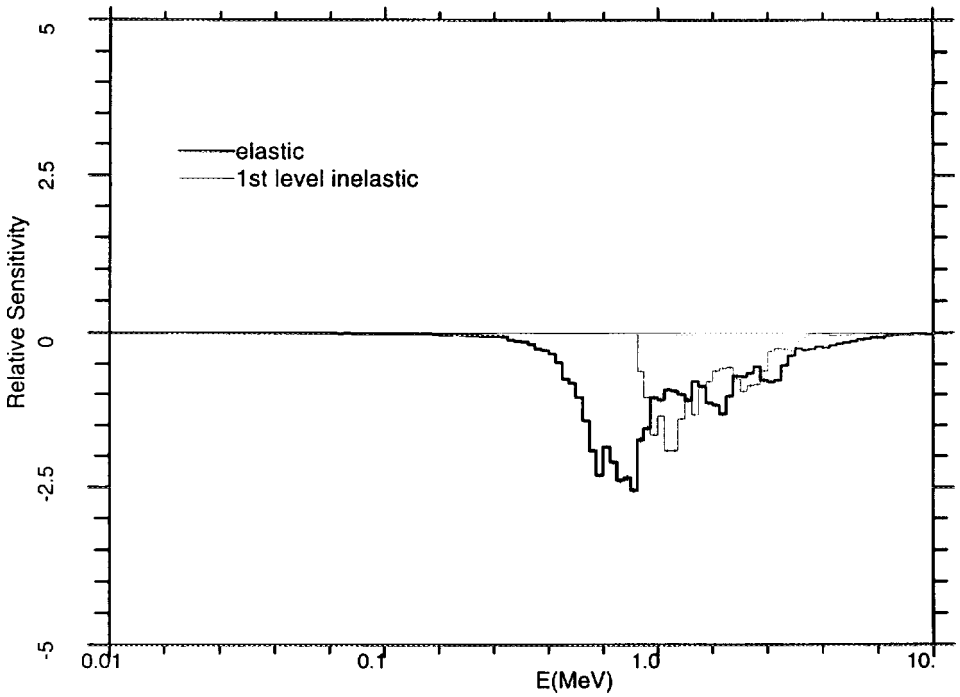

Fig 2: The relative sensitivities of the ^{237}Np fission rate, at 30 cm from the center of the NIST iron sphere, to the ^{56}Fe elastic- and first-level-inelastic-scattering cross sections

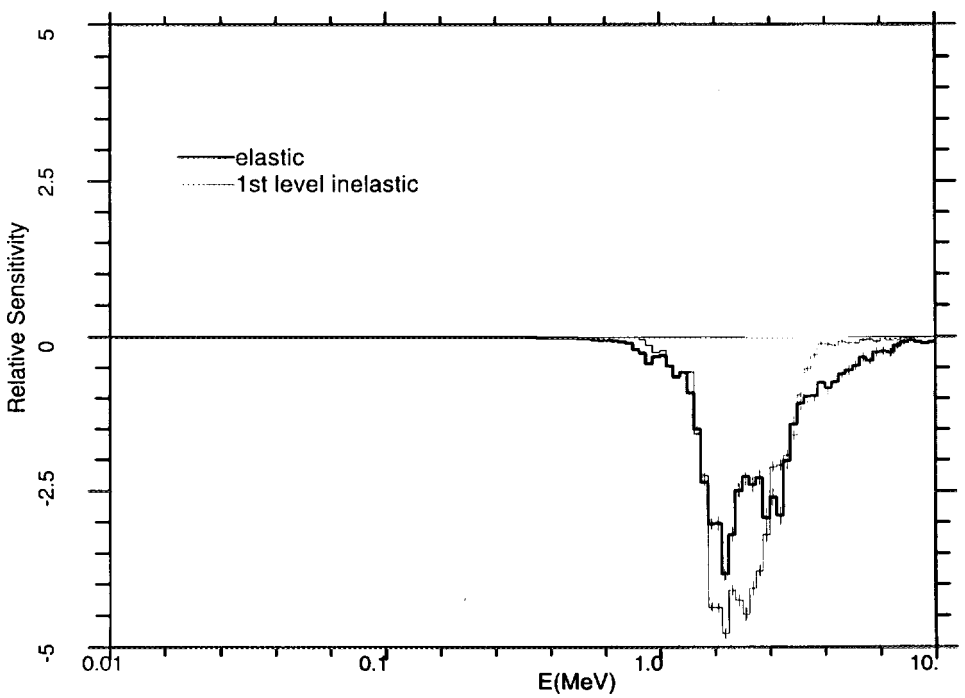

Fig 3: The relative sensitivities of the ^{238}U fission rate, at 30 cm from the center of the NIST iron sphere, to the ^{56}Fe elastic- and first-level-inelastic-scattering cross sections

Much insight can be gained by understanding what is behind each peak or valley in the sensitivity curves. The physical picture becomes much more intelligible as one examines the sensitivities of each reaction rate apart, and recalls that the relative sensitivity of the ratio is just the difference between the two respective relative sensitivities of the numerator and denominator. Figs. 2 and 3 respectively represent the relative sensitivities of the ^{237}Np and ^{238}U reaction rates to the ^{56}Fe elastic- and first-level-inelastic-scattering cross sections. Both elastic and inelastic scattering slow the neutrons down, and thus, unless there is a very substantial change in the relevant cross section, fission in our case, these sensitivities will be negative. In other words, the response will be smaller for an increase in a scattering cross section. An interesting difference between Figs. 2 and 3 can be noticed in the energies at which the sensitivities start to differ from zero. Since the ^{237}Np fission threshold is lower than the ^{56}Fe first excited level, we can see in Fig. 2 that the sensitivity to the ^{56}Fe elastic-scattering cross section starts to become negative at the fission threshold and that the sensitivity to the first-level-inelastic-scattering cross section starts to differ from zero only at energies higher than the first excited level energy. In Fig. 3, on the other hand, both sensitivities start to become negative at energies that are slightly higher than the effective fission threshold of ^{238}U, which is higher than the 847 keV first excited level. Thus we can now understand the features of the two curves in Fig. 1, which are just the respective differences between the two curves in Fig. 2 and the corresponding curves in Fig. 3. The sensitivity analyses of other fission reaction-rate ratios outside the NIST iron sphere are just as illuminating.

Referring to the MC calculation of responses and sensitivities, an additional remark is worth our while. Direct simulation is extremely inefficient. Therefore, in a practical game paths are sampled collision by collision, and the contributions of individual collisions to a response are collected and their sum is the path's estimate of this response. The differential-operator method addresses the simultaneous evaluation of the contributions of each collision to all the relevant sensitivities of the response. The result is a convenient and highly efficient tool for the one-shot evaluation of the multitude of sensitivities, of as many responses as there might be, together with the very responses, which in fact makes the kind of analysis we have presented possible and even very practical.

REFERENCES

1. P.F. Rose, ed., *ENDF/B-VI Summary Documentation.* BNL-NCS-17541 (ENDF-201), 4th edition. (National Nuclear Data Center, Brookhaven National Laboratory, 1991)
2. M.C.G. Hall, Nucl. Sci. and Eng. **81**, (1982) 423
3. H. Rief, in *Uncertainty Analysis,* Y. Ronen, ed. (CRC Press, 1987) p. 187
4. R.L. Perel, J.J. Wagschal and Y. Yeivin, Nucl. Sci. and Eng. **124** (1996) 197
5. J.S. Nico, J.M. Adams, C. Eisenhauer, D.M. Gilliam and J.A. Grundl, "^{252}Cf Fission Neutron Transport Through an Iron Sphere," in *Ninth International Symposium on Reactor Dosimetry* (Prague, September 1996).
6. D.M. Gilliam et al., in *Nuclear Cross Sections and Technology,* R.A. Schrack and C.D. Bowman, eds.(NBS special publication 425, 1975) Vol. I, p. 270
7. R.E. Maerker, B.L. Broadhead and J.J. Wagschal, Nucl. Sci. and Eng. **91** (1985) 369

Transport in Stochastic Multi-Dimensional Media

O. Haran, D. Shvarts, NRC, Negev & **R. Thiberger,** Ben-Gurion University, Beer-Sheva

Purpose: Many physical phenomena evolve according to known deterministic rules, but in a stochastic media in which the composition changes in space and time. Examples to such phenomena are heat transfer in turbulent atmosphere with non uniform diffraction coefficients, neutron transfer in boiling coolant of a nuclear reactor and radiation transfer through concrete shields. The results of measurements conducted upon such a media are stochastic by nature, and depend on the specific realization of the media.
In the last decade there has been a considerable effort[1-7] to describe linear particle transport in one dimensional stochastic media composed of several immiscible materials. However, transport in two or three dimensional stochastic media has been rarely addressed[8,9]. The important effect in multi-dimensional transport that does not appear in one dimension is the ability to bypass obstacles. The current work is an attempt to quantify this effect.

Method: We considered the multi-dimensional purely scattering binary stochastic transport problem. The work is based on various Monte Carlo simulations. It included one, two and three dimensional simulations of transport in random media, and also several 'modified' one dimensional simulations aimed to approximate the multi-dimensional effects.
A straight forward way to investigate transport in stochastic media is to create multiple realizations of the media, solve for the particle flux through them, and then ensemble average the results. Realizations of stochastic media can be created using various algorithms. In this work, we considered binary markovian realizations created using a Kubo-Anderson process[9]. In this process, a random grid is build, in which the distance between adjacent lines is sampled from a given chord length distribution function. A one dimensional random media is thus a line composed of alternating material segments. A two-dimensional random media is a plane cut by a random two-dimensional grid to rectangles of different widths and lengths. A three-dimensional random media is a space cut by the three-dimensional grid to paralleloids of different widths, lengths and depths. The materials that fill the segments (1D), rectangles (2D) and paralleloids (3D) are randomly chosen. Monte Carlo method is then used to calculate the transmission and reflection of the media. In order to be able to compare between the results reached in media of different dimension, the chord length distribution seen by a crossing particle should be the same in all simulations. Therefore, the particles were allowed to move only along the discrete directions defined by the grid - X (1D), X,Y (2D) or X,Y,Z (3D). Effective one material cross sections for the 1D, 2D and 3D randomly mixed media were found by comparing the results to those obtained for 1D, 2D and 3D homogeneous media. The solid lines in figure 1 describe the effective cross sections of the 1D, 2D and 3D random media versus the media's optical depth. The 1D effective cross section exhibits a bell shaped minimum for intermediate optical depths, matching previously published results[5]. However, the 2D and 3D effective cross sections remain low for optically thick media, implying relatively high transmission, as a result of the bypassing effect.

As noted earlier, the main difference between 1D and multi-dimensional transport is the ability to bypass obstacles, due to the particles' ability to scatter sideways. As a result of such a sideways scattering followed by a forward scattering, the particle face different packet sizes, and can even find itself in a different material ('*scattering coupling*'). In the following lines we shall introduce a quantification of the bypassing effect by using an equivalent notation to multi-dimensional scattering in one dimensional calculations, resulting in an effective cross section that approximates multi-dimensional behavior. The notation is as follows:

An equivalent 1D scattering is considered as an event in which the particle can forget its former path. We denote the particle's probability to remember its path after a collision as 'Immediate Correlation per Collision (*ICC*)'. It is analogous to the particle's probability to be scattered forward or backward along its former path, and not sideways. The *ICC* of one dimensional transport is 1.0 since there exists only one possible path. In optically thin packets, the *ICC* fit to describe discrete directional transport (transport parallel to the gridlines) in 2D stochastic media is $\approx 1/2$ and in 3D is $\approx 1/3$. However, in thick packets, multiple scattering interactions can redirect the particle to its former path while still in the same packet, so the particle has a certain probability of restoring the information about its past trajectory (its 'memory').

We introduce the 'Immediate Correlation per Packet (*ICP*)', which describes the particle's probability of exiting a packet along the entering path. In Kubo-Anderson packets and discrete directional transport, the *ICP* is exactly 1.0, 1/2 or 1/3 depending on the dimension of the media. Most real random packets are not paralleloids/rectangular, so it is harder to quantify their *ICP*. Future work will consider the *ICP*'s quantification for packets of different shapes.

The *ICC* notation is easier to implement into simulations and analytical models than the *ICP*'s. However, a physical packet is best described by the *ICP* parameter. These two parameters are connected through the number of collisions per packet. A simple connection can be constructed assuming that there are τ_i scattering interactions in a packet (τ_i being the average optical depth in packet of material i). The *ICP* is equal to the probability that the particle retains its memory after τ_i interactions,

$$ICP = ICC^{\tau_i} \tag{1}$$

We introduced *ICC*'s smaller than 1.0 to one dimensional Monte Carlo simulations. The scattering routine samples a random number and chooses whether or not the particle retains the information about the realization. When the particle loses its memory, a new realization is created around it as it moves through the media. The results of such partial memory simulations are described in figure 1 using dashed lines - *ICC=0* result and the result from choosing *ICC* according to eq. 1. '*Scattering coupling*' was also introduced by means of letting the scattering interaction occasionally change the surrounding material, but only in the interactions that caused a lack of memory.

We introduced the *ICC* concept as an interpolation between two models - the *Levermore model*[4](an analytical description of no-memory transport in markovian chord statistics, that matches the *ICC=0* simulation results) and the *Interface model*[7](an improvement to the *Levermore model* using a higher order closure for the flux near the interfaces. This model is a fair approximation to normal 1D transport (*ICC=1*)). The difference between the two models is in the scattering term in the equations for the fluxes near the interfaces. Use of a linearly interpolated scattering term results in an effective cross section that fairly agrees with the effective cross-section from equivalent partial memory Monte Carlo simulations.

The *ICC/ICP* formulation lacks the ability to evaluate the "Late Correlation" of the media, the particle's probability of returning to packets it encountered during its history. This probability was also introduced to one dimensional simulations, in the following way. At each scattering event, if a particle lost his memory, it had a certain probability of moving along previous paths. The Late Correlation was found to be of less importance then the *ICP*.

Results: The results obtained referred to markovian pure scattering media in which the materials occupy equal length(1D)/area(2D)/volume(3D) fraction, the ratio between their cross-sections is 100:1, and the averaged optical lengths of packets is 2.0. Fig. 1 shows the effective cross-section divided by the averaged (homogenized) cross section evaluated in 1D, 2D and 3D simulations, along with the *ICC=0* line which is equivalent to the *Levermore model*[4], and the result of one dimensional simulation where the *ICC* was chosen to approximate 2D obstacle bypassing according to eq.1. Results are plotted versus the media's optical depth. The difference between the last simulation and the real 2D results is due to the inexact connection *ICC-ICP* , inexact *scattering coupling* and the lack of *Late Correlation.*

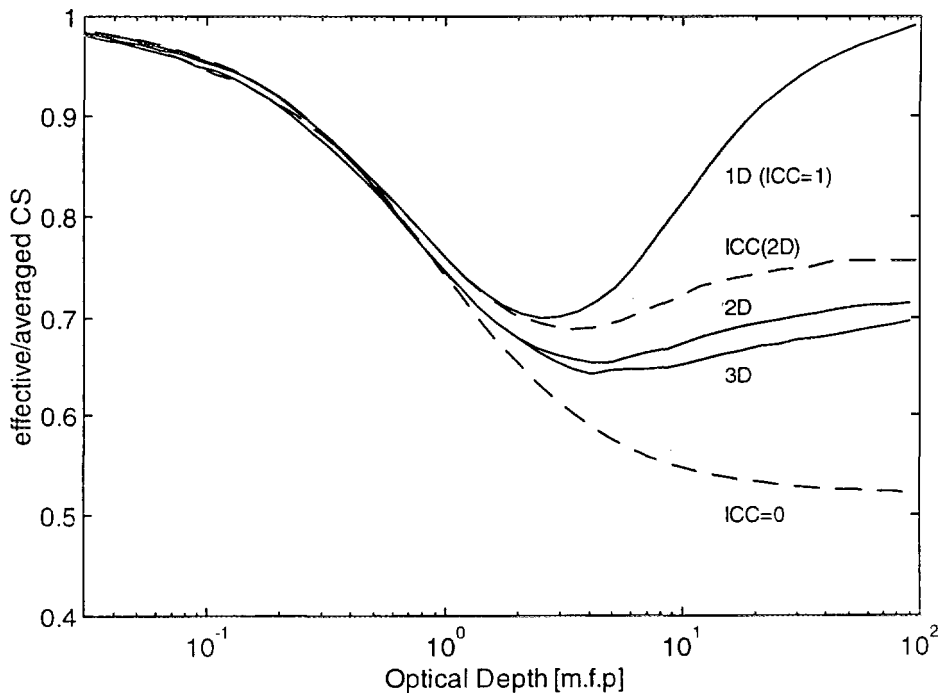

figure 1 - Effective scattering cross-section vs. media optical depth. The results shown are from 1D, 2D and 3D Monte Carlo simulations, from 1D simulation with *ICC*=0 (no memory transport), and from 1D simulation with *ICC* chosen to approximate 2D obstacle bypassing (eq. 1). The statistical accuracy of the Monte Carlo simulations are negligible ($< 1/2\%$).

Conclusions: This work considered multi-dimensional effective transport in randomly mixed media. It was shown that it differs from 1D effective transport as a result of the bypassing effect. This effect was analyzed using the concepts of partial memory per collision and partial memory per packet.

[1] C. D. Levermore, G. C. Pomraning, D. L. Sanzo and J. Wong, '*Linear Transport Theory in a Random Medium*', J. Math. Phys. **27**,2526 (1986)
[2] D. Vanderhaegen, '*Impact of a Mixing Structure on Radiative Transfer in Random Medium*', JQSRT **39**,333 (1988)
[3] D. Vanderhaegen, '*Radiative Transfer in Statistically Heterogeneous Mixtures*', JQSRT **36**,557 (1986)
[4] D. C. Levermore, J. Wong, G. C. Pomraning, '*Renewal Theory for Transport Processes in Binary Statistical Mixtures*', J. Math. Phys. **29**,995 (1988)
[5] D. Vanderhaegen, C. Deutsch, '*Linear Radiation Transport in Randomly Distributed Binary Mixtures: A One Dimensional And Exact Treatment for the Scattering Case*', J. Stat. Phys. **54**,331 (1989)
[6] G. C. Pomraning, '*Radiative Transfer in Random Media with Scattering*', JQSRT **40**,479 (1988)
[7] G. C. Pomraning, '*A Model for Interface Intensities in Stochastic Particle Transport*', JQSRT **46**,221 (1991)
[8] P. Boisse, '*Radiative Transfer Inside Clumpy Media: The Penetration of UV Photons Inside Molecular Clouds*', Astron. Astrophys. **228**,483 (1990)
[9] S. Audic, H. Frisch, '*Monte Carlo Simulation of a Radiative Transfer Problem in a Random Medium, Application to a Binary Mixture*', JQSRT **50**,127 (1993)

Revised Dose Limits and a New Respiratory Tract Model and Their Implications for the Annual Limits of Intake of Radioactive Materials - A Review of Recent ICRP Publications

T. Shlesinger, I. Silverman and M. Shapira
Soreq - NRC, Yavne 81800, Israel.

Introduction

Ionizing radiation may cause immediate and/or delayed biological damages to the body of the exposed person and/or his/her progeny. The exposure may be caused by an external source or may arise due to internal contamination by a radioactive material. In order to prevent such exposure, or to reduce the probability that it will occur, national authorities and international organizations that are engaged in radiation safety and protection have set limits for the exposure to ionizing radiation from either source. The sensitivity of the body to ionizing radiation usually decreases with age. For this reason and due to the limited possibilities to control the exposure of the general public, different limits have been set for for occupational exposure and for the exposure of members of the public of different age groups. The general principles of these limits and guidelines for their calculations are set by the International Commission on Radiological Protection (ICRP) and published in the Annals of the ICRP. The basic philosophy of the Commission, which includes the principles of justification, optimization and dose limits, the basic radiobiological models, and the distinction between stochastic and non-stochastic effects has been presented in its publication no. 26 [1]. Based on this philosophy, the Commission issued between 1979 and 1988 a series of publications followed by annexes and addenda known as publication no. 30 ([2]- [9]). This series presented models describing the metabolism of radioactive materials which enter the body by inhalation and ingestion, the transfer of such materials from the respiratory tract and the gastrointestinal tract to the blood, and from there to the body organs and the excretion of the material from the body. This series presented also values for biokinetic parameters of these systems and transfer paths, and methods for calculating limits on intake which ensure that the exposure from internal contamination will not exceed the dose limits set by the Commission.

In 1990, the ICRP issued publication no. 60 [10], which is a revision to and extension of no. 26 published in 1979. In publication no. 60 the Commission presented revised dose limits. These limitations are based on evidence from recent research indicating that the carcinogenic risks of exposure to ionizing radiation are greater than previously thought. The new risk factors were found to be 4 to 8 times greater than those presented in publication no. 26. Following publication no. 60, the Commission recalculated the ALI values, based on the new recommendations, and presented the new values in publication no. 61 [11]. The epidemiologic data from these research studies enabled the Commission to establish detailed quantitative estimations for the probabilities of cancer morbidity and mortality due to exposure of specific organs and tissues to ionizing radiation. These and other research projects helped to establish improved biokinetic parameters regarding the inhalation and ingestion of radioactive materials and their distribution in the human body. A new respiratory tract model, based in part on these data, was presented in publication no. 66 [12].

The next section of this review describes the features of the new model and the differences between the new and the old respiratory tract models. Following this, the revised dose limits and annual limits on intake, based on the new model and new biokinetic data, are presented.

The new respiratory tract model

A need to estimate the effect of exposure of the general public to ionizing radiation due to internal contamination via inhalation motivated the ICRP to develop a new respiratory tract model in 1994 (presented in publication no. 66 of the ICRP [12]). This is a detailed model of the respiratory tract that is much more accurate than the old model described in part I of publication no. 30 [2]. The new, detailed description, of each part of the respiratory tract, the size and function of which are age-dependent, enables the estimation of doses, due to inhalation of radioactive material, for the general public including infants and children of all ages. Moreover, it provides a way to calculate actual doses to specific groups of people due to known incidents, a task impossible with the old model. A full and interpreted description of the new model was published by us in Hebrew [13].

The model divides the respiratory tract into five compartments based on its anatomical and physiological structure (see fig. 1). The extrathoracic airways are divided into two compartments: ET_1, the anterior nose, and ET_2, the posterior nasal passages, larynx, pharynx and mouth. The bronchial region, BB, consists of the trachea and bronchi; the bronchiolar region, bb, consists of the bronchioles and terminal bronchioles. The alveolar-interstitial region, AI, consists of the respiratory bronchioles, the alveolar ducts, alveoli, and interstitial connective tissue.

As in the old model, the deposit of aerosols in different parts and compartments of the respiratory tract and their clearance from these parts and compartments are

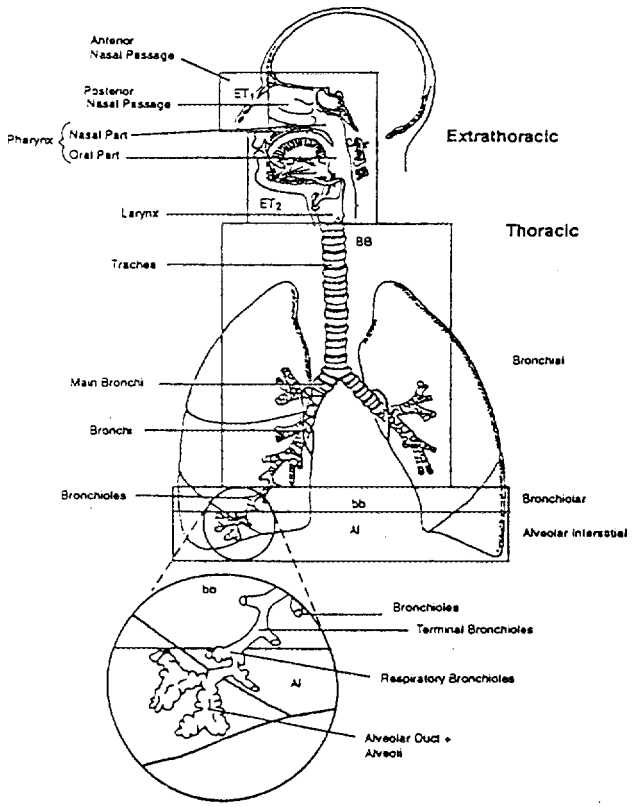

Figure 1: The anatomical structure of the respiratory tract model.

treated as two distinct processes. However, the description of each process in the new model is different from that in the old model. Regarding deposition, the new model assumes a polydisperse aerosol of particles with diameters of 0.6 up to 100 micron. It assumes that the AMAD of a typical aerosol that occurs in environmental contamination to which the general public might be exposed is 1μm, but uses an AMAD of 5μm for the working environment (while the old model used an AMAD of 1μm for the latter condition too). This change alone lead to the fact that, for conditions characteristic of a working environment, a smaller fraction of inhaled particles reaches the inner parts of the respiratory tract. The fraction of the inhaled activity that is deposited in ET_1 and ET_2 is 2.5 times higher than that deposited in the equivalent parts of the old model, whereas those deposited in compartments BB and bb and in compartment AI are 2.5 and 4.7 times smaller, respectively, than in the equivalent parts of the old model.

Regarding the clearance of material from the respiratory tract and uptake by the blood, the old model assumed that division of the radioactive chemical compounds into types D, W and Y is appropriate to describe rates of both clearance from

the respiratory tract and uptake by the blood. In contrast, the new model uses different and independent rates for the two processes. It divides the radioactive compounds into types F (fast), M (medium) and S (slow) according to their rate of absorption by the blood and uses a different rate for the transfer through the respiratory tract. However, the division of the compounds into types F, M and S is, in general, equivalent to their division into types D, M and Y.

As explained earlier, the new division of the respiratory tract into parts and compartments was done according to the tract's anatomical and physiological structure and is not related solely to the clearance process, as in the old model. In the new model, particles which are deposited in each compartment are simultaneously absorbed into the blood and transported to other compartments. The fraction that takes each route depends on the relative rates of each process. Based on recent experimental studies, the new model includes two new subprocesses of the clearance process which have different half-times than that of the main process. The first subprocess accounts for the possibility that a fraction of the inhaled particles deposited on airway surfaces in the BB and bb regions may be cleared much more slowly than most particles, which are cleared rapidly. A clearance half-time of 20d is assigned to this fraction. The second subprocess accounts for possible sequestration in the airway wall of a fraction of the particles deposited in the BB and bb regions. This sequestered fraction is considered to be cleared out to the thoracic lymph nodes with a half-time of 70d.

The new model is applicable to all members of the public, including infants and children. Parameters that characterize the transport and clearing processes related to each compartment of the model are given for each age group separately.

Dose calculations are made now for each anatomical compartment of the respiratory tract, and the relative sensitivity of each compartment to ionizing radiation is accounted for when the equivalent dose for different sections of the respiratory tract is calculated. The combined weighted doses to compartments BB, bb, AI and LN give the dose-equivalent to the lungs. ET_1 and ET_2 together are called the extrathoracic airways and their combined weighted dose is accounted for when calculating the equivalent dose to the "remainder".

Dose limits and intake limits

Since 1979 when publication no. 26 was issued, new information on the effects of exposure to ionizing radiation on the human body has been accumulated. During the last decade, a new evaluation of the exposure to ionizing radiation by the survivors of the atomic bomb dropped on Hiroshima indicated that the equivalent dose to which they were exposed was much smaller than had been estimated previously.

The recommendations of ICRP for dose limits for the general public and people who work with radioactive materials are summarized in table 1. Together with

the new limits, the table presents the old recommendations which were given in publication no. 26. As can be seen, the Commission reduced the maximal permitted exposure to ionizing radiation. The new limits are 2 to 5 times lower than the old ones but the new limits are related to the average annual exposure over 5 years where as the old ones referred to the maximal exposure for a single year. The Commission still allows maximal annual doses as high as those specified in the old recommendations, but only if the average dose over 5 years complies with the new recommendations.

	Workers		Public	
	ICRP-26	ICRP-60	ICRP-26	ICRP-60
Effective dose	50 mSv	20 mSv	5 mSv	1 mSv
Equivalent dose to tissues:				
All	500 mSv			
Eyes	300 mSv	150 mSv	15 mSv	15 mSv
Skin	500 mSv	500 mSv	50 mSv	50 mSv
Legs	500 mSv	500 mSv	50 mSv	50 mSv

Table 1: Dose limits per year for the general public and for workers, according to ICRP-26 and ICRP-60

With the revision of the dose limits the Commission also redefined the old terms *dose equivalent* and *effective dose equivalent*, and renamed them *equivalent dose* and *effective dose*, respectively. There are also some changes in (a) the method for calculating these terms and (b) the weighting factors for the different organs have been changed and new organs have been added to the list. Regarding the "remaining" organs, which do not have a specific weighting factor, the Commission suggests two ways to calculate their contribution to the calculated effective dose to the whole body: (a) If neither of these organs received the greatest equivalent dose of all organs, including those which have a specific weighting factor, then the effective dose to this group of organs is calculated by using a mass weighted average of the equivalent doses to each organ and multiplying this value by a weighting factor of 0.05 for the calculation of the effective dose to the whole body; (b) Otherwise, the organ which absorbed the greatest equivalent dose gets a weighting factor of 0.025, which is half the weighting factor of all the remaining organs, and the other organs in this group are weighted as before and get a weighting factor of 0.025. The integration time for the calculation of the committed doses (equivalent and effective) is taken to be from the age of exposure – but not above 20 – to the age of 70.

The extensive revisions in the dose limits, the new respiratory tract model and the revised biokinetic parameters of most radioactive chemical compounds, used in evaluating the distribution in the body of ingested and inhaled radionuclides, required recalculation of the annual limits on intake (ALI values). However, since the new dose limits are not conclusive (there are limits to average annual dose and

Radioactive element		Inhalation ALI			Ingestion ALI		
	(class, f_1)	ICRP-30	ICRP-61	ICRP-68	ICRP-30	ICRP-61	ICRP-68
^{32}P	(M, 0.8)	$1.0*10^7$	$5.0*10^6$	$6.9*10^6$	$2.0*10^7$	$8.0*10^6$	$8.3*10^6$
^{60}Co	(S, 0.05)	$1.0*10^6$	$4.0*10^5$	$1.2*10^6$	$7.0*10^6$	$3.0*10^6$	$8.0*10^6$
^{90}Sr	(S, 0.3)	$1.0*10^5$	$6.0*10^4$	$2.6*10^5$	$1.0*10^6$	$6.0*10^5$	$7.1*10^5$
^{232}Th	(M, 0.0005)	$4.0*10^1$	$9.0*10^1$	$6.9*10^2$	$3.0*10^4$	$5.0*10^4$	$9.1*10^4$
^{238}U	(S, 0.02)	$2.0*10^3$	$6.0*10^2$	$3.5*10^3$	$5.0*10^5$	$8.0*10^5$	$4.5*10^5$
^{241}Am	(M, 0.0005)	$2.0*10^2$	$3.0*10^2$	$7.4*10^2$	$5.0*10^4$	$3.0*10^4$	$1.0*10^5$

Table 2: Annual limits on intake for six radioactive elements as calculated with the old and new limits and models

maximal annual dose), it is impractical to give ALI values. Hence, the Commission calculated and presented effective dose coefficients (in units of Sv) per unit of activity (Bq) of inhaled or ingested material. The ALI value for a specific dose limit (maximal, average or other) can be calculated by dividing the dose limit by these coefficients. For the purpose of studying the effect of the new dose limits, new respiratory tract model and revised biokinetic parameters on the ALI values, we calculated the new ALI value for a few radionuclides using the average annual dose limit and compared them with the ALI values given in earlier publications. The results of this comparison are presented in table 2.

The new calculated values are generally more liberal than the old ones although the new dose limits are lower. As explained before, the availability of new information since 1979, when the Commission presented the earlier ALI values in publication no. 30, enables a better estimation of biokinetic data of radioactive chemical compounds and the development of improved models and calculation methods. Hence, the new biokinetic parameters, revised calculation methods of the effective dose and ALI values, and new respiratory tract model use smaller safety factors, which lead to more liberal calculated ALI values.

For example, the ALI for inhalation of ^{232}Th is 7.6 times higher than the value given in ICRP-61 [11] and 17.25 times higher than the value given in ICRP-30 (although the ICRP-30 values are based on an annual effective dose of 50 mSv whereas the newer values are based on an annual effective dose of only 20 mSv). For all the compounds listed in table 2, the ALI values calculated from the dose coefficients given in ICRP-68 [14] are higher than those given in ICRP-61; only for ^{32}P is the value given in ICRP-30 higher than the newly calculated value. Even the new ingestion ALI values are usually higher than the previously calculated ones although here the Commission uses the same model as presented in ICRP-30 (only the biokinetic parameters have been revised). In this case, for example, the new ALI value of ^{241}Am is 3.3 times higher than that given previously in ICRP-61 which was based on the same annual dose limit.

Conclusions

In 1991, the ICRP issued publication no. 60 [10], which is a revision to and extension of publication no. 26 from 1979. A new respiratory tract model, based in part on those data, was presented in publication no. 66 [12].

The detailed description, in the new model, of each part of the respiratory tract enables its use to estimate doses from inhalation of radioactive material, to the general public, including infants and children of all ages. Moreover, it provides a way to calculate actual doses to specific groups of people due to known incidents, a task that was impossible to accomplish with the old model. An extensive interpretation of the new model is given in [13]. Dose calculations are done now for each anatomical compartment of the respiratory tract, and the relative sensitivity of each compartment to ionizing radiation is accounted for when the equivalent dose for a few compartments is calculated.

The new limits are 2.5 and 5 times lower than the old ones, for workers and the public respectively, but these limits are for the average annual exposure over 5 years whereas the old ones where for the maximal exposure per year. The Commission still permits maximal annual doses as high as those allowed in the old recommendations, as long as the average dose over 5 years does not exceed the new recommendations.

To conclude, new data and improved models which where used to establish and calculate new dose limits and ALI values indicate that the old dose limits where too liberal. However, high safety factors embedded in the old models, methods and parameters used to calculate values of ALI, made the previously calculated values conservative. For example, the most recent calculated value of the ALI for inhalation for ^{232}Th is 7.6 times higher than the previously calculated value. The ingestion ALI currently calculated for ^{241}Am is 3.3 times higher than the previous limitation.

References

[1] ICRP. Recommendation of the International Commission on Radiological Protection, ICRP publication no. 26. *Annals of the ICRP*, 1977. Pergamon Press, Oxford.

[2] ICRP. Limits for intakes of radionuclides by workers, ICRP publication no. 30, part 1. *Annals of the ICRP*, 2(3/4), 1979. Pergamon Press, Oxford.

[3] ICRP. Recommendation of the International Commission on Radiological Protection, ICRP publication no. 30, supplement to part 1. *Annals of the ICRP*, 3(1-4), 1979. Pergamon Press, Oxford.

[4] ICRP. Limits for intakes of radionuclides by workers, ICRP publication no. 30, part 2. *Annals of the ICRP*, 4(3/4), 1980. Pergamon Press, Oxford.

[5] ICRP. Limits for intakes of radionuclides by workers, ICRP publication no. 30, supplement to part 2. *Annals of the ICRP*, 5(1-6), 1981. Pergamon Press, Oxford.

[6] ICRP. Limits for intakes of radionuclides by workers, ICRP publication no. 30, part 3 (including addendum to parts 1 and 2). *Annals of the ICRP*, 6(2/3), 1981. Pergamon Press, Oxford.

[7] ICRP. Limits for intakes of radionuclides by workers, ICRP publication no. 30, supplement A to part 3. *Annals of the ICRP*, 7(1-3), 1982. Pergamon Press, Oxford.

[8] ICRP. Limits for intakes of radionuclides by workers, ICRP publication no. 30, supplement B to part 3 (including addendum to supplements to parts 1 and 2). *Annals of the ICRP*, 8(1-3), 1982. Pergamon Press, Oxford.

[9] ICRP. Limits for intakes of radionuclides by workers, ICRP publication no. 30, part 4, an addendum. *Annals of the ICRP*, 19(4), 1988. Pergamon Press, Oxford.

[10] ICRP. 1990 recommendation of the International Commission on Radiological Protection. ICRP publication no. 60. *Annals of the ICRP*, 21(1-3), 1991. Pergamon Press, Oxford.

[11] ICRP. Limits for intakes of radionuclides by workers based on the 1990 recommendation. ICRP publication no. 61. *Annals of the ICRP*, 21(4), 1992. Pergamon Press, Oxford.

[12] ICRP. Human respiratory tract model for radiological protection. ICRP publication no. 66. *Annals of the ICRP*, 1994. Pergamon Press, Oxford.

[13] Ido Silverman, Tuvia Shlesinger, and Moshe Shapira. Limits for internal contamination from radioactive materials - for workers and the general public. Technical Report 2603, Soreq - NRC, 1996. in Hebrew.

[14] ICRP. Dose coefficients for intakes of radionuclides by workers, replacement of ICRP publication 61. ICRP publication no. 68. *Annals of the ICRP*, 1995. Pergamon Press, Oxford.

DOSE CALCULATION DUE TO ELECTRONS INTERACTION WITH DNA

S. Mark+, I. Orion+* , G. Shani+ and B. Laster[x]
+ Dep. of Nuclear Engineering, Ben Gurion university, Beer-Sheva, Israel.
* Soreq Nuclear Center, Yavne, Israel 81800.
[x] Medical Dep., Brookhaven National Laboratory, N.Y., U.S.A.

Experiments done with gadolinium loaded V79 Chinese Hamster cells, irradiated with thermal neutrons, showed that cells lethality increased by a factor of 1.8 compared to the case where the Gd atoms were located outside the cell.[1] It was obvious that the dramatic increas in cell lethality is due to the emission of Auger electrons following the $^{157}Gd(n,\gamma)^{158}Gd$ reaction. Electrons of various energies from about 40 keV (very few) to less than 1 keV, are emitted.

In the present work, energy absorbed in DNA was calculated, due to interaction of electron of different energies: 30, 15, 10, 8, 5 and 2keV. The Monte Carlo code EGS4[2] was used for the calculations. The DNA was modeled as a series of alternative layers of sugar (phosphate - $C_5O_5H_7P$ ρ=1.3gr cm^{-1}) and water. The sugar layer thickness was assumed 2.5nm and the water layer thickness 10nm. An isotropic electron source was assumed to be located in a water layer and the electrons interactions (absorption and scattering) were calculated in the forward hemisphere. The energy absorbed in a group of 8 layers, (4 sugar and 4 water) was calculated for each one of the electron energies. An example of the energy deposited by a 10keV electron beam is shown in Fig. 1. An interesting fact found in those calculations; when the source electrons energy is 10 keV or more, most of the electrons are absorbed in the DNA-water system, are at energy about 2keV. There is no good explanation for this phenomenon except for assuming that when the electron's energy reaches a low point of about 2keV, it cannot escape absorption in the medium. As seen in Fig.1, 10% of the 10keV electrons deposite their entire energy in the 8 layers range.

The energy deposited in each of the sugar and water layers was calculated as a function of distance from the source. The total energy deposited in these regions is shown in Fig. 2 (and the attached table) for 1000 electrons of energy 10keV. Each value in this nomogram is the total energy deposited in the sugar and water layers from the source to each particular layer. Up to about 20 layers (10 sugar and 10 water)the total energy deposition increases. Above 25 layers there is almost no additional deposition of energy in the DNA. All electrons were either absorbed or backscattered.
For 5keV electrons, the leveling off takes place at about 5 layers. Since the water layer is 4 times thicker than the sugar, more energy is absorbed in the water layers than in the sugar layers.

The purpose of this work was to calculate the dose delivered to the DNA due to Auger electrons emitted from a source located in the DNA. Knowing the energy deposited in each sugar layer should be helpful in assessing the damage to the cell and the probability of killing it. It was stated it the past[3] that absorption of 500eV or more has a high probability of double strand breaking, leading to cell lethality. When the $^{157}Gd(n,\gamma)^{158}Gd$ reaction takes place, about 20 Auger electrons are emitted with enegy about 1keV and higher, therefore this reaction has a high probability of killing cells, as demonstrated by Laster et al.[1]

REFERENCES

1. The Biological Effect of Auger Electrons Compared to Alpha Particles and Li Ions. B.H. Laster, G. Shani, S.B. Kahl and L. Warkentien, Acta Oncologia, 1996

2. The EGS4 Code System, W.R. Nelson, H. Hirayama and D. Rogers, SLAC-265, 1985.

3.D.E. Charlton, J.L. Humm and H. Nikjoo, Calculations of Initial Yields of Single and Double-Strand Breaks. J. Radiat. Biology, 56 , 1989.

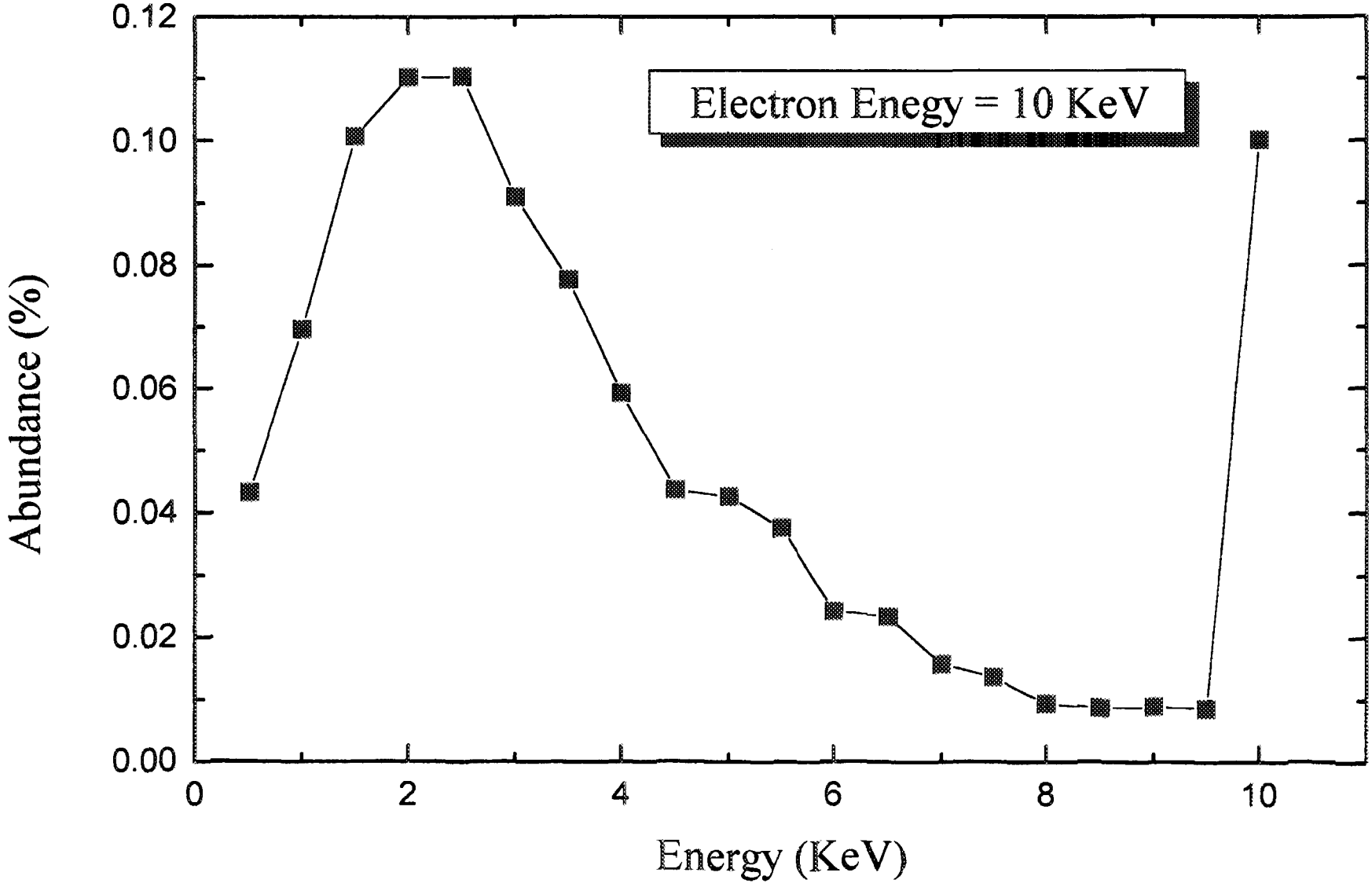

Figure 1. Energy Deposition Distribution in 8 Sugar-Water Layers

Width (nm)	Energy (MeV)
187.5	6.5543
177.5	6.5683
175	6.5717
165	6.5257
162.5	6.5589
152.5	6.5192
150	6.5112
140	6.4368
137.5	6.4791
127.5	6.4352
125	6.189
115	6.4094
112.5	6.1657
102.5	6.3104
100	6.0327
90	5.9891
87.5	5.8372
77.5	5.7357
75	5.5271
65	5.3976
62.5	4.9723
52.5	4.9062
50	4.4102
40	4.2372
37.5	3.7816
27.5	3.6294
25	2.9371
15	2.7542
12.5	2.0349
2.5	1.7148
0	0.3607

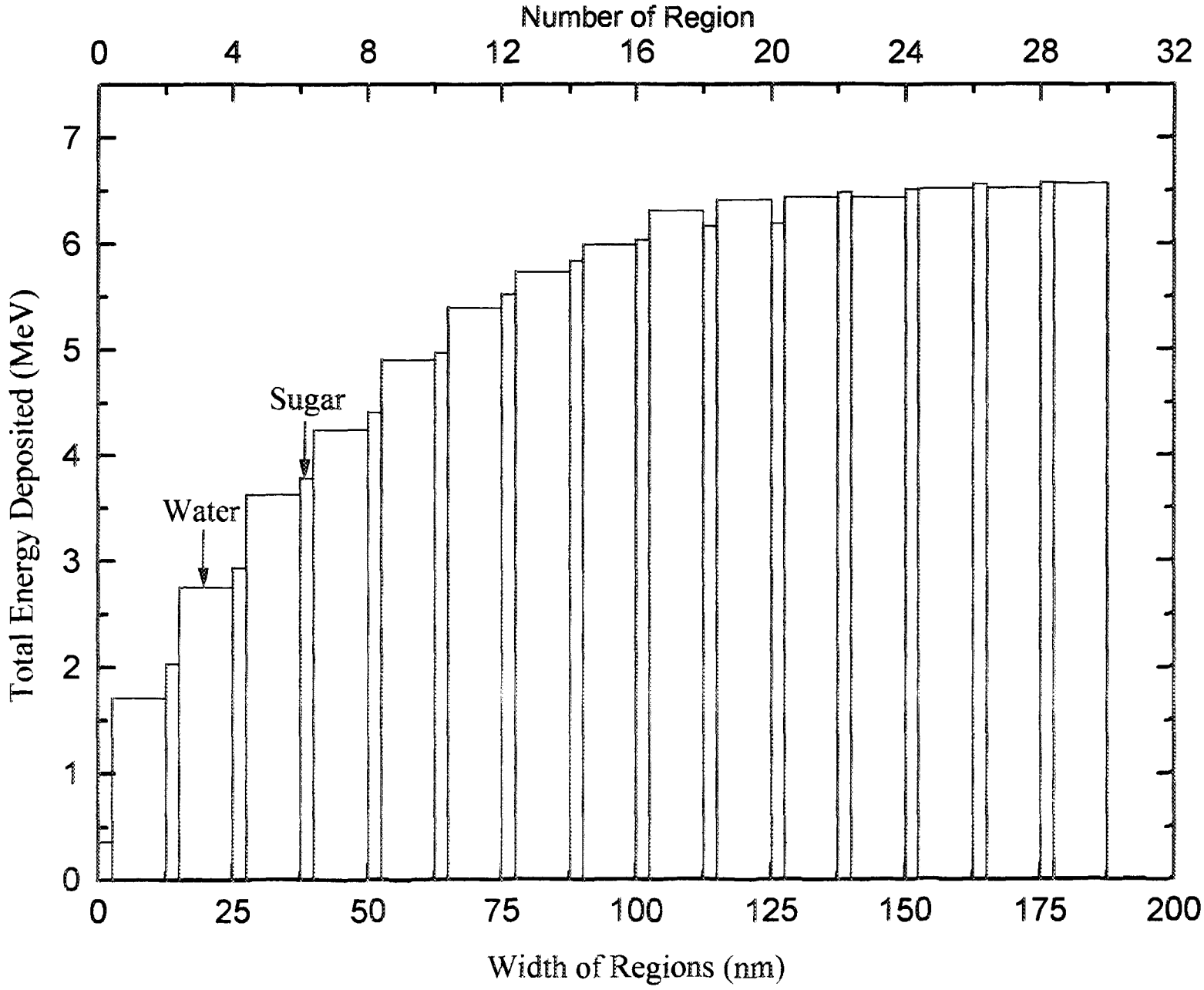

Figure 2. Energy Deposited in DNA Regions Due to 1000 Electrons of 10 KeV Energy.

Magnetic versus Electric fields in RF safety standards - The physical origin of difference and the practical implications.

M. Margaliot , R. H'areuveny, R. Ruppin and T. Schlesinger.
Soreq Nuclear Research Center.
Yavne 81800, Israel.

Electromagnetic (EM) radiation in the frequency range from a few kHz, up to 300 GHz is commonly defined as Radio-Frequency radiation (RFR). The utilisation of RF is widening rapidly, and the number of devices emitting this kind of radiation, the intensities emitted and the consequent occupational and public exposure to RFR is growing very rapidly. Together with the expanded use of RFR, the awareness - both scientific and public, to the possible health hazards involved in human exposure to RFR, has grown recently. This resulted in the formulation of various safety standards, relating to restrictions on human exposure to RFR. Two safety standards dominate recently the RFR safety field:
A- The IRPA (International radiation protection association) RF exposure guidelines (issued in 1988, adopted in many European countries)
B- ANSI/IEEE C-95 (American National Standards Institute) issued in 1992, and adopted in 1995 by the ACGIH.
Two new main features have been introduced in both standards:
-a differentiation between the general public and workers. (the latter group with reduced safety factors).
-a differentiation between the relative risks of the electric and magnetic fields, which attributes most of the risk to the **electric** field.
The basis for the second differentiation is stated in the rationale given by the IRPA guidelines in reference to two distinct frequency ranges:
For low frequencies (<10 MHz) the hazard of exposure is not related to energy absorption, but rather to the risk of electric shocks, to which the magnetic field contributes weakly only. For frequencies above 10MHz the coupling of the electric field is approximately 5-6 times stronger than that of the magnetic field.
ANSI/IEEE states that the energy absorption due to the magnetic component alone is much weaker than that due to the electric component. In the present work, an attempt is made to give an intuitive physical basis for the dominance of the electric field in these two safety standards. This is based on a direct application of the Lorentz force on charges exposed to electromagnetic fields. The practical implications of the new standards are also discussed

The biological effects of exposure to RFR are believed to be due to the energy imparted to the physiological system by the RFR, and thus, the RFR power density (energy flux per unit time) incident on the the body is commonly considered to be the quantity of interest.
The power density of RFR is given (Du68) by the Poynting vector:

$$\underline{P} = \underline{E} \times \underline{H} \qquad (1)$$

where P is the power density (W/m^2), E is the electric field (V/m), and H is the magnetic field (A/m).
Under normal (i.e. plane wave in vacuum) conditions, a simple relation between the electric and magnetic fields can be used (Du68):

$$E / H = 376.6\ \Omega\ (\sim 377\Omega). \qquad (2)$$

Power densities can thus be expressed (Du68) by either the electric or the magnetic fields alone by:

$$P = E^2/377 = 377H^2 \qquad (3)$$

As stated above, the basic safety exposure restriction is related to the energy (or rather - the power) imparted to the body by RFR. It thus follows that the restrictions can be expressed in terms of incident power density, and that the related electric and magnetic fields can be derived from Eq.3.

However, under near field conditions (less than a few wavelengths away from the transmitting antenna) Eq. 3. fails, and separate restrictions on the magnetic and electric fields must be given (and consequently - separate measurements for the electric and magnetic fields must be conducted).

In the former standards (e.g. the 1982 ANSI C95, ACGIH up to 1993), separate expressions for the two fields were indeed given, but the equivalent power densities for these E and H values, were identical (according to Eq.3.).

In recent standards, however, this was revised: over the lower part of the RFR frequency range(<10MHz), the separate restrictions on E and H, **do not** lead to the same equivalent power density.

In the following, the IRPA and ANSI/IEEE exposure restrictions are presented and attention is drawn to the differences between the restrictions on electric and magnetic fields in these two standards.

1) IRPA guidelines:

The IRPA exposure restrictions are presented in table 1 below:

Table 1: IRPA restrictions for *occupational* RFR exposure

frequency -f (MHz)	electric field (V/m)	equivalent power density (W/m^2)	magnetic field (A/m)	equivalent power density (W/m^2)
0.1-1.0	614	1000	1.6/f	$1000/f^2$
1-10	614/f*	$1000/f^2$	1.6/f	$1000/f^2$
10-400	61	10	0.16	10
400-2000	$3f^{1/2}$	0.025f	$0.008f^{1/2}$	0.025f
2000-300000	137	50	0.36	50

*f -the frequency in MHz

It can be noted that in the lowest frequency range (i.e. - 0.1-1 MHz), there is a clear differentiation between the electric and magnetic fields: while the electric field restrictions are expressed as a constant (equivalent P = 1000 W/m^2), the magnetic field restrictions are given as a function of the frequency f (and range from 1000 to 100,000 W/m^2).

At 100 kHz the discrepancy between E and H restriction is thus two orders of magnitude.

In addition to that , in situations when the E/H relation differs from eq. 2. (as in the near proximity of the transmitting element - the so called "near field"), IRPA states that the electric and magnetic field should both be measured, and the results should be combined by:

$$\mathbf{P}(\text{equivalent})=\mathbf{5/6}\ E^2/377 + \mathbf{1/6}\ 377H^2 \qquad (4)$$

It is thus apparent that the magnetic field is considered (under equivalent power density conditions) to be less hazardous (by a factor of 5), than the equivalent electric field *in* **all** *frequency ranges*.
This same attitude (although not the same in magnitude) appears in the IEEE standard:

2) The IEEE/ANSI RF standard: The IE92 publication in this field is more detailed than the IRPA guidelines presented above, but bears a resemblance to it regarding the reduced potential hazard attributed to magnetic fields.
The 1992 IEEE/ANSI c-95.1 RF exposure restrictions are presented in table 2 below:

Table 2: IEEE RFR maximal permissible exposure for controlled environments.

frequency (MHz)	electric field (V/m)	magnetic field (A/m)	power density* (W/m^2)	averaging time (min)
0.003-0.1	614	163	1000 (E), 10^7(H)	6
0.1-3.0	614	16.3/f	1000(E), $10^5/f^2$(H)	6
3-30	1842/f	16.3/f	$9000/f^2$(E), $10^5/f^2$(H)	6
30-100	61.4	16.3/f	10 (E) $10^5/f^2$(H)	6
100-300	61.4	0.163	10 (E & H)	6
300-3000			f/30	6
3000-15000			100	6
15000-300000			100	$616000/f^{1.2}$

*E and H for power density measured by E & H respectively.

On comparing the restrictions on electric and magnetic fields, (in terms of equivalent power density), it becomes apparent that at the higher frequencies (> 300 MHz), the two fields have the same weight (rather: the power density can be determined by measuring either field, assuming eq. 3.). However, for the lower frequencies, the permitted magnetic fields are significantly higher than the equivalent (power density) electric fields. In fact, for frequencies <100 kHz, this discrepancy is 10^4
The relative physiological insensitivity to magnetic fields, as viewed by both bodies, can be explained by a direct reference to the basic physical law governing the EM wave- matter interaction, namely, the Lorentz force:
The force on a charge due to electric and magnetic fields acting on it, is given (Du68) by the Lorentz equation :

$$\underline{F}=q\underline{E}+q\underline{V} \times \underline{B} \qquad (5)$$

where F is the force on the charge, E is the electric field, B is the magnetic flux density (which is proportional to H) and V - the velocity of the charge.
From eq. 5. it is apparent that the force due to the E field is independent of the charges velocity, but the magnetic component of the force is linearly dependent upon it, and vanishes at V=0.
It thus follows that when an EM wave impinges on a charge which is initially at rest, the magnetic component of the Lorentz force does not contribute to the force, and

the wave-matter interaction is initiated by the electric component (as the charges in the irradiated body are initially nearly at rest). Only after these charges, due to their interaction with the electric components, have attained a non-zero velocity, can the magnetic component act on them.
It thus follows that if the magnetic field is acting in the presence of a weak (in terms of equivalent power density) electric field, its interaction with matter will be weaker than in the presence of a strong electric field, thus leading to a reduced potential hazard (and hence - lighter restrictions), of the magnetic field.
The exact computation of this effect has not been conducted yet, but must take into account the following parameters:

- the nature of charge carriers (at frequencies up to a few GHz - ionic solutes, at higher frequencies - rotation of the polar water molecules).
- the initial (mostly thermal in origin) distribution of the velocities of the charges.

This computation will be presented elsewhere.

Practical implications:
The typical situation in which the electric and magnetic fields do not obey eq 1. is in the near field, namely, in the near proximity (less than a few wavelengths) of the radiation source. In this situation, it is normally the magnetic field that is larger than can be expected from eq 1 above. In these situations (rather common in occupational exposure, especially at wavelengths exceeding a few meters), the relaxations of the IEEE and IRPA restrictions, have a significant impact on the practical work conditions. The most significant change relates to plastic welding machines: these operate normally in the ISM band (mostly - 27 MHz $\cong \lambda$=11.1 m). These machines have rather high output power (typically - a few kW, up to a few tens of kW), and the operator works in the near proximity (less than one meter is typical) of the welding head. While the electric field can easily be shielded, with a significant reduction in field value, this is not true for the magnetic component. As a result, high magnetic fields, often exceeding the **former** (i.e. AC93) occupational exposure restrictions,can be measured at the operators positions, thus rendering the machines inoperative on safety grounds.
However, according to the new standards (IRPA, and especially - the ANSI/IEEE) most of these machines will now be in compliance with the exposure restrictions.

References:

AC93: ACGIH TLV pub. 1993, ACGIH OH 45211- 4438.

Du68: Duffin WJ: Advanced Electricity and Magnetism, 1968 McGRAW - HILL - London

IE92: IEEE/ANSI pub C-95, 1992, IEEE NY 10017.

IR88: IRPA Guidelines, 1988, Health Phys.**54**:115

Carcinogenic and Other Health Effects of 50/60 Hz Electric and Magnetic Files - Status Report

R. Hareuveny, M. Margaliot, and T. Schlesinger
Radiation Safety Division, Soreq NRC, Yavne, Israel 81800

Abstract

Nearly 20 years ago, Wertheimer and Leeper (1979) reported that children who had died from cancer were 2-3 times more likely to have lived within 40 m of a high voltage power line than were other children. Since then, thousands of papers have been published and the issue of the possible health hazards related to Electromagnetic Fields (EMFs) in the range known as Extremely Low Frequency (ELF) arouse very significant public attention. Important reviews were written by EPA (1990), NRPB (1992, 1993), WHO/IRPA (1984), APS (1995) and others. One review has been published recently also in Israel (Margaliot et al. 1994).

Electric fields are present whenever electric voltage exists, while magnetic fields result from electric currents. Magnetic fields in the very close proximity of electrical appliances are often stronger than the fields directly beneath power lines but decrease with distance more quickly than power line fields. Electric fields are greatly reduced by objects like buildings, trees and vehicles. Magnetic fields are not blocked by almost all common materials. A typical American home has background average magnetic field level of 0.9 mG in the range of 0.5-4 mG (DoE 1995), a little higher than the average European home. From our own experience typical domestic levels in Israel are closer to the European ones.

Reported health effects of EMFs include:

1) Changes in calcium efflux through membranes.

2) Decrease in the hormone melatonin produced in the pineal gland.

Melatonin has been reported to slow the growth of some cancer cells in laboratory experiments.

3) Alterations of immune systems.
4) Accelerated tumor growth.
5) Changes in biorhythms.

Over 50 epidemiologial studies related to either general public or workers have been published. Some of them have suggested that a link may exist between exposure to EMFs and certain types of cancer, primarily leukemia and brain cancer, but many others did not find such link.

Many of the results, especially those related to low level fields, are controversial and hard to reproduce. All important reviews conclude that at present there is insufficient biological and epidemiological data to make a health risk assessment or even to determine whether there is a potential hazard.

The International Commission on Non Ionizing Radiation Protection developed guidelines for EMF exposure (IRPA/INIRC 1990) which have been adopted by nearly all western countries including Israel. The continuous exposure of the general public for 24 hours a day to electric and magnetic fields is restricted to 5 kV/m and 1000 mG respectively , while the occupational exposure limit for an eight hour working day is 10 kV/m and 5000 mG. These guidelines are based on established effects of EMFs, such as nerve stimulation. These limits are much higher than EMF levels found typically in occupational and residential environments. They are not meant to correspond to the low-level field strengths allegedly associated with elevated cancer incidence reported in some recent epidemiological studies and should not be interpreted as distinguishing "safe" from "unsafe" EMF levels.

The presentation will introduce:

1) Sources and typical levels of exposure.
2) Research findings including latest epidemiology.
3) Ways to reduce exposure.

4) Worldwide standards and policy.

5) Recommendations for future activities in Israel.

Bibliography

APS, Power line fields and Public Health. Adopted by council - 23.4.95

Doe (U.S. Department of Energy), Questions and answers about EMF, DOE/EE-0040, 1995.

EPA, Evaluation of the potential carcnogenicity of electromagnetic fields (review draft), Report EPA/600/6-90/005b, 1990

IRPA/INIRC, Interim guidelines on limits of exposure to 50/60 Hz electric and magnetic fields, Helath Physics, Vol 58:113-122, 1990

Margaliot M.; Rupin R.; Hareuveny R.; Biological effects of extremely low frequency electromagnetic fields, Soreq NRC Report, 1994

NRPB, Electromagnetic fields and the risk of cancer, Documents of the NRPB Vol 3(1), 1992

NRPB, Board statement on restrictions on human exposure to static and time varying electromagnetic fields and radiation, Documents of the NRPB Vol 4(5), 1993

Wertheimer N. and Leeper E., Electrical wire configurations and childhood cancer, American Journal of Epidemiology Vol 109:273, 1979

WHO/IRPA, Extremely low frequency (ELF) fields, Environmental Health Criteria 35, Geneva 1984.

Radiation Protection Implications Related to Cellular Communication

R. Hareuveny, M. Margaliot, and T. Schlesinger
Radiation Safety Division, Soreq NRC, Yavne, Israel 81800

Abstract

The huge increase in the use of cellular communication had led to concern about risk to health from electromagnetic radiation (EMR) emissions of such telephones and base stations (in the frequency range 0.8-2 GHz). The industry estimates that by the year 2000 over 60 million people in the U.S will be using a portable cellular communicating device (GAO 1994).

The International Commission on Non Ionizing Radiation Protection (ICNIRP) published in (1996) a statement related to electromagnetic emissions from hand held radiotelephones and base transmitters. The ICNIRP'S statement is based on the assumption that the only established biological interaction is thermal. Such interaction may be expressed by the magnitude of the Specific Absorption Rates (SAR) in tissue. The commission concluded that there is no substantive evidence that adverse health effects, including cancer, can occur in people exposed to local SAR bellow 10 W/kg averaged over any 10 g mass of tissue in the head.

The U.S Federal Communications Commission (FCC) has recently adopted regulations for exposure to EMR based in large parts on those of the National Council on Radiation Protection and Measurements (NCRP 1986). The FCC will now require that all new cellular hand held telephones will be tested to assure that users are not exposed to SAR over 1.6 W/kg.

Laboratory tests on phantoms (Kuster et al. 1993) found typical SAR in the brain up to 1 W/kg while worst case exposure (antenna touching head) SAR were up 5 W/kg. SAR calculations (Dimbylow and Mann 1994) found typical SAR values of 1-2 W/kg. However, some works support the existence of non thermal effects, e.g: Mann and Roschke (1996) found an influence of EMR emitted from digital cellular phones on the sleep of volunteers, including reduction of duration of REM sleep.

To summarize, there is presently no evidence on adverse health effects from extended use of mobile phones, but the possibility cannot be ruled out: No research has been completed on long term human exposure to low levels of radiation specifically from portable cellular phones (GAO 1994). Regarding base towers, their emission at ground levels is usually at least 100 time less than the exposure levels, therefore they are considered to be safe (CSIRO 1994).

The presentation will first introduce the basic principles and radiological characteristics of cellular hand-held telephones and base stations. Possible health implications will be reviewed. Finally the international standards and policy will be presented followed by presentation and recommendations for the Israeli situation.

Bibliography

CSIRO Australia (Division of Radiophysics), Status of research on the biological effects and electromagnetic radiation: Telecommunication frequencies, June 1994.

Dimbylow P.J. and Mann S.M, SAR calculations in an anatomically realistic model of the head for mobile communication transceivers at 900 MHz and 1.8 GHz, Phys. Med. Biol 39:1537-1553, 1994.

GAO (USA), Status of research on the safety of cellular telephones, Report to the chairman, subcommittee on telecommunications and finance, committee on energy and commerce, House of Representatives, Report GAO/RCED-95-32, Nov 1994

ICNIRP/IRPA, Health issues relates to the use of hand-held radiotelephones and base transmitters, Health Physics Vol 70(4):587-593, 1996.

NCRP, Biological effects and exposure criteria for radiofrequency electromagnetic fields, NCRP Report No 86, 1986.

Kuster N; Schmid T. and Meier K., Proceedings of VDE Meeting, Bad Nauheim, Germany, Nov 9-10 1993.

Mann K and Roschke J, Effects of pulsed high frequency electromagnetic fields on human sleep, Neuropsychopbiology 33:41-47 1996.

Calculations of Criticality of the AP600 Reactor with the KENO V.a Code

Krumbein A., Caner M. and Shapira M.
Soreq Nuclear Research Center
Yavne 81800

The Westinghouse AP600 PWR has been modeled using the KENO V.a three dimensional Monte Carlo criticality program of the SCALE-PC code system. These calculations and the use of a Monte Carlo neutron transport code such as KENO will provide us with an independent check on our WIMS/CITATION calculations for the AP600 as well as for other reactors. It will also enable us to model more complicated geometries.

The SCALE-PC system system which we have used for these calculations performs two functions namely, problem dependent multigroup cross section processing and criticality safety analysis. In our calculations of the criticality of the AP600 we have used two modules of the overall system. These are NITAWL-II which calculates resonance self-shielding and the KENO V.a, three dimensional Monte Carlo criticality program. The cross section library used was the 27 group ENDF/B-IV library which is one of the libraries supplied in the SCALE-PC package.

The NITAWL-II code [1] does two things. First, it calculates problem dependent resonance shielding by applying the Nordheim treatment and it is also used to read the cross section library to be employed in the given problem and to produce a new library in the AMPX working format as input to the KENO V.a code. NITAWL-II combines the shielded cross sections with the thermal data to produce this working library which is organized by reaction type and scattering expansions.

The KENO V.a program is a multigroup Monte Carlo criticality code which is used to calculate the k_{eff} of a three-dimensional system. It can also calculate lifetime and generation time, energy-dependent leakages and energy and region dependent absorptions, fluxes, fissions and fission densities.

KENO V.a utilizes weighted tracking rather than analog tracking in order to minimize the statistical deviation of k_{eff} per unit computer time. Geometry in the program is restricted to the use of specific shapes namely cubes, cuboids (rectangular parallelepipeds), spheres, cylinders, hemispheres and hemicylinders. Intersections are not allowed. Each successive geometry region must completely enclose the preceding region. To alleviate this restriction, the program allows multiple sets of geometry regions with each set independently governed by this restriction. Each of these sets are called *units*. Units can be stacked together in a 3-D rectangular parallelepiped called an *array* just as children's blocks can be stacked. An array can be treated as a building block and be used as a unit within another array. The use

of *holes* allows a unit to be emplaced within another unit, alleviating the restriction that each region within a unit must completely enclose all preceding regions within that region.

The data for the AP600 reactor were taken almost entirely from the Safety Analysis Report (SAR) [2]. Unfortunately, not all the necessary data were available as some parameters (such as the description of the reflector and core barrel) are considered proprietary and were omitted from the released version of the SAR.

The fuel assembly of the AP600 is a 17×17 array of fuel rods with feed enrichment of 2.00, 2.50 and 3.00 w/o. Interspersed among the fuel rods in various numbers, depending on the assembly, are WABA's (wet annular burnable absorber rods).

The AP600 was modeled as follows. All fuel rods were specified as having a void gap and zircalloy clad and were centered in a water cuboid. In the vertical direction, fuel rods and enclosing cuboids were given a length equal to that of the active fuel length of the rod (i.e. fuel assembly top and bottom structures were neglected). The burnable poison rods were modeled according to the specifications given in the SAR. The different fuel assemblies, called arrays, were made up of fuel rods with either no burnable poison rods or 9, 10, 12 or 24 poison rods respectively. The guide thimbles and instrumentation tube are modeled as water holes within zircalloy tubes and each fuel assembly is centered in a water cuboid. Fig. 1 shows the full core with the fuel assembly specifications (both enrichment and number of burnable poison rods). Finally, the core was surrounded by the reflectors and the core barrel.

Two problems were run, both using 40,000 initial neutrons. The first problem was all control rods out and no soluble boron. This gave a $k_{eff} = 1.0263 \pm 0.0033$. The second was for a nominal critical boron concentration of 1020 ppm of boron [2]. Here the calculated k_{eff} was 0.9356 ± 0.0093. Both results are too low. For comparison, previous WIMS/CITATION calculations of the second problem yielded $k_{eff} = 0.9667$ [3]. It would seem that at least part of the discrepancy may be due to the lack of accurate data on the reactor as cited above. For the 40,000 neutrons run the average final deviation was about 3×10^{-3}, so it seems that running more particles would not appreciably affect the result. (Incidentally, Bowman's group at ORNL ran a million neutrons for their analysis of the Westinghouse Sequoyah reactor [4].) These are, of course, preliminary calculations and we hope to improve our results with additional runs.

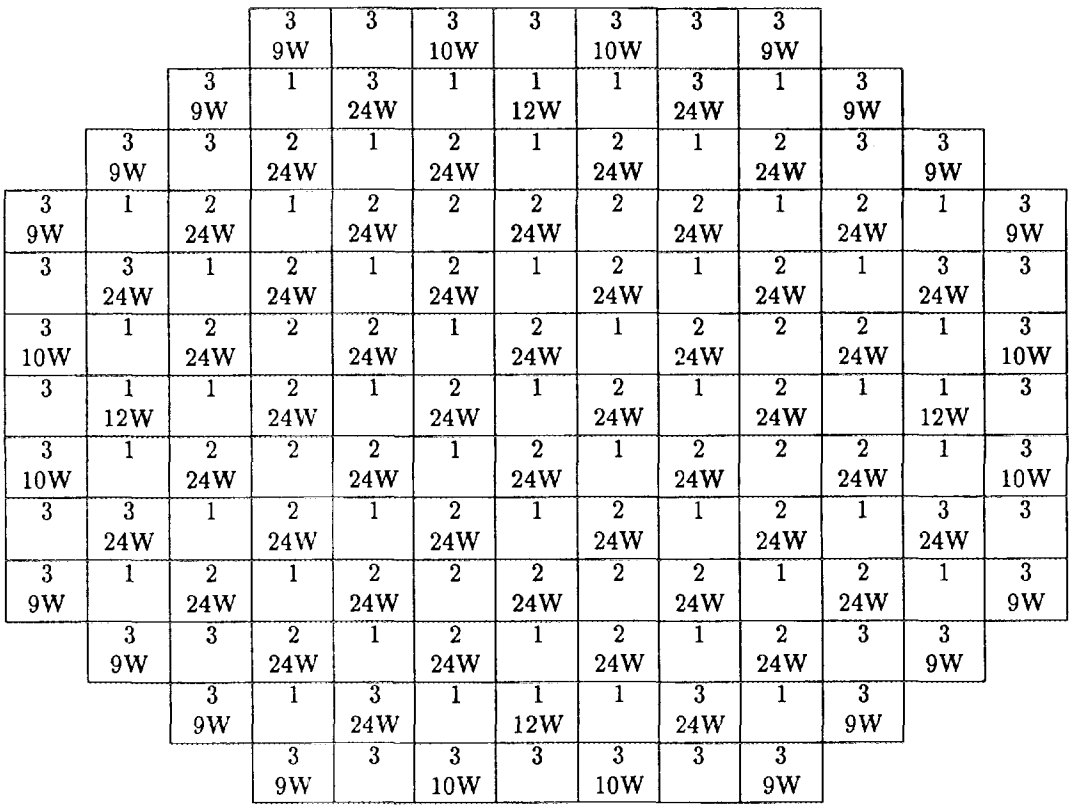

Enrichment (w/o)	Code
2.00	1
2.50	2
3.00	3

Burnable poison pattern description	Code
# = number of WABA rodlets	#W

Figure 1: AP600 core map used in calculation

References

[1] SCALE-PC: *A Modular Code System for Performing Criticality Safety Analyses for Licensing Evaluations*, Version 4.1 Parts 1 and 2, CCC-619, Oak Ridge National Laboratory (1993).

[2] AP600 Original SAR/PRA : Accession number 9207160108,
AP600 Rev. 1 SAR : Accession number 9401250172,
AP600 Rev. 1 PRA : Accession number 9408120126,
U.S. NRC Public Document Room, Washington, D.C. 20555 (1994).

[3] M. Caner, A.D. Krumbein and M. Shapira, *Progress Report on AP600 Data Update and Core Calculation*, Soreq Rep. RASG-185-95 (1995).

[4] S.M. Bowman, O.W. Hermann and M.C. Brady, *SCALE-4 Analysis of Pressurized Water Reactor Critical Configurations: Volume 2 - Sequoyah Unit 2 Cycle 3*, ORNL/TM-12294/V2 (1995).

A Computerized Energy Systems Code and Information Library at Soreq *†

I. Silverman, M. Shapira, M. Caner and D. Saphier
Soreq - NRC, Yavne 81800, Israel.

Introduction

In the framework of the contractual agreement between the Ministry of Energy and Infrastructure and the Division of Nuclear Engineering of the Israel Atomic Energy Commission, both Soreq-NRC and Ben-Gurion University have agreed to establish, in 1991, a code center. This code center contains a library of computer codes and relevant data, with particular emphasis on nuclear power plant research and development support.

The code center maintains existing computer codes and adapts them to the ever changing computing environment, keeps track of new code developments in the field of nuclear engineering, and acquires the most recent revisions of computer codes of interest. An attempt is made to collect relevant codes developed in Israel and to assure that proper documentation and application instructions are available. In addition to computer programs, the code center collects sample problems and international benchmarks to verify the codes and their applications to various areas of interest to nuclear power plant engineering and safety evaluation.

Recently, the reactor simulation group at Soreq acquired, using funds provided by the Ministry of Energy and Infrastructure, a PC work station operating under a Linux operating system to give users of the library an easy on-line way to access resources available at the library. These resources include the computer codes and their documentations, reports published by the reactor simulation group, and other information databases available at Soreq. Registered users set a communication line, through a modem, between their computer and the new workstation at Soreq and use it to download codes and/or information or to solve their problems, using codes from the library, on the computer at Soreq.

*Paper submitted to the 19th Annual Conference of the Israeli Nuclear Societies. Herzelia, Israel. December 9-10, 1996.

†This work was partially supported by the Ministry of Energy and Infrastructure.

This paper presents some of the codes and information databases available for the users of the Energy Systems Code and Information Library and the methodology to make a connection.

Making a connection

The new communication mechanism which enables the user a direct access to all resources available at the library is open for registered users. After a user gets permission to use this communication method he should provide information regarding the computer and operating system he uses and the telephone number to which his modem is connected to. For security purposes, a call-back mechanism is used where whenever a user wants to make a connection he makes a call (through his communication software) to the number of the workstation of the library and provides his user ID and password. After a verification process, the connection is closed and the workstation of the library makes a call back to the telephone number which was given by the user at the time of registration. The user modem and computer should be able to get this call and to enter into a communication mode. The library is able to provide or to recommend on hardware and software suitable for this communication method. After a communication line is set the user may download the codes and information he needs or use the codes on the computer of the library.

Computing environments

The ever changing computing world, the development of new types of computers (mainframes, workstations and personal computers (PC)) and operating systems (IBM VM-CMS for mainframes, UNIX for workstations and UNIX and/or DOS/Windows for PCs) with higher capabilities and new communication technologies like networks and the Internet motivate and require adaption and revision of the codes for these new technologies and computing systems. Most computer codes mentioned here have been developed for and are available from Soreq (usually old versions only) for mainframes operating under the IBM VM-CMS system. This configuration is referred to as configuration number 1 in the following lists of codes and databases.

The reactor simulation group at Soreq uses for some years a IBM RS/6000 computer operating under the AIX system which is a flavor of standard UNIX (configuration no. 2) and PCs with DOS/Windows operating systems (configuration no. 3). The group started recently to use PCs with the Linux operating system which is another, public domain, flavor of UNIX (configuration no. 4). Most of the codes which have been found useful and are used by the staff of the simulation group at Soreq have been ported to these two new systems.

The expertise developed in the group for this porting work are available for any new porting project as required.

Codes list

The following codes are currently available at Soreq:

WIMS-D4 (NEA0329) A code for lattice calculations. It has its own fine group cross section data library, based on pre-1976 experimental data. The code is used at Soreq and available for all configurations.

CITATION (NESC0387) A full core diffusion code for neutronics calculations. It can treat up to three space dimensions in Cartesian, cylindrical, hexagonal-z and trigonal-z configurations. The code is used at Soreq and available for all configurations.

COBRA-4I (NESC0659) A thermal-hydraulics code for steady-state calculations as well as flow and enthalpy in rod bundle nuclear fuel element subchannels during transient conditions. Boiling and non-boiling conditions are included, as well as cross-flow mixing. The code is used at Soreq and available for configurations 2, 3 and 4.

DSNP A thermal-hydraulic and neutronics code which has been developed and is maintained at Soreq. The code is used at Soreq and available for all configurations.

Other codes available at Soreq are listed in [1].

Databases

The following databases are currently available at Soreq:

International Handbook of Evaluated Criticality Safety Benchmark Experiments A digital version of this handbook of the Organization for Economic Co-Operation and Development (OECD) together with the software needed to browse through it is available.

NEA Data Bank, Nuclear Program Abstracts The June 1996 version of this database from OECD, together with the software needed to browse through it is available.

Other databases available at Soreq are listed in [1].

Conclusions

Using modern technologies, the Energy Systems Code and Information Library at Soreq, is working to provide better and easier ways for its users to access the resources available from the library. Recently, the reactor simulation group at Soreq acquired, using funds provided by the Ministry of Energy and Infrastructure, a PC work station operating under a Linux operating system to give users of the library an easy on-line way to access resources available at the library.

These resources include the computer codes and their documentations, reports published by the reactor simulation group, and other information databases.

The expertise developed in the reactor simulation group at Soreq to port computer codes from one computation environment to another and to revise them to use new technologies are available for any new porting project as required.

We would like to extend the collection of computer codes relevant to nuclear engineering and of relevant databases which is available at the library. We would appreciate contributions from members of the Israel Nuclear Societies, and other, of any new code which they think is of interest for other people.

References

[1] M. Caner and D. Saphier. The energy systems code library. Technical Report RASG-164-92, Soreq Nuclear Research Center, 1992.

Plasma-Wall Interactions in Controlled Fusion Reactors: an Overview

E. Abramov

Ben-Gurion University of the Negev, P.O. Box 653 Beer-Sheva; and

Nuclear Research Centre Negev, P.O. Box 9001 Beer-Sheva

Understanding and controlling of plasma-wall interactions are key issues in the development of future fusion reactors. Above all, the interaction of hydrogen isotopes atoms with plasma-facing components will have an important role on the fuel recycling and therefor on plasma performances. Tritium inventory and permeation are the most crucial due to safety problems involved and the possible effect on materials properties. The situation become very complicated since while only few moles of deuterium and tritium will be confined as a plasma, their inventory in the wall is estimated to be some order of magnitude higher.

In order to estimate the plasma-wall recycling process in general one must consider the following issues: radiation damage and helium generation; ion penetration and tunnelling effects; trapping and release process; diffusion and permeation of helium and hydrogen isotopes; and surface behaviour (sputtering, erosion, blistering, exfoliation, etc.). It is also very important to understand the effects of aging and temperature cycling on the above mentioned process. The studies needed here are very complicated, due to the synergism of these process.

The present article will give an overview on the above mentioned process, their origin and role on plasma or wall materials performances. An emphasis will be given to helium and hydrogen isotopes generation, penetration, trapping, diffusion and desorption process.

A "Big-Mac" High Converting Water Reactor

Y. Ronen and Y. Dali

Department of Nuclear Engineering

Ben-Gurion University, Beer-Sheva , Israel

Currently an effort is being made to get rid of plutonium . Therefore, at this time, a scientific study of a high converting reactor seems to be out of place . However , it is our opinion that the future of nuclear energy lies, among other things in the clever utilization of plutonium .

It is also our opinion that one of the best ways to utilize plutonium is in high converting water reactors[1] .

One of the major problems of the high converting water reactors, which are tight lattice reactors , is the void coefficient , which is either positive or only slightly negative . For those cases that it is negative , the conversion ratio is not high.

The present paper suggests a reactor concept with high conversion ratio and negative void coefficient . This concept is named the "Big -Mac" reactor, due to the fact that the core consists of zones with higher and lower enrichments.

The core consists of fuel elements as presented in Figs.1. The fuel compositions of the different regions are given in Table 1. The dimensions of the reactor are the same as a typical 3000 MWth PWR.

Isotope	H.E-14%	H.E-12%	L.E	Hom.(6%)	Hom.(7%)
^{239}Pu	2.46219E-3	2.11044E-3	—	1.05522E-3	1.231095E-3
^{240}Pu	9.84078E-4	8.44170E-4	—	4.22085E-4	4.924390E-4
^{241}Pu	7.87900E-4	6.75340E-4	—	3.37670E-4	3.939500E-4
^{242}Pu	2.14730E-4	1.89844E-4	—	9.49225E-5	1.107365E-4
^{235}U	—	—	2.35044E-2	8.22850E-5	8.228000E-5
^{238}U	1.87584E-2	1.93951E-2	1.64560E-4	2.12270E-2	2.090442E-2
O	4.64300E-2	4.64300E-2	4.64300E-2	4.64300E-2	4.643000E-2

Table 1: The Fuel Compositions of Different Regions $\left(\frac{\text{atoms}}{\text{barn}\cdot\text{cm}}\right)$

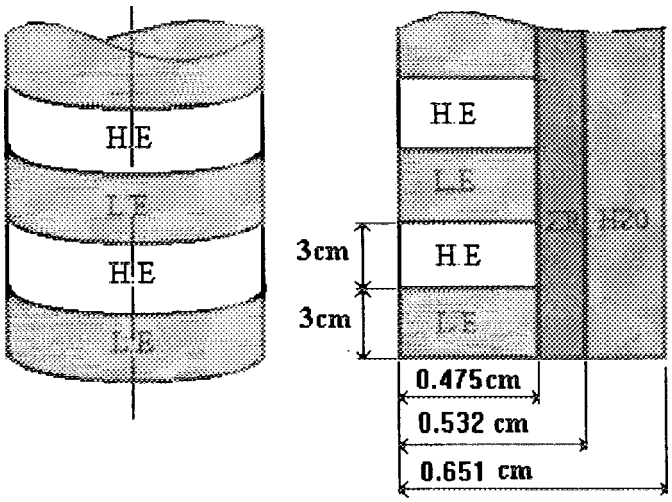

The Core
(not scale)

Unit Cell
(H.E-High Enrichment)
(L.E-Low Enrichment)

Fig.1: The Core and a Unit Cell of the Reactor

We have considered two enrichments. The first case is denoted as 14% and the second is denoted as 12% , as presented in Table 1. The Initial Conversion Ratio (ICR) for these two fuels are : ICR(14%)=0.866 and ICR(12%)=0.935 .

The reactivity void coefficients of these two reactors , in comparison to homogeneous reactors , are given in Figs.2 and 3 . By 'homogeneous reactor' we mean that the fuel elements have an homogeneous fuel composition . The amount of fuel in the fuel elements is the same in the homogeneous and the heterogeneous reactors . We can see from Figs.2 and 3 that the heterogeneous "Big-Mac" reactors have negative void coefficients compared to positive coefficients for the homogeneous reactors.

The void coefficient in the "Big-Mac" reactor is determined by two factors . The first factor is the hardening of the neutron spectrum when the reactor is voided . The second factor is the leakage , positive and negative , from the high to the low enrichment zones. These factors and their influence on the void coefficient will be presented and discussed in this paper.

References

1.Y. Ronen , "High converting water reactor ",CRC Press.,Boca Raton, FL 1990

BOL WITH BORON 14% ENRICHMENT

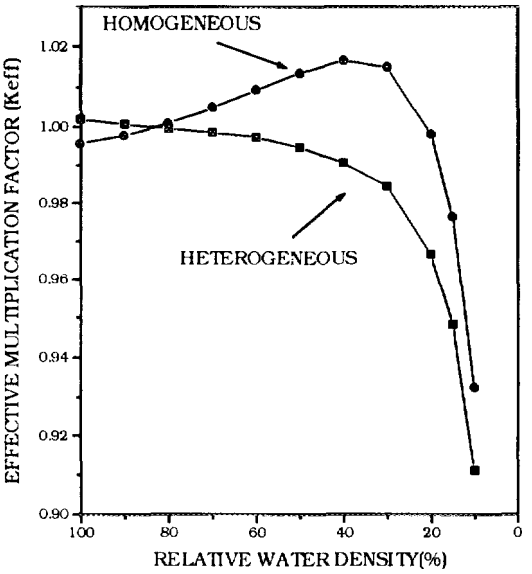

Fig.2:The Effective Multplication Factor for Different Water Densities-14%

BOL WITH BORON 12% ENRICHMENT

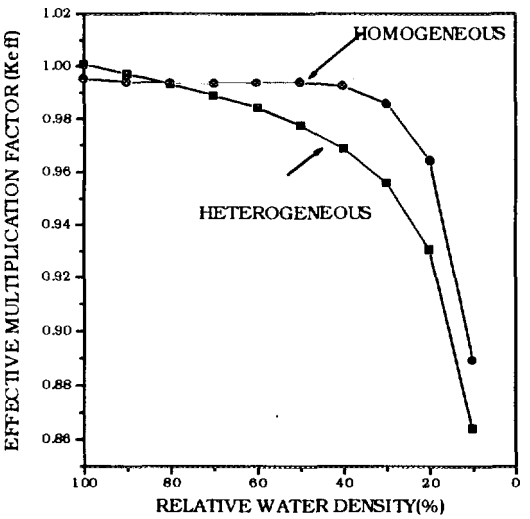

Fig.3:The Effective Multplication Factor for Different Water Densities-12%

Radiation Dose to the Patient in Several Diagnostic X-Ray Examinations Performed With Conventional Radiography Equipment in 3 Major Medical Centers is Israel, a comperative stady

A. Ben-Shlomo *, T. Shlesinger *, A. Kushilevsky **

Abstract

Conventional radiology is an important part of the medical diagnosis and treatment. It includes film radiography of the chest, abdomen, spine, extremities etc. The radiation dose of the patient under such examinations depends on several parameters :

- The constant parameters of the equipment (filtration, wave form, tube structure, etc).
- For systems equiped with photo-timer, the positioning of the organ image in front of the photo-timer (misalignment leads to changes in the exposure).
- The structure of the patient's body (different body sizes require different levels of entrance exposure).
- The radiographers assesment of the patient body size. This influences the choice of the exposure parameters (mA, kVp, time, distance, field size, and the choice of photo-timer mode).
- Irregular functioning of the equipment.
- The film-screens combination (determines the output requirements).
- Image quality problems. These influence the exposure parameters choice - kVp and mAs, when trying to overcome them, e.g lower/higher kVp and mAs to overcome poor contrast.

* Radiation Safety Division - Soreq NRC, Yavne, Israel.
** Dep. of Biomedical Engineering, Ben-Gurion Univ., Beer Sheva, Israel.

In this survey we determined the effective dose to the patient in specific x-ray diagnostic procedures performed in the radiology department and emergency rooms in 3 major hospitals (A, B, and C) in Israel. In each hospital we measured the dose area product (DAP) in a number of several major diagnostic procedures. In each hospital we carried out measurements in two X-ray departments (A1, A2. B1, B2, C1, C2). The DAP measurements were carried out using a Diamentor Dose Area Product meter (DAP). The entrance dose was obtained using calibration measurements relating the exposure at a reference distance to the imaging parameters (kVp, mAs, filtration and distance) that were recorded in the examinations. The results will be presented and compared to the reference international guidance values (1).

The dose area product measured for 3 diagnostic procedures are presented in fig 1 a, b, and c (additional results will be presented). The results for each procedure are the average values for a number of measurements performed by several radiographers, using 1-4 X-Ray machcines in the department. The number of measurements for each station is indicated above the columns. The patient sample included males and females 167.5 ± 7.5 cm high and weighing 67.5 ± 7.5 Kg.

The measured dose area product valus were used to calculate the effective dose, using conversion coefficients given in reference (2). The results are presented in table 1.

	Effective Dose (mSv)		
Hospital	Chest PA	Chest Lat	Abdomen AP
A1	0.02	0.04	0.33
A2	0.05	0.11	0.75
B1	0.09	0.19	1.14
B2	0.11	0.2	1.1
C1	0.12	0.38	1.07
C2	0.16	0.27	1.16

Table 1 - Effective dose to the patient in 3 diagnostic x-ray procedures in 6 departments in 3 hospitals.

The results emphasize several points :

1. The effective dose differs from department to department and hospital to hospital. A factor of 8, 9.5, and 3.5 was found between the minimal and maximal DAP for chest PA examinations, chest LAT examinations, and for abdomen AP examinations respectively.
2. The smallest effective dose was obtained in department A1. This department was the only one in the survey in which rare earth screens are used.
3. DAP values measured in different departments in the same hospital are similar. The maximal spread in the same hospital (excluding the hospital in which rare earth screens are used in one of the departments) is 40% .
4. Comparison of the average effective dose measured in department A1 (rare earth screens) and department A2 (ordinary $CaWO_4$ screens), shows that even in the same hospital a reduction of more then 50% in the effective dose can be achieved by using rare earth screens.

We can conclude that :

1. In a survey carried out in 6 radiology departments and emergency rooms, we observed great difrences in the effective dose to the patient for the same diagnostic x-ray procedure. A broader survey might show larger differences.
2. The advantage of using rare earth screens is obvious.

Based on the reported data and on other surveys performed in other countries, it is clear that a thorough quality assurance program will lead to a reduction of the mentioned spread and to a reduction in the dose to the patient.

Refrences

1. International Basic safety Standards for Protection Against Ionizing Radiation and for the Safety of Radiation Sources, Gov/2715, IAEA 1994.
2. Estimation of Effective Dose in Diagnostic Radiology from Entrance Surface Dose and Dose Area Product, NRPB-R262, 1994.

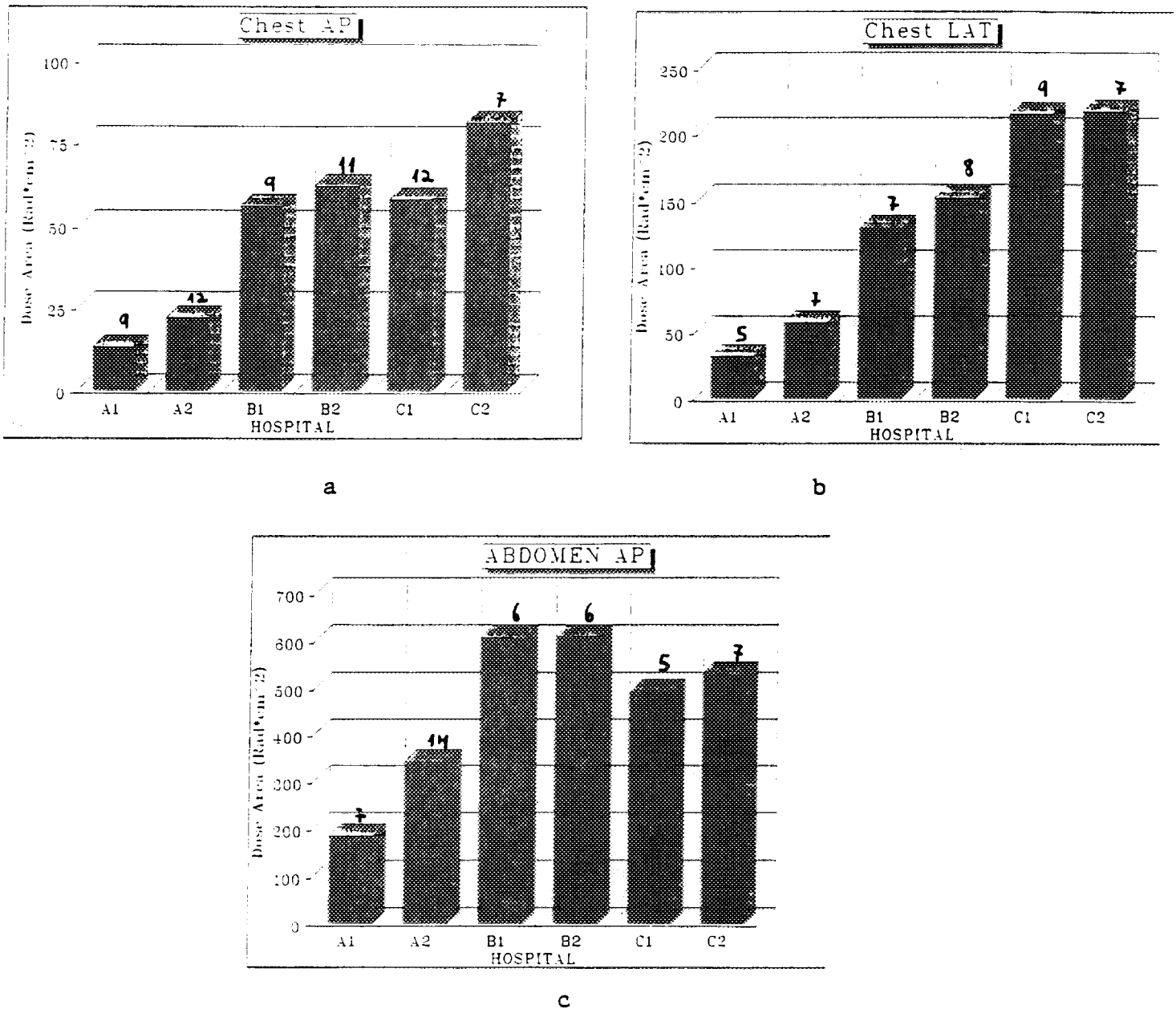

Fig. 1 - Dose Area Product measured in hospitals A, B and C. In station A1, rare earth screens are used. The values are the average of several measurements (indicated on each column).

AN ECONOMIC EVALUATION OF THE USE OF RARE-EARTH SCREENS TO REDUCE THE RADIATION DOSE FROM DIAGNOSTIC X-RAY PROCEDURES IN ISRAEL

G. M. Ginzburg[1] , T. Schlesinger[2] and A. Ben-Shlomo[2]

INTRODUCTION

In developed western countries (e.g. U.K.) doses received by patients from medical (mainly diagnostic X-rays account for the large majority (87%) of the total collective dose of the population from all artificial sources of radiation, the remaining 13% coming from nuclear medicine, fallout from weapons tests and nuclear disasters, air travel, occupational doses and nuclear power discharges [1].

X-rays are considered to be a carcinogenic agent. The carcinogenic effects of ionizing radiation in general and of diagnostic X-rays in particular are well established [2-6]. The quantitative carcinogenic risk of exposure to ionizing radiation was re-estimated in 1991 and found to have risen fourfold from 1.25% Sv^{-1} [4] to 5% Sv^{-1} [2].

Since diagnostic X-rays undoubtedly contribute to improving medical diagnosis and treatment, hence, health care, any efforts to reduce patient doses should in no way jeopardize the potential clinical benefits of X-rays [1]. Therefore, measures to reduce patient doses should involve reduction of unnecessary medical exposures as well as the use of more sophisticated equipment and more sensitive X-ray detection devices.

Unnecessary exposures can be eliminated partially by reducing the use of X-rays in cases where the probability of obtaining useful clinical information is extremely low [7-9]. Another source of unnecessary exposure arises from the unavailability of previously taken films [1,10-11]. Unsatisfactory image quality due to lack of suitable quality control procedures also results in unnecessary exposure from repeat X-rays, which are required in as many as 15% of all patients [10-12].

Reductions in patient dose resulting from changes in referral practices, or the establishment of quality control procedures require not only great initial effort, to overcome the inertia of established practices, but also continuous and constant effort in order to maintain the benefits. Despite these obstacles, attempts should be made to institute such changes as a means of reducing radiation exposure from diagnostic radiology.

[1] Dep. of Information and Computing, Ministry of Health, Jerusalem
[2] Radiation Safety Div. Soreq NRC, Yavneh

In contrasts, reducing the patient dose by using improved radiology equipment will often result in a constant reduction without further managerial effort for the lifetime of the equipment. Changing equipment is administratively far easier than altering long-established work practices.

There are several methods available to achieve dose reduction in diagnostic radiology via this second category. For example, dose reductions of between 10% and 20% can be achieved independently by reducing attenuation between patient and image receptor to a minimum by means of carbon fibre components in couch tops, cassette fronts and anti-scatter grids [13-15]. Radiation dosage in film radiography can be reduced by approximately 50% by the use of rare-earth screens, which enable a faster film speed to be utilized (thus reducing exposure time) without significant loss in the diagnostic quality of the image [15-16]. Rare-earth screens have been found in England to be the most cost-effective method of reducing dosage in film radiography, providing large dose reductions at considerably lower costs than carbon fiber components [17].

The use of rare-earth screens, which have been available since the early 1970s, is now widespread throughout the world, being common even in Russia and India. In Germany it is illegal to take X-rays in film radiography other than rare-earth screens. In the USA, fear of malpractice suits has catalyzed the diffusion of rare-earth screen technology throughout the health system. Diffusion of rare-earth screen technology was slower [18] in England. where by 1986 fewer than 50% of hospital examinations used rare-earth screens [19]. In 1990, the National Radiological Protection Board in England recommended that prime consideration be given to using rare-earth screens [1].

Only in 1995 did the first of Israel's 34 general hospitals start to use rare-earth screens extensively. However, rare-earth screens have been used for the past decade in military out-patient clinics. The second largest sick-fund, insuring approximately 18.8% of the population, has plans to increase greatly the small number of rare-earth screens currently in use in their ambulatory clinics.

The aim of this paper is to undertake a cost-benefit and cost-effectiveness analysis of the use of rare-earth screens in Israel in order to catalyze the establishment of guidelines, recommendations and even possible legislation regarding the use of rare-earth screens in Israel.

We estimated the total effective radiation dose from diagnostic film radiography amenable to reduction by use of rare-earth screens, based on the number of hospital and ambulatory diagnostic X-ray procedures amenable to use of rare-earth screens. This number was multiplied by the computed radiation dose per body site for a series of diagnostic procedures. The annual dose avertable by the introduction of rare-earth screen technology was estimated to be, approximately, 0.53 mSv per capita in Israel.

Based on a fatality risk of 3%/Sv (appropriate for a population with the age distribution characteristic to adult patients) it is estimated that the adoption of rare earth film technology might reduce the annual incidence of cancer in Israel by some 88 cases, half of which would be fatal (after an average latent period of 18.4 years).

The cost of purchasing rare earth screens on a nationwide basis is estimated to reach $2.8 million. Assuming a 5% rise in film prices (in comparison to the cost of the existing film-screen combination), the additional costs for the period 1995- 2004 are expected to reach $7.0 million. This additional costs are outweighed by saving $12.2 million on X-ray tube replacement costs in the same period.

METHODS

Data on the number of regular diagnostic procedures using X-rays in 1994 by body site (excluding dental, fluoroscopy and CT scans), were collected from 12 general hospitals (including out-patient clinics) which accounted for 43.1% of the 4.3 million general hospitalization days in Israel in 1993 [20]. Data were also collected from the largest rehabilitation hospital, which accounted for 72.0% of the 124,000 hospitalization days in Israel's three specialist rehabilitation hospitals in 1993 [20]. In addition, data on X-ray utilization were obtained from all the relevant geriatric institutions. National estimates of the use of hospital-based X-rays were made by multiplying our sample data by hospital type, by the reciprocal of our sample population's total utilization figure (e.g. general hospital data from our sample were multiplied by 100%/43.1%=2.32). Data from the military were excluded, since military facilities already use rare-earth screens.

Data were also collected on the number of X-ray procedures by body site in 1994 in the community-based ambulatory clinics operated by the General Sick Fund (Kupat Cholim Haklalit) which covers 63.5% of Israel's population (Research Department, National Insurance Institute, personal communication, 1995). Using age and sex-specific ambulatory care utilization rates [21], we estimated that because of their older age profile, general sick fund members account for approximately 66.2% of all non-hospital-based ambulatory visits. Thus, a multiplier of [100%/66.2%=1.51] was used to estimate national ambulatory X-ray usage. Finally, all the 1994 utilization data were adjusted upwards by 2.1% to reflect the population growth between 1994 and 1995.

A current study calculating the average effective dose per examination in Israel in only in its preliminary stages; hence, national estimates of the annual number of examination by body site were multiplied by the average effective dose (i.e., the weighted radiation dose to the different body organs) per examination by body site, based on data from the UK [18] and the USA [22]. For procedures which utilized both fluoroscopy and film radiography, we estimated the contribution to the effective dose of the film radiography alone. Utilization data (excluding those which included fluoroscopy) were adjusted upwards by a conservative figure of 10%

[10,12] to take into account retakes, which are currently not recorded in the X-ray utilization data systems. This enabled us to quantify the total national effective dose in Israel received in 1995 from diagnostic X-rays potentially amenable to reduction by the use of rare-earth screens.

Estimates of the number of cancers that may be attributed to exposure to radiation from diagnostic X-rays in Israel were made, using the figure estimated by the International commission on Radiological protection (ICRP) of 500 fatal cancers [2] per 10,000 man-Sieverts (5% Sv^{-1}) given to a standard population. The ICRP figure already takes into account the fact that, due to the latency period between exposure and cancer diagnosis, a part proportion of the affected population will die from other causes before the radiogenic cancer appears. With regard to diagnostic X-rays, we have to take into account that the exposure is not given to a standard population because a large proportion of a lifetime's exposure to diagnostic X-rays occurs during the patient's last illness, when radiogenic cancer is irrelevant [23].

In Israel, elderly persons (over 65 years old) use diagnostic tests (X-rays, mammography, CT and ultrasound) at a rate 4.5 times higher than 15-24 year olds [21]. Therefore, we reduced our fatal cancer risk rates, attributable to diagnostic X-rays, by the fraction suggested by Russell [23] and Wall [24] of the order of 40% to 300 fatal cancers per 10,000 man-Sieverts (3% Sv^{-1}).

We estimated the total attributable number of fatal cancers by multiplying the total national annual collective dose (man-Sv) from diagnostic X-rays by 3% Sv^{-1}. Based on the relative expected distribution of leukemia and all solid cancers, an average latency period of 18.4 years was assumed for mortality from X-ray induced cancers[2]. A further detriment of diagnostic X-rays, various curable non-fatal cancers (mainly of the skin and thyroid), approximately equal to the number of fatal cancers [21,23].

Costs ofrare aerth screens, films and X-ray tubes were obtained from the distributors of the equipment as well as from hospitals. Extra costs of the films adapted to the new screens were estimated to reach 5% of the conventional film prices. All costs and benefits occurring in the future were discounted back to mid 1995 price levels using a 5% annual discount rate. Israeli population growth was assumed to be at a rate of 2% per annum over the period 1995-2004.

RESULTS

Table 1 presents estimates of the number of persons examined and radiation doses received for film diagnostic X-rays, by body site for 1995. In 1995, Israel's population of 5.5 million underwent, approximately, 7.1 million film radiography examinations (including retakes), the dosage of which could potentially be reduced by the introduction of rare-earth screens. These figures are based on extrapolation from data collected from 12 general

hospitals. While X-rays of the limbs and chest accounted for 32.6% and 26.6%, respectively, of all such examinations, they accounted for only 0.8% and 2.2%, respectively of the total annual effective dose received (due to their low effective dose per examination). In contrast examinations of the bowel (barium tests) accounted for only 1.9% of all examinations but they accounted for 19.6% of the total effective dose.

Table 1. Film Diagnostic X-ray Examinations by Body Site (Israel 1995)

(excluding dental and CT)

BODY SITE	EFFECTIVE DOSE[a] (mSv) per exam	NUMBER OF EXAMINATIONS	(%)	TOTAL COLLECTIVE EFFECTIVE DOSE Man-(mSv)	(%)
LIMBS	0.01	2,319,000	32.6	23,000	0.8
CHEST	0.034	1,892,000	26.6	64,000	2.2
DORSAL SPINE	1.00	606,000	8.5	606,000	20.7
SKULL	0.10	550,000	7.7	55,000	1.9
CERVICAL SPINE	0.10	414,000	5.8	41,000	1.4
ABDOMEN	1.30	245,000	3.4	318,000	10.7
SHOULDER	0.10	409,000	5.8	41,000	1.4
LUMBAR SPINE	2.40	222,000	3.1	534,000	18.2
UPPER GI TRACT	2.16	218,000	3.1	470,000	16.3
BOWEL-INTESTINE	4.33	133,000	1.9	575,000	19.6
IV UROGRAPH	2.30	67,000	0.9	166,000	5.8
ESOPHAGUS	1.00	18,000	0.3	17,000	0.6
OTHER SITES	0.89	19,000	0.3	17,000	0.5
GRAND TOTAL		7,112,000	100	2,931,000	100

[a] According to UK (6, 7) and USA (22) calculations. For procedures which utilized both fluoroscopy and film radiography, we estimated the contribution to the effective dose of the film radiography according to the above list.

The annual total collective radiation dose received by the Israeli population from film radiography (including that in fluoroscopy procedures) amenable to reduction by the use of rare-earth screens in 1995 was approximately 2931 man-Sv (0.53 mSv per person). Considering a fatality risk of 3% Sv^{-1} we estimate that approximately 176 cases of cancer per year (half of which may be fatal) may in the future be attributable to diagnostic X-ray examinations performed in 1995, and whose radiation dose was amenable to reduction by the use of rare-earth screens.

The adoption of rare-earth screen technology in 1995 would have resulted in approximately 50% reduction [14-16] in radiation dosage from diagnostic X-rays in film radiography, reducing cancer fatalities by 44 lives per year compared with use of the present X-ray radiographic units, after the 18.4 year average latency period [2]. Similar mortality reductions (adjusted for population growth) would also be achieved in subsequent years, resulting in a total of 482 averted fatal cancers as a result of using rare-earth screens during the period 1995-2004.

There are currently approximately 1250 conventional X-ray machines employed in Israel, using an average of some ten cassettes per machine. The cost of immediately replacing these 12,500 cassettes with cassettes containing rare-earth-type screens is estimated at $225 per cassette, or $2.8 million.

The average number of films used per examination was found to be 1.8, of approximately 12.8 million films in 1995. Assuming an average cost per conventional film of $1.25 and a 5% average rise in film costs when using the new rare earth films this would lead to an additional cost of $800,000 in 1995, or $7.0 million over the period 1995-2004 (taking into account a population grouth of 2% per year and a discount rate of 5% per year).

On the other hand as a consequence of the use of faster films and hence the shorter exposure times, the utilization of rare-earth screens will result in an extension of the life of the X-ray tubes. Assuming that the 1250 tubes, which cost on the average approximately $15,000 each, will at a conservative estimate, need to be replaced every 12.5 years instead of every 6.25 years (personal communication. Yacov Hai, Ministry of Health, Unit for Licensing and Inspection of Medical Radiation Machines). There will be an annual reduction in tube replacement costs of $1.5 million, or a total of $12.2 million over the time period 1995-2004.

The above calculation does not include cancer treatment costs and lost life year costs saved due to the averted cancer cases .

SUMMERY

Adoption of rare-earth screen technology will have a net cost of $2.1 million in 1995, but will save $2.3 million overall during the period 1995-2004, since the reduction in tube costs ($12.2 million) will more than offset the extra costs of the screens ($2.8 millon) and films ($7 million). In addition such a move may also prevent during this period , approximately 960 cancers, half of which couldl be fatal.

REFERENCES

1. Report by the Royal College of Radiologists and the National Radiological Protection Board. Patient Dose Reduction in Diagnostic Radiology. Documents of the NRPB 1990; Vol. 3, NRPB-Didcot, Oxford (1990).

2. International Commission on Radiological Protection (ICRP) 1990. Recommendations of the International Commission of Radiological Protection (ICRP Publication 60). Ann. ICRP 21, 1-3 (1991)

3. Committee on the Biological Effects of Ionizing Radiation. Health Effects of Exposure to Low Levels of Ionizing Radiation (BEIRV). Washington, DC: National Academy of Press (1990).

4. United Nations Scientific Committee of the Effects of Atomic Radiation (UNSCEAR). Sources, Effects and Risks of Ionizing Radiation: 1988 Report to General Assembly. New-York: United Nations (1988).

5. Russell, J.G.B., How dangerous are diagnostic X-rays? Clin. Radiol. 35, 347-351 (1984)

6. Smith, P.G and Doll, R., Mortality among patients with ankylosing spondylitis after a single treatment course with X-rays. Br. Med. J. 284, 4449-460 (1982).

7. Bransby-Zachary, M.A.P and Sutherland, G.R., Unnecessary X-ray examinations. Br. Med. J. 298, 1294 (1989).

8. Menuhin. S.,X-rating the X-rays. The Guardian, Sept. 7 (1990).

9. Royal College of Radiologists Working Party. Making the Best Use of a Department of Clinical Radiology. Guidelines for Doctors (2nd ed.). Royal College of Radiologists, London (1993).

10. Berry, R.J, and Oliver, R., Spoilt films in X-ray departments and radiation exposure to the public from medical radiology. Br. J. Radiol. 49, 475-476 (1976).

11. Watkinson, S., Moores, B.M and Hill, S.J., Reject analysis: Its role in quality assurance. Radiology 50, 189-194 (1984).

NEUTRON ACTIVATION ANALYSIS FOR ENVIRONMENTAL TRACE ELEMENT RESEARCH DETERMINATION OF ELEMENTAL COMPOSITION OF SEDIMENTS IN THE SEA OF GALILEE, ISRAEL

N. LAVI, E. NE'EMAN, S. BRENNER, V. Butenko
INSTITUTE FOR ENVIRONMENTAL RESEARCH
TEL-AVIV UNIVERSITY, SACKLER MEDICAL SCHOOL,
RAMAT AVIV 69978 TEL-AVIV, ISRAEL

Summary

During the last twenty years, neutron activation analysis (NAA) has been extensively used for the trace element determination of airbone particulate matter in environmental and atmospheric transport studies.[1] The influence and distribution of air-pollutants on sedimentation processes is widely discussed in the literature.[2]
Characterization of the elemental composition can reveal the features involved in the processes of sediment formation and transportation.

The feasibility of applying both thermal and epithermal neutron activation analysis for simultaneous determinations of elemental composition in sediments, collected from the Sea of Galille (Kineret Lake), Israel, was experimentally investigated. In the present work, the concentrations of 30 elements (Al, Ba, Br, Ca, Ce, Co, Cs, Cr, Eu, Fe, Hf, K, La, Lu, Mg, Mn, Na, Nd, Rb, Sc, Si, Sr, Ta, Tb, Th, Ti, U, V, Yb and Zn) in sediments were determined.
The validity of the method was checked by analyzing the U.S. NBS Standard Reference Material SRM-1633a; the elemental content found agreed well with the published certified data.
Aluminim was determined by reactor neutron activation analysis (RNAA) taking into account the contribution of silicon to the total ^{28}Al activity by the $^{28}Si(n,p)^{28}Al$ reaction. Measurements of irradiated mixtures of Si and Al showed that the dependence of log Si:Al mass ratio vs. log cadmium ratio (R_{Cd}) of ^{28}Al is almost linear.

Epithermal neutron activation analysis (ENAA) followed by high resolution gamma-ray spectrometry has in recent years become one of the most promising and attractive methods[3,4] for simultaneous multielemental analysis of biological and geological materials.
The method is especially suitable for the analysis of geological and biological materials by INAA, since the principal interfering elements,

12. Rogres, K.D., Matthews, I.P and Roberts, CJ. ,Variation in repeat rates between 18 radiology departments, Br. J. Radiol. 60, 463-468 (1987).

13. Hufton, A.P, and Russell, J.G.B., The use of carbon fiber material in table tops, cassette fonts and grid covers: magnitude of possible dose reduction. Br. J. Radiol. 59, 157-163 (1986).

14. Davison, M., Does it pay to be optimistic? Br. J. Radiol. 61, 1189-1190 (1988).

15. Russell, J.G.B and Gray, J.E., X-rays: keeping the doses down. World Health Forum 13, 213-217 (1992).

16. Israel Ministry of Health. Report of the Committee for Reducing Radiation and Improving the Picture Quality of X-rays using Different Combinations of Films and Screens. (Chairperson Y. Berlovitz).Ministry of Health, Jerusalem, April 1993 (in Hebrew).

17. Wall, B.F and Russell, J.G.B., The application of cost-utility analysis to radiological protection in diagnostic radiology. J. Radiol. 8,221-222 (1988).

18. Shrimpton, P.C, Wall, B.F, Jones, D.G, et al. A National Survey of Doses to Patients Undergoing a Selection of Routine X-ray Examinations in English Hospitals. Chilton NRPB-R200 London: Her Majesty's Stationery Office (1986)

19. Russell, J.G.B., Assessment of the current use of rare-earth screens in the United Kingdom. Br. J. Radiol. 59,630(1986).

20. Israel Ministry of Health Division of Computing and Information Hospital Institutions and Units for Day Care in Israel 1993. Jerusalem, Oct. 1994 (in Hebrew).

21. Israel Central Bureau of Statistics & Ministry of Health. Use of Health Services Survey January-March 1993. Special Series No. 970. Central Bureau of Statistics, Jerusalem (1994).

22. Protection of the Patient in Diagnostic Radiology. Annals of the CRP. vol. 9, no. 2/3 CRP pub. 34 (1982)

23. Russell, J.G.B AND Webb, G.A.M., Valuing the man-Sievert in X-ray diagnosis. Lancet 83-87, July 17 (1979).

24. Wall, B.F., Radiological hazards to parents from diagnostic nuclear medicine procedures in the UK. Med. Biol. Eng. & Comput. 23, Suppl. 2(1985).

sodium and chlorine have a low ratio of resonance integral to thermal neutron cross section.[5] The application of ENAA has been studied extensively and advanatge factors[6] were calculated for many elements. The aims of this work were to:

a) demonstrate the effectiveness of instrumental neutron activation anlysis for determining the background concentrations of trace elements in the sediments collected from the Sea of Gallile.
b) determine the advantage factors for epithermal neutron irradiation.
c) determine the contribution of silicon to the total ^{28}Al activity by the $^{28}Si(n,p)^{28}Al$ reaction.
c) check the validity of the method by determining the elemental content of U.S. NBS Standard Reference Material SRM-1633a (fly ash).
d) calculate the average enrichment factors for the elements in sediments.
e) determine the concentrations of the artificial radionuclides ^{134}Cs, ^{137}Cs and the naturally occuring radionuclides ^{40}K, ^{226}Ra and ^{232}Th in sediments by gamma ray spectrometry using Marinelli Beaker Sample containers of 450 cm^3.

Results and discussion

The average enrichment factors calculated for the elements in sediments and compared with the average enrichment factors of dustfall following Sahara dust storms[7] and soil[8] are shown in Fig. 1.

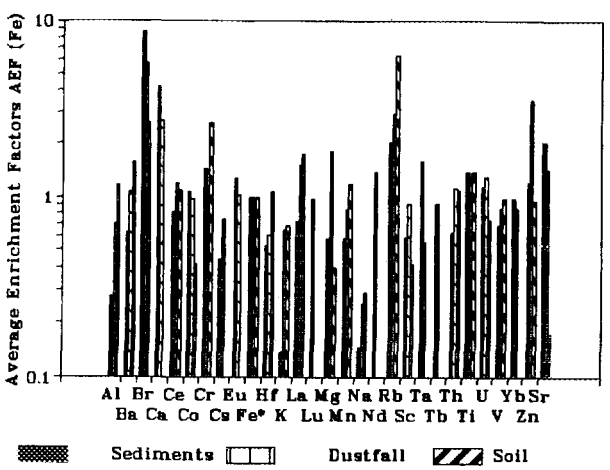

Fig. 1. Average Enrichment Factors AEF (normalized to Fe) calculated for the elements in sediments, soil and dustfall (following Sahara dust storms).

The concentration, C, of an element of interest, E, found in sediments (CE_S) was compared with the average concentration of the same element in the earth's crust (CE_C) and the enrichment factors (EF) were calculated by the following equation:

$$EF = \frac{CE_S/CE_C}{CFe_S/CFe_C}$$

where CFe_S and CFe_C are the concentrations of iron (which was selected as the normalizing element) in the sediments (s) and the earth's crust, (c) respectively. The enrichment factors were calculated using the average crustal values given by Mason and Moore.[9]

From the results obtained it was found that the sediment samples in the Sea of Galilee are relatively enriched in Ca and Br.

The concentrations of the fission radionuclide ^{137}Cs, an activation radionuclide ^{134}Cs and the naturally occuring radionuclides ^{40}K, ^{226}Ra and ^{232}Th in the sediments were measured by gamma ray spectrometry.

In order to check the origin of radiocesium in the sediment samples we determined the activity ratio of $^{134}Cs/^{137}Cs$ (recalculated to May 1986) which ranged from 0.30 to 0.46. The $^{134}Cs/^{137}Cs$ activity ratio determined in soil[10] and recalculated to May 1986, was found to be 0.528. The radioactivity (Bq kg^{-1}, dry weight) deduced from measurements of sediments collected from the Sea of Galilee, Israel, is shown in Fig. 2.

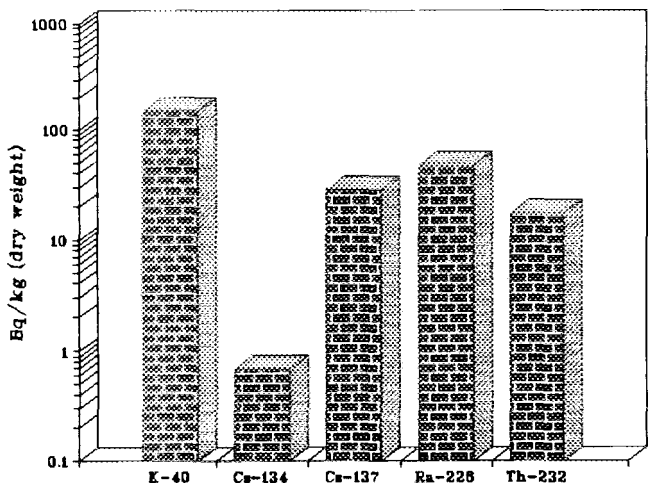

Fig. 2. Measurements of radioactivity in sediments collected from the Sea of Galilee, Israel, by gamma ray spectrometry using Marinelli Beaker Sample Containers of 450 cm^3.

Conclusions

This ecological study was carried out in order to provide useful information concerning the elemental composition of sediments in the Sea of Galilee which serves as a drinking water resource of Israel.
It is of importance to determine and to verify the concentration of sediments that could affect the water composition and quality.

Determination of the background concentrations of trace elements in the sediment would enable detection in the future of any pollution transport that can be revelead.

The method of instrumental neutron activation analysis (INAA) using both reactor and epithermal neutron irradiation, is nondestructive, accurate, highly sensitive and may be routinely applied on a laboratory scale. Analysis by epithermal neutron activation leads to an improvement in the precision and sensitivity of the determination of trace elements in which the ratio of the resonance integral (I_o) to the thermal cross section (σ_o) is large.

References

1. C. E. Amundsen, J. E. Hanssen, J. P. Rambak, A. Semb and E. Steiness, Modern Trends in Activation Analysis, Copenhagen, Vol. 2, (1986) p. 947.
2. M. Bernhard, Ocean Management 3 (1978) 253
3. H. Bem, DE. Ryan, Anal. Chim. Acta, 135 (1982) 129.
4. T. Bereznai, TD. MacMahon J. Radianal. Chem., 45 (1978) 423.
5. AO. Brunfelt, E. Steiness, Anal. Chim. Acta, 48 (1969) 13.
6. D. Brune, K. Jirlow, Nukleonika, 6 (1964) 272.
7. N. Lavi, E. Ganor, E. Ne'eman, S. Brenner, "Determination of Elemental Composition of Settling Particles in Israel following Saharan Dust Storms by Neutron Activation Analysis", J. Radioanal. Nucl. Chem., 163 (1992), No. 2, 313.
8. A. P. Vinogradov, "The Geochemistry of Rare and Dispersed Chemical Elements in Soil", Consultants Bureau, Inc., New York 1959, p. 183.
9. B. Mason, C. B. Moore, Principles of Geochemistry, 4th ed., John Wiley, New York, 1982, p. 46.
10. G. Kirchner, D. Baumgartner, "Migration rates of radionuclides deposited after the Chernobyl accident in various north German soils", Analyst, 117, (1992) 475.

^{129}I in sea-weeds determined by AMS

Feldstein H., Berkovits D., Peled A., Soreq Nuclear Research Center, and Paul M., Ghelberg S., Kashiv Y., Racah Institute for Physics, Hebrew University, Jerusalem.

The aim of the work: The aim of the present work was to determine the concentration of ^{129}I accumulated in sea-weeds in various places along the Israeli Mediterranean coast and in Eilat. Sea-weeds are known to accumulate iodine and its concentration varies from few tens to about 2000 ppm (dry basis), depending on the kind of the plant. The natural background of ^{129}I is extremely low and the isotope, produced mainly by nuclear fission may serve as a monitor of the distribution of contamination due to human activities like - nuclear weapon tests, fuel reprocessing and disasters, like Chernobyl.

Methods: Direct counting of ^{129}I is unfeasible because of its long half-life ($1.6x10^7$ years) but it may be determined indirectly, by neutron activation followed by gamma counting of ^{130}I ($T_{1/2}$=12.5 h.). The detection limit is about 10^{11} atoms and a very clean separation process is required. In this work the AMS. (Accelerator Mass Spectrometry) technique[1], which is a novel and very sensitive method, was applied for the quantitative determination of ^{129}I. A primary beam of negative ions, produced by bombardment of a target sample with Cs ions is mass separated and a chosen mass is further accelerated by a positive voltage of 11.5 MV. The accelerated ions pass through a thin carbon foil which decomposes all the molecular clusters and strips some of the electrons, and the resulting highly charged ion beam is again mass separated. At the collector, single ion counting methods are applied with an ultimate sensitivity of about 10^5 atoms. The AMS facility uses the 14UD Pelletron at the Weizman Institute of Science.

Results and conclusion: Preliminary results indicate that the concentration of iodine-129 in samples collected in Eilat is one order of magnitude lower than in samples collected in the Mediterranean. At this stage it is impossible to tell whether the difference results from the Chernobyl accident or is due to water contamination by the nuclear countries in the Mediterranean basin.

[1] R.C. Finkel and M. Suter, Advances in Analytical Geochemistry 1 (1993), 1-114.

ENHANCED DNA REPAIR—A NEW MODALITY FOR IMPROVED RADIOPROTECTION AND PHOTOPROTECTION

Emanuel Riklis
EDNAR R&D, former chief scientist. Nuclear Research Center- Negev, PO Box 9001, Beer Sheva, Israel

Classical radioprotection which began in 1949 by Harvey Patt, has reached a deadlock where the maximum protection factor attained by various chemicals is around 2. Furthermore, the compound considered to be the best, WR-2721, is too toxic to be of general use in emergency situations.

A more important mode of protection is offered by the biological parameters of DNA repair capacity, enabling cells with a high repair capacity to be far more resistant to radiation than cells with deficient repair capabilities.

A formula of enhanced DNA repair was offered in 1981 by Riklis as a model for improved protection, combining DNA repair capabilities with chemicals that may enhance these capabilities. This property of enhanced repair is particularly of importance for protection from the genetic effects of low level and chronic radiation due to its antimutagenic effects.

The enhancement of DNA repair was first demonstrated by the addition of WR-2721 when added even after exposure to ionizing radiation and to UV radiation (Riklis 1983). Later, some natural non-toxic compounds were found to have the same effect. Thus the vitamin nicotinamide at a low concentration of 3 mM can enhance DNA repair synthesis with up to 5 fold dose dependent increase in ^{3}H-thymidine uptake into damage sites.

In solar radiation, UVA mimics the effects of ionizing radiation in terms of oxidative damage, which cause DNA single strand breaks. UVB, like UVC radiation produces specific photoproducts which are repaired through excision repair (Riklis 1965). Recently, a combination of nicotinamide and certain antioxidants was developed, affording a unique system for enhancement of DNA repair after exposure to either solar radiation or ionizing radiation.

Such a combination has been included in a preparation named EDNAR (Enhanced DNA Repair), which provides better protection from sun light, a skin protection system without the need for chemical filtering sunscreen. The lotion shows also antimutagenic and anti-inflammatory properties. This offers a new dimension to solar protection and to skin protection from radiation (Riklis 1996). The possible internal use of EDNAR to replace classical (but toxic) radioprotectors is being considered.

Riklis, E., Studies on mechanism of repair of UV-irradiated viral and bacterial DNA in vivo and in vitro, Canad. J. Biochem. 43, 1207-1219, 1965.

Riklis, E., DNA repair as a probe of radiosensitivity and radioprotection, in "Radioprotectors and Anticarcinogens" (Edit: O.F. Nygaard and M.G. Simic) 363-380, 1983 Academic Press

Riklis, E., Biochemical protection: antioxidants and enhancement of DNA repair, cellular and molecular mechanisms, in "Ozone-Sun-Cancer (Edit: L. Dubertret, R. Santus, P. Morliere) 199-204, 1995, Les Edition INSERM, Paris

Chernobyl Ten Years After - Sum-up of the Radiological and Health Effects as Reported by IAEA and WHO

J. Koch

Applied Physics Division
Soreq Nuclear Research Center
81800 - Yavne, Israel

D. Ilberg

Licensing Division
Israel Atomic Energy Commission
61070 - Tel-Aviv, Israel

Introduction

This paper will summarize the main findings presented by the scientific community at international conferences convened to sum-up the consequences of the Chernobyl accident at its tenth anniversary. It will only deal with the radiological and health consequences, as they were presented at the EC/IAEA/WHO International Conference "One Decade after Chernobyl" (Vienna, 8-12 April 1996) and the WHO International Conference on Health Consequences of the Chernobyl and Other Radiological Accidents (Geneva, 20-23 November 1995).

The release

It is today estimated that the total activity of radioactive material released is much higher than the 1986 estimate of 1-2 x 10^{18} Bq, which was based only on the activity deposited within the former USSR. Around 12 x 10^{18} Bq were released, amounting to 3-4% of the used fuel present in the core, as well as close to 100% of the rare gases (6-7 x 10^{18} Bq) and 20-60% of the volatile radionuclides. The radioactive isotopes of iodine and cesium are of special radiological significance, in the short term and in the long term respectively: the release included 50-60% of the radioiodine (about 2 x 10^{18} Bq of ^{131}I) and 20-40% of the radiocesium (about 0.09 x 10^{18} Bq of ^{137}Cs and about 0.06 x 10^{18} Bq of ^{134}Cs).

Radiation doses

Although the material released into the atmosphere deposited and was measurable over the whole northern hemisphere, the largest part deposited in regions around the plant site in northern Ukraine, southern Belarus and the southwestern part of the Russian Federation. Fig.1 shows the most contaminated districts of the three countries and the areas where the deposition density of ^{137}Cs is higher than 185 kBq/m^2 (5 Ci/km^2).

Different population groups of interest were defined according to the deposition density of ^{137}Cs:

- The "evacuees": those who were permanently evacuated in April-May 1986 from the town of Pripyat and from the 30-km "exclusion zone" around the plant (^{137}Cs deposition density above 1,480 kBq/m2).
- The residents of the "strict control zones" (^{137}Cs deposition density above 555 kBq/m2). In these areas, typically within a few hundred km of the plant, radiation

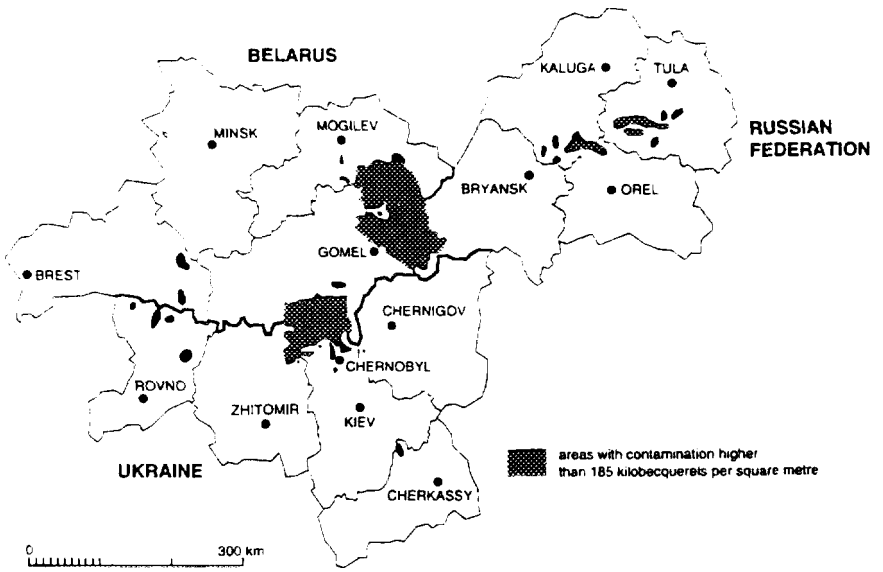

Fig. 1. The contaminated districts in Belarus, Ukraine and the Russian Federation (Source: WHO).

monitoring and preventive measures have been taken to maintain doses within permissible levels.

- The general population of the "contaminated territories" (^{137}Cs deposition density above 37 kBq/m2) in the three countries.

Table 1 presents the number of persons exposed in each group, as well as the average individual effective dose and the collective effective dose.

Table 1. The radiation doses received by the different population groups of interest.

Deposition density of ^{137}Cs		Area	Population size	Average effective dose	Collective effective dose
kBq/m^2	Ci/km^2	km^2		mSv	person x Sv
>37	>1	131,000	6,800,000	6-20	40,000-110,000
"contaminated territories"					
>555	>15	10,300	270,000	50-60	10,000-20,000
"strict control zones"					
>1,480	>40	3,100	135,000	Prypiat:12	1,300
"exclusion zone"				others:18	

Another group of interest includes the workers which took part in activities to "liquidate" the consequences of the accident (the "liquidators"). They include plant operators and emergency personnel (firefighters, soldiers), workers in the clean-up around the reactor, in construction of the "sarcophagus" to cover the damaged core, in decontamination, in building of roads and in destruction and burial of contaminated buildings, forests and equipment. They also include many others who worked in the

contaminated territories and were much less exposed, such as physicians, teachers, cooks and interpreters. About 200,000 liquidators worked in the Chernobyl region during the period 1986-87 and were the most exposed. They received an average dose of about 100 mSv, while 10% received doses of the order of 250 mSv and a few percent doses higher than 500 mSv.

Clinically observed early effects

Exposure to high doses of radiation affect acutely and severely blood cell production, resistance against infections and intestinal function and may result in severe damage to the skin. The complex disease is known as Acute Radiation Sickness (ARS). Its common symptoms are initially nausea, vomiting and diarrhea and later on, bleeding and generalized infections. If untreated, ARS is lethal.
Among the plant staff, the firefighters and the emergency workers who initially responded to the accident, 237 people were hospitalized as suspected of suffering from ARS. 28 of these died within the first three months after exposure. Three more people died immediately due to other causes (the explosion, thermal burns and a coronary thrombosis), bringing the total to 31.
The distribution of the 237 patients according to the severity of ARS (related to the received dose) is shown in Fig.2, together with the numbers of lethal outcome in the acute phase and in the following years.

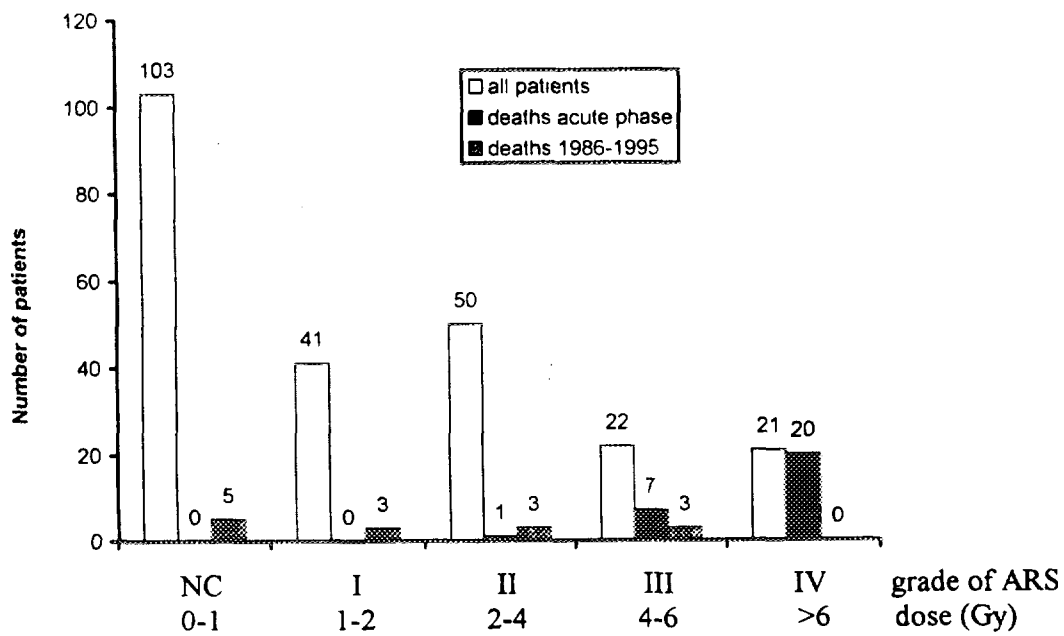

Fig.2. Numbers of ARS patients and mortality as a function of dose (NC: diagnosis of ARS not confirmed) (Source: Guskova A.K., State Scientific Centre of the Russian Federation, Moscow).

It can be seen that the diagnosis of ARS was confirmed in 134 cases and that the acute lethality is strictly related to dose. Of the 134 cases, 41 had mild (Grade I) ARS and all survived. 50 patients had Grade II ARS, of which one died. 7 patients died out of 22 with Grade III ARS. 21 patients suffered of Grade IV ARS following a whole-body

exposure larger than 6 Gy. All but one died despite intensive treatment. Among the latter, the gastrointestinal damage was a most severe problem in 11 patients who received doses higher than 10 Gy. Deaths in 26 of the 28 patients who died in the first 3 months were associated with radiation skin burns involving over 50% of the total body surface area.
After the acute phase, 14 additional patients have died over the last 10 years. However, their deaths may not be attributable to the radiation exposure, since they are not correlated with the original ARS severity.
The therapy of bone marrow transplantation, recommended at the time, was of little benefit. From today's knowledge this is well understandable, in view of the intrinsic immunological risks of the procedure, the heterogeneous irradiation during the accident (causing part of the lymphocytes to survive and the subsequent rejection) and the complicating factors (gastrointestinal damage and skin lesions). Rapid administration of haemopoietic growth factors will probably be recommended in future cases of bone marrow damage, in order to stimulate the recovery of the blood and immune system. However, research is still needed to develop pharmaceutical products and to establish the optimal combination.

Thyroid cancers

During the first few weeks after the accident ^{131}I was the most important radionuclide, since it accumulates in the thyroid when absorbed through inhalation or ingestion of food. Many people in the affected areas had a shortage of iodine in their diet and were expected to absorb radioiodine readily. More than five million people are reported to have received stable iodine tablets to block absorption of radioiodine, but large numbers of children did not receive these tablets. Thus some people, especially children, received large radiation doses to the thyroid.
There has been a substantial increase in reported cases of thyroid cancer in those exposed as children in Belarus and Ukraine, and to a lesser extent in some parts of the Russian Federation.
The numbers of cases of childhood thyroid cancer in the three countries, as well as the incidence rates, are shown in Table 2 for each year since 1986.

Table 2. Childhood thyroid cancer 1986-1994 in Belarus, the Russian Federation (Bryank and Kaluga districts) and Ukraine (Source: WHO).

	Number of cases per year									
	1986	**1987**	**1988**	**1989**	**1990**	**1991**	**1992**	**1993**	**1994**	**Total**
Belarus	2	4	5	7	29	59	66	79	82	333
Russian Federation	0	1	0	0	2	0	4	6	11	24
Ukraine	8	7	8	11	26	22	47	42	37*	208*

	Incidence (rounded) per million children								
	1986	**1987**	**1988**	**1989**	**1990**	**1991**	**1992**	**1993**	**1994**
Belarus	0.9	1.7	2.2	3.0	13	26	28	34	36
Russian Federation	0.0	2.0	0.0	0.0	4.0	0.0	8.0	12	22
Ukraine	0.7	0.6	0.7	0.9	2.2	1.8	3.9	3.5	3.1*

Note: * = incomplete number
Belarus has 2.3 million children, Ukraine has 12 million and the Bryansk and Kaluga oblasts of the Russian Federation have 500 000.

Up to the end of 1995, a total of about 800 cases (including 400 in Belarus alone) have been reported in children who were under age 15 at the time of diagnosis.
There is strong evidence that the increased incidence of childhood thyroid cancer is due to exposure to radioiodine following the accident, based on the geographical and temporal distribution of the cases. Most cases are concentrated in areas that have been heavily contaminated and they are observed only in children who were born before the accident or less than 6 months thereafter.
Over the next decades, there will most probably be an increase in the incidence of thyroid cancer among those who were children in 1986, those exposed as very young children being at the greatest risk. The estimated number of cases is in the range of a few thousand, but there is considerable uncertainty about this. The group at risk should be closely monitored throughout their lives.
The latency period between the exposure and the diagnosis is a little shorter than expected on the basis of previous experience. It ranges at present between 4 and 10 years, with a mean of about 6 years.
More than 95% of the reported cases are papillary carcinomas. They are also highly invasive, spreading both within the thyroid gland and into surrounding soft tissues, lymph nodes, blood vessels and the lungs. In spite of their aggressiveness, the cancers appear to respond favorably to standard therapeutic procedures and so far, a very small number of children (three) have died of their disease.

Long-term radiation health effects

Apart from thyroid cancer, there has been no statistically significant deviation in the incidence rates of other cancers attributable to radiation exposure due to the accident. In particular, no consistent attributable increase has been detected to date in the rate of leukemia, one of the major concerns after radiation exposure.
The predicted lifetime excess over normal mortality from solid cancers and leukemia is presented in Table 3 for the four above-mentioned exposed population groups.

Table 3. Predicted background and excess deaths from solid cancers and leukemia in the population groups of interest (Source: Cardis E., IARC, Lyon, France).

Population	Population size	Cancer type	Background number of cancer deaths	Predicted lifetime excess	
				Number	Percent.
Liquidators (1986-87)	200,000	Solid cancers	41,500	2,000	5%
		Leukemia	800	200	20%
Evacuees from "exclusion zone"	135,000	Solid cancers	21,500	150	0.7%
		Leukemia	500	10	2%
Residents of "strict control zones"	270,000	Solid cancers	43,500	1,500	3%
		Leukemia	1,000	100	9%
Residents of "contaminated territories"	6,800,000	Solid cancers	1,100,000	5,000	0.5%
		Leukemia	24,000	400	1.5%

If the experience of survivors of the atomic bombing and of other exposed populations is applicable, the greatest numbers of excess cancer deaths should be observed among the 200,000 liquidators and among the 6,800,000 residents of the contaminated territories, 2,000 and 5,000 respectively. However, these increases would be difficult to detect epidemiologically against the expected background (41,500 and 1,100,000 deaths respectively).
It can also be seen that leukemia among liquidators is the significant health effect most likely to be detected (200 excess deaths against a background of 800). It is therefore important to carry on large scale studies among the liquidators, which should also provide information on the effect of exposure rate and exposure type in the relatively low dose range (0-500 mSv).

Psychological consequences

There are significant non-radiation-related health disorders and symptoms, such as anxiety, depression and various psychosomatic disorders attributable to mental stress among the population in the region. The psychosocial effects result from the following factors:

- the lack of information immediately after the accident.
- the mistrust of authorities and official statements.
- a poor understanding by the public of radiation and the effects of radiation exposure.
- the stress and trauma of compulsory evacuation and relocation.
- the social disruption following relocation.
- the fear for one's health and his children's health following radiation exposure.

The effects are widespread and long-lasting and have been intensified by the appearance of the radiation-related thyroid cancers. Severe conditions are characterized by a sense of helplessness and despair, leading to social withdrawal, and little hope for a positive future. On the other hand, it is very difficult to dissociate these effects from those attributable to the breakup of the centralized political and economic systems of the Soviet Union.
It is known that stress can be alleviated in a number of ways. Although the original stressor cannot be removed in the present case, it is possible to provide people with a sense of control over the stressor, for instance by voluntary food controls, resettlement or community action. It is also possible to change the way in which the source of stress is perceived by diffusing trustworthy knowledge. These tasks are being performed by UNESCO, which established a few community centers ("Centers of Trust") to provide psychological support, information seminars and social activities.
The importance of a correct diagnosis was emphasized and the term "Chronic Environmental Stress Disorder" was suggested.

Summary

The health effects of the Chernobyl accident can be summarized ten years later as follows:

- Early effects

134 workers exposed to high doses of radiation at the early stage of the accident suffered of acute radiation sickness and 28 of them died within the first three months. 3 more people died during the accident due to other causes.

- Late effects

There is a very significant increase in the number of childhood thyroid cancers, which is attributable to the exposure to radioiodine released by the accident. Up to the end of 1995, about 800 cases (including 400 in Belarus alone) have been reported in children who were less than 15 years old at diagnosis. The thyroid cancers are aggressive in nature, but they appear to respond favorably to standard therapy. Their incidence is still increasing.

Apart from thyroid cancer, there has been to date no significant deviation in the incidence rates of leukemia and other cancers attributable to radiation exposure due to the accident. The health effect most likely to be detected in the future is an increased rate of incidence of leukemia among the 200,000 liquidators exposed during 1986-87.

- Psychological effects

Extensive effects are apparent in the affected regions, manifested as anxiety, depression and various psychosomatic disorders linked to mental stress. Their treatment involves providing psychological support and restoring trust.

Acknowledgments. The authors express their gratitude to Dr. A.K. Guskova (State Scientific Centre of the Russian Federation, Moscow) and to Dr. E. Cardis (International Agency for Research on Cancer, Lyon, France), who gave their permission to reproduce a table and a figure which were presented at the Vienna Conference. They also thank WHO for its authorization to reproduce a table and a figure from its 1995 publication "Health consequences of the Chernobyl accident".

A new approach to the Nuclear Power Plant Site licensing.

Alfred A. Kidron, Nuclear Project Manager, R&D Division, The Israel Electric Corporation Ltd.

STATUS OF THE SITE LICENSING

The Israel Electric Corporation Ltd.(IEC) conducted a survey to determine the geotechnical suitability of the Shivta Site for the purpose of erecting a Nuclear Power Station and presented the results in a Preliminary Safety Analysis Report (PSAR) to the Licensing Division of the Israel Atomic Energy Commission (LD). The studies for selecting a site in the NW Negev were conducted by multi-disciplinary teams of Israeli and US professionals, beginning in 1982, over a twelve-year period. The investigations involved comprehensive geological, geophysical, geotechnical, hydrological, as well as geomorphic and pedologic evaluations of the region and the then-proposed site locale. The prior studies were completed using highly advanced and modern tools and approaches and provided a significant amount of information related to the tectonic and seismic characteristics of the NW Negev region.

Following the review of the PSAR, the LD notified IEC that the Shivta Site did not sufficiently satisfy the criteria required for licensing a site and did not acccpt the IEC's conclusions. The LD recommended to IEC to extend the survey of the geotechnical suitability to a site situated approximately 7 km NNW of the Shivta Site and to resubmit the PSAR.

THE NEW APPROACH

In order to comply with the LD's requests, the IEC prepared a Program Plan which includes all the activities agreed upon in a series of workshops. These workshops, attended by representatives of the IEC and representatives of the LD were held in 1995. It should be noted that the proposed Program Plan utilizes most, if not all, of the results of prior studies. Without the prior studies, the proposed program would have to be significantly more extensive and would probably have to start with many of the items done as part of these prior studies.

Further, the IEC decided to adopt a new approach to the site licensing, based on the experience learned at a similar problematic site, licensed by Pacific Gas & Electric, the Diablo Canyon site. Following this example, the IEC appointed a Technical Advisory Board (TAB) to assist the IEC in achieving a successful result of the licensing process. The TAB is a five man panel of scientists and engineers experienced in siting and licensing of critical facilities.

The primary function of the TAB is to provide guidance to ensure that the objectives of the licensing criteria are achieved and that relevant theories, analytical techniques and other pertinent newly developed information were considered. This function has to be accomplished through review of technical developments and results, as they become available. According to the definition of the TAB, its main purpose is to objectively judge the adequacy of the combined IEC activities, toward the licensing of a seismically safe nuclear power plant and recommend to IEC a course of action and scope of activities to successfully license a nuclear power plant site in Israel. In order to ensure complete independence, the TAB members will not participate actively in the performance of the work within the frame of the Program Plan.

The TAB should advise the IEC and its staff on the Program Plan development and its revision if necessary, evaluate investigative methods, suggest priorities of work tasks and review work in progress. While working in close cooperation with the IEC's Nuclear Project Department, the TAB reports directly to the IEC General Manager or to his authorized representative

The TAB's activity will be initiated whenever a project milestone is reached, when new results are available or when a tactical decision is to be taken. It is expected that during the 3 years of the work on the Program, six meetings of the TAB will be necessary. The first meeting took place in Israel in September 1996.

THE TECHNICAL ADVISORY BOARD

The TAB started its activity by reviewing the IAEC siting and licensing criteria, and relevant IAEC reports and position papers. The TAB also reviewed the prior work done by the IEC and its consultants toward siting and licensing a nuclear site in Israel including the revision 1 of the PSAR prepared for the Shivta site as well as some of the Basic Data Reports.

The members of the TAB participated in site visits to examine places relevant to the feasibility, as well as to the design aspects of the project. In addition, the TAB met with IEC, its consultants, and with the LD.

The TAB generally supported IEC's Program Plan but suggested modifications on several activities and their priorities. Those issues for which the TAB suggested changes in timing and emphasis, are the hypothetical tectonic activity of the Qeren anticline and the geophysical seismic investigations in the Revivim syncline.

The TAB members have individually been involved in many projects and professional activities where similar methods, techniques, and exploration tools, have been used in previous investigations. The TAB is satisfied that these methods, techniques, and exploration tools used in the Shivta project, are all appropriate, and many of them are representative of the state-of-the-art.

Other important conclusions of the TAB were the following:

1. The current degree of activity, if any, of the Qeren anticline, is a very critical issue in the site investigation. This is because the fault or faults which underlie it (and have, over time, caused the anticline to develop) are not only relatively close to the Site but, because they may extend over a number of kilometers, they could also pose a threat in terms of strong earthquake vibratory ground motions at the site.

2. The TAB appreciates, that the seismic imaging must play an important role in the investigations. The TAB fully supports the acquisition of further

high-resolution data in critical localities. The proposed high-resolution seismic lines, whose primary purpose is to locate and evaluate faults in the Revivim syncline within the proposed site area, are critical to the understanding of whether or not the tectonic processes that formed the syncline and its associated structures are active in the present tectonic environment. The TAB fully endorses the emphasis put by the LD on making sure that the seismic requirements (e.g., penetration, resolution, calibration with drilling results) are of high caliber and result in high-quality products.

3. The TAB, while recognizing that "fatal flaws" could yet be found within the Potential Sites Envelope, does not *at this time* recognize any features that would necessarily disqualify the site. The TAB is optimistic that further investigative work has a reasonably high probability of demonstrating licenseability of the site, perhaps also including areas outside of the currently designated Potential Sites Envelope. The TAB made this judgment, at least partly, on the basis of the exceedingly low slip and deformation rates that seem to characterize the geologic structures of this area, particularly as compared to other worldwide areas of significant seismic hazard. It should be kept in mind, however, that if some of the nearby faults are eventually deemed "capable," the proposed site might then fail to meet the current licensing criteria. That is why it is crucial that this part of the investigation be given the highest priority and be initiated at the earliest possible date.

CONCLUSION

Based on the first visit in Israel and the communications with the IEC staff and the LD, the TAB members are optimistic that further investigative work has a reasonably high probability of demonstrating, under the current criteria, the licenseability of a nuclear plant site in the proposed area.

Employment of MATLAB in the analysis of radionuclide deposition and leakage

L. Reznik, B. Tavron, Nuclear Engineering Department, Research and Development Division, Israel Electric Corporation

In reactor safety studies of postulated severe accidents it is important to estimate accurately the rates of the release and transport of fission products (like iodine and cesium) within the containment as well as their leakage into the environment. Although the main processes (such as gravitational settling, thermophoresis and diffusiophoresis) are well understood there is a wide range of uncertainty in regard to numerical values of key parameters. This is due to the fact that the rates of various deposition processes are very sensitive to the prevailing thermohydraulic conditions in the primary system and the containment compartments. Even for cases where the containment event timing and other governing parameters (such as compartment temperature, pressure, air-steam mixture flow rates, steam mole fraction and temperature gradients at surfaces) are well known, there is still large uncertainty in many important characteristics such as chemical form of released fission products or aerosol particle size distribution. Aerosol agglomeration during various stages of transport has also a significant impact on deposition velocity.

In this situation various empirical correlations based on laboratory tests become of special importance for proper safety characterization of the reactor under various beyond-design conditions. Since most of these correlations are system-dependent and sometimes valid only for a limited range of conditions derived from the tests - a thorough judgement should be exerted when extrapolating these data to predict reactor conditions in an particular accident.

During the last two decades various computer codes for fission product transport (like NAUA, CORRAL, MATADOR) have been developed and employed in reactor safety analyses. However their success in prediction of actual benchmarking tests has been somewhat limited. This in turn has lead to new experiments and new empirical correlations with better reflection of the complex physico-chemical aspects of fission product deposition and transport. Instead of a usual update of the above FORTRAN - based computer codes in light of the available new experimental information, we have tried to create a new analytical tool based on MATLAB. The MATLAB provides a relative easy environment for changes in computation logic (such as modification of empirical corellations), replacement of validity range limits and updates of data bases. This application program - BULL ("Build - Up Levels of Leakage") employs at present the basic computational models of CORRAL and MATADOR. However the user-transparency of models, results, parameters and data provided by the MATLAB environment and graphic interface would permit to use it in the future as the basis for efficiently updated knowledge base. Results of preliminary analysis using BULL and their comparison with the similar results of CORRAL and MATADOR will be presented at the conference.

Critical Pressure of Non-Equilibrium Two-Phase Critical Flow

U. Minzer, Nuclear Engineering Department,
Research & Development Division, Israel Electric Corporation

Introduction

Critical pressure is defined as the pressure existing at the exit edge of the piping, when it remains constant despite a decrease in the back. According to this definition the critical pressure is larger than the back pressure and for two-phase conditions below saturation pressure. The two-phase critical pressure has a major influence on the two-phase critical flow characteristics. Therefore it is of high significance in calculations of critical mass flux and critical depressurization rate, which are important in the fields of Nuclear Reactor Safety and Industrial Safety.
At the Nuclear Reactor Safety field is useful for estimations of the Reactor Cooling System depressurization, the core coolant level, and the pressure build-up in the containment. In the Industrial Safety field it is helpful for estimating the leakage rate of toxic gases from liquefied gas pressure vessels, depressurization of pressure vessels, and explosion conditions due to liquefied gas release.
For physical description of non-equilibrium two-phase critical flow it would be convenient to divide the flow into two stages. The first stage is the flow of subcooled liquid at constant temperature and uniform pressure drop (i.e., the case of incompressible fluid and uniform piping cross section). The rapid flow of the liquid causes a delay in the boiling of the liquid, which begins to boil below saturation pressure, at thermal non-equilibrium. The boiling is the beginning of the second stage, characterized by a sharp increase of the pressure drop. The liquid temperature on the second stage is almost constant because most of the energy for vaporization is supplied from the large pressure drop. The present work will focus on the two-phase critical pressure of water, since water serves as coolant in the vast majority of nuclear power reactors throughout the world.

The Influence of Water Temperature

A large amount of tests measuring two-phase critical mass fluxes and critical pressures have been described by Ilic et al (1986). The Reocreux (1974) tests deserve special attention. Reocreux classified his tests according to the critical pressure, as shown in Table 1. From Table 1 it is easy to diagnose correlation between the critical pressure and water temperature. Pressure curves of the four groups of tests with the same critical pressure of 1.75 bar are drawn in Figure 1. From here there does not seem to be any correlation between inlet pressure and critical pressure. An additional conclusion from Figure 1 is the independence of critical pressure from pipe geometry. Clearly the pressure drop, which is geometry dependent, does not influence the critical pressure. One can easily assume according to Figure 1 four pipes with different length, but with the same water temperature and the same inlet pressure, having the same critical pressures at their end.
Reocreux tests from # 400 to # 435 were found by Ilic et al (1986) as qualified database for the critical flow of water. More detailed observations of these tests appear in Table 2. It is obvious from this table that the main parameter governing critical pressure is water temperature. This conclusion matches the assumption of Burnell (1947) that the critical pressure depends on water stagnation temperature as expressed by the following empirical correlation:

$$P_{Crit} = P_{Sat}(1 - 5.366\sigma)$$

While the saturation pressure depends on water temperature and surface tension, σ is also a function of water temperature. The above conclusion is reinforced by the wide use of empirical curves of critical pressure ratio versus water saturation pressure in the valve industry. Due to these curves, the critical pressure of water depends only on water temperature. A typical example for such curve appears in "FISHER CONTROLS" handbook (1977).

Table 1: Critical pressure classification table according to Reocreux (1974).

Critical pressure [bar]	Test number	Critical mass flux [kg/(m²·s)]	Water temperature [°C]	Saturation pressure [bar]
1.5	403 - 404	4180	116.7	1.787
	400 - 402	6500	116.65	1.784
	405 - 407	8650	116.3	1.763
	408 - 411	10300	115.9	1.741
1.75	423 - 428	4360	121.75	2.098
	420 - 422	6500	121.1	2.055
	429 - 433	8500	121.0	2.049
	433 - 435	10100	120.85	2.040
2.0	446 - 450	4210	126.1	2.400
	440 - 445	6400	125.4	2.349
	451 - 454	8520	125.2	2.335
	455 - 459	10180	125.1	2.327

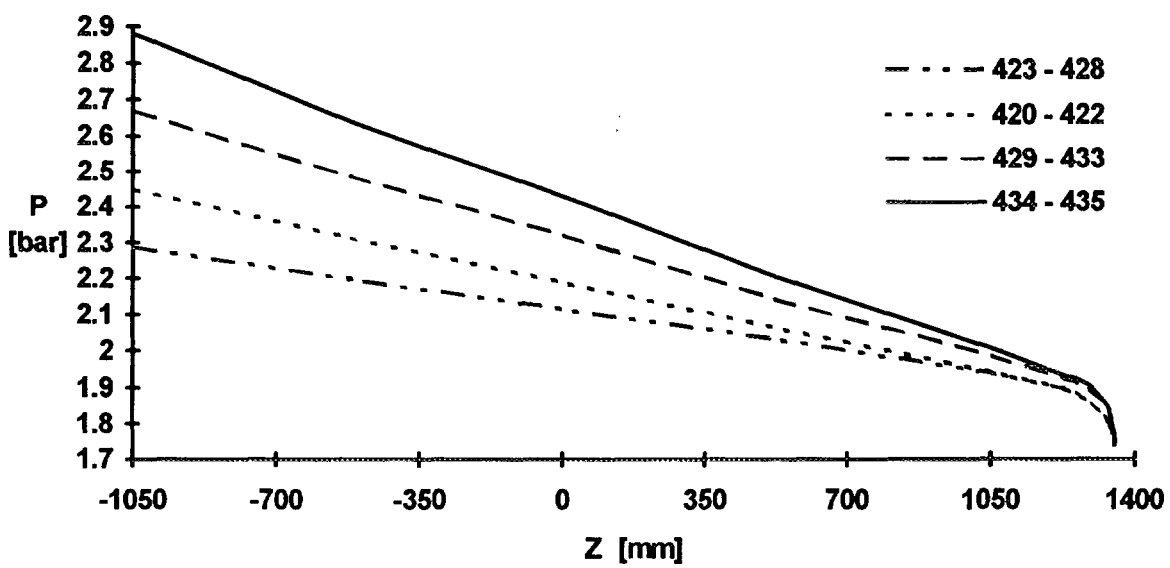

Figure 1: The pressure curves of tests 420 to 435 (Z coordinates are identical to Reocreux coordinates).

Table 2: Thermodynamics parameters of Reocreux qualified tests.

Test number	Inlet pressure [bar]	Critical mass flux [kg/(m²·s)]	Water temperature [°C]	Saturation pressure [bar]	Critical pressure [bar]	Critical void fraction
403 - 404	1.993	4180	116.7	1.787	1.506	0.55
400 - 402	2.181	6500	116.65	1.784	1.502	0.25
405 - 407	2.412	8650	116.3	1.763	1.501	0.12
408 - 411	2.630	10300	115.9	1.741	1.505	0.07
423 - 428	2.286	4360	121.75	2.098	1.755	0.57
420 - 422	2.449	6500	121.1	2.055	1.752	0.31
429 - 433	2.669	8500	121.0	2.049	1.752	0.20
433 - 435	2.877	10100	120.85	2.040	1.750	0.16

On Figure 2 the critical pressure ratio of some empirical databases qualified by Ilic et al. (1986) are shown as function of water temperature. Burnell and "FISHER" curves are also presented on this graph. It is clear from this graph that the "FISHER" empirical curve matches well the empirical results. Within the range of most practically important water temperatures, from 100 °C to 350 °C it is acceptable to limit the two-phase critical pressure by lower and upper bounds:

$$P_{Crit} = P_{Sat}(0.95 - T/1000)$$

$$P_{Crit} = P_{Sat}(1.1 - T/1000)$$

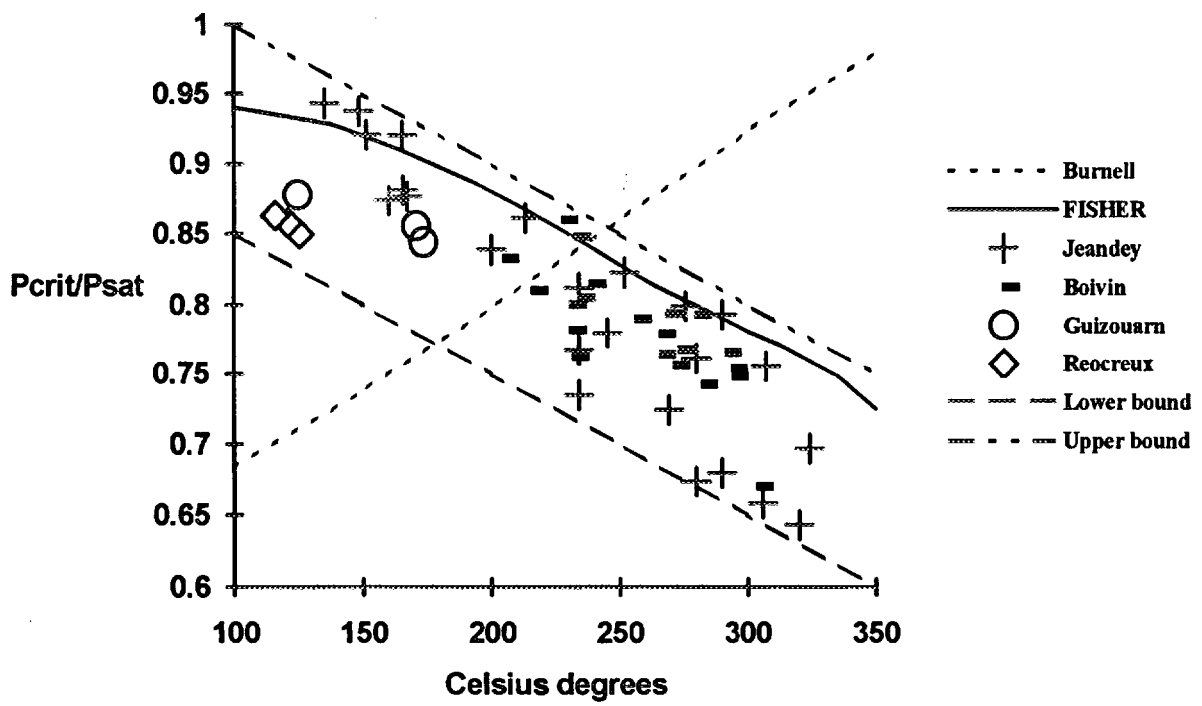

Figure 2: Critical pressure ratio versus water temperature.

Conclusions and Discussion

The main conclusion of this work is the existence of strong dependence of two-phase critical pressure on water temperature. There is no evidence of any significant influence of the inlet pressure or the geometrical conditions on the critical pressure. All of the above mentioned discussion points to the water temperature as the parameter that determines the two-phase critical pressure. Despite this conclusion an analytical relation between water temperature and critical pressure is not available. This analytical relation could be the aim of further research.
The range between the empirical bounds of critical pressure suggested in this work is narrower than the analytical range proposed by Minzer and Elias (1996). The new bounds may improve the two-phase critical mass flux predictions calculated by the bounding method proposed in that same paper.

Nomenclature

P - pressure [bar]
T - temperature [°C]
σ - surface tension [N/m]

Subscripts

Crit - critical
Sat - saturation

References

[1] Burnell J. G.: FLOW OF BOILING WATER THROUGH NOZZLES, ORIFICES, AND PIPES; *ENGINEERING, pp. 572-576, December 12, 1947.*
[2] CONTROL VALVE HANDBOOK; *FISHER CONTROLS, 1977.*
[3] Ilic V., Banerjee S. and Behling S.: A QUALIFIED DATABASE FOR CRITICAL FLOW OF WATER; *EFRI NP-4556 May 1986.*
[4] Minzer U. and Elias E.: A BOUNDING SOLUTION OF TWO-PHASE CRITICAL FLOW; *THE 26TH ISRAEL CONFERENCE ON MECHANICAL ENGINEERING, pp. 412-414 May 1996.*
[5] Reocreux M.: CONTRIBUTION TO THE STUDY FLOW RATES IN TWO-PHASE WATER VAPOR FLOW; *Ph.D. Thesis, Volume III, Medical University of Grenoble, 1974.*

The 19th Conference of the Nuclear Societies of Israel

Aerosol Particles Sampling In Sampling and Transport Systems

T. Kravchik, U. Gherman, Y. Laichter
Nuclear Research Center - Negev

Purpose of work - In nuclear facilities, real-time measurements of the radioactivity associated with aerosol particles are made with continuous air monitors (CAMs). Often, these monitors may be physically remote from the sampling location, in which case aerosol particles have to be transported from the sampling location to the monitor through a transport line. Typically, this system consists of straight tubes, elbows and an inlet nozzle. Losses of aerosol particles can occur as a result of deposition during transport through the sampling system. It is highly important that aerosol losses in the transport lines be minimal in order that the CAMs can provide reliable alarms if the radioactivity exceeds a certain level. There is also a need to evaluate the sampling efficiency (ratio of aerosol mass concentration reaching the CAM to that at the sampling point) of the system.

In the present work, a theoretical parametric study was conducted to evaluate the influence of the sampling system and the flow characteristics on the sampling system efficiency. Based on the parametric study, general principles are set up concerning the aerosol sampling systems, with reference to their sampling efficiency.

Methods - The efficiency of the aerosol particles sampling system is calculated using the "DEPOSITION 2.0" code, a PC-based software program which was developed at the Texas A&M University, and was recommended by the "U.S. Nuclear Regulatory Commission - Regulatory Guide 8.25" for sampling efficiency calculations at the workplace. The code is based on several theoretical and empirical submodels which take into consideration the various aerosol deposition mechanisms at the system inlet and transport lines (gravitational settling, diffusional deposition and turbulent inertial deposition in straight tubes and inertial deposition in bends and elbows).

Results - The parametric study was conducted on a sampling system that consists of several parts (horizontal and vertical straight tubes, elbows, etc.), which are typical of sampling systems in the nuclear industry, and only with respirable aerosol particles (particles with aerodynamic diameter less than 10 μm).

Based on the parametric study it is concluded that for a certain air flow rate and aerosol diameters there is an optimal tube diameter (with the maximum sampling efficiency). Fig. 1, for example, shows the efficiency of a sampling system as a function of tube diameter for several aerosols aerodynamic diameter. The system consists of a 3-m vertical tube, a 5-m horizontal tube and two 90°-bends. At a flow rate of 60 liter/min, the optimal tube diameter is about 25 mm.

Conclusions - Based on the parametric study several principles can be defined concerning aerosol particles sampling system:

a. Isokinetic sampling (sampling velocity equal to ambient velocity) and isoaxial sampling should be used whenever possible.
b. Elbows and tube bends should be eliminated as much as possible.
c. Whenever possible, vertical tubes should be preferred to horizontal ones as their sampling efficiency is much higher.
d. Too low air flow rate should be avoided in sampling systems. At low flow rate the air linear velocity is also low and as a result the period of time in which the aerosol particles are contained inside the transport lines and consequently their deposition increase. For a 25-mm tube, it is recommended to work with an air flow rate of 60 liter/min.

e. For a certain air flow rate there is an optimal tube diameter.
f. Electrostatic deposition should be avoided. It is therefore not recommended to use sampling lines that are not electrically conductive.

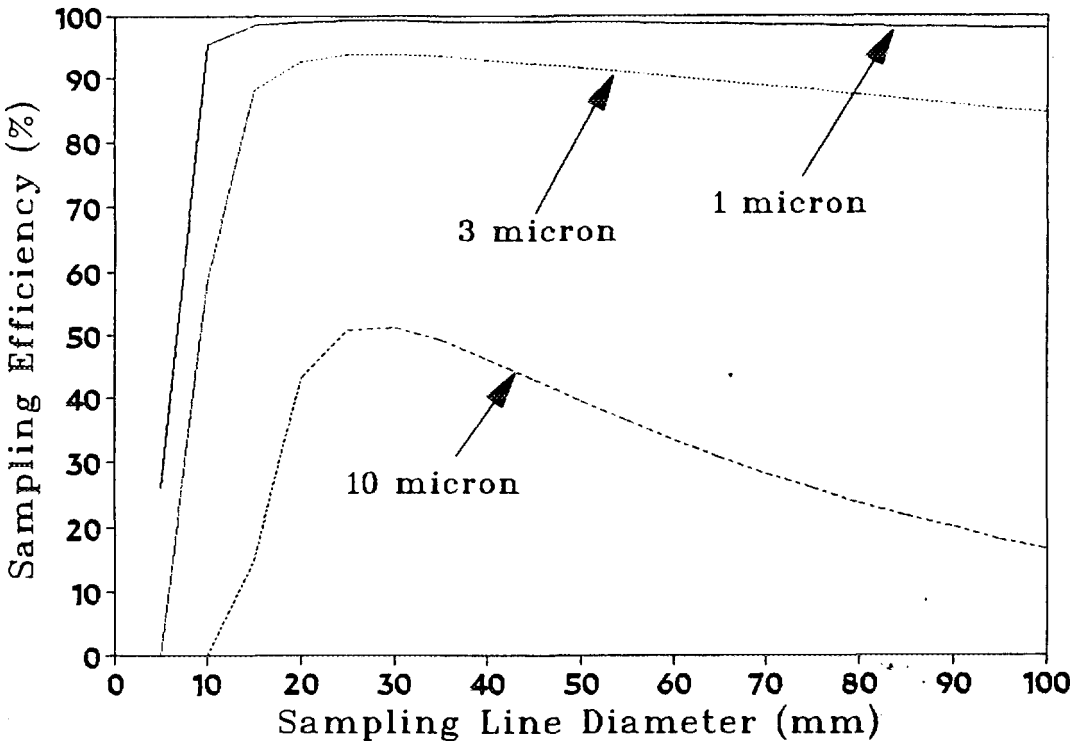

Fig. 1 - Efficiency of a sampling system as a function of tube diameter for different aerosol particles aerodynamic diameters. The system consists of a 3-m vertical tube, a 5-m horizontal tube and two 90°-bends. Air flow rate - 60 liter/min.

STATISTICAL CRITERION FOR BUBBLY–SLUG FLOW TRANSITION

Jutta Zingler* and Ezra Elias
Faculty of Mechanical Engineering
Technion — Israel Institute of Technology
Haifa 32000, Israel

1 Introduction

The investigation of flow pattern transitions is still an interesting problem in the research of multiphase flow. It has been studied theoretically, e.g. by Taitel *et al.* (1980), and experimental confirmation of the models has been found by many investigators.

The present paper deals with a statistical approach to bubbly-slug transitions in a vertical upward two phase flow and a new transition criterion is deduced from experimental data.

2 Experimental setup

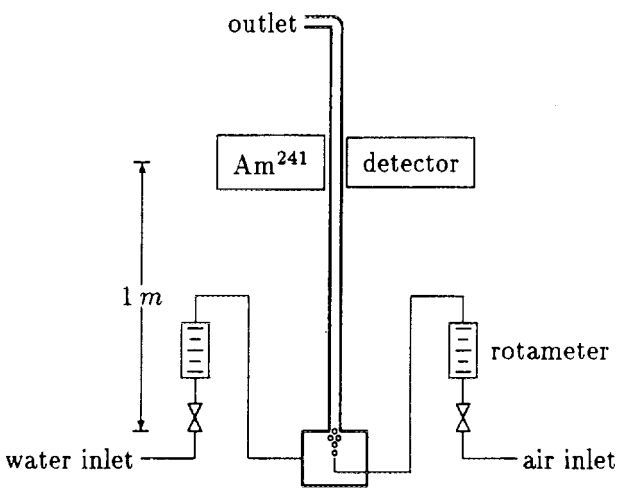

Figure 1: Flow-diagram

An experimental system was constructed in order to perform fast on–line measurements of air–water mixtures flowing in a glass tube. A schematic diagram of the experimental facility is shown in figure 1. The test section consisted of a glass tube, having an inner diameter of 15.5 mm and

*visiting student from RWTH Aachen, Germany

an outer diameter of 20 mm. The column length from the point of air injection to the top of the conduit was 1.5 m. Air was supplied at 2 bar from a compressed air line. Flow rates of the air and water supplies were measured by rotameters.

Void fraction was measured by a γ-transmission system. The γ-ray system consisted of a shielded 3 Ci Am^{241}-source, focussed to a 2 mm beam and a NaI(Th)-scintillation detector, connected to a fast preamplifier/amplifier-unit (TC 243). The detection point was located at a distance of 1 m above the air injector. The γ-transmission pulses were digitized and counted by a Multichannelscaler (The Nucleus PCA) in 4096 channels, where each channel corresponds to a time intervall of 80 ms. In other words, for a given test conditions the air-water mixture density was measured 4096 times within about 5.5 min.

3 Results

A first analysis of the γ-transmission data led to a frequency distribution of the cross sectional average void fraction which varied according to the flow patterns in the pipe. Because of the limited air velocity, which could be obtained in the present system, annular flow could not be reached. Furthermore, since the system configuration (such as the tube's diameter) had not been optimized, the frequency distribution for the different flow patterns was not as clear as shown e.g. in Jones & Zuber (1974), but a significant difference between bubbly and slug flow could still be observed.

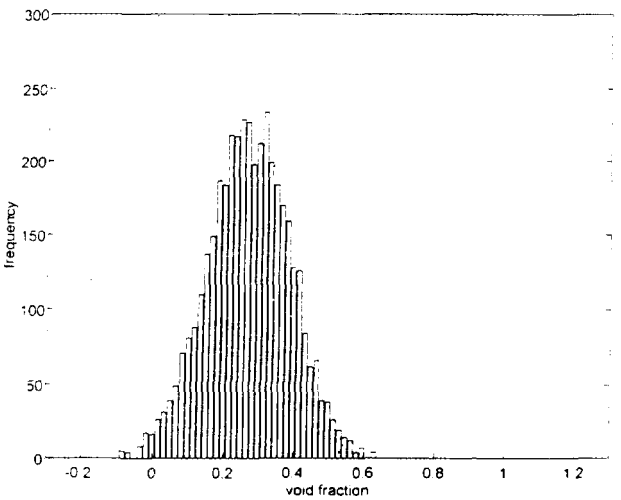

Figure 2: Frequency distribution for bubbly flow

In the bubbly case only one (gaussian shaped) peak appeared in the void frequency distribution with maximum at void fractions α usually smaller than the theoretical limit $\alpha = 0.52$ mentioned in Taitel *et al.* (1980) which was based on spherical shaped bubbles arranged in a cubic lattice. A sample of a void fraction distribution plot is given in figure 2. With the transition to slug flow the distribution widened and it was characterized by two lower humps, one for $\alpha \leq 0.5$ and one at $\alpha \geq 0.5$ (see figure 3).

Although it seemed, that no further information could be obtained from those results because of the limited accuracy, a simple calculation of the standard deviation σ of the mean void

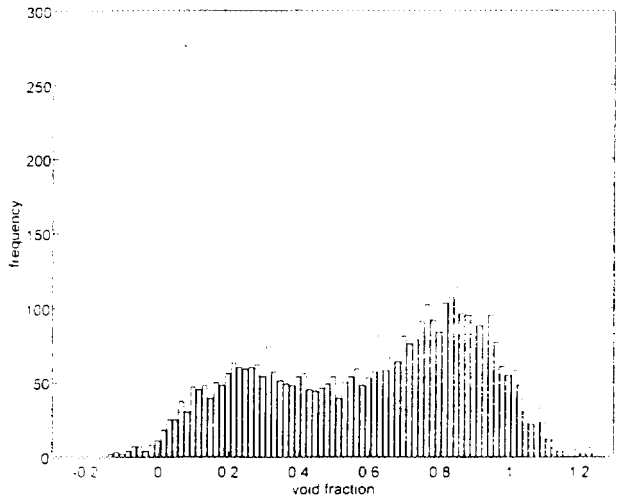

Figure 3: Frequency distribution for slug flow

fraction in the considered distribution led to clear observations of the bubbly-slug transition in the diagrams. It could be expected that σ for slug flow would be greater than for bubbly flow. A first plot of σ vs. the superficial air velocity showed rather constant values of σ for the single peak patterns (bubbly flow) but a sharp increase at the transition point from bubbly to slug which could also be checked visually in the tube. The transfer to a polar graph of σ vs. the changing parameter (here the superficial air velocity j_g) resulted in an arc shaped line with approximately constant small radius for the bubbly case (small σ) and one with significant larger radius (larger σ) for the slug part, whereas a jump takes place at the transition point. A typical graph of the measurements can be seen in figure 4.

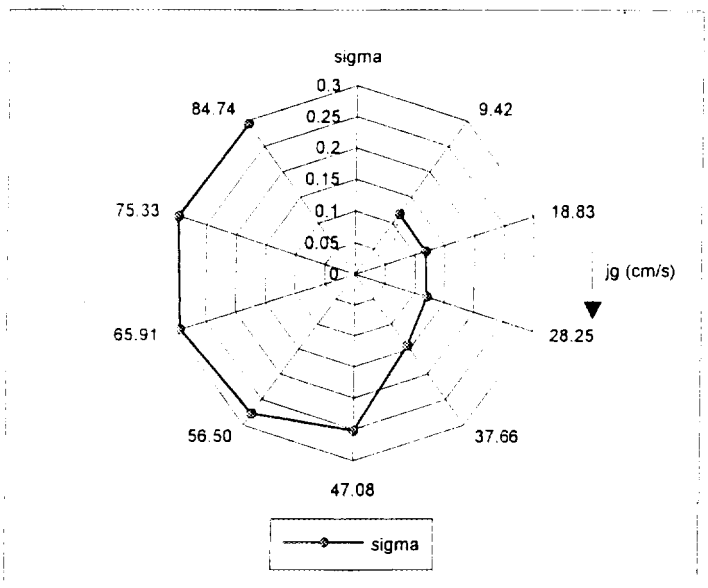

Figure 4: Polar flow regime map

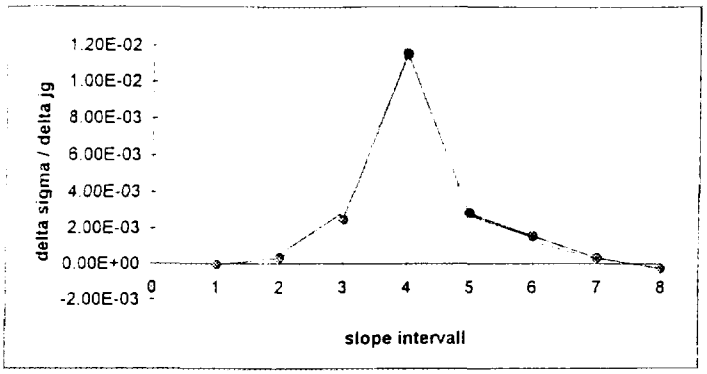

Figure 5: Slope diagram

Since different runs led always to similar results for σ at the transition point, the idea was conceived to define a "transition radius", σ_{BS}, which was found to be $\sigma_{BS} \approx 0.2$ for the present measurement system. Thus, the radial diagram can be understood as an instrument orientated flow regime map for bubbly and slug regimes.

Considering the slope of $\sigma(j_g)$, the transition was even more significant as it showed a clear maximum at the transition point which is supposed to be rather narrow under optimized measuring conditions (cf. figure 5) whereas the other values stayed close to zero.

4 Conclusions

On the way of trying to understand the phenomena taking place at flow pattern transitions it has been found that they can be made observable via calculation of the standard deviation, σ, of a measured frequency distribution of the void fraction α, even without visual access to the fluid. The results were conveniently presented by a polar flow pattern map. An improved method to elucidate the transition point was defined using the derivative of σ (in this case only the difference quotient $\Delta\sigma/\Delta j_g$). The present results can be expanded to slug–annular transitions at which the same statistical events in the opposite way are supposed to occure.

5 References

JONES, O.C., JR. & ZUBER, N. 1974 The interrelation between void fraction fluctuations and flow patterns in two–phase flow. *Int.J. Multiphase Flow* **2**,273–306

TAITEL, Y., BORNEA, D. & DUKLER, A.E. 1980 Modelling flow pattern transitions for steady upward gas–liquid flow in vertical tubes. *AIChE Journal* **26**,345–354

Operation Program for an Automatic Alpha-Beta Counting System - FAG

U.German, S.Levinson, Y.Shemesh, O.Peled, M.Weinstein
Nuclear Research Center Negev

An alpha and beta counting system - FAG*, for planchette samples is operated at the Health Physics department's laboratory of the NRCN. The system consists of a proportional detector of 8" diameter operated in coincidence with a guard detector, an automatic sample changer (FAG-FHT770E) and electronics (FAG-FHT1100 digital counter and controller). The original operation mode of the system was based on manual tasks handled by the FHT1100 electronics. An option for a basic computer keyboard operation was available too. A computer with appropriate I\O card was connected to the system and a new operating program was developed which enables full automatic control of the various components. The program includes activity calculations and statistical checks as well as data management. The FAG counting system is shown in fig 1.

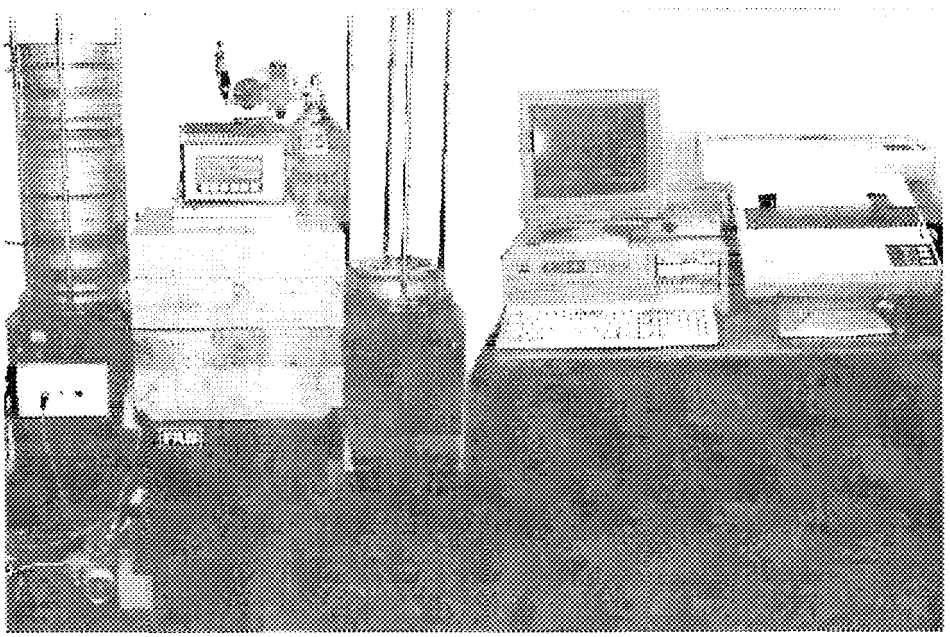

Fig 1: FAG alpha\beta counting system

The program which was developed enables computer control of all components of the system, based on bi-directional communication. The computer software controls the FHT1100 electronics using the RS232 protocol and the sample changer by an additional I\O card Contec model PIO-48W(PC). The computer controls the whole operation of the system: change of samples, high voltage change, start, stop etc. It handles in the appropriate order the different commands and operates the electronic and mechanic components accordingly. Status information of the different components including messages and alarms

are also displayed . The counting results are used as input data for alpha and beta activity calculations. The general flow chart of the program is given in fig 2.

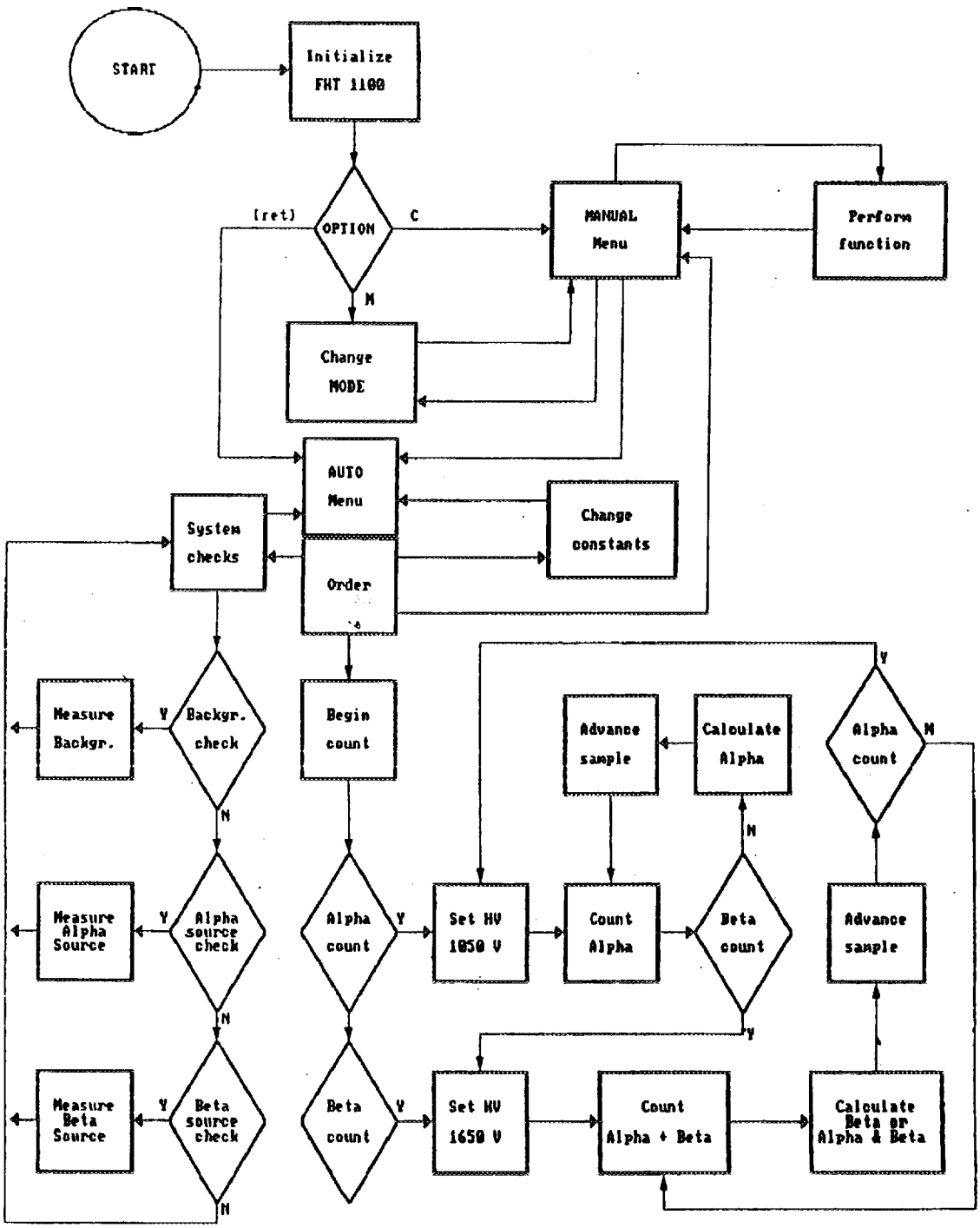

fig 2: The general flow chart of the operating program

The program is written in Quick-Basic version 4.5 and it consists of three main parts:

1. Manual operation: This part of the program is mainly the original version and it enables the operator to control manually the system and its different components. Trough the computer's keyboard the high voltage can be changed, counting time can be determined, start and stop counting operations can be controlled, etc.

2. Automatic operation and calculations: This part of the program consists of different sets of orders in logical sequence including status checks and commands to and from the FHT1100 electronics and the sample changer. A full automatic alpha and beta recycle counting procedure is performed as well as data transferring from the FHT1100 to the computer. Minimum detectable activities are calculated and the activity values for alpha and beta radiation are compared to these values. The final results, as well as the original data, are printed and stored in files. Every sample can be counted a predetermined number of times. In this case, statistical analysis is performed and indication is given about results which lay outside normal statistical variations. This analysis is performed on line and may cause an automatic recounting of the sample. An example of results for a sample counted 4 times for alpha and beta, is given in fig 3.

```
*ab_A   10  1   6       Cnts    300s 23:42 050996
*ab_B   10  1   5120    Cnts    300s 23:47 050996
*ab_A   10  2   5       Cnts    300s 23:52 050996
*ab_B   10  2   5073    Cnts    300s 23:58 050996
*ab_A   10  3   15      Cnts    300s 00:03 060996
*ab_B   10  3   5190    Cnts    300s 00:08 060996
*ab_A   10  4   3       Cnts    300s 00:13 060996
*ab_B   10  4   5049    Cnts    300s 00:19 060996
*Alpha:
*Rep: 1  dpm:  0.689      ±: 2.287
*Rep: 2  dpm:  0          ±: 2.180
*Rep: 3  dpm:*6.896       ±: 3.084    <---Out Rep 3: Avr:1.896 ; SigAvr: 1.207
*Rep: 4  dpm:  0          ±: 1.951
#avA  10  300s 00:13 060996     0.23 dpm ± 1.24(538.5%)    ; MDA3S= 4.63dpm/Samp       ≤MDA
*Beta:
*Rep: 1  dpm: 2000.107    ±: 57.986
*Rep: 2  dpm: 1981.745    ±: 57.719
*Rep: 3  dpm: 2024.09     ±: 58.433
*Rep: 4  dpm: 1972.14     ±: 57.572
#avB  10  300s 00:19 060996     1994.52dpm ± 28.96(1.4%)   ; MDA3S= 13.17dpm/Samp

SampKind: Liquid 10cc dpm/Samp     BarCode:A45          | BareCode: A45 ;       060996
α:  Eff(%): 29      Bkgr(cpm): 1   Kfac:1.12           | α: ≤MDA (4.63 dpm/Samp)
β:  Eff(%): 50      Bkgr(cpm): 24                      | β: 199.45 dpm/cc ± 1.4%
                                                       | MDA 3Sig (99.73%) for 300sec
                                                       | β Eff for Sr90
```

fig 3: Example of results print

3. Calibration checks: This part of the program operates the system for automatic counting of background and known activity alpha and beta sources. Statistical checks are performed and deviations from expected values are reported. A special option of alpha and beta plateau display was also added to the calibration process to enable easy determination of the high voltages.

* FAG Kugelfischer Georg Schafer KGaA, Erlangen Germany

A Manual Low Background Alpha and Beta Counting System

S.Levinson, U.German, O.Peled, S.Turgeman,
U.Vangrovitz, D.Tirosh, S.Piestun, H.Assido
Nuclear Research Center Negev

An Alpha and Beta counting system consisting of a microcontroller-based electronic unit and detectors assembly was developed. The radiation detection unit consists of two proportional detectors (a main detector and a cosmic-ray guard detector) which can be easily disassembled for decontamination or repair. The detectors are mounted in a manual operating sample changer shielded by 5 cm of lead. Simplicity of maintenance and functional operation were taken into consideration in the design. The electronic unit supplies the high voltage and enables the operational functions including controls and alarms. Calculations of net cpm of Alpha and Beta counting are displayed and can be printed. RS-232 communication option enables connection to a computer and operation of more sophisticated programs for calculations and data storage in the future. The system is shown in Fig. 1.

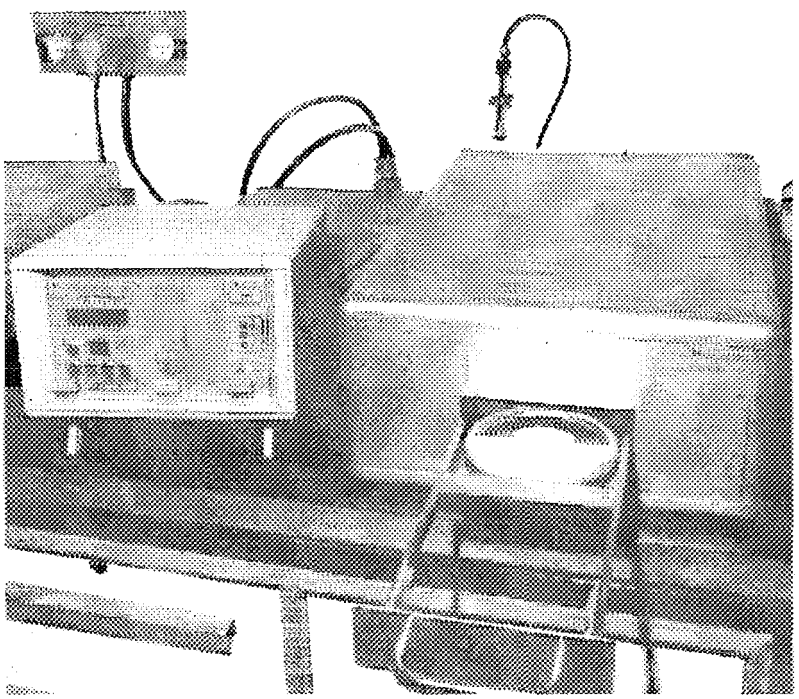

Fig 1: The Alpha and Beta counting system

The counting system is based on a proportional detector with high voltage changing to the appropriate high voltage plateau point. The radiation-detector(1) is 4.5" diameter and is made of oxygen free copper. As the system was designed for a low background, it has a cosmic 7.5" PVC square guard detector(2) and an anti-coincidence circuit to minimize the cosmic and background radiation contributions.

The present version of the detectors structure is based on the principle of one strip of stainless still anode wire. This technique leads to easier manufacturing and assembly and only two solders are needed in the wire's edge. It also improves the detector's response - the high voltage plateau is larger. Fig 2 shows the structure of the two detectors.

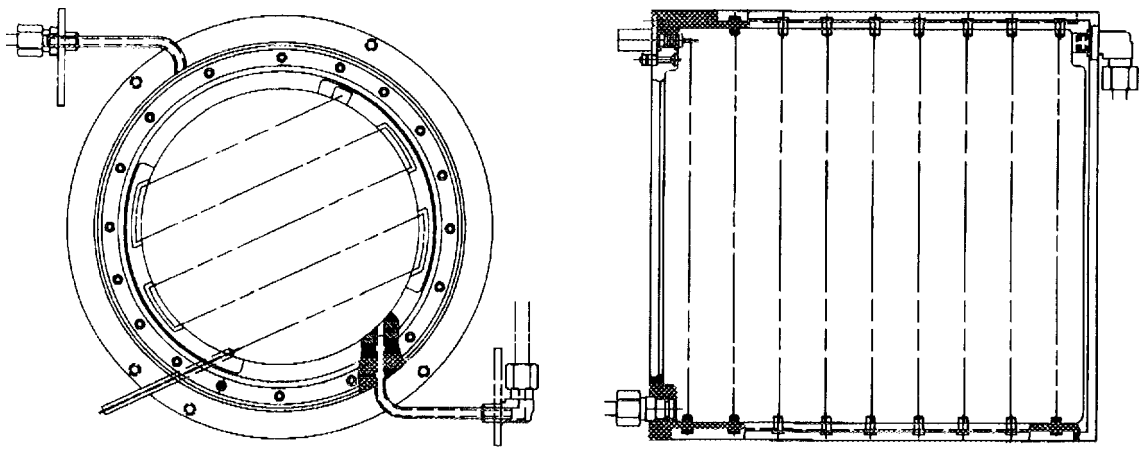

Main detector Guard detector

Fig 2: The structure of the main and the cosmic-ray detectors

The detectors are mounted in a manual sample changer(3) that was designed for low background, therefore it has a 5 cm overlapping lead bricks that can easily be taken apart. Most of the changer parts are made of low background copper. The sample is positioned on an aluminum planchette of 4.5" diameter which is placed in front of the detectors by a moving tray. The tray is inserted manually towards the detector and at the end point the sample is lifted towards the detector to improve the counting efficiency.

The electronic unit(4) operates a set of functions selected by two digit switches located on the front panel. Some functions including high voltage adjustments, calibration and background parameters changing and alarm thresholds are enabled only by a switch-key to prevent non permited setting. Most of the functions lead the operator step by step for simplicity of operation. The counting principle for Alpha and Beta radiation is based on alternate changing of the high voltage supplied to the detectors, counting first in the Alpha mode and then in the Alpha+Beta mode. From the counting data the Alpha and Beta net cpm are calculated after background subtraction and taking into consideration the Alpha rate contribution in the Alpha+Beta one. The final activity results are compared to the system's minimum detectable activity.

Several counting systems were built and are in routine use for about a year at the Health Physics department of the NRCN. Further development is planned as connecting a computer to the system which will enable more extensive calculations and statistical evaluations. In addition, the development and

assembly of a sandwich detector(5) for simultaneous Alpha and Beta detection is considered.

References:

1. "Development of 2π Proportional Gas-Flow Counter That Can be Taken Apart for Decontamination and Repair"
   S.Levinson, H.Assido, E.Reich, U.German
   Israel Atomic Energy Research Laboratories 1986 Annual Report IA-1427, pp. 201-202.

2. "A Square 7.5" Proportional Guard Detector"
   S.Levinson, H.Assido, Y.Shemesh, S.Piestun, U.German
   Research Laboratories Annual Report 1993 IA-1486 pp.139-141

3. "A Manual Sample Changer for 5" Proportional Detector Counting System"
   S.Levinson, Y.Elbaz, U.German, E.Naim
   Research Laboratories Annual Report 1993 IA-1486 pp.141-142

4. "Alpha and Beta Radioactivity Contamination Counting System"
   U.Wengrowicz, D.Tirosh, S.Piestun, Y.Shemesh, H.Assido
   Research Laboratories Annual Report 1993 IA-1486 pp.134-135

5. "A Sandwich 2 π Proportional Gas-Flow counter for Simultaneous Alpha and Beta Counting"
   S.Levinson, H.Assido, U.German, Y.Shemesh, S.Piastun, Y.Ronen, E.Naim
   1990 Transactions of the Joint Meeting of The Nuclear Societies of Israel 17-18/12/90, pp 95-97.

A Bar-code Reader for an Alpha-Beta Automatic Counting System - FAG

S.Levinson, Y.Shemesh, N.Ankry, H.Assido, U.German, O.Peled
Nuclear Research Center Negev

A bar-code laser system for sample number reading was integrated into the FAG* Alpha-Beta automatic counting system. The sample identification by means of an attached bar-code label enables unmistakable and reliable attribution of results to the counted sample.
Installation of the bar-code reader system required several modifications:
(I) Mechanical changes in the automatic sample changer, (II) Design and production of new sample holders,. (III) Modification of the sample planchettes, (IV) Changes in the electronic system, (V) Update of the operating software of the system. The scheme of the integrated new system is shown in fig. 1.

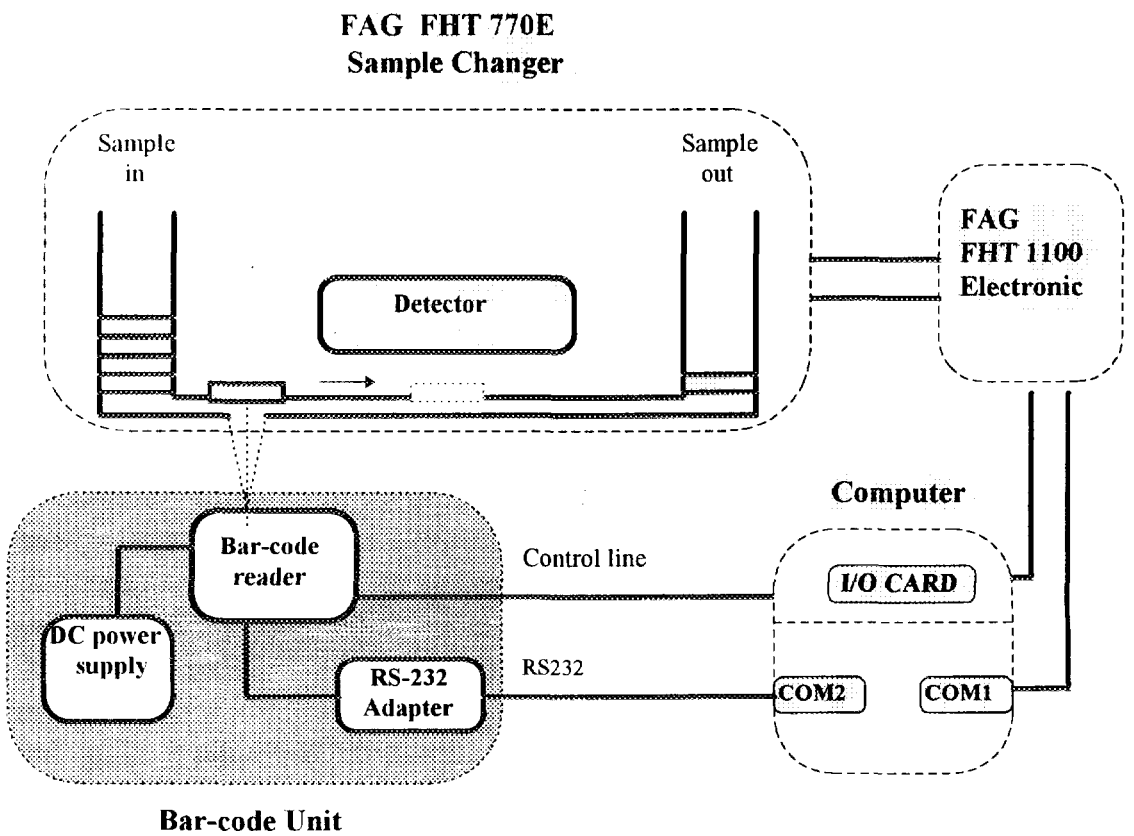

Fig 1: Scheme of the system including the bar-code reader

Mechanical modifications:
Due to mechanical limitations, and in order to minimize the modifications in the sample changer and its original operation, it has been decided to integrate a laser bar-code system which can detect the number from a distance of 15 cm. The bar-code reader is placed in the lower part of the loading device, between the feed unit and the detector. An adequate slot was cut to enable the passage of the

bar-code laser beam. A bar-code label is attached to the bottom of the planchette holding the sample, which is placed in the sample holder, so that the laser beam scans the sample code on its way to the detector, before the counting starts.
The holder's motion along its path is achieved by means of a moving bar that pushes the holder on two parallel tracks. Because it moves freely, the holder may turn during its movement, which may cause out of range reading angles. In order to ensure an only limited turn of the holder and laser beam passage to the planchette bottom, a new holder was designed with a flat area at the contact surface to the moving bar and with a hole structure. The new holder is made of PVC instead of aluminum and needs less material and its weight was reduced by 25%, thus the number of samples which can be loaded on the sample changer was increased accordingly. A scheme of the new sample holder is given in figure 2.

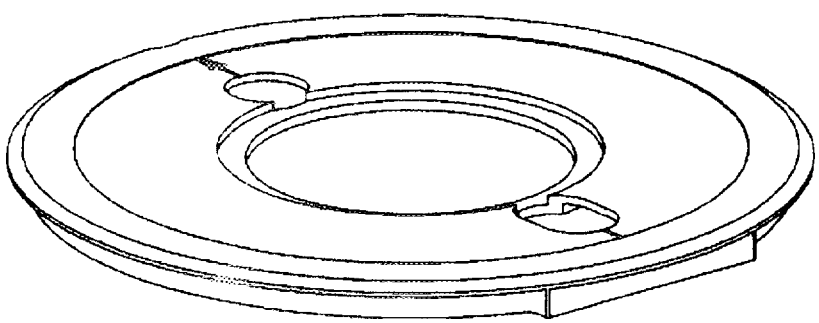

Fig 2: The new sample holder

Electronic modifications:
The bar-code reader installed in the automatic sample changer system is from Symbol Technologies**, model SE-1022. The hardware control method has been chosen for operating the bar-code reader instead of software control via serial communication channel, in order to achieve independent control, simple operation and reliability. The bar-code reader has been initiated to scan code 39. This code was selected since it employs letters, numbers and enables reading of many characters. The bar-code reader control lines are connected to the existing I/O card in the computer (Contec***, model PIO-48W(PC)). A communication adapter card has been designed and built to convert the bar-code reading data to the RS-232 communication standard. This data is transferred to COM-2 of the computer, at a rate of 9600 bytes per sec.

Software update:
The operating software contains a new subroutine written to handle the bar-code reader on/off, scanning, identification and alarm conditions. The bar-code scanning process is initiated 10 seconds after the start command to the sample changer. The control of the bar-code reader operations is performed through the I/O card. Up to four readings are attempted for the code identification. If a code is identified, the scanning process is stopped and data is transferred to COM-2.

The bar-code reading is displayed and saved on a file together with the results attributed to the sample. If no bar-code number was detected, an audible alarm is activated and a corresponding message is displayed and printed without stopping the counting cycle

Bar-codes numbers including parameters like sampling location, type, weight or volume, enable automatic normalization according to the specified data. This unique sample number linkage to the results enable sample identification and direct data handling and it cancels the need of operator interference, with the result of time sparing and increased reliability.

* FAG Kugelfisher George Schafer KGaA - Erlangen Germany.
** Symbol Technologies Inc., 116 Wibur Place, Bohemia, NY 11716 U.S.A
***Contec Microelectronics U.S.A Inc., 2188 Bering Drive, San Jose, California 95131

SOME DOSIMETRIC PROPERTIES OF THE LiF:Mg,Ti EVALUATED BY THE AUTOMATIC 6600 THERMOLUMINESCENT READER

B. Ben-Shachar, M. Weinstein and U. German
NRC-Negev, P.O.B. 9001, Beer-Sheva, 84190, Israel.

ABSTRACT

Some dosimetric properties of the new LiF:Mg,Ti TLD cards were checked, when evaluated by the new automatic 6600 TLD reader. The cards were calibrated to a dose of 1.0 mGy by five identical irradiations, and the TL-dose response was measured for a range of 75 - 1100 μGy.

A very high accuracy was found for the three kind of chips measured (TLD-100, TLD-700 and TLD-600) and a low minimum measurable dose (MMD) was found, too. There is a good fit between the analytical evaluation and the theoretical calculation of the MMD.

The results obtained are much better than those of the LiF:Mg,Ti cards evaluated by the older automatic 2271 reader used in the last two decades.

INTRODUCTION

Lithium fluoride is the most popular thermoluminescent material used in radiation dosimetry in the last four decades[1] . The characteristics which lead to this popularity is its approximate tissue equivalence, which makes it a good dosimetry material [2-5] , together with a lack of difficulties which are associated with other approximately tissue equivalent materials such as lithium borate. It is not as sensitive as certain other materials, but allows doses of 0.1 mGy to be measured with high performance equipment [6] . From the solid state point of view, however, the behaviour of thermoluminescent lithium fluoride is rather complex. This leads to some complications when it is used for dosimetry purposes. It has nevertheless continued to be widely used, and obviously the users considered that its advantages outweight the disadvantages connected with its complex solid state physics.

The purpose of the present work is to check some dosimetric properties of the Bicron/Harshaw manufactured LiF:Mg,Ti TLD cards (TLD-100, TLD-700 and TLD-600 chips), when evaluated by the new automatic 6600 thermoluminescent reader.

MATERIALS AND METHODS

The measurements were performed with the Bicron/Harshaw manufactured LiF:Mg,Ti cards. The LG1110 cards contain three chips of the natural LiF (TLD-100) (3mm X 3mm X 0.38mm) and the BG6667 cards containing three chips of TLD-700 and one chip of TLD-600. The cards were irradiated to several doses in the range 0.075 - 1.125 mGy, by a calibrated Sr-90/ Y-90 source and evaluated immediately after the irradiation. The heating profile is a preheat to 50°C and heating rate of 25°C up to 300°C, for a total time of 13.3 seconds. The TLD cards were read by the automatic 6600 Bicron/ Harshaw reader.

EXPERIMENTAL RESULTS

Glow curve.

In figure 1 we are presenting the glow curve of LiF:Mg,Ti (TLD-100), irradiated to a dose level of 1 mGy. Peak 2, 3 ,4 and 5 can be seen, while peak 6 and 7 are low . The glow curve is accumulated and stored automatically by the 6600 system and can be used for more sophisticated data analysis.

Figure 1 : The Glow Curve of LiF:Mg,Ti

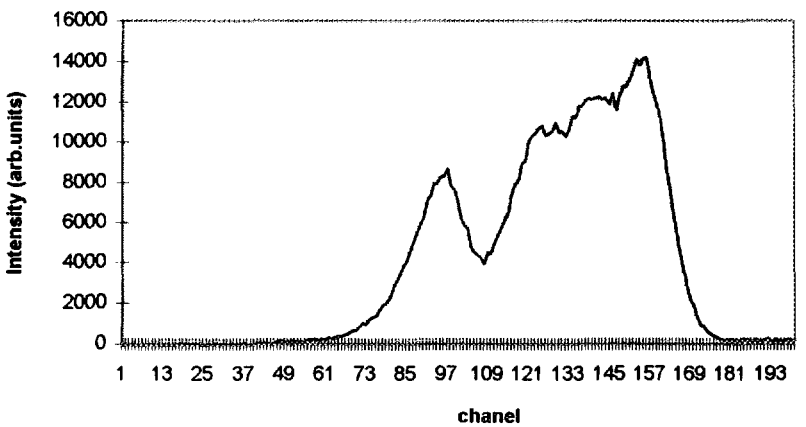

Accuracy.

The TLD cards were calibrated individually by five repeated irradiations of each card to a dose of 1.0 mGy. A second reading (residual dose) was evaluated and subtracted from the first reading. The relative standard deviation of all the 18 TLD-100 chips, 15 TLD-700 chips and 5 TLD-600 chips were calculated. We received a very low standard deviation (0.3 - 1.5 %), which emphasizes the high accuracy of the TLD cards and the reader.

Linearity.

The TL-dose response was measured for six G-1 cards (each of them including 3 chips of TLD-100) and five G6-7 cards (including three TLD-700 chips and one of TLD-600). All the cards were irradiated to six different doses in the range of 0.075 - 1.1 mGy. A second reading (residual dose) was performed and subtracted from the first one and individual calibration of each dosimeter was performed. The average results of the absorbed doses and the deviations from the exposure are presented in table 1.

Table 1 : The results of the TL-dose response for the 3 TLDs and the deviations from the calculated exposure.

	TLD - 100		TLD - 700		TLD - 600	
Exp. (μGy)	abs. dose (μGy)	Dev. (%)	abs. dose (μGy)	Dev. (%)	abs. dose (μGy)	Dev. (%)
1111	1125	1.3	1110	-0.1	1102	-0.8
744	750	0.9	732	-1.5	734	-1.3
590	600	1.7	595	0.7	593	0.5
372	375	0.8	368	-1.2	364	-2.3
222	225	1.2	223	0.3	221	-0.6
76.3	75	-1.7	75	-1.7	74.1	-2.9

The dosimeters show a good linear response, the maximum deviation being less than 1.7% for TLD-100 and TLD-700 and less than 3% for the TLD-600.

Minimum Measurable dose.

A semi-empirical expression following Zarand and Polgar [7,8] was fitted to the relative standard deviation for different exposures. The MMD is defined as the dose level where the relative standard deviation is 0.2 (20%). In figure 2 we are presenting the graph of the relative standard deviation versus the exposure for the LiF:Mg,Ti chips, and the MMD was calculated from this graph. We received a very low MMD - about 15 μGy (see figure 2).

Figure 2: Relative Standard deviation vs. the exposure for LiF:Mg,Ti

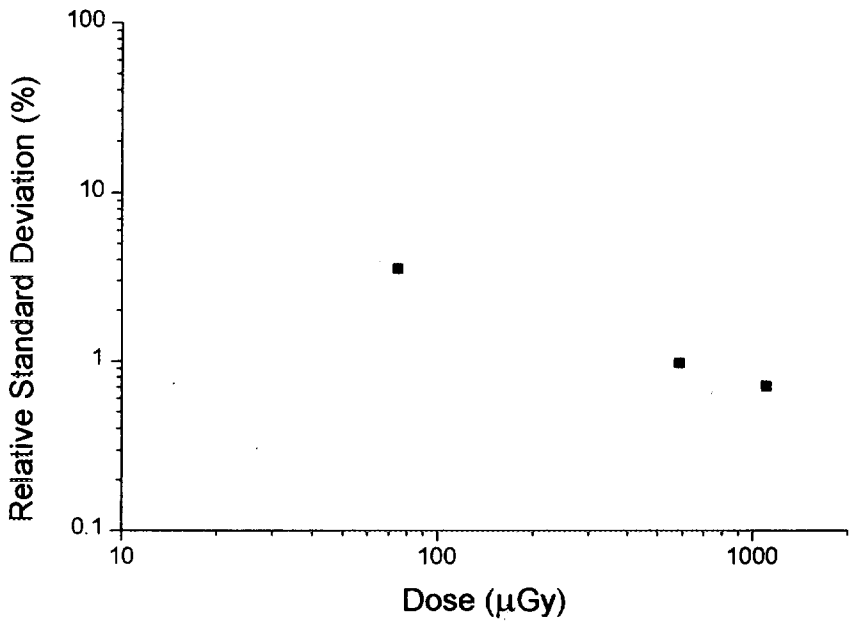

The MMD was also evaluated by reading the unirradiated chips of TLD-100, TLD-700 and TLD-600 and taking three times the standard deviation. We received a MMD of 16.4 μGy for the TLD-100, 14.3 μGy for the TLD-600 and 14.7 μGy for the TLD-700.

CONCLUSIONS

1. A very good accuracy was found for the three chip types (TLD-100, TDL-700 and TLD-600) when calibrated to dose of 1.0 mGy and evaluated by the 6600 automatic reader (a relative standard deviation of 0.3 - 1.5 %).

2. A good linear response was found for the three chips, from the TL-dose response in the low ranges (75 - 1100 μGy).

3. We received a low minimum measurable dose, lower by a factor of three compared with the MMD of the LiF:Mg,Ti cards evaluated by the automatic 2271 reader (~45 μGy)[9].

4. There is a good fit between the MMD evaluated by analytical fit and _ the MMD received by three times the standard deviation of unirradiated cards.

5. We believe that by applying the computerized glow curve deconvolution (CGCD), we can improve the accuracy and the MMD of the LiF:Mg,Ti cards.

REFERENCES

1. V.K. Jain, Rad. Prot. Dosimetry., 1982, 2(3) , 141.
2. J.R. Cameron et al. , Scienec, 1961, 134, 333.
3. B. Burgkhardt et al., Nucl. Instr. Meth., 1980, 175, 183.
4. N. Suntharalingam, Nucl. Instr. Meth., 1980, 175, 191.
5. T.F. Gessel et al., Nucl. Instr. Meth., 1980, 175, 186.
6. G. Portal, Rad. Prot. Dosimetry., 1986, 13, 351-357.
7. P. Zarand and I. Polgar, Nucl. Instr. Meth., 1983, 205, 525.
8. P. Zarand and I. Polgar, Nucl. Instr. Meth., 1984, 222, 567.
9. B. Ben-Shachar et al., Health Physics, 1990, 58, S24.

Computerized Operation of a Multi Detector Spectrometry System

S.Levinson, M.Messing, Y.Gilad, I.Ballon, O.Peled, U.German
Nuclear Research Center Negev

A spectrometry System consisting of a PCA-II (Personal Computer Analyzer) and a DMR (Digital Mixer Router) of Nucleus Inc.* is operated to collect spectra from 8 NaI(Tl) detectors. As most of the functions including calibration, counting and data handling are similar for all the detectors, the option of automatic tasks is a natural choice. An external computer program which controls the operation and data handling of the 8 spectrometer system was developed.

The Nucleus PCA\DMR hardware is operated by task commands which enable activation of various control functions. A set of sequential orders operated as a batch file enables automatic operation of the functions as a task, fitted to a desired spectrometry process. High level programs can be implemented in the batch file to achieve more sophisticated calculations and data handling.
The main daily routine process in spectrometry applications consists of source calibration checks (energy calibration and detector's efficiency), background counting, samples counting and activity determination.

The source energy curve calibration task loads 8 empty spectra including only the efficiency curve parameters and marked channels defining the position of the expected peaks of the calibration source. The calibration process is done by amplifier's gain adjustment for each detector to match the peak centroid to the marked ROI (Region Of Interest).
The detectors efficiency check task loads 8 empty spectra having the appropriate ROIs of the various peak regions of the source calibration cocktail. After sequential counting of the cocktail by the 8 detectors for a preset time, an external Quick Basic version 4.5 (QB4.5) program calculates the appropriate integrals from the binary spectra files, compares the data to expected count rates and prints a comparison table.
The background spectra task loads 8 empty spectra with 7 ROIs. The system is operated to accumulate background spectra for further reference during spectra analysis. After the acquisition the spectra are stored and printed out. An external QB4.5 program saves and prints the minimum detectable activity's table of the 8 detectors and their 7 background's integral. The calibration and background values are stored and their variation with time can be observed.

The sample counting procedure operates some helpful tasks such as loading the 8 empty spectra with the 7 ROIs, start counting, printing the displayed spectra, etc. After accumulation is completed the operator defines the peaks in the spectrum: For low activity samples the ROIs remain as they were determined in

the empty spectra - the 7 background's ROIs. A QB45 program compares the ROIs, by statistical criteria, to the appropriate detector's background.
For active samples the peak ROIs are determined by the operator and the program calculates the peak's net area (the calculation uses the trapez method). For low count rates the appropriate peak's spectrum, the trapez calculated channels counts and the background's ROI are compared and printed. The operator can decide which method fits best: the trapez or the background subtraction. Fig 1 shows a result of a sample containing a small amount of Cs-137. It can be seen that in the case shown the proper method is the integral background subtraction. For higher activity samples the background's integral in the peak is expected to be negligible and the trapez calculation is to be subtracted.

```
*** Area\Integral calc prg. due PCA-II ROI's ***  AI110696
============================================================
DetNum: 4
Area:
-----

Current Date: 09-09-1996  13:08

Elt:  600  Seconds

spec start aquire date: Sep 09, 1996     time:  1:04:21 pm
spec stop  aquire date: Sep 09, 1996     time: 01:07:13 pm

Saved drive & file name: a:lastspec.sp
ID: 1234567
Units: KeV   a0 = +3.62E+01   a1 = +8.64E+00   a2 = +5.17E-03
Num of E_Calib Points:  5
DetBackSpec FileName: 090996s .10

ROI#: 1        Beg Ch: 64 ( 610.58 KeV)      End Ch: 75 ( 713.56 KeV)
               Hst Ch: 70 ( 666.6 KeV)
               Gross  Integral: 487          Counts
               Trapez Area    : 204          Counts
               Net    Area    : 283          Counts
                              : 28.3         CPM
               Err             : 24.12       %

Ch#      BackC     TrapezC     SpecC
64         19          20         20
65         21       19.45         25
66         19       18.91         44
67         31       18.36         49
68         35       17.82         63
69         25       17.27         64
70         18       16.73         73
71         25       16.18         55
72         20       15.64         42
73         22       15.09         23
74         11       14.55         15
75         15          14         14

NetIntegral: 487 - 261 = 226          Counts ( .377 cps)    <+++10/12ch
NetArea    : 487 - 204 = 283          Counts ( .472 cps)

[Net Area Error: 1.65 Sigma (90% Conf.) & 1 End-Point]

E calc is done without Adc Offset
```

Fig 1: Small amount Cs-137 peak and the two calculation methods.

* Nucleus Inc. 761 Emory Vally Road, Oak Ridge, TN 37831-2561, U.S.A

A New Thermal-Hydraulic Core Module Based on the Drift-Flux Model for the DSNP*

I. Silverman, M. Shapira and D. Saphier
Soreq - Nuclear Research Center
Yavne, 81800

E. Elias
Dep. of Mechanical Engineering
Technion
Haifa ,32000

Abstract

As a part of expanding the capabilities of the reactor calculations group at Soreq - NRC a new core fuel channel module is under development. The module solves the energy equations inside the fuel rod and mass, momentum and energy equations in the coolant channel. The module uses an approximation to the drift-flux model for the solution of the coolant conditions. This module is a part of DSNP library of modules and is used in the transient simulation of nuclear power plants. Several test cases were executed simulating the AP600 PWR. Comparison of the channel model with COBRA-4I and RELAP-5 calculations have shown good agreement. It was found that the previous homogeneous equilibrium model produced adequate results for power plant simulation until boiling conditions appear in a fuel channel.

Introduction

The DSNP is a special purpose block-oriented simulation language by which a large variety of nuclear reactors can be simulated. The dominant feature of DSNP is the ability to transform a flowchart or block diagram of the reactors' primary and secondary loops directly into a simulation program. The user is required to recognize the symbolic DSNP statements for the appropriate physical component, and list these statements in a logical sequence according to the flow of physical properties in the simulated power plant. At present most of the component modules in DSNP are of the lumped parameter type. In order to upgrade the two–phase modeling capabilities of the DSNP code a drift–flux model approximation is being introduced

*Paper submitted to the 19th Annual Conference of the Israeli Nuclear Societies. Herzelia, Israel. December 9-10, 1996

in certain components. This paper describes the improvements in the core fuel-pin and coolant channel module.

The diffusion models (which include the drift-flux model) have been introduced by Zuber and Findlay [7] and studied in detail by Ishii [3]. These models are based on a two–fluid analysis and significantly reduce some of the difficulties associated with the full two-fluid models. In two-fluid models an inaccurate modeling of the complex inter-facial interaction terms can bring about incorrect results and sometimes can induce numerical instabilities. The most important underlying assumption of the drift-flux model is that the motion of both phases can be considered as a whole single mixture whenever strong coupling between the phases exists. Therefore, the model usually consists of four balance equations: mass, momentum and energy conservation equation for the mixture and additional mass conservation equation for one of the phases.

The next section describes the physical model of a core channel. Following is a section presenting some reults for a small break loss of coolant accident (SLOCA) transient for an AP600 reactor. The last section concludes this paper with a discussion of the advantages of this module.

The Model

Axial and radial geometries of a fuel element and the surrounding cooling channel are shown in Fig. 1. The fuel rod is built of a core of fuel material which is inside a cylindrical clad. Between the fuel and the clad there is a gap filled with gas. The fuel element is immersed in flowing coolant.

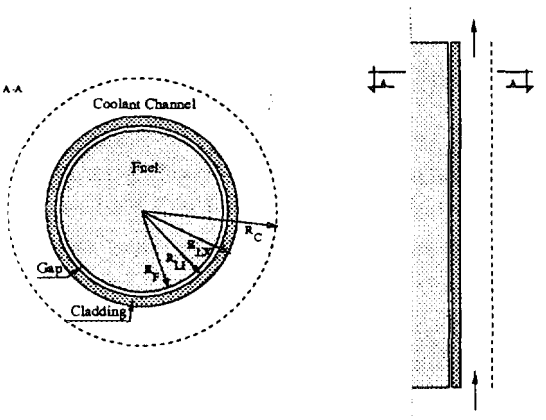

Figure 1: Fuel rod geometry.

The total heat, fission and decay heat, generated mostly in the fuel and partly in the cladding, coolant and structure is calculated by other modules that solve the

neutronic equations and calculate the thermal power. The new fuel channel module that simulates the fuel rod and coolant channel is a part of the core module used to simulate the whole core. The core module can receive any number of fuel channel modules to describe the core with as much detail as needed. Together, they enable the simulation of a reactor core including the feedback effects. This combination of the new fuel-rod and coolant channel module and the other DSNP components enables calculation of the power distribution along the core and the fuel and coolant temperature in specified channels. Finally, the thermodynamics properties of the various materials used are calculated by the relevant functions of DSNP and might be of any functional form.

The core channel module solves the energy equation for the rod and the mass, momentum and energy conservation equations in the coolant channel. The thermal-hydraulic equations for the fluid are based on the "drift-flux model" [7]. The basic assumption of this model is that the dynamics of the two phases can be expressed by the mixture momentum equation with the kinematic equation specifying the relative motion between phases. The use of the drift flux model is appropriate when the motion of two phases are strongly coupled. This model is therefore different from the previous model in which homogeneous flow and equilibrium conditions were assumed. The equations for the coolant are obtained by an area averaging over the flow cross section, $A(z)$, of the local time–averaged equations of the basic drift flux model derived in [3].

For system modeling one can greatly simplify the basic drift-flux model equations by using a simplified diffusion model. In this case, if the mixture is not far from the homogeneous conditions and the drift velocity is small, the vapor differential conservation equation can be replaced by an algebraic equation and the terms involving the slip velocity in the mixture momentum and energy equations can be neglected. An extensive review of the model and its use is given in [6].

Results

The new model is under an extensive test program. One part of this program includes solution of a small break loss of coolant accident (SLOCA) transient for an AP600 reactor (see [4]). Results for this transient together with results from COBRA-4I and RELAP-5 are given in Figs. 2 to 3. Data relevant to these calculation are summarized in Table 1. Results for a loss of feed-water ATWS in a PWR have been presented at [5].

The DSNP and COBRA simulations of the LOCA transient are of the core thermo-hydraulics only, while the RELAP simulation is of the whole primary loop. The boundary conditions needed by DSNP and COBRA are taken from the results of RELAP-5. These boundary conditions include the inlet flow rate, inlet coolant enthalpy, exit pressure and power. Fig. 2 shows normalized values of the boundary

Table 1: Parameters of the AP600 reactor core.

Active length of core	144	[in]
Fuel pin diameter	0.36	[in]
Fuel material diameter	0.287	[in]
Clad thickness	0.0228	[in]
Coolant channel hydraulic diameter	0.144	[in^2]
System pressure	2250	[psi]

conditions given to DSNP and COBRA.

The transient starts at 50s by a break which causes a loss of coolant and a sharp drop in system pressure. The pressure decrease initiates a scram to shut down power. Although fuel and coolant temperatures decrease after the nuclear activity is stopped, the decrease in pressure causes formation of voids as the liquid boiling temperature decreases to the coolant temperature. Pressure decrease due to loss of coolant is compensated now by pressure increase due to boiling and from about 100s the pressure remains constant. Together with the stopping of nuclear activity the scram also stops the pumps of the primary loop and at t=220s the flow rate to the core becomes almost zero.

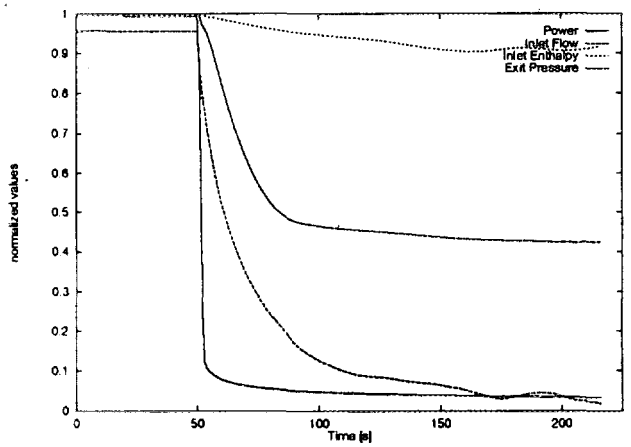

Figure 2: The boundary conditions for the DSNP and COBRA simulations.

The coolant temperature, (fig. 3), decreases with the decreasing power. RELAP gives that the coolant temperature, at the exit from the channel, follows the saturation temperature which decreases with the pressure. COBRA and DSNP, however, give that the initial decrease of the coolant temperature is faster and only at about t = 90s the pressure reaches coolant saturation levels. From this time, depending on the exact location, two phase flow is initiated, and the temperatures

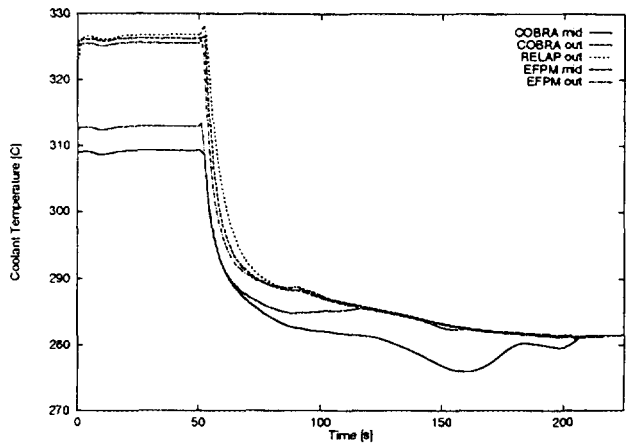

Figure 3: Coolant temperature transients as calculated by RELAP, COBRA and DSNP.

follow the saturation line. The clad temperature (fig. 4), which is higher then the coolant temperature follows closely the transient of the coolant temperature. As the clad temperature increases above the saturation temperature of the coolant nucleate boiling begins and the heat transfer coefficient increases (see fig. 5).

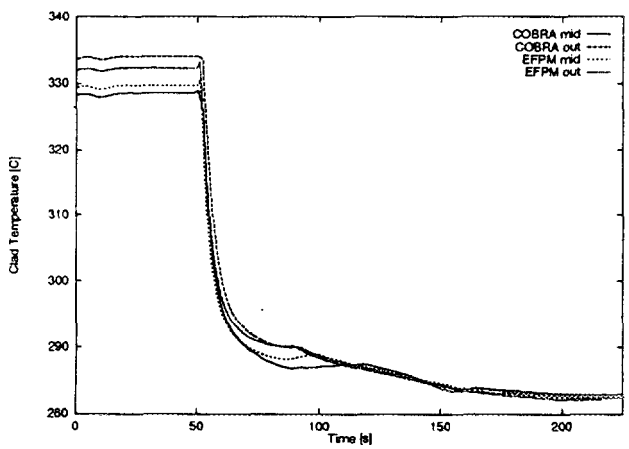

Figure 4: Clad temperature as calculated by RELAP, COBRA and DSNP.

Figures 6 and 7, present the coolant quality and void fraction at the mid-point and exit of the coolant channel. At about $t = 90$s, as the saturation temperature decreases to the coolant temperature at the exit from the coolant flow channel voids appear. Since COBRA uses an homogeneous model the void fraction it calculates follows the results for the coolant quality. The new DSNP coolant channel model is non-homogeneous, however, and can account for slip between the phases. This effect can be noticed by comparing the results of COBRA and DSNP for the coolant

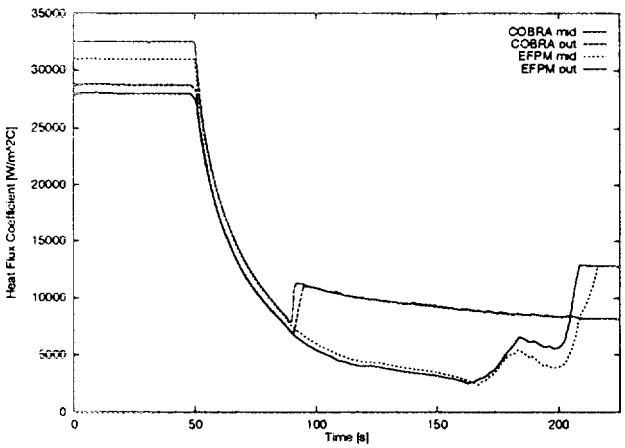

Figure 5: Heat transfer coefficients as calculated by COBRA and DSNP.

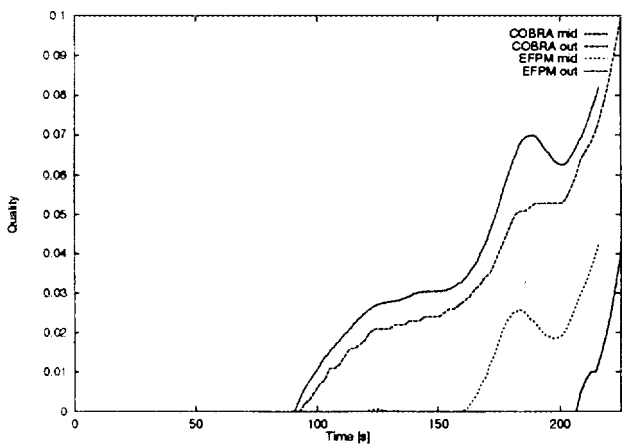

Figure 6: Coolant qualities as calculated by COBRA and DSNP.

quality and void fraction at the exit from the channel. Although the results of DSNP for the coolant quality follows closely those of COBRA it gives much lower values for the void fraction. The higher velocity of the vapor calculated by DSNP, since it is able to account for the slip between the vapor and liquid, results in lower void fractions than those calculated assuming that both phases has the same velocity, as COBRA does.

Conclusions

From preliminary calculations with the new fuel channel model developed for the DSNP it can be seen the the new model gives physically correct results. Comparison of results of the DSNP using the new channel model, for loss of coolant transient in a AP600 PWR, with COBRA-4I and RELAP-5 calculations have shown good

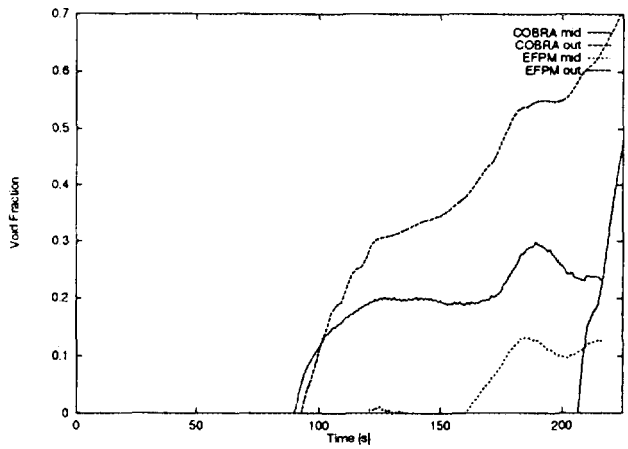

Figure 7: Coolant void fractions as calculated by COBRA and DSNP.

agreement. Comparing the new module with old modules used by DSNP for core flow calculations indicates that the new module extends the region of conditions which can be analyzed by the DSNP and gives more accurate results.

References

[1] B. Chexal and G. Lellouche. A full range drift-flux correlation for vertical flows. Technical Report EPRI NP-3989-SR, Electric Power Research Institute, 1985.

[2] B. Chexal, G. Lellouche, J. Horowitz, and J. Healzer. A void fraction correlation for generalized applications. In *NURETH-4*, pages 996–1002, 1989.

[3] M Ishii. *Thermo-Fluid Dynamic Theory of Two-Phase Flow.* Eyrolles, 1975.

[4] I. Silverman, M. Shapira, and E. Elias. Core transient simulations of an AP600 using COBRA. Technical Report RASG-175-94, Soreq Nuclear Research Center, 1994.

[5] I. Silverman, M. Shapira, and D. Saphier. Recent advances in DSNP - a simulation language for Dynamic Simulation of Nuclear power-Plant. In *Fifth International Conference on Simulation Methods in Nuclear Engineering.* Canedian nuclear society, September 1996.

[6] I. Silverman, M. Shapira, D. Saphier, and E. Elias. A new termal-hydraulic core module based on the drift-flux model for the DSNP. Technical Report RASG-202-96, Soreq Nuclear Research Center, Yavne, Israel, 1996.

[7] N. Zuber and J.A. Findlay. Average volumetric concentration in two-phase flow systems. *Journal of Heat Transfer*, 87:453–468, 1965.

Thermohydraulic modeling of the dry air PCCS process in the Westinghouse AP-600 ALWR

R. Harari[1], Y. Weiss[1] and Y. Barnea[1,2]
(1)N.R.C.Negev, P.O.Box 9001, Beer-Sheva, 84190.
(2)IAEC-Licensing Div., P.O.Box 7061, Tel-Aviv,61070.

INTRODUCTION

Following postulated events of a LOCA, the Passive Containment Cooling System (PCCS) uses dry air to transfer the residual heat by natural circulation. The air flow path, designed between the steel reactor containment hot shell and the concrete shield building, creates an open thermosyphon. The purpose of this inherently safe process is to assure the long term steady-state cooling of the nuclear core after an emergency shutdown.

The schematic draw of the PCCS is shown in *Fig.1*. The external cold air is introduced through special designed shutters, located in the upper level of the concrete shield building. Cooling the hot steel containment generates an upward air flow due the buoyancy forces and consequently the reduction of the static pressure. In order to maintain an open thermosyphon, the cold air drawn downwards by the pressure gradient should overcome the friction forces along the flow path.

Motivated to evaluate the feasibility of this passive cooling process and identify its parametric trends, an ongoing research program is carried on in the Laboratory of Thermohydraulics at NRC-Negev[1,2].

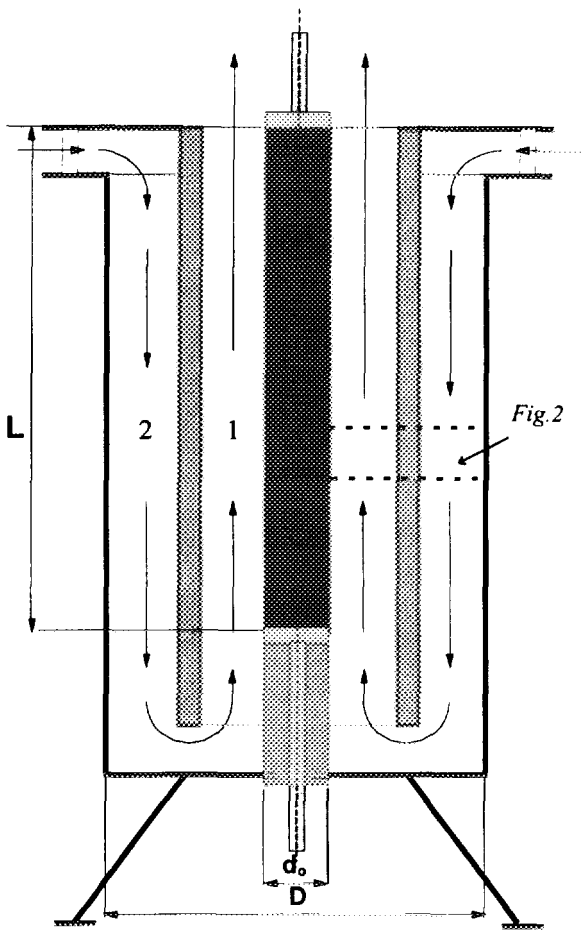

Figure 1: Schematics of the test section.

Based on a previous integral calculation procedure[3], the present work delineate a comprehensive model to calculate mass and heat transfer parameters in the PCCS process such as: pressure drop, air mass flowrate, hot surface temperature and convective heat transfer coefficient as a function of the system configuration. Database and order of magnitudes were taken from the official Westinghouse PCCS Integral Test[4].

ANALYSIS

Assuming that a positive flow is created as the buoyant forces overcome the friction forces (Fig.1), a complex heat transfer process is established. The heat transfer process from the inner surface to the surroundings is depicted by an electrical network analogy in *Fig. 2*.

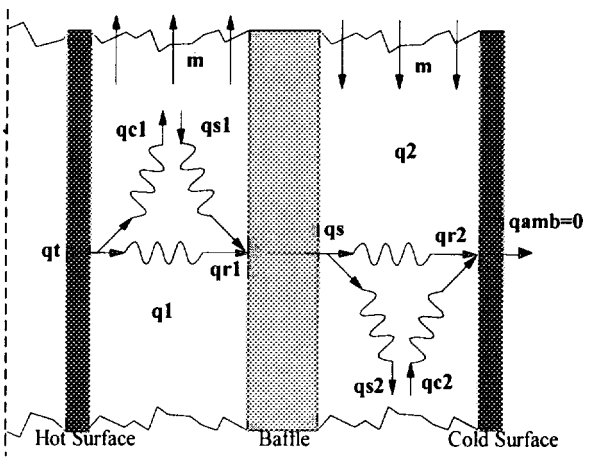

Figure 2: Heat Transfer mechanisms in PCCS.

The heat transfer balances are:

- from the hot outer surface: $q_t - q_{C1} - q_1 = 0$ [1]

- in the hot air(Chn.1,Fig.1): $q_{C1} - q_{S1} - q_1 = 0$ [2]

- in the insulating baffle: $q_{S1} - q_{r1} - q_S = 0$ [3]

- from the insulating baffle: $q_S - q_{S2} - q_{r2} = 0$ [4]

- in the cold air(Chn.2,Fig.1): $q_{S2} - q_{C2} - q_2 = 0$ [5]

- to the cold surface: $q_{r2} - q_{C2} = 0$ [6]

where:

$$q_t = \frac{\rho_{SS}\left[1 - \alpha_{SS}(T_{W1} - T_0)\right] L I^2}{A} \qquad [7]$$

$$q_{C1} = \pi d_0 h_1 (T_{W1} - T_1) \qquad [8]$$

$$q_{S1} = \pi d_{S1} h_1 (T_1 - T_{S1}) \qquad [9]$$

$$q_{r1} = \frac{\pi \sigma d_0}{\left[1/\varepsilon + (1-\varepsilon)/\varepsilon \; d_0/d_{s1}\right]} \left(T_{w1}^4 - T_{S1}^4\right) \qquad [10]$$

$$q_1 = m C_P \frac{dT_1}{dx} \qquad [11]$$

$$q_S = \frac{2\pi k_S}{\ln(d_{S1}/d_{S2})} (T_{S1} - T_{S2}) \qquad [12]$$

$$q_{S2} = \pi d_{S2} h_2 (T_{S2} - T_2) \qquad [13]$$

$$q_{C2} = \pi D h_2 (T_2 - T_{w2}) \qquad [14]$$

$$q_{r2} = \frac{\pi \sigma d_{S2}}{\left[1/\varepsilon + (1-\varepsilon^s)/\varepsilon^s \; d_{S2}/D\right]} \left(T_{S2}^4 - T_{W2}^4\right) \qquad [15]$$

$$q_2 = m C_P \frac{dT_2}{dx} \qquad [16]$$

By substituting Eqs.[7÷16] into Eqs.[1÷6], and assuming an arbitrary mass flowrate, it is possible to use a predictor-corrector numerical technique and calculate the axial temperature profile: along the hot and cold surfaces (T_{w1},T_{w2}), the insulating baffle (T_{S1},T_{S2}), and the air in both the hot and the cold channels(T_1,T_{w2}). For a given channel geometry i.e. hydraulic diameter and length, the iterative procedure enable to calculate the true mass flowrate and respectively the total pressure drop along the flow path. Further details regarding the numerical technique is presented elsewhere[2].

RESULTS and DISCUSSION

Data reduction emphasized that the heat transfer boundary conditions have a minor effect on the results, as the hot surface temperature (T_{w1}) is almost constant along the test section, depending only on the constant value of heat flux. The results presented in *Fig. 3* are lower by 30÷40°C than the values calculated earlier by the integral

approximate method[3]. Based on the results it is anticipated that the flow regime in the hot channel is fully developed after less than 2m and no further information is expected from longer test sections.

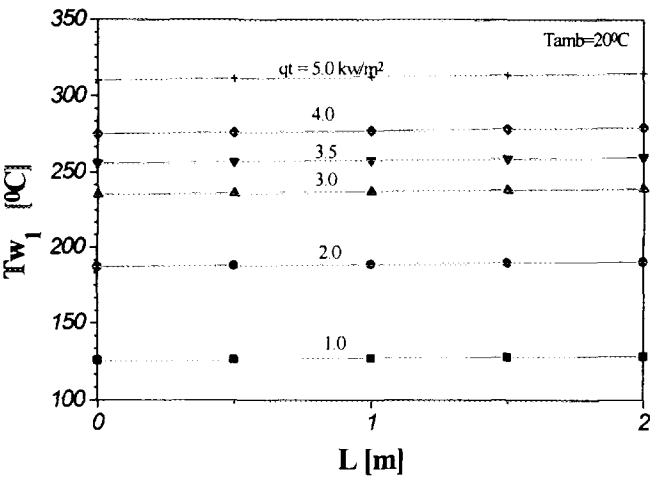

Figure 3: Hot surface axial temp. distribution (test section nominal geometry&qt=3.5kW/m² [2])

Two additional items of interest were investigated: a)Scaling-up the hydraulic diameter of both the hot and the cold channel by increasing the external diameter (D) by one order of magnitude (up to actual reactor containment size) and maintaining a constant hydraulic diameter along the flow path. b) Different ratios between the hot and cold channel diameters ($D_{h1}/D_{h2\neq}\neq 1$) and a possible optimal design.

Hydraulic Parameters: (Figs. 4 & 5)

The mass flowrate and the overall pressure drop indicate maximum and minimum values respectively for $D_{h1}/D_{h2} \approx 1$. Lower values will increase the pressure drop due higher friction forces caused by higher velocity in the hot channel while higher hydraulic diameters will increase the friction forces in the hot channel due the increase of the area of contact. Increasing the absolute values of the hydraulic diameters results in a slightly decrease in the mass flowrate due an overall increase in friction and in the overall pressure drop respectively.

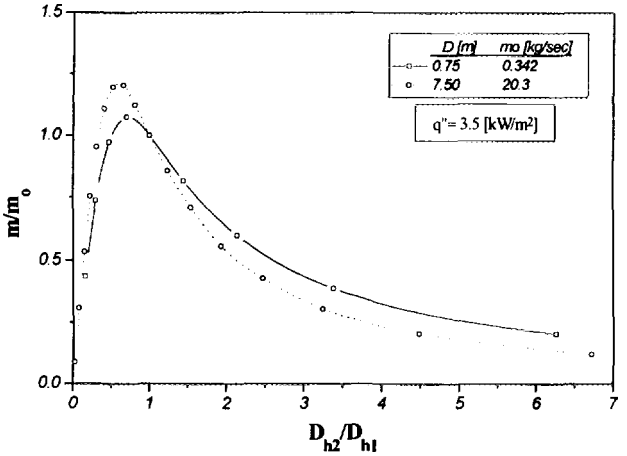

Figure 4: Coolant mass flowrate vs. hydraulic diameter ratio

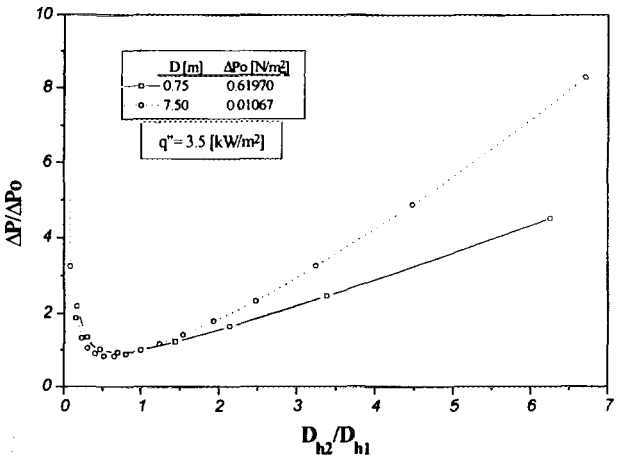

Figure 5: Pressure drop vs. hydraulic diameter ratio

Thermal Parameters: (Figs. 6 & 7)

The maximum temperature of the hot surface and the convective heat transfer coefficient reflect the efficiency of the cooling process by the thermosyphon. As the mass flowrate peaks for $D_{h1}/D_{h2} \approx 1$, the flow regime becomes turbulent and the maximum temperature is reduced (*Fig. 6*). The shift of the minimum value towards for $D_{h1}/D_{h2} \approx 2$ is explained by the conjugated heat transfer process in which the decrease of maximum temperature cause the decrease of heat

transfer by radiation. Nevertheless, the increase of the hydraulic diameter ratio will monotonicaly increase the convective heat transfer coefficient in the hot channel (*Fig. 7*) as the Reynolds number is increased indicating a higher turbulent regime.

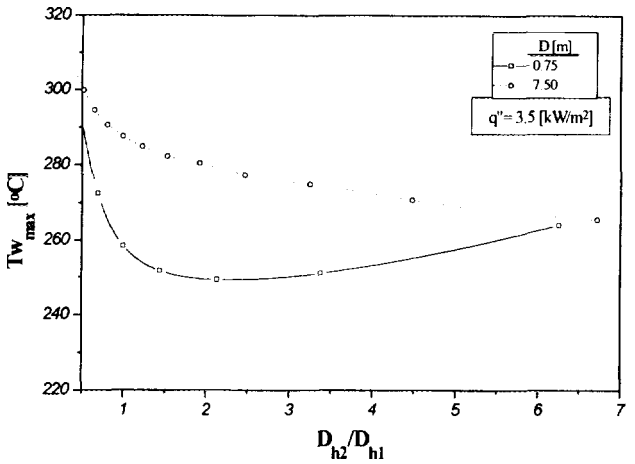

Figure 6: Max. surface Temp. vs. hydr. dia. ratio

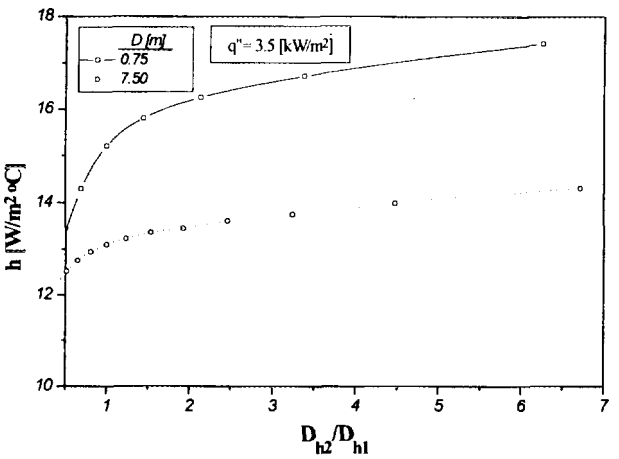

Figure 7: Convective heat transfer coefficient in the hot channel vs. hydraulic dia. ratio

ACKNOWLEDGMENT

The authors acknowledge the financial support of the research program by the Ministry of Energy and Infrastructure (Office of Head Scientist - Contract 94-11-011) and by the Nuclear Engineering Division of the IAEC.

NOMENCLATURE

A - heater X-section
C_P - heat capacity
D - external dia.
d - diameter
h - conv. heat trans. coefficient.
I - electrical current (dc)
k - thermal conductivity.
L - length *(Fig. 1)*
m - mass flowrate.
P - pressure
q - heat flow
T - temperature.
x - axial coordinate
α - coeff. of thermal expansion.
ε - emmisivity
ρ - electrical ressistivity.
σ - Stephan-Boltzman const.

Subscripts:

$_{C1}$ - convection in hot channel (1). *(Fig.2)*
$_{C2}$ - convection in hot channel (2). (")
$_{h1}$ - hydraulic dia. of hot channel (1).
$_{h2}$ - hydraulic dia. of cold channel (2).
$_{0}$ - outer dia. of heater (Eqs. 8;10)
$_{o}$ - nominal (exp. test conditions) (*Figs.*3÷6).
$_{r1}$ - radiation from hot surface. *(Fig.2)*
$_{r2}$ - radiation to cold surface. (")
$_{S}$ - conduction through the insulating baffle(")
$_{S1}$ - convection to the insulating baffle (")
$_{S2}$ - convection from the insulating baffle (")
$_{SS}$ - stainless steel (heater).
$_{1}$ - in hot channel (1). *(Fig.2)*
$_{2}$ - in hot channel (2). (")

REFERENCES

[1] י. ברנע, קרור פסיבי יבש של מאטם כור מדגם *AP-600, ALWR* - בעת עצירת חרום - הצעת מחקר, דו"ח קמ"ג/אמו"פ/מפח"ת 859/94/08, אוגוסט 1994.

[2] ר. הררי, י. אהרון, י. וויס, מ. חיים, מ. סנטו, ק. להב וי. ברנע, קרור פסיבי יבש של מאטם כור מדגם *AP-600, ALWR* בעת עצירת חרום - דו"ח מסכם שנת פעילות ראשונה, דו"ח קמ"ג/אמו"פ/מפח"ת 859/95/07, דצמבר 1995.

[3] Y. Barnea, Y. Weiss, M. Haim and Y. Aharon, Evaluating the Dry Passive Containment Cooling of the *Westinghouse AP-600* Reactor, The 25th Mechanical Engineering Conference, May 1994, Technion, HAIFA.

[4] van de Venne *et al.*, The *Westinghouse AP-600* PCCS Test Analysis Program, Proceedings of 2nd ASME/JSME Nucl. Engng. Joint Conf., 1,pp.1(1993)

Aerosol Filtration by Fibrous and Membrane Filters

T. Kravchik, U. Gherman,Y. Laichter
Nuclear Research Center - Negev

Purpose of work - Filtration is one of the most widely utilized technique in the nuclear industry for air cleaning and radioactive aerosols sampling, due to its simplicity and low cost. A wide spectrum of filters is available commercially with a wide selection of filtration, geometric and pressure drop characteristics.

In the present work, the various filters' types are presented with reference to their advantages and limitations and to their typical industrial applications. Filtration theories of the major filters' types are presented with the basic parameters of the filtration process including the filtration efficiency and the filter media resistance.

Methods - The aerosol filtration by fibrous and membrane filters has been a subject of numerous analytical, numerical and experimental studies during recent years. Based on these theoretical models a code has been developed in "Quattro-Pro", which calculates the filtration efficiency of the filters as a function of the filter, aerosol and flow parameters.

Results - The important filtration mechanisms of all filters are: Brownian diffusion, interception, inertial impaction and gravitational settling. The influence of these mechanisms depends on the aerosol diameter. Fig. 1 presents the filtration efficiency of a fibrous filter by the various mechanisms. At the low diameter's range (<0.2 μm) the Brownian diffusion is dominant whereas over 0.5 μm the interception and inertial impaction are dominant. As a consequence, there is an intermediate particle size region where none of the filtration mechanisms is dominant. In this region the particle penetration through the filter is maximal and the filtration efficiency is minimal.

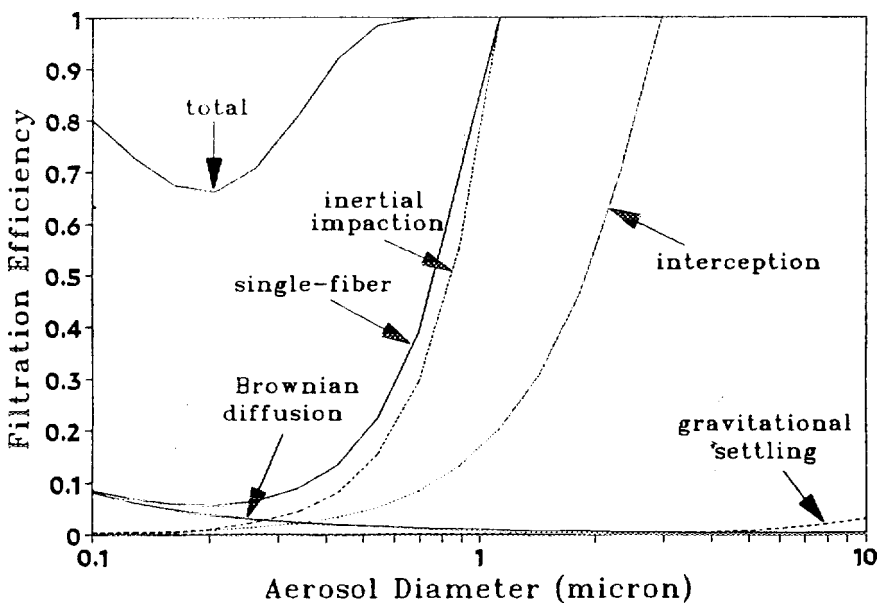

Fig. 1 - Filtration efficiency by the various mechanisms, single-fiber efficiency and total efficiency of a fibrous filter as a function of the aerosol particle's diameter. Fiber diameter - 3 μm, filter porosity -0.9, filter width - 400 μm, flow face velocity - 10 cm/s, aerosol density - 1 gr/cm^3

Filtration process in the fibrous filter takes place through the whole filter width and therefore its efficiency increases with this thickness. In contrast, the filtration in the membrane filter takes place basically at its surface and the filter thickness has a very minor influence on its filtration efficiency, as can be seen in Fig. 2.

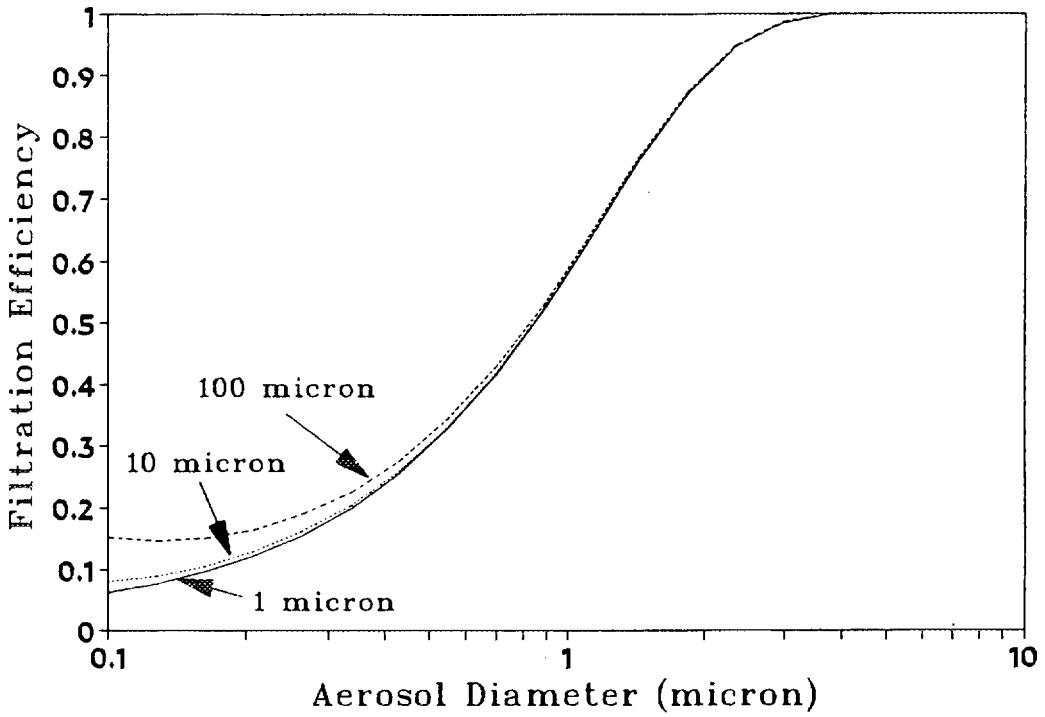

Fig. 2 - Total filtration efficiency of a membrane filter as a function of the aerosol particle's diameter at different filter thickness values. Filter pore size - 4 μm, filter porosity -0.05, face velocity - 10 cm/s, aerosol density - 1 gr/cm^3.

Conclusions - Based on the parametric study it is concluded that increasing the filter diameter, decreasing the filter thickness and especially increasing the filter porosity reduce the filtration efficiency of the fibrous filter substantially. In contrast, a change in the membrane filter thickness has a minor influence on its filtration efficiency. The influence of the flow face velocity on the filtration efficiency depends on the aerosol particle diameter.

The Importance of Proper Feedback Modeling in HWR [1]

By D. Saphier, Z. Gorelik, M. Shapira

Soreq Nuclear Research Center, Yavne 81800, Israel

Abstract

The DSNP [1] simulation language was applied to study the effect of different modeling approximations of feedback phenomena in nuclear power plants. The different methods to model the feedback effects are presented and discussed. It is shown that HWR's are most sensitive to the correct modeling since the usually have at least three feedback effects acting at different time scales, and to achieve correct kinetics a one dimensional representation is needed with correct modeling of the in core time delays. The simulation methodology of lumped parameters and one dimensional models using the DSNP simulation language is presented.

Simulation Methodology

Simulating accidents and transients in nuclear reactors requires first of all a "good" neutronics and thermal hydraulic representation of the core. The possible models range from simple lumped parameter models to full scale 3-D models. Full scale 3-D models are rare, and only recently became available [2] at very high cost. Most of the accident and transient analyses are still performed with system codes which use mostly lumped parameter models for the core kinetic representation although some have introduced 1-D neutronics models.

The present study investigates the importance of improved feedback representation in system codes using the point kinetic model to describe the core neutronics. The importance of proper representation increases if several feedback phenomena exist, each having a different time scale. Such conditions exist in reactors where the bulk of the moderator is separated from the coolant, and has a much larger heat capacity than the coolant. The GCR and HWR reactors belong to this category. In these reactors at least three different feedback effects can be identified.

1. A prompt Doppler feedback from the fuel

[1]Summary of paper submitted to the 5th International Conference on Simulation Methods in Nuclear Engineering, Montreal, Canada, Sept. 8-11, 1996(pap185ab)

2. A coolant temperature feedback from the coolant channel with a short time delay

3. A feedback effect from the moderator with a long delay.

An additional complication arises from the fact that the delayed neutron time constants might interact with the thermal-hydraulic time constants, since they are of the same order of magnitude. It was shown by the author [3] that the delayed feedback effects, even if all are negative, can cause instability. In the same reference it was shown that the correct representation of the effective delayed neutron fractions can move the simulated system from stable to unstable conditions and vice-versa.

Feedback Models

The following models were compared in the present study:

1. A lumped parameter model, (Fig 1a).

2. A one-dimensional fuel model and coolant channel model with lumped parameter representation of the moderator using an ideal mixing approximation, (Fig 1b).

3. A one-dimensional fuel model and coolant channel model with a single transport delay representing the moderator, (Fig 1d).

4. A one-dimensional fuel model and coolant channel model with a one-dimensional moderator model representing the moderator average temperature, (fig 1c).

5. A one-dimensional fuel model and coolant channel model with several transport delays each representing a single moderator node situated opposite the corresponding fuel channel node, (fig 1e).

The models are presented schematically in Fig. 1. As can be seen from the figure the moderator region can be modeled either as a single node or a number of thermal-hydraulic regions, in each the appropriate conservation equations are solved, and some heat transfer from the fuel is introduced, or as a series of transport delay elements in which case the heat transported across the boundary and the mixing are neglected.

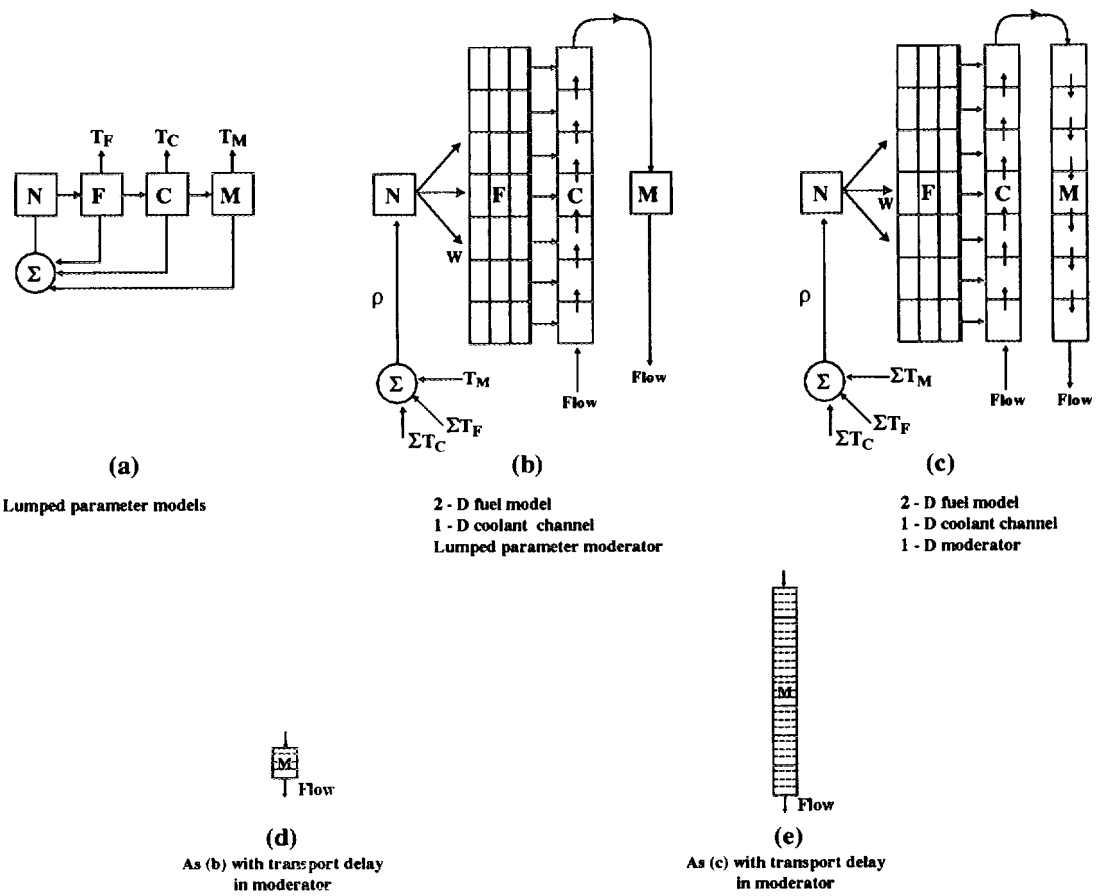

Figure 1: Schematic core feedback models. (fdb.eps).

Results of the Study

Each of the models presented in Fig. 1 was included in a full scale simulation program which included a detailed representation of the core and the primary loop. The model does not represent any particular reactor, but some of the system parameters were taken from the Canadian NPD power plant [4]. The basic phenomena that drives the system behavior is the rapidly responding coolant temperature with a relatively small feedback, and a slowly responding moderator region with a large feedback.

The hypothetical system was investigated both, with the full scale simulation model and by performing stability analyses using one dimensional transfer functions.

Fig. 2 shows the response of the power plant to a step change in reactivity with a) representing the moderator by a single lumped parameter region and b) as a one dimensional thermal hydraulic model having 7 regions. As can be observed the lumped parameter model gives a false impression of a very stable system, while the one dimensional model results in oscillatory behavior,

There are also differences between the 1-D model and the model that approxi-

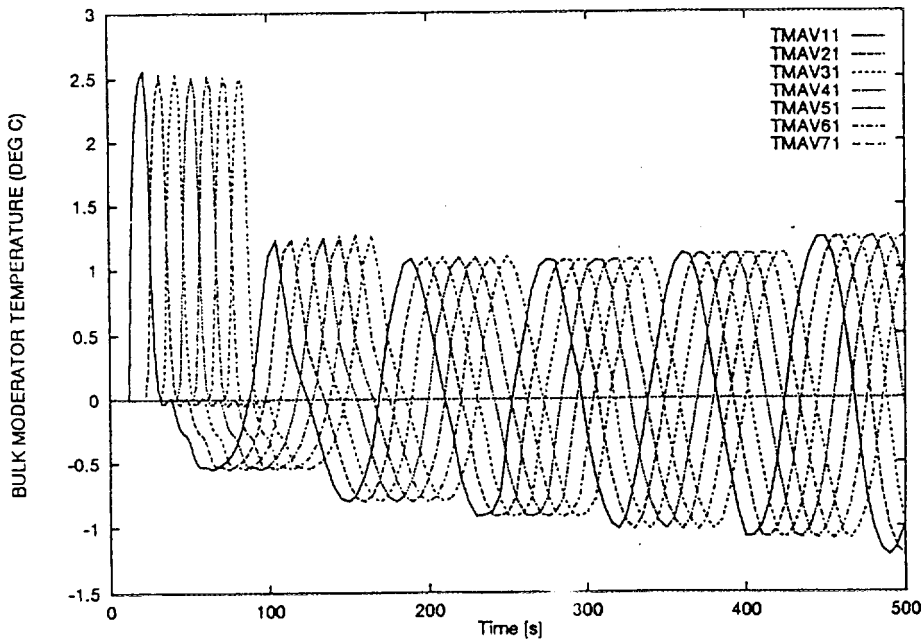

Figure 2: Response to a step change in reactivity from a lumped parameter and one dimensional moderator model

mates the moderator by several transport delay elements. The transport delay model tends to enhance the simulated system instability and the oscillatory behavior.

It can be concluded that modeling of the feedback dimensionality and its distribution along the core is rather important for the understanding of system transient behavior and phenomena of instability. The recommended correct modeling is the one dimensional representation of the core fuel, coolant, and moderator zones along the core with correct distribution of feedback in each of the modeled nodes.

References

[1] D. Saphier, *The DSNP User's Manual, Dynamic Simulator for nuclear Power Plants*, Vol. 2, Rev 4.4, RASG-115-85, Soreq Nuclear Research Center, (1985)

[2] L. E. Eisenhart, A.F. Dias, J.M. Sorensen, *CORETRAN/A Theory and Numerical Analysis*, Vol. 1, S. Levy Incorporated, (1994)

[3] D. Saphier, *Reactor Dynamics*, CRC-Press, Handbook of Nuclear Reactors Calculations, Vol-II, (1986)

[4] *Directory of Nuclear Reactors, Vol-IV, Power Reactors*, IAEA, STI/PUB/53 (1962)

Coupling of Conduction with Laminar Free Convection from a Vertical Flat Plate - An Experimental Study

J. Aharon[1] ,C. Lahav[1], H. Kalman[2], I. Shai[2]

[1] NRCN, P.O. Box 9001, Beer-Sheva, 84190, Tel. 07-567827, Fax. 07-554848
[2] Pearlstone Center for Aeronautical Engineering Studies, Dept. of Mech. Engn., Ben Gurion University of the Negev, P.O. Box 653, Beer-Sheva

ABSTRACT

The present work deals with natural convection on a vertical flat plate, where one side of the plate is maintained at a uniform temperature - T_a, and the other side of the plate is exposed to an environment of constant temperature -T_∞. The plate is consisted of several layers of conductive and non-conductive materials such that the series thermal resistance can be expressed as an equivalent heat transfer coefficient $h_{eq} = \frac{1}{\Sigma(k_i/\delta_i)}$. It is also assumed a negligible axial conduction, which can be neglected. The present investigation treats the heat transfer problem in the laminar zone in air (Pr≈1).The wall effective heat transfer coefficient is in the range of 4.3 to 11.5 $W/m^2 - ^\circ C$. An experimental apparatus was constructed to confirm the heat transfer features predicted analytically in a previous work. The local experimental Nusselt number was correlated with the modified Rayleigh number, for the laminar range.

INTRODUCTION

In the novel design of passive safety systems of nuclear reactors, the main idea is to reduce operator's responsibilities and add an extra margin of safety. Natural safety systems use the fundamentally dependable forces of gravity and natural circulation to cool the reactor core and to transfer the heat throughout the containment walls to the atmosphere. The main mechanism in those systems is the natural convection along the walls, where, from safety reasons, the walls are thick and are made of several layers of different materials. The arrangement of a thick wall exposed to the atmospheric air to one side and to the thermal conditions within the core at the other side, form a conjugate problem of conduction and natural convection along a vertical flat plate.

Natural convection heat transfer from a vertical plate has been a subject of numerous investigations in the past few decades. Laminar free convection along vertical plates with uniform surface temperature or uniform surface heat flux has been extensively studied analytically by Ostrach [1] and Sparrow and Gregg [2] and experimentally for both laminar and turbulent regimes by Warner and Arpaci [3] and Lock and de Trotter [4].

In a large number of technical applications, the surface heating conditions are non uniform. Laminar free convection with non uniform surface heating has also received considerable attention in the past. Sparrow [5] formulated the boundary-layer problem for free convection along a non-uniform heated vertical flat plate, by the Karman-Pohlhausen method and obtained solutions by a series expansion technique. Similarity solutions for free convection on a non isothermal vertical plate were provided by Sparrow and Gregg [6].

Several works treat more general natural convection problems in which the heat transfer condition in one side of the plate induces a natural convection in the other side.

The present work considers experimentally, a vertical flat plate that transfers heat by natural convection to a fluid at temperature - T_∞ at a general boundary condition, namely the other side of the plate is exposed to an environment of a constant temperature-T_a, with which heat is exchanged at an equivalent heat transfer coefficient (h_{eq}).

In engineering solutions for heat transfer problems, the effective heat transfer coefficient, could be a result of a forced convection or one dimensional conduction in the wall. The physical model is shown in Fig. 1. The analytical solution of that general natural convection problem, for the laminar and turbulent regimes, was presented in a previous work by Weiss et al. [7]. In the present work the laminar regime is considered.

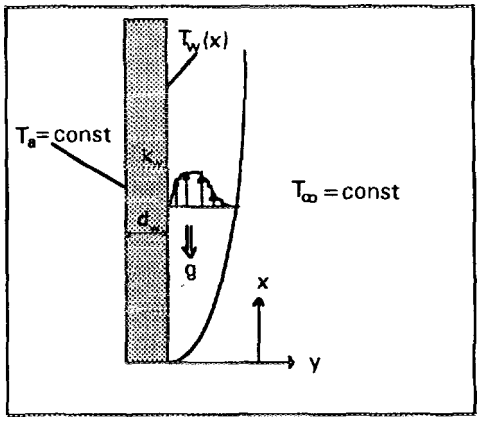

Fig. 1: Schematic description of the problem, geometry, configuration and coordinate system.

EXPERIMENTAL APPARATUS

The plate used in the experiments is shown schematically in Fig. 2 .

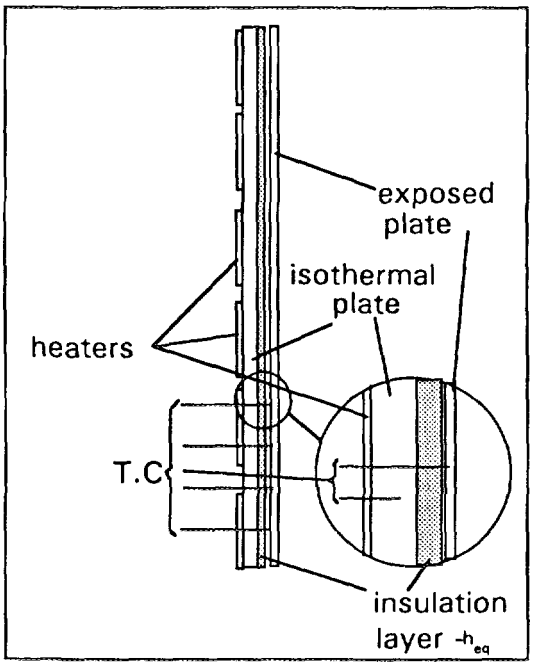

Fig 2. Scheme of the experiment plate.

The experiment plate consists of three layers: The exposed stainless steel plate, the aluminum isothermal plate and an insulation layer between the two plates. The exposed plate which is the heat transfer surface is 600 mm wide, 1020 mm high and 0.5 mm thick. That plate dissipates the heat to the surrounding's air. The isothermal plate is 600 mm wide, 1020 mm high and 6 mm thick. The high thermal conductivity of the aluminum and the fact that the aluminum plate is 6 mm thick keep the plate isothermal. Eight couples of heating strips was bonded on the back side of the isothermal plate. Each couple was controlled by a temperature controller to keep the whole surface at a uniform temperature. The constant temperature of the aluminum plate represents the hot temperature- T_a. A number of ceramic paper layers, each of 3 mm thick with a thermal conductivity of about 0.08 W/m-°C, is inserted between the aluminum plate and the stainless steel plate. Those insulation layers represent the effective heat transfer coefficient - h_{eq}. By changing the number of the insulating layers one can change the value of the effective heat transfer coefficient.

In order to measure the surface temperature of the stainless steel plate (the exposed surface), twenty thermocouples of chromel alumel of about 1 mm dia. were brazed on that surface. The junctions of these thermocouples were placed in the vertical direction along the center line of the plate. The spanwise temperature distributions of the heated plate was measured by six other thermocouples which placed along three horizontal lines at different distances from the leading edge as is shown in Fig. 3.

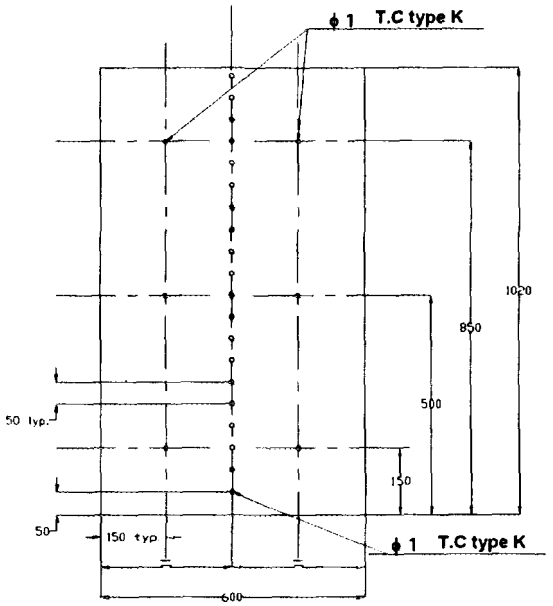

Figure 3: View of the experimental heat transfer plate (stainless steal).

In order to measure and control the temperature of the aluminum plate, eight thermocouples were bonded to the plate covering the entire controlled heating zone.

Figure 4 presents the test chamber containing the experimental plate and the peripheral measuring instruments. To reduce heat losses from the rear of the plate, two, 50 mm, layers of Rock wool insulation covered the back side of the heaters and the isothermal plate. Temperature stratification in the test chamber was measured by using K- type thermocouples, as is shown in Fig. 4.

The experiments were carried out in the closed perspex chamber to avoid any air currents. A hot wire anemometer was used to determine the laminar zone along the plate.

Three tests were conducted with three values of equivalent heat transfer coefficients- h_{eq}. The value of h_{eq} in each test was varied by using a different number of ceramic paper layers. Each couple of heaters were connected to the temperature controllers, and the temperature T_a of the aluminum plate was tuned. After reaching steady-state conditions and a uniform aluminum plate's temperature, all the temperatures of the stainless steel plate ($T_w(x)$) measured together with the ambient temperature (T_∞) in the test chamber at various heights. This procedure was repeated for each value of h_{eq}.

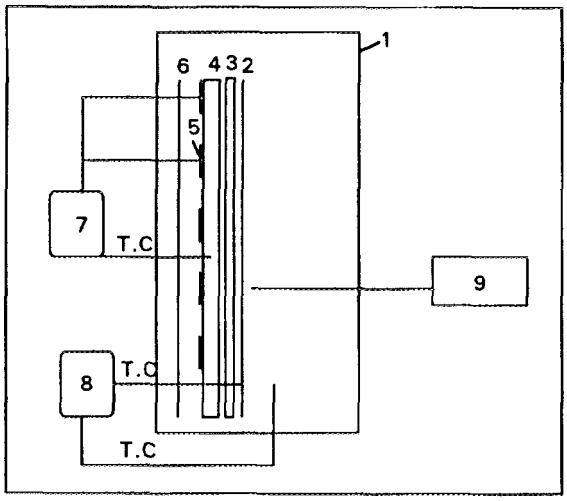

Fig. 4: Schematic diagram of the experimental apparatus: (1) perspex test chamber, (2) stainless steel plate, (3) insulation layer - h_{eq}, (4) isothermal plate, (5) heaters, (6) backup rock wool insulation, (7) temperature controller, (8) temperature measuring instrument, (9) hot wire anemometer.

RESULTS AND DISCUSSION

The results reported here were presenter elsewhere [8] and are based on three tests performed at various values of equivalent heat transfer coefficient - h_{eq}.

The variation of the dimensionless wall temperature is shown in Fig. 5. It shows that the minimum wall temperature is near the bottom edge and increases along the plate. That wall

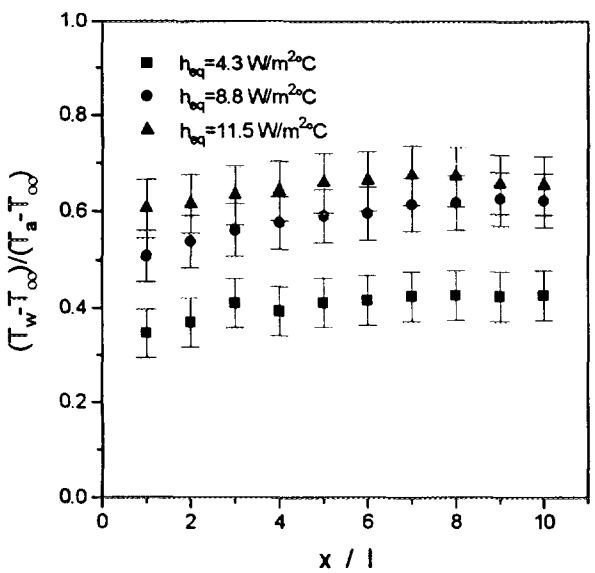

Fig. 5: Measured wall dimensionless temperature along the wall.

temperature's behavior can be explained by the increasing of the boundary layer thickness which decreases the heat convection. The wall temperature is also increased with the effective heat transfer coefficient.

The local heat flux along the wall was calculated by the next equation:

$$q''(x) = h_{eq}\left(T_a - T_w(x)\right) \quad (1)$$

and the local convective heat transfer coefficient is given by:

$$h(x) = \frac{q''(x)}{T_w(x) - T_\infty} \quad (2)$$

Equation (2) was solved by using the measured local wall temperature and the calculated heat flux (fig. 5 and eq. 1 respectively). The local heat transfer coefficient is presented in Fig. 6.

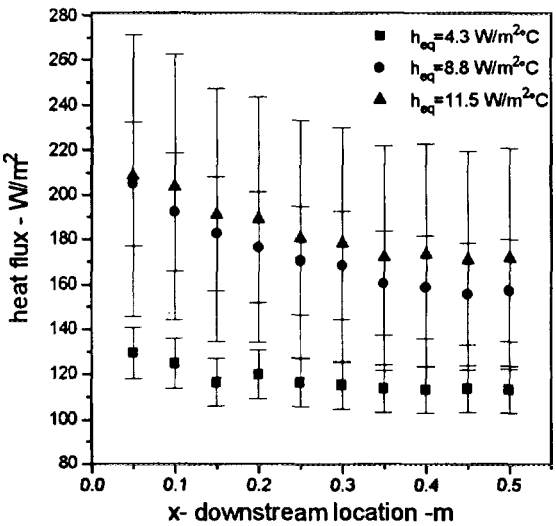

Fig. 6: Local heat transfer coefficient.

In the present case the heat transfer coefficient depends not only on the distance from the leading edge -x, but also on the temperature difference (T_a-T_∞) and the effective heat transfer coefficient- h_{eq}. Therefore, the results compiled in terms of the dimensionless groups, namely the local Nusselt number and the local modified Rayleigh number:

$$Ra^* = \frac{h_{eq}}{h(x) + h_{eq}} \frac{g\beta(T_a - T_\infty)\,x^3}{\nu^2} Pr \quad (3)$$

Where the fluid properties were taken at the mean stream temperature and the distance - x was measured from the bottom. The local heat transfer coefficient - h(x) is determined from the local heat flux - q" and the local wall and free stream temperature difference.

Figure 7 shows the experimental data for the three values of - h_{eq}. The plot is given on logarithmic scales with ordinates Nu(x) as function of $Ra^*(x)$ on the abscissa. Figure 7 covers local Rayleigh numbers in the range of $1.3\ 10^5 \div 2.46\ 10^8$. Various - h_{eq} values are denoted by different symbols in the figure.

As can be seen from this figure the experimental results converge well along a line of inclination - 0.266. The bulk of the data can be correlated with a maximum deviation of less than ± 12 % by the following relation:

$$Nu = 0.5613\left(Ra^*\right)^{0.266} \qquad (4)$$

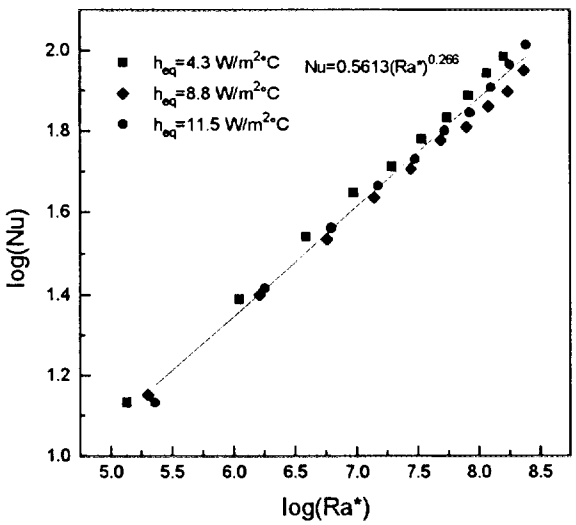

Fig. 7: Free-convection heat-transfer correlation for heat transfer from heated vertical plate.

CONCLUSIONS

The results presented in this paper indicate that the convective heat transfer coefficient increases with the equivalent heat transfer coefficient - h_{eq} and decreases with the distance from the bottom of the plate. The wall temperature increases with the distance from the bottom of the plate. The flow regime is laminar in all of the measured local Rayleigh number range.

NOMENCLATURE

d_w- wall thickness

k_w- wall thermal conductivity

q"(x) - local heat flux

h_{eq}- equivalent heat transfer coefficient

T_a - hot side temperature

$T_w(x)$ - local wall temperature

h(x)- local convective heat transfer coefficient

T_∞- ambient cold side temperature

Nu - hx/k local Nuselt number at distance x.

Ra*- local modified Rayleigh number (eq. 3)

References

[1] S. Ostrach, "An analysis of laminar free convection flow and heat transfer about a flat plate parallel to the direction of generating body force," NACA, TN2635, 1952.

[2] E. M. Sparrow, J. L. Gregg, "Laminar free convection from a vertical plate with uniform surface heat flux," Trans. ASME 78, pp. 435-440, 1956

[3] C. Y. Warner and V. S. Arpaci, "An experimental investigation of turbulent natural convection in air at low pressure along a vertical heated flat plate," Int. J. Heat Mass Transfer, Vol. 11, pp. 397-406, 1968.

[4] G.S.H Lock, F.J de Trotter, "Observation on the structure of turbulent free convection boundary layer," Int. J. Heat Mass Transfer, vol. 11, pp 1225-1232. 1968.

[5] E.M. Sparrow, "Laminar free convection on a vertical plate with prescribed monuniform wall heat flux or prescribed nonuniform wall temperature," NACA, TN 3508, 1955.

[6] E.M. Sparrow, J.L. Gregg, "Similar solution for free convection from a nonisothermal vertical plate," Trans. ASME 80, pp 379-386, 1958.

[7] Y. Weiss, Y. Aharon, I. Shai, "Natural convection on a vertical flat plate at general boundary condition," 10th Int. Heat Transfer Conf. , 16-NC-32, 1994

[8] J. Aharon, C. Lahav, H. Kalman, I. Shai, "An experimental investigation of laminar free convection from a vertical flat plate at general boundary condition," Proc. 26th Israel conf. on mechanical engineering, 21-22 May 1996

"R.I.S.-125" - ^{125}I Air Monitoring System

Belaish I., Levinson S., German U., Pelled O, .Laichter Y.,
Wangrovitz U., **Tirosh D.**, Barak D.
Nuclear Research Center - Negev

Introduction

We have developed at NRCN a prototype of a continuous X-Ray air monitoring (CAM) system called "R.I.S.-125" (Radioactive Isotope Sampler for ^{125}I). The system was checked according to ANSI N42.17B -1989 (1).

System Description

The "R.I.S.-125" is a stationary single-channel analyzer. It consists of three main parts:

1. A PM-10 (2) low energy scintillation detector. This detector uses a nominal 2 inch diameter NaI(Tl) 1 mm thickness, coupled to a photomultiplier tube. The surface sensitivity of the detector is 440 cpm/(Bq/cm^2) when calibrated to ^{125}I (approx. 30keV).
2. An electronic unit containing the processing display module, a control module to drive the whole system and a communication module. This unit is based on standard modules developed at NRCN.
3. A pumping unit of up to 100 lit/min flow rate, and charcoal cassette to collect the Iodine aerosols (or gases).

The detector and cassette holder are lead shielded to reduce the background to enable measuring of very low radioactive aerosol concentration.

The system can be easily switched to ^{131}I continuous air monitoring system by replacing the PM-10 detector to PM-11. This detector uses a nominal 2 inch diameter , 2 inch length NaI(Tl) detector coupled to a photomultiplier tube. A block chart of the system is shown in fig. 1.

Figure 1 - A Block diagram of "R.I.S. - 125"

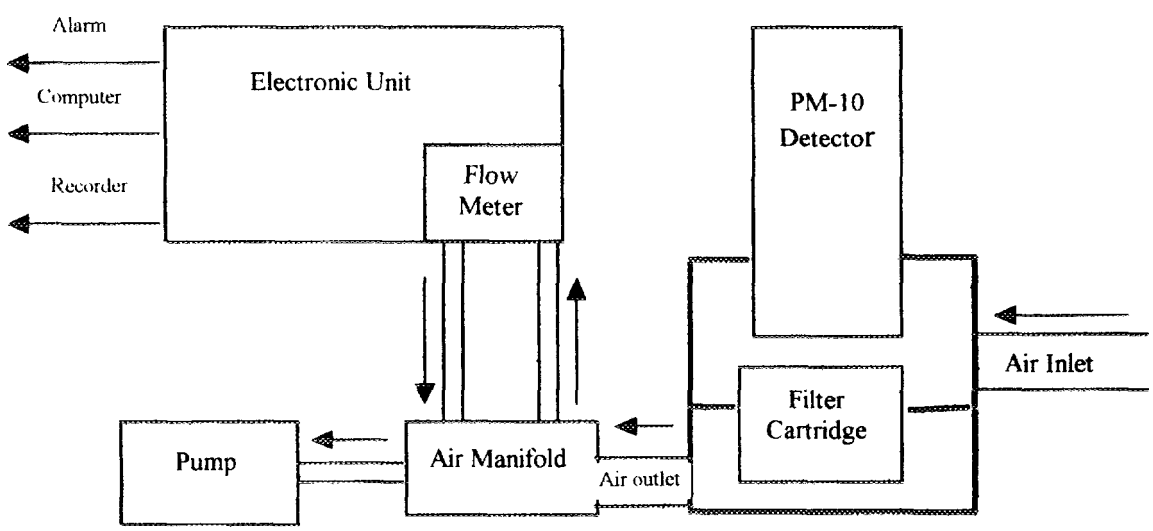

Experiments and results

The efficiency was measured using 4 calibrated point sources of ^{125}I. These measurements were repeated several times. Table 1 shows the sensitivity of the "R.I.S.-125" for two sets of measurements. Measurement number 2 was performed about two months after the first one.

Table 1 - Sensitivity of the "R.I.S.-125"

Source number	Sensitivity ± σ (cpm/dpm) measurement No. 1	Sensitivity ± σ (cpm/dpm) measurement No. 2
1	0.19±0.01	0.21±0.01
2	0.21±0.01	0.23±0.01
3	0..22±0.01	0.24±0.01
4	0.21±0.01	0.23±0.01

The sensitivity that was measured is higher then the sensitivity of a commercial system, LB 151-2 (made by Berthold).

The sensitivity of the system was also checked for filter cartridge. The sensitivity thus found is 0.035 cpm/dpm. The Iodine is absorbed on the first 5 mm of the cartridge (3).

The MDA (minimum detectable activity) and Lc (decision limit) (4) were calculated according to ANSI N13.30 (4) for ^{125}I. The MDA and the Lc are determined by the background level, the system sensitivity and the counting time. An estimation of the time required to pass the decision limit is presented in table 2 for some background levels.

Table 2 - Time needed in order to achieve Lc = 1 DAC

T - Time required for Lc to reach 1 DAC (sec) according to Vienna 115 safety series (4) for gases.	T - Time required for Lc to reach 1 DAC (sec) according to Vienna 115 safety series (4) for aerosols.	Background (cpm)
6.0	3.1	1
10.2	5.4	5
12.9	6.7	10
22.1	11.6	50
27.8	14.6	100

Long range stability measurements were done using an ^{125}I source. Each measurement lasted 5 seconds and each result is an average over 250 seconds. Figure 2 presents the results of 620 hours of continuos measurement. The error bars represent one standard deviation.

Figure 2 - Stability measurements of the "R.I.S.-125"

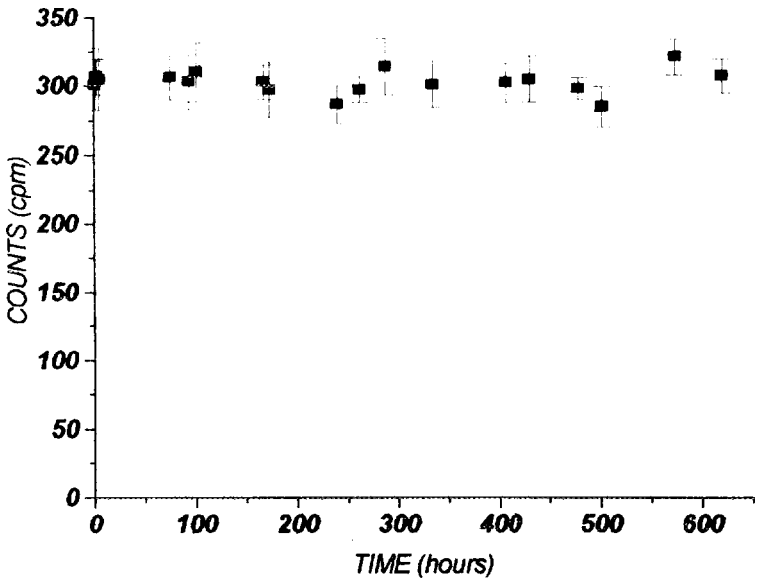

Over a period of about one month the measurement process (system and sources) was stable.

The air flow stability was also checked for a long time (500 hours). The readings needed calibration but their stability is according to the standard.

Conclusions

There are some repairs that should be done before completing the developing of the system. The main malfunctions are:

1. Overflow indication should be added.
2. There are no means for subtracting the background.

Bibliography

1. ANSI N42.17B-1989 - Performance Specification for Health Physics Instrumentation - Occupational Airborne Radioactivity Monitoring Instrumentation.
2. ROTEM prospectus : The PM-10 for Improved X-Ray and Low Energy Gamma Radiation Detection.
3. Metal Impregnation on The Adsorbents Efficiency Toward Radioiodine (Respirator Filters Adsorbents). H. Rotem, NRCN- 589 (1990).
4. ANSI N13.30 1989. Draft American National Standard for Performance Criteria for Radiobioassay.
5. Basic Safety Standards for Radiation Protection and for the Safety of Radiation Source Gov/2715, IAEA, April 1994.

LIMITATIONS OF ABS0LUTE ACTIVITY DETERMINATION OF I-125 SOURCES.

O.PELLED, U.GERMAN , R.KOL , S.LEVINSON , M.WEINSTEIN , Y.LEICHTER
Nuclear Research Center Negev
Z.ALPHASY - Ben Gurion University of the Negev

A method for absolute determination of the activity of a I-125 source, based on the counting rate values of the 27 keV photons and the coincidence photon peak is given in the literature (ref.1). It is based on the principle that if a radionuclide emits two photons in coincidence , a measurement of its disintegration rate in the photopeak and in the sum-peak can determinate it's absolute activity.

When using this method , the system calibration is simplified and parameters such as source geometry or source position relative to the detector have no significant influence. However, when the coincidence rate is very low, the application of this method is limited because of the statistics of the coincidence peak.

If N1 is the counting rate (cps) of the 27keV photons and N2 the coincidence rate ,see fig.1, the source activity A (in Ci) can be determined by using the equation (1):

$$A = \frac{(N1 + 2 * N2)^2}{4 * N2 * 3.7 * 10^{10}}$$

Fig. 1: I-125 gamma ray spectrum

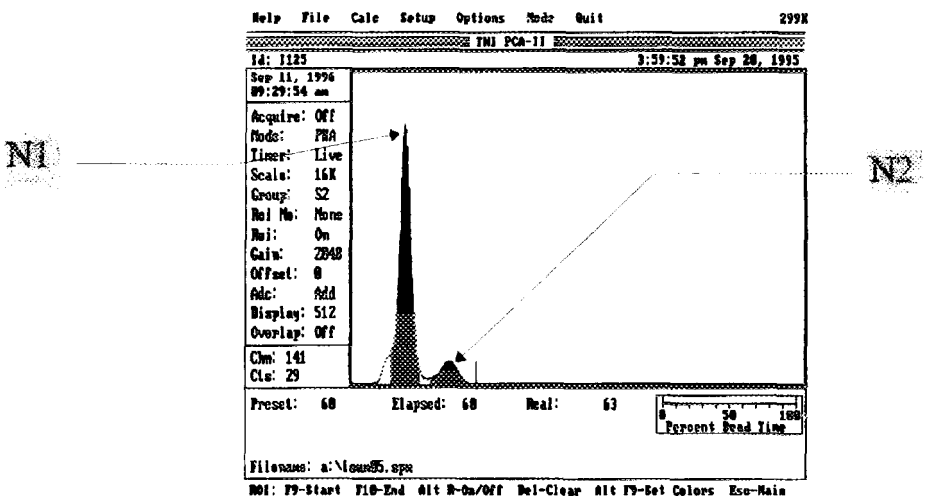

We checked the geometrical limitations of this method in respect to the following parameters:

* The distance between the source and the detector.
* The source dimensions.
* The thickness of the shielding between the detector and the source.

Fig.2 shows the ratio Ai/Ao as a function of the absorber (aluminum) thickness, were: Ai is the activity obtained using the equation given above with an absorber placed between the source and the detector and Ao is the activity obtained with no absorber (the actual activity).

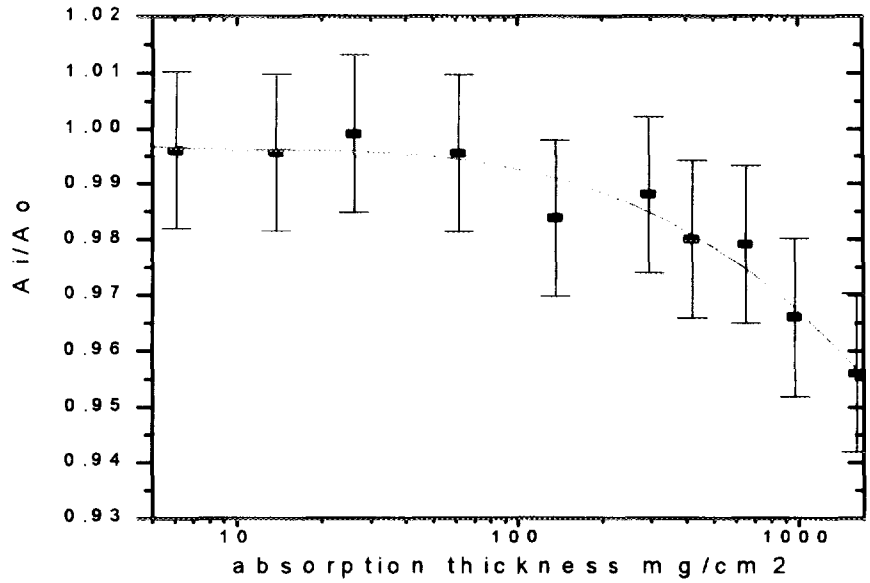

fig. 2: A1/A2 as function of absorption thickness

Fig.3 shows the ratio Ai/Ao as a function of the distance of a point source
and a 8.5cc bottle containing 4cc of I-125 solution from the detector.

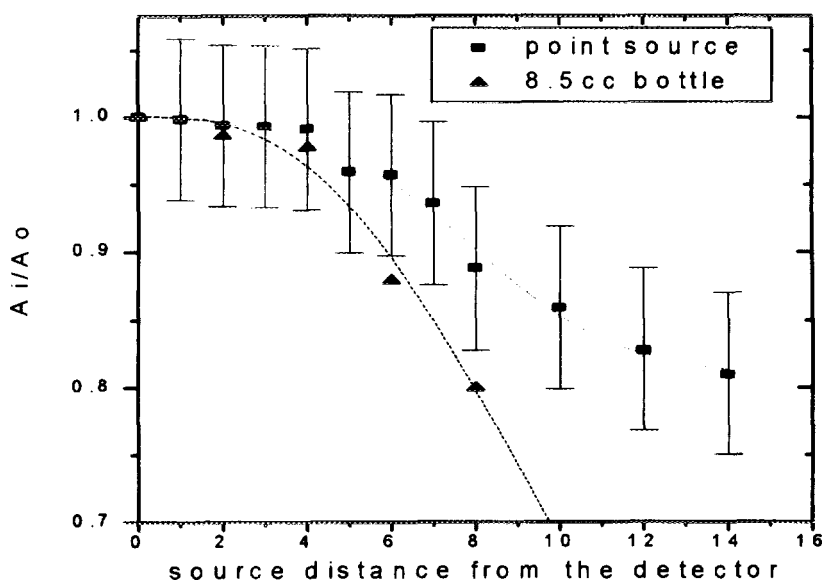

fig. 3: A1/A2 as function of absorption thickness

The results in fig.2 and fig.3 indicate that within the ranges shown in the figures , activity evaluation can be performed with good accuracy, without specific calibrations, although the count rates change by factors of 10 to 20.

Table 1 summarizes the evaluations of the geometrical limitations to obtain accuracies of up to 5%.

Table 1: The Limitations of the Absolute Determination Method for up to 5% error

parameter	range	maximal error
source distance from the detector	up to 5cm	5%
source volume (on the detector)	8.5cc bottle: any volume (in horizontal position)	3%
	20cc bottle: up to volume of 15cc (in horizontal position)	5%
absorption thickness	up to 1600mg/cm^2 aluminum	4%

Our checks indicate that this method can be used successfully for determination of the absolute activity of diverse sources, samples and applications within the stated limitations.

Reference:

1. S.Eldrige , "Absolute Determination of I-125", Nucleonics, June 1964

"ASIA" - A Radioactive Aerosols in Air Monitoring System

Belaish I., Pelled O., Levinson S., German U., Laichter Y., Wangrovitz U., Gonen E., Tirosh D., Barak D.
Nuclear Research Center - Negev

Introduction

We have developed at NRCN a prototype of a continuous alpha air monitoring (CAM) system called "ASIA" (Aerosols Sampler In Air). The system was checked according to ANSI N42.17B -1989 (1).

System Description

Basically, the "ASIA" is a stationary multi-channel analyzer. Air passes through a filter and the radioactivity accumulated on it is monitored by a solid state detector (Si detector , 2.5 cm detector diameter, 2.5 cm diameter filter collection area). The display unit can be detached from the sampling and counting unit and operated from outside a contaminated area. The system uses modern hardware and software in order to improve noise and background reduction and to allow flexible use. Remote communication is also available. The detector housing and the filter holder are made from treated aluminum. The distance between the detector and the filter is about 3 mm. The relative sizes (detector size, filter size and the detector - filter distance) were chosen in order to have maximum efficiency.

Detector unit: Resolution - 33 keV, gaussian pulses, pulse width - 5μs, air flow - 0 to 50 l/min.

Display unit: input gain 1.3, 1.34, 8 byte, 256 channels, graphics display (240X64 dot),

Software: Hebrew interface, friendly menus, algorithm for background reduction.

A block chart is shown in fig. 1.

Figure 1.a - Block Diagram of The "ASIA"

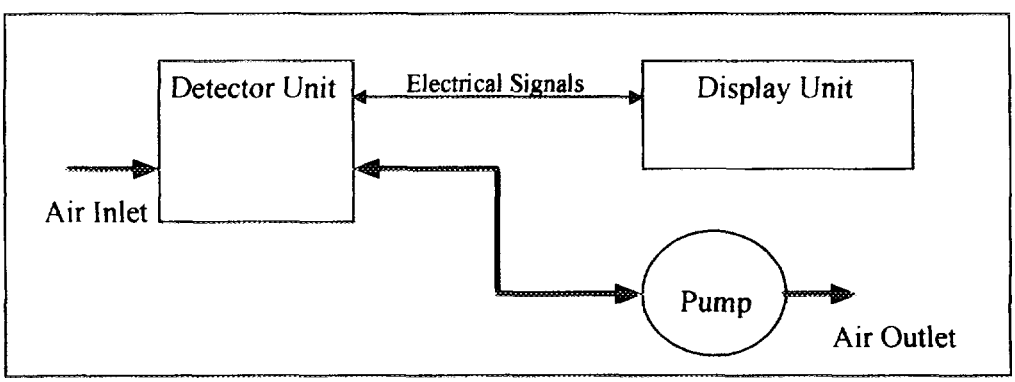

The efficiency was measured using calibration sources of ^{nat}U, ^{230}Th and ^{241}Am. Table 1 demonstrates the efficiency of the "ASIA" compared to the efficiency of a commercial unit ("ALPHA-6-1" from Eberline). The efficiencies which are presented are absolute values.

Table 1 - Absolute efficiencies of "ASIA" and "ALPHA-6-1"

Isotopes	Energy (MeV)	Activity (dpm)	"ASIA" efficiency (%)	"ALPHA-6-1" efficiency (%)
^{230}Th	4.65	1378	24.5±0.6	23.5±0.9
^{nat}U	4.74, 4.17	2220	20.0±0.1	-
^{241}Am	5.50	1494	23.2±1.1	21.1±0.7

The total efficiency for the whole process (the ability to collect aerosols and measure their activity) as function of aerosols diameter could not be measured because of lack of adequate experimental systems. Instead, we have measured the activity due to the natural Radon-Thoron with the two systems operated at the same place simultaneously. The results are presented in table 2.

Table 2 - Measurements of natural Radon-Thoron concentration with "ASIA" and "ALPHA-6-1"

"ASIA"			"ALPHA-6-1"		
monitored volume (m^3)	counts	(cts/m^3)	monitored volume (m^3)	counts	(cts/m^3)
43.7	284,924	6520	63.3	411,000	6493

The total efficiency of the two systems seems to be similar.

The MDA (minimum detectable activity) and Lc (decision limit) (2) were calculated according to ANSI N13.30 (2) for ^{nat}U. The MDA and the Lc are determined by the background level, the system sensitivity and the counting time. An estimation of the time required to pass the decision limit is presented in table 3 for some backgrounds level.

Table 3 - time needed in order to achieve Lc = 1 DAC

T-time required for Lc to reach 1 DAC (min)	background (cpm)
15.7	10
12.5	5
10.6	3
7.3	1

Long range stability measurements were performed using ^{nat}U source. Each measurement lasted 1 minute and each result is an average over 20 minutes. Figure 3 presents the results of 500 hours of continuos measuring. The error bars represent one standard deviation.

Figure 1,b - Block Diagram of the detector

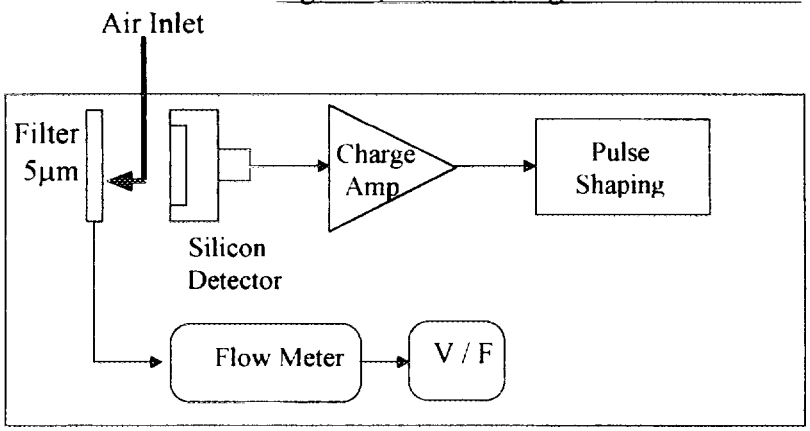

Figure 1,c - Block Diagram of display unit

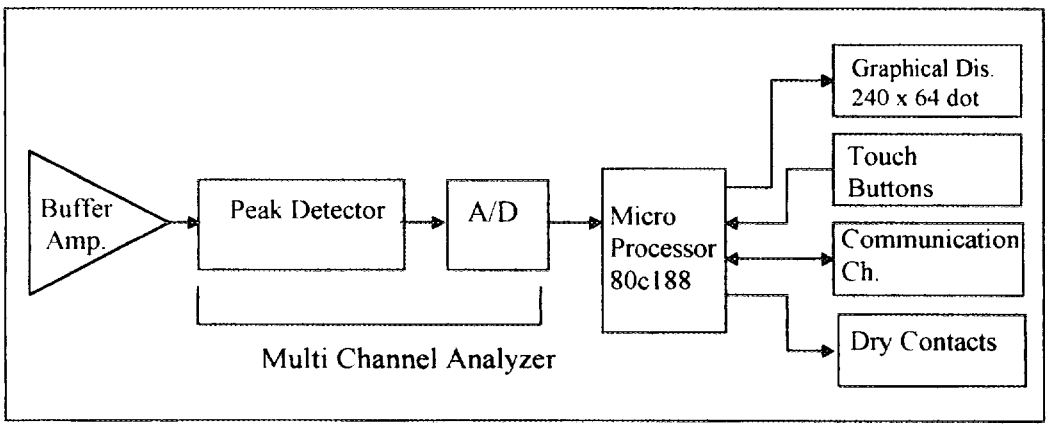

Experiments and results

The linearity was checked over the energy range from 4.17 MeV (^{238}U) to 8.78 MeV (^{212}Po) using various alpha sources and Radon - Thoron background. The linearity is shown in fig. 2.

Figure 2 - Calibration Curve of "ASIA"

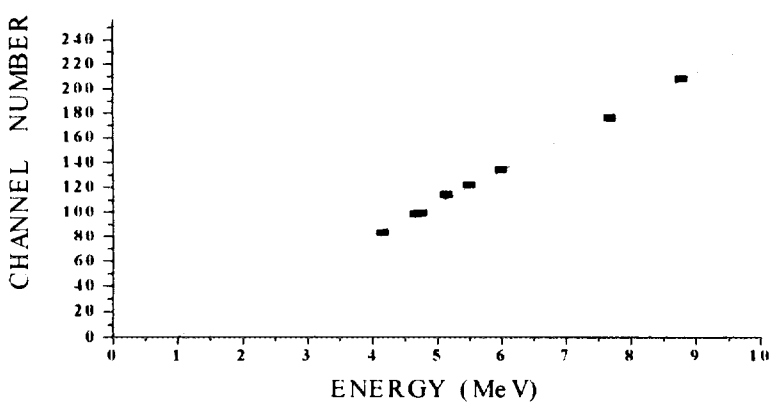

Figure 3 - Stability measurements of the "ASIA"

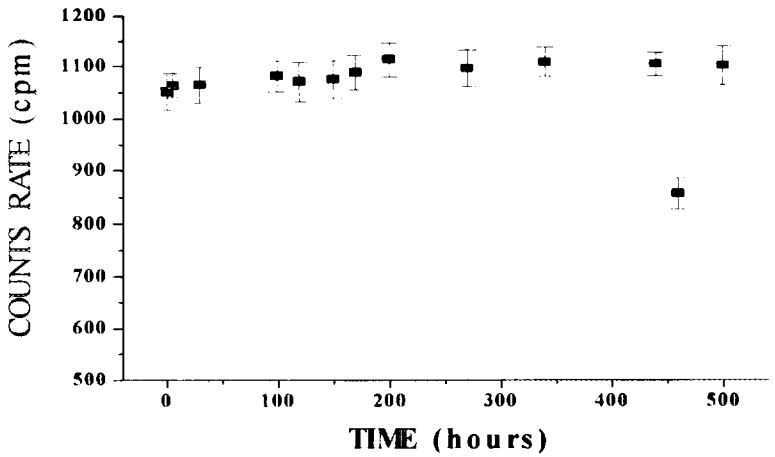

The "ASIA" system remains stable over long counting period. The point showing decrease after 450h is attributed to overflow of the counts buffer which was indicated by warning light.

The "ASIA" can be used also for β emitters measurements. We have used calibrated sources of ^{36}Cl, ^{99}Tc and ^{90}Sr - ^{90}Y to determine the efficiency of the system. The efficiency is about 2%. The relevant channels are the low channels (4 to 20) and therefore electronic noise interferes with the true signal. It is expected that by a better gaussian pulse shaping and by improving the grounding, the signal to noise ratio for the low region can be improved. Experiments done with a newer version of the system shows already a better signal to noise ratio.

Bibliography

1. ANSI N42.17B-1989 - Performance Specification for Health Physics Instrumentation - Occupational Airborne Radioactivity Monitoring Instrumentation.
2. ANSI N13.30 1989. Draft American National Standard for Performance Criteria for Radiobioassay.

LOCATING GAMMA RADIATION SOURCES BY SELF-COLLIMATING BGO DETECTOR SYSTEM

Orion I.[1,2], Pernick A.[1], Ilzycer D.[1], Zafrir H.[1] and Shani G.[2]
(1) Soreq Nuclear Research Center, Yavne 81800, Israel
(2) Ben-Gurion University of the Negev, Beer-Sheva 84105, Israel

Abstract

The need for airborne collimated gamma detector system to estimate the radiation released from a nuclear accident has been established. A BGO detector system has been developed as an array of separate seven cylindrical Bismuth Germanate scintellators, one central detector symmetrically surrounded by six detectors. In such an arrangement, each of the detectors reduced the exposure of other detectors in the array to a radiation incident from a possible specific spatial angle, around the array. This shielding property defined as "self-collimation", differs the point source response function for each of the detectors. The BGO detector system has a high density and atomic number, and therefore provides efficient self-collimation. Using the response functions of the separate detectors enables locating point sources as well as the direction of a nuclear radioactive plume with satisfactory angular resolution, of about 10 degrees.

The detector's point source response, as function of the source direction, in a horizontal plane, has been predicted by analytical calculation, and was verified by Monte-Carlo simulation using the code EGS4 [1]. The detector's response was tested in a laboratory-scale experiment for several gamma ray energies, and the experimental results validated the theoretical (analytical and Monte-Carlo) results[2].

Point Source Response Functions

Analytical calculations

The analytical calculation is based on the attenuation coefficients of BGO for photopeak energies. These coefficients were taken from the BGO producer data [3]. The total peak energy flux was calculated, for every detector in the array. A parallel beam source was assumed for the uncollided flux on the detector, for relatively distant sources relative to the detector system dimensions (200 m >>20 cm). The top view of the detector system is shown in Fig. 1.

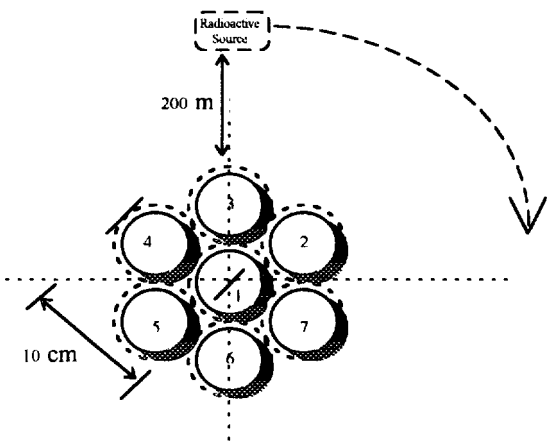

Figure 1: Top view of detector system and a point source.

The diameter of a BGO crystal is 5.08 cm (2") (smooth circles); the 6.7 cm diameter (dash circles) includes 1.62 cm of air between every detectors. The center of detector 1 is defined as (0,0), the y-axis passes through the centers of detectors 3 and 6, and the x-axis tangential to detectors 2 and 7. First, we assumed a point source located on y-axis in front of detector 3 (Fig. 1). In this case, the central detector's shielding depends on the length of every detector's element along the y-axis, as the width of every element in detector 1 determines it's response. The photons that interact in detector (i) are:

$$I_i = \int \int_0^{2\sqrt{2.54^2 - x^2}} \exp(-\mu \cdot (y + 2\sqrt{2.54^2 - x^2}))dy\,dx \qquad (1)$$

Each detector's relative total peak response is normalized by dividing the given detector's integral by the result of detector's 3 integral when the source is positioned as described (maximal shielding). Changing the direction of the source by angular transformation, and using this relative response calculation technique, will provide a full angular response function for every detector.

Monte-Carlo Simulation

A User's Code for the EGS4 code system [1] was developed to calculate the total energy peak response in each of the seven BGO detectors in the array as a function of source direction. Calculations were performed for two different point sources - ^{137}Cs (0.661 MeV) and ^{60}Co (1.173, 1.332 MeV). The detector system's geometry was described in the code's subroutine HOWFAR using suitably modified macros of the subroutines CYLIN (describing an infinite cylinder) and PLSN2P (describing the planes which define cylinder length).

As the objective is to calculate ratios of the total energy peak responses of the different detectors, a monoenergetic parallel-beam source was described. The ratios of the total energy peak responses in the different detectors were calculated as a function of the source direction within the 60 degree range determined by the detector system's symmetry.

Point Source Response Experiment

The directional shift of the source was controlled by rotation of the detector system on its axis. A $3.7 \cdot 10^7$ Bq (1 mCi) source of ^{137}Cs (0.662 MeV) and of ^{60}Co (1.172, 1.332 MeV) was fixed at a distance of 5 m from the detector system at the height of the system's vertical center. Measurements were performed every 5 degrees in the 0 - 60 degrees range, and every 10 degrees in the 60 - 120 degrees range. A 300 second measurement duration resulted in satisfactory counting statistics. The ^{137}Cs count rate was measured in the energy window of 0.504 - 0.747 MeV, and the ^{60}Co count rate in the energy window 1.068 - 1.440 MeV; background count rates measured for each direction were subtracted from the total.

Results

The results of analytical calculations proved to be reliably close to the experimental results obtained for the BGO detector array. Additionally results from the Monte-Carlo simulation were close to both the experimental results and the analytical results (an example is shown in Fig. 2). Using the response functions, the direction of a point source can be determined within a resolution of at least 10 degrees, depending on the count rates statistics. The angular resolution of higher energy point sources is slightly lower. This resolution level encourages application of this detector system and methods for more complicated radioactive sources.

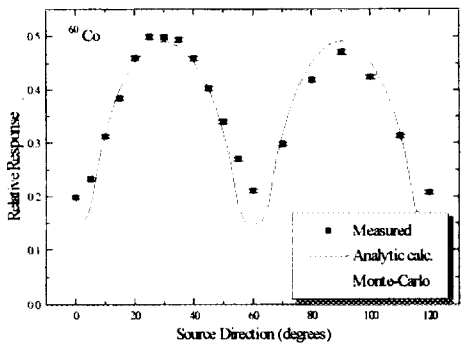

Figure 2: An example of central detector's (detector 1) relative angular response to a ^{60}Co point source location.

A Multi-point Source Location Model

The theoretical or the experimental detector's point source response functions for a single point source in the angular range of 0-120 degrees, can be fitted to a polynom of order five or less. The response of the central detector (detector 1) has a period of 60 degrees and can be fitted to a cosine function.

The response effect of several equal intensity point sources around the detector system, multiplying by the squared distance ratio of the points to the detector system, is additive. By using the experimental results for a point source, we created data sets for some examples of two or three point sources in different directions and in different relative distances, in horizontal plane, to the detector system.

These data sets were inserted into a Non-Linear Regression program, which allowed the user to define parameter functions for the regression. For every data set, the range of the adjustable parameters was defined by input parameters.

The parameter function was derived from a given detector's response function and included two parameters for every point source, r^2 and ϕ:

$$y_x(r, \phi) = \sum_x r_x^2 . F(\theta + \phi_x) \qquad (2)$$

r^2- The ratio of the squared distance from the system to one of the point sources and to the closest point source.

ϕ- The phase angle of a point source from the y-axes of the detector system .

$F(\theta)$- The response function of a given detector.

x- Number of point sources around the system.

A Line source Response

Simulation

In a previous work [2] we showed the ability of this detector array system to estimate the direction of a line approximation of a radioactive plume, in a stable (non dispersive) atmosphere. The assumed plume contained the fission products released in a PWR1 and PWR2 type accident [4], and was detected by measurement of the highest energy gamma line. Consideration of photon energy, probability per decay, core inventory , fraction released and decay rate, led to the selection of ^{88}Kr. This nuclide emits a 2.39 MeV photon with a probability per decay of 0.346, and its half-life is 2.8 hr.

The EGS4 calculation of total energy peak response in different BGO system detectors was performed by dividing the plume into 100 m length segments, each being represented as a point source, and calculating the additive flux. The detector array's y-axis

is oriented perpendicularly to the plume's direction. The EGS4 code calculational method for each segment was in principle identical to that previously described.

Experiment

The source employed was an irradiated NaHCO3 solid, which emits 2.75 MeV photons, being similar in energy to photons from ^{88}Kr (2.39 MeV). Twenty three points of $1.48 \cdot 10^6$ Bq (0.04 mCi) sources of ^{24}Na were installed homogeneously on a 6.8 m horizontal rod at a distance of 2 m from the detector system. The count rate was measured in the energy window 2.552 - 2.967 MeV for 300 seconds. The detector system's orientation was changed from 0 to 30 degrees in steps of 5 degrees.

Results And Conclusions

Locating multi-point sources of two or three points in a horizontal plane, is possible for sources separated by at least 10 degrees relative to the detector system. For an arbitrary arrangement of a three point source, angle and relative distance can be obtained from a non-linear regression technique. In all cases a good correlation was achieved. In most cases, the quality of the regression output was not depending on the initial input parameter's "guess" values. For sources separations less then 10 degrees the uncertainty of the results is substantial, due to the limitation of point source angular resolution. Relocation of the detector system to another site can increase the angular separation and thus assist in overcoming this difficulty.

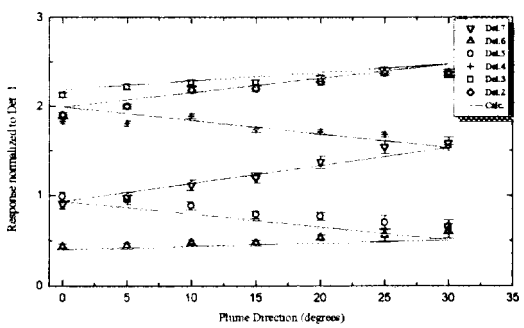

Figure 3: The detector system response to a line plume, normalized by the central detector response. The data points represents the experimental results, and the straight lines represents the simulation.

Assuming a line source approximation of a nuclear plume, airborne monitoring enables an immediate determination of plume direction within ±30 degrees. Slightly changing the flight direction until attaining equalization of detector response in given detector pairs enable determination of plume direction, with improved resolution.

As shown in Fig. 3, the laboratory scale line source experiment, validates the method presented here, and indicates a 10 degrees resolution in the determination of plume direction, considering count rates statistics.

References

[1] Nelson, W. R., Hirayama, H. and Rogers, D., The EGS4 Code System, SLAC-265 (1985).

[2] Pernick, A., Orion, I., Ilzycer, D. and Zafrir H., Application of a Self-Collimating BGO Detector System to Radiological Emergency Response, Health Phy. (accepted for publication).

[3] BICRON Product Bulletin SC-103A (1989).

[4] U.S. Nuclear Regulatory Commission Reactor Safety Study- An Assessment of Accident Risks in U.S. Commercial Nuclear Power Plants, App.VI, WASH-1400; Washington D.C.: U.S. Government Printing Office (Oct. 1975).

THE USE OF ACOUSTIC RESONANCES TO DETERMINE THE MECHANICAL PROPERTIES OF A MEDIAN LAYER IN A MULTI-LAYERED STRUCTURE

Tareef F., Dickstein P, Technion, Haifa

The present work deals with the problem of characterizing non-destructively the mechanical properties of a median layer in multilayered structures. This characterization may be essential in compartments which may be subjected to harsh working and/or harsh environmental conditions, and subsequently, may exhibit deterioration in their mechanical properties. As an example one may consider the adhesive layer in structural adhesive joints exposed to elevated temperatures and humidity. A methodology has been developed and applied in this work, for the evaluation of the mechanical parameters of the median layer through the acoustic resonances of the structures. This inverse-problem is complicated because of the mathematical ill-posedeness of the model, so that regularization procedures should be employed. The model is introduced, and the experimental results are presented and discussed.

Thorium Fuel for Light Water Reactors - Reducing Proliferation Potential of Nuclear Power Fuel Cycle

by

Alex Galperin and Alvin Radkowsky
Ben-Gurion University of the Negev

The proliferation potential of the light water reactor fuel cycle may be significantly reduced by utilization of thorium as a fertile component of the nuclear fuel. The main challenge of Th utilization is to design a core and a fuel cycle, which would be proliferation-resistant and economically feasible. This challenge is met by the Radkowsky Thorium Reactor (RTR) concept. So far the concept has been applied to a Russian design of a 1,000 MWe pressurized water reactor, known as a VVER-1000, and designated as VVERT. The following are the main results of the preliminary reference design:

- The amount of Pu contained in the RTR spent fuel stockpile is reduced by 80% in comparison with a VVER of a current design.
- The isotopic composition of the RTR-Pu greatly increases the probability of pre-initiation and yield degradation of a nuclear explosion.
- An extremely large Pu-238 content causes correspondingly large heat emission, which would complicate the design of an explosive device based on RTR-Pu.
- The economic incentive to reprocess and reuse the fissile component of the RTR spent fuel is decreased. The once-through cycle is economically optimal for the RTR core and cycle.
- To summarize all the items above: the replacement of a standard (U-based) fuel for nuclear reactors of current generation by the RTR fuel will provide an inherent barrier for nuclear weapon proliferation. This inherent barrier, in combination with existing safeguard measures and procedures is adequate to unambiguously disassociate civilian nuclear power from military nuclear power.
- The RTR concept is applied to existing power plants to assure its economic feasibility.
- Reductions in waste disposal requirements, as well as in natural U and fabrication expenses, as compared to a standard VVER fuel, provide approximately 20% reduction in fuel cycle cost.

The main challenge encountered in the design of a thorium based system is the necessity to supplement natural thorium with a pre-generated fissile component. Several design solutions were proposed and investigated, such as: initial start-up of the thorium cycle by enriched U, continuous addition of uranium as a fissile component to supplement self-generated U-233, reprocessing and recycling U-233, and addition of Pu to supplement self-generated U-233.
The improvement in natural uranium utilization by using thorium could be achieved only if the self-generated U-233 fissile material was separated and recycled into a closed fuel cycle. This approach, adopted by the LWBR, violated the non-proliferation requirement.
The RTR concept proposed by Professor A. Radkowsky offers a solution to the Th utilization problem. The basic idea is to use the heterogeneous, seed/blanket (SBU), fuel assembly. The Th

part of the fuel assembly is separated from the U part of the assembly. This separation allows separate fuel management schemes for the thorium part of the fuel (a subcritical "blanket") and the "driving" part of the core (a supercritical "seed"). The design objective of the blanket is an efficient generation and in-situ fissioning of the U-233 isotope, while the design objective of the seed is to supply neutrons to the blanket in a most economic way, i.e. with minimal investment of natural uranium.

The SBU geometry provides the necessary flexibility to satisfy a major design constraint - full compatibility with existing pressurized water reactor (PWR) power plants. In addition, the heterogeneity of the SBU design allows the necessary (and separate) optimization of seed and blanket lattices. The design constraints are prescribed mainly by considerations of technical and economic feasibility. These constraints are imposed to support economic justification of the research and development activity required to design, verify, licence and implement the RTR fuel within a reasonably short period of time. The design constraints are summarized below:

1. The RTR concept should be realized as a new fuel design, and thus, be completely compatible with existing power plants. Only minor plant hardware modifications, directly related to a different fuel assembly internal arrangement will be acceptable.
2. All safety and operational parameters of existing power plants will be preserved.
3. The fuel design will be based mainly on existing (not necessarily commercial) fuel technology. The maximum allowable fresh fuel enrichment will be kept below 20% of U-235 content.

The reference design of the RTR core and fuel cycle was carried out based on objectives and constraints discussed above.

The VVERT design is an implementation of a RTR fuel reload for a standard VVER-1000 core, where "T" stands for Thorium. The VVERT core is identical to an existing VVER-1000 core with 163 hexagonal fuel assemblies and 3,000 MWth power output. The average power density of 106 kW/l is somewhat higher than that of a similar PWR core of a western design. The hexagonal SBU and a corresponding square SBU (for the PWRT version) are shown in Figure 1. The VVERT fuel assembly - SBU consists of two spatial regions: internal region (seed) and external region (blanket). The design objective of such arrangement is to maximize power production of the blanket region. The seed region volume and consequently its power share are minimized subject to two constraints: 1) total amount of uranium loaded in seed each cycle should sustain (drive) the subcritical blanket for a given inter-refuelling interval, and 2) the total surface of seed fuel should be adequate to sustain required temperature and heat flux values. The seed fuel was chosen as U/Zr alloy rods, which is consistent with fuel technology capabilities of the fuel vendor industry of Russian Federation (RF). The size of the seed rod and unit cell geometry were determined by consideration of neutronic and heat removal aspects as mentioned above.

The blanket fuel considered in present design was thorium oxide with addition of uranium oxide. The uranium was added to blanket fuel for two main reasons: 1) natural thorium does not include a fissile component, therefore enriched uranium is required to provide a reasonable power density in the blanket during the initial burnup period of U-233 gradual buildup, and 2) addition of U-238 assures that U-233 accumulated and discharged with the blanket fuel is sufficiently diluted to present no diversion (proliferation) potential.

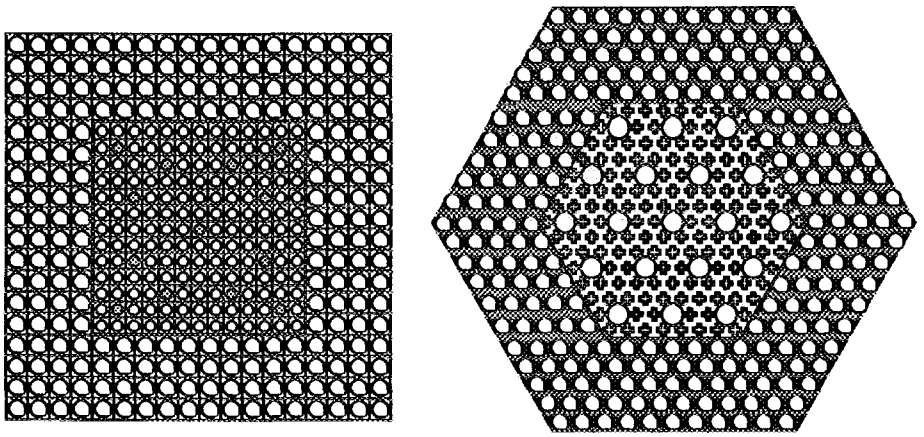

PWRT SBU Assembly VVERT SBU Assembly

Fig. 1 VVERT SBU Geometry

The fuel cycle cost savings of approximately 20% may be derived from the Table 1 data. The amount of natural U per cycle is about 140 Mt compared with 170 Mt of a standard PWR, and the number of fuel rods fabricated is 11,000 compared with 15,000 rods per PWR annual reload. The fabrication cost of a metal alloy fuel rod (RTR seed fuel), produced by an extrusion process, is significantly lower than that of a PWR oxide rod. These three components of the front-end, as well as back-end savings in spent fuel storage expenses, results in a 20 to 25% reduction in an overall fuel cycle cost. This estimate is supported by a detailed fuel cycle cost calculation.

The basis for the back-end of cycle analysis is the amount (weight) and composition of the fuel discharged from the core. This fuel is discharged, stored and finally, disposed of in a permanent storage facility. Its fissile content, mainly amount and composition of Pu defines the proliferation potential of the fuel cycle. The isotopic composition of the spent fuel stockpile defines its radioactivity and heat emission levels, as well as the overall toxicity of the spent fuel as a function of time.

The basis for the back-end of cycle analysis is the amount (weight) and composition of the fuel discharged from the core. This fuel is discharged, stored and finally, disposed of in a permanent storage facility. Its fissile content, mainly amount and composition of Pu defines the proliferation potential of the fuel cycle. The isotopic composition of the spent fuel stockpile defines its radioactivity and heat emission levels, as well as the overall toxicity of the spent fuel as a function of time.

Table 1: Fuel Cycle Data - Normalized to 1000 MWe Plant
(Comparison with "representative" PWR fuel cycle)

Fuel Cycle Transactions	PWR	RTR
Total Core Fuel Weight Mt H.M.	U = 80	U = 10 Th= 36
Average U Enrichment weight % U^{235}	3 - 4	20
Annual Fuel Reload Weight Mt H.M.	U = 27	U = 3.6 Th = 3.6*
Annual Natural U Requirement Mt H.M.	170	140
Annual Separative Work Requirement (enrichment) Mt S.W.U.	~160	~160
Annual Fuel Discharge Weight (Mt H.M.) : Volume (m^3) :	27 ~8	7.2* ~5
Annual Spent Fuel Storage/Disposal Cost**	$\$7x10^6$	$\$4x10^6$
Total Fuel Cycle Cost (arbitrary units)	1	0.75

Table 2: Discharged Fuel Fissile Content (Pu)
(fraction of total Pu)

Nuclide	PWR	RTR-Seed	RTR-Blanket	Weapon Grade[(1)]	super grade (Trinity)[(1)]
Pu-238	0.010	0.065	0.120	0.00012	-
Pu-239	0.590	0.465	0.382	0.938	0.98
Pu-240	0.210	0.225	0.150	0.058	0.02
Pu-241	0.140	0.155	0.147	0.0035	-
Pu-242	0.050	0.090	0.201	0.00022	-
Total Pu/year (kg)	~250	36.6	11.8[c]	-	-
Total H.M./year (kg)	26,000	3,206	4,450[c]	-	-

Proliferation potential of a fuel cycle, or its proliferation resistance is defined by the quantity and the quality of the fissile material, which could be diverted to military use. An additional factor is the measure of complexity required to separate the fissile component from the normal material flow of the fuel cycle.

The assessment of proliferation potential depends to a great extent on the specific proliferation scenario. The scenarios related to a civilian nuclear power fuel cycle are national diversion scenarios, either clandestine or open. In both cases international treaties and safeguards may not be effective, because they can be abrogated and avoided. It is clear that in order to separate completely the development and expansion of nuclear power from the danger of nuclear weapon proliferation, international safeguards are necessary but not sufficient.

A decisive barrier to proliferation should be based on inherent properties of the fuel cycle itself. The fuel design should provide assurance that the quantity and quality of the fissile component of the fuel cycle material flow would reduce the proliferation potential below an acceptable threshold in the context of industrial capabilities and economic realities.

The quantity and the quality of the fissile material contained in the RTR spent fuel stockpile is compared with that of a standard PWR cycle. The proliferation potential of a material is assessed qualitatively following a simple model of reference 1.

The fissile material weapon quality is evaluated by considering three properties:

1. The critical mass. A critical mass is different for different isotopic composition of Pu and U.
2. The weapon yield degradation due to pre-initiation caused by spontaneous fission neutrons.
3. The weapon stability derated by heat emission.

The spontaneous fission source (SFS) defines an important characteristic of the weapon material, namely the yield degradation. Neutrons released by spontaneous fissions cause pre-initiation, i.e. the start of the explosion before the device reached its highest supercriticality value, which in turn causes a reduction of the device yield. A simple qualitative model described in reference 1 is used to estimate the yield degradation of the explosion device based on RTR Pu and to compare it with PWR grade Pu and weapon grade Pu.

The smallest value of the explosion yield results from pre-initiation, which occurs at the same moment when a device becomes critical. This, smallest yield, designated as "fizzle" yield, is estimated as 0.027 of the nominal yield.

A qualitative information published in an open literature with regard to expected performance of the Trinity explosion device (1) allows an estimate of the probabilities of the nominal yield and the fizzle yield. The relevant data for all considered Pu compositions is summarized in Tables 2 and 3. The first column shows a spontaneous fission source for one gram of a given isotope. The rest of the table shows the SFS in neutrons/sec for a critical mass of all considered Pu compositions. The last row presents the value of N, i.e ratio of a SFS for a given Pu composition to that of a weapon grade Pu, assumed for a Trinity device.

The total spontaneous fission source for a critical mass of PWR grade Pu is 7 times larger than that of a weapon grade Pu, and for the RTR seed and blanket Pu is 13 and 22 times larger respectively. The nominal and fizzle yields are estimated for each of the considered Pu compositions and are presented in Table 4.

The probability that an explosion device, constructed from the RTR Pu, will deliver a nominal yield is small (seed) to negligible (blanket), and a probability of a fizzle yield is relatively high. Thus, it is shown, that the RTR Pu will produce an unreliable weapon.

An additional barrier for a possible diversion of a reactor grade material is the heat emitted by its isotopes. The thermal power produces an increase of the temperature of a device and causes

two effects: one is a temperature increase of metallic Pu, which undergoes a metallurgical phase transition at 115°C, and second is an overheating of a high explosive around the Pu core, which may cause the disintegration of this high explosive. The specific heat produced by different Pu isotopes is summarized in Table 5 and is used to estimate the total heat produced by a Pu metal critical mass in each case.

Table 3: Spontaneous Fission Rate for Pu Isotopes

nuclide	spontaneous fission rate $(gm\text{-}sec)^{-1}$	spontaneous fission source $(kg\text{-}sec)^{-1}$				
		super grade (Trinity)	weapon grade	PWR grade	RTR- Seed grade	RTR - Blanket grade
Pu-238	2,600.0	0	312	$26x10^3$	$169x10^3$	$312x10^3$
Pu-239	0.022	0.022	21	13	10	8
Pu-240	910.0	18,200	52,780	$191.1x10^3$	204,750	$136x10^3$
Pu-241	0.049	0	0.2	7	8	7
Pu-242	1,700.0	0	374	$85x10^3$	$153x10^3$	$342x10^3$
total/kg of Pu	-	18,200	53,487	$302x10^3$	$526x10^3$	$790x10^3$
total/critical mass	-	$78.3x10^3$	$230x10^3$	$1,661x10^3$	$3,103x10^3$	$5,135x10^3$
ratio to super grade	-	1	3	21	40	66

Table 4: Probability of an Indicated Yields

Yield	super grade (Trinity)	weapon grade Pu	PWR grade Pu	RTR - seed grade Pu	RTR - blanket grad Pu
Nominal	0.88	0.68	0.07	0.006	0.0002
Fizzle	0.02	0.06	0.35	0.55	0.74

Table 5: Decay Heat Emission for Different Pu Compositions

nuclide	Specific decay heat (watts/kg)	weapon grade (watts/kg Pu)	PWR grade (watts/kg Pu)	RTR seed grade (watts/kg Pu)	RTR blanket grade (watts/kg Pu)
Pu-238	560	0	12.88	38.64	70.56
Pu-239	1.9	1.77	1.08	0.85	0.65
Pu-240	6.8	0.42	1.54	1.58	0.89
Pu-241	4.2	0.03	0.54	0.60	0.54
Pu-242	0.1	0	0	0.01	0.03
total (watts/kg)	-	2.22	16.04	41.68	72.66
total (watts/critical mass)	-	10	88	244	475

It is shown that the total heat produced by the RTR seed and blanket Pu is much higher than that produced by the PWR grade Pu. Heat loads at the level of seed and blanket Pu are likely to require special heat removal measures to be incorporated in the design of a weapon. The nature and effectiveness of such measures is beyond the scope of this paper, but it is reasonable to assume that the device stability will be impaired.

The RTR generated spent fuel stockpile will still require a safeguarded disposal facility, but taking into account the reduced quantity and quality of the fissile material, the combination of safeguards and inherent fuel cycle parameters can provide an adequate answer to the problem of weapon proliferation potential of nuclear power.

References

1. J. C. Mark, "Explosive Properties of Reactor-Grade Plutonium", Science & Global Security, 4, 111, 1993.

Improvements in PWR Automatic Optimized Reloading Methods Using Genetic Algorithms

S. H. Levine, K. Ivanov, and M. Feltus
The Pennsylvania State University
University Park, PA 16802

The objective of using automatic optimized reloading methods is to provide the Nuclear Engineer with an efficient method for reloading a nuclear reactor which results in superior core configurations that minimize fuel costs. Previous methods developed by Levine et al required a large effort to develop the initial core loading using a priority loading scheme. Subsequent modifications to this core configuration were made using expert rules to produce the final core design. Improvements in this technique have been made by using a genetic algorithm to produce improved core reload designs for PWRs more efficiently.

Introduction

An ultimate in-core fuel management code for PWRs was proposed[1] which should minimize fuel costs, perform multicycle analysis, be very user friendly, use accurate high speed neutronic codes, and print out concise but appropriate output. Further improvement has been made in minimizing the fuel costs by utilizing a newly developed genetic algorithm[2] to finalize the fuel placement in the core. Basically six tasks are employed to optimize the reload, i.e., 1) develop the priority loading scheme (PLS), 2) determine the number of fresh fuel and the used fuel to reload the core and load the core with these fuel assemblies according to the PLS, 3) determine the enrichment for the fresh fuel to give the assigned energy for the cycle by using the Haling power distribution (HPD), 4) finalize the loading pattern by making appropriate changes and analyzing each change using the HPD so that the peak power constraints have adequate safety margins, 5) design the BP placement to minimize power peaking, and 6) fine tune the final core design to meet all objectives in an optimum manner.

The PLS required major efforts to effect[3],[4]. All of these PLSs produced low leakage cores having the lowest k_{inf} fuel assemblies loaded on the core periphery, the highest k_{inf} placed just inside the core periphery, and the remaining fuel assemblies scatter loaded in the remaining positions. The PLS is a hierarchical scheme for loading the fuel into the core based on the k_{inf} of the fuel. It defines specific positions for each fuel assembly. Once the core is loaded as prescribed by the PLS, the enrichment and possibly the number of fresh fuel must be adjusted to meet core lifetime requirements. In addition, the core configuration must be changed to reduce the peak power to meet safety constraints. All of these operations can be performed using the HPD eliminating the need for using burnable poisons (BP).

Turinsky et al[5] have stated that the HPD cannot be used because practical designs cannot meet the safety constraints. This is true if the peak power in the HPD is at the peak power limit. If the HPD peak power is 4% to 5% below the limit, practical BP designs can be effected to keep the peak power well within allowed values even though it exceeds the peak power attained in the HPD calculation.

The above procedure is improved by incorporating a genetic algorithm (GA) to perform task (4) using the HPD analysis. A GA utilizes the methods of evolution to search for superior solutions. A bit-string representation of the core loading pattern, called a genotype, is the basic genetic component for a GA. It acts as the DNA for humans. The first step is to create a population of genotypes representing many different solutions. The GA then performs crossover and mutation type changes in the genotypes to develop improved solutions. The technique for making crossover and mutations is a statistical process which selects the improved genotypes based on an objective function. Thousands of calculations are performed to obtain the improved genotypes for creating the next population. Special methods are used for selecting the genotypes for crossover and mutation operations and for creating the different populations.

DeChaine calculated improved core designs for the Beaver Valley PWRs using Li's PLS in providing some of the genotypes for the population. DeChaine's calculations were all HPD solutions; BP's were not designed for the core. Nevertheless his GA found many core loadings that were slightly superior to Li's and one that was impressive. For example, Li's best solution had a lifetime of 16.49 GWD/ MTU whereas DeChaine's was 16.984 GWD/MTU. The GA can also be used to design the BP solution. Also, different PLS's can be developed using heuristic rules to create genotypes for the population, avoiding the large effort normally needed to produce a PLS for a new core.

Core Calculations Using a Genetic Algorithm (GA)

DeChaine created a genotype which is a sequential set of binary bits, each representing both a loading position of the core and a specific k_{inf} of a fuel assembly, and used a fixed inventory of fuel assemblies to load the core. DeChaine then used the fuel assemblies that were in Li's best design and had the GA search for superior configurations. The two most difficult of the six tasks are task (1) and task (4). DeChaine showed that the GA can help define the PLS ,task (1) from the results of the GA calculations. In addition the objective function sorted out the superior reload designs effecting task (4).

The first step in the GA is to create a population. Some degree of randomness is incorporated using a random generator to generate the bits, but some of the population is spiked with special core designs. It is easy to convert a loading pattern (phenotype) into

a genotype. The available fuel types are first ranked in order of their k_{inf}. Then at each core position its k_{inf} is assigned that rank and its corresponding bit. The genotype is the array of bits representing that loading pattern. Converting a genotype into a loading pattern is more difficult, because a match must be made between the available inventory and the set of bits in the genotype. This problem is solved by selecting the appropriate fuel assembly for each core position based on core symmetry and the rank of the bit; the lower the bit number the higher the k_{inf}.

The next step is to evaluate the population using reactor physics codes and a "fitness" or objective function. For a core pattern to be valid, its Normalized Power (NP) must be sufficiently low to prevent the peak power from exceeding thermal limits, and it should meet or exceed core lifetime, L, requirements. The objective function, O(NP,L),greatly penalizes phenotypes that have NPs above a maximum value and it increases with core lifetime.

$$O(NP,L) = w_{NP} \times P(NP) + w_L \times L$$

where

$$P(NP) = NP - NP_{max} \quad \text{when } NP > NP_{max}$$
$$P(NP) = 0 \quad \text{when } NP < NP_{max}$$

Once the NP is = or < than NP_{max}, The objective function depends only on L.

A selection operator then chooses which genotypes will contribute to the next generation. It creates the "breeding pool" for the crossover and mutation operators to work with based on their "fitness". In this way the GA creates new generations with increase "fitness",i.e. improved core patterns. However, each new generation remains constant in population.

The crossover operator mixes two genotypes to create two different genotypes referred to as their children. It does this by swapping bits at the same location in the genotype. The mutation operator changes the state of a bit by flipping the bit. It only changes a selected number of bits randomly chosen. The mutation operator diversifies the population allowing the search to move into new regions not yet examined. The GA continues to create and evaluate new core loadings until the number of analyses has been completed. Superior reloads are easily identified.

DeChaine created expert populations for the Beaver Valley PWRs using solutions obtained from Li's PLS plus random selected loading patterns. A sample of his results are shown in the figure at the top of the next page. What is significant about his results is that he has identified many core configurations superior to Li's best design. DeChaine's best design had a lifetime of 16.984 compared to Li's best design of 16.492. Also of importance is the fact that by studying past PLSs for different core it is possible to establish several good PLSs for any new core heuristically. The central core

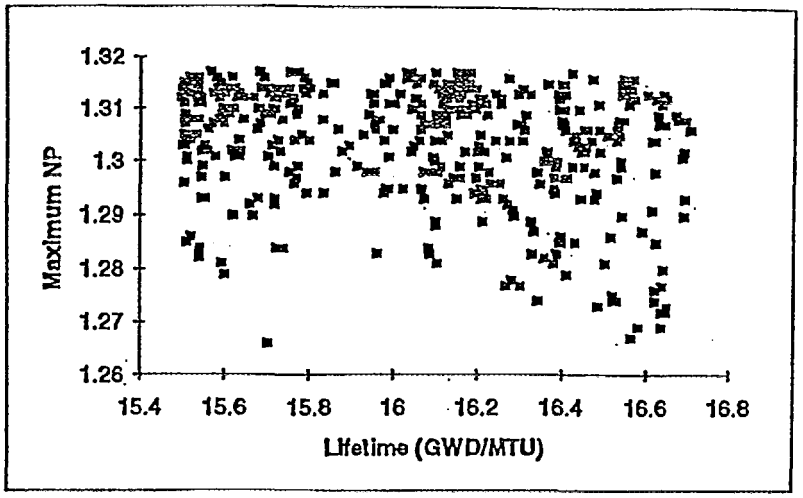

Core lifetimes and maximum NPs for the 466 unique loading patterns.

fuel assembly is basically fixed. The core periphery uses low k_{inf} fuel and the most of the positions adjacent to the core periphery use the fresh fuel which are easily identified. The remaining core positions are scatter loaded. Using these guidlines, it is possible to create several excellent solutions. It is important to spike the initial population for the GA with such superior solutions. In addition, by studying the superior loading patterns produced by the GA, the PLS can be improved. Also the improved PLSs can be used for future reloads.

Hence, all of the six tasks can now be made to work sequentially and automatically to produce optimum type reloads. The GA is used to solve both tasks 1 and 4, the two most difficult tasks. It could also solve task 5; however, it is believed that the present heuristic method will perform this task more efficiently.

Conclusions

It is now believed that using the GA provides a most efficient method for producing extremely good reload patterns automatically. This technique lays a foundation for developing efficient multicycle codes. Here it is suggested that the multicycle code allow for changes in cycle length and different constraints for the different cycles. Such conditions are usually dictated by the utility.

References

1. S.H. Levine, D. Bai, and Z. Li, INS Int. Meeting, Tel Aviv, (1993)
2. M. DeChaine, PhD Thesis, The Pennsylvania State University, (1996)
3. H.Y. Huang, S.H. Levine, Trans. Am. Nucl. Soc., **30**: 339 (1978)

4. Z. Li, S. H. Levine, Nucl. Sci. Eng., **118**: 67 (1994)

5. D.E. Kroparzek, P. J. Turinsky, Nucl. Tech., **95**: 9 (1991)

Whole Core Burnup Calculations Using "MCNP"

Haran O., Shaham Y. Nuclear Research Center - Negev

Purpose of this work: Core parameters such as the reactivity, the power distribution and different reactivity coefficients calculated in simulations play an important role in the nuclear reactor handling. Operational safety margins are decided upon, based on the calculated parameters. Thus, the ability to accurately calculate those parameters is of uppermost importance. Such ability exists for fresh cores, using the Monte-Carlo method. The change in the core parameters that results from the core burnup is nowadays calculated within transport codes that simplifies the transport process by using approximations such as the diffusion approximation. The inaccuracy in the burned core parameters arising from the use of such approximations is hard to quantify, leading to an increased gap between the operational routines and the safety limits. A Monte Carlo transport code that caries out accurate static calculations in three dimensional geometries using continuous-energy neutron cross-section data such as the *MCNP*[1] can be used to generate accurate reaction rates for burnup purposes. Monte Carlo method is statistical by nature, so that the reaction rates calculated will be accurate only to a certain known extent. The purpose of this work was to create a burnup routine that uses the capabilities of the Monte Carlo based MCNP code. It should be noted that burnup using Monte Carlo has been reported in the literature[2], but this work is the result of an independent effort.

Method: We developed a routine that is exterior to the MCNP, meaning that no changes in the MCNP were made. The burnup routine (denoted by "BURNCORE") is very flexible, allowing the user to change the burnup via a user supplied *Burnup Input File* which contains general information concerning the burnup.
The BURNCORE Algorithm (fig. 1) is as follows:
a. Prior to activating BURNCORE the user has to create two input files - a regular MCNP input describing the core geometry and composition and a *Burnup Input File* containing information such as the power, the lengths of the time steps, the nuclide burnup chains and fuel shuffling instructions.
b. The first program reads information from both input files. From reading and analyzing the mixture section in the MCNP's input file, the program determines which mixtures should undergo burnup. Those mixtures are modified to include infinitesimal amounts of all non-existing isotopes that are connected by burnup chains to existing ones. Then, the program pairs the mixtures and the cells, thus discovering in which cells reaction rates should be asked for. The MCNP input is rewritten so that its output will include reactions rates in all burnup-prone cells and for all isotopes that shall undergo burnup
c. The MCNP code is invoked, calculating the core reactivity and the relevant reaction-rates.
d. The second program reads the MCNP's output and the burnup information imbedded in the *Burnup Input File*, and solves numerically the burnup equations describing the change in the burnup isotopes concentration. Consequently, it creates an input describing the core at the end of the time step.
e. Before continuing to the next burnup step, a third program checks the *Burnup Input File* for instructions concerning fresh fuel loading & exchange among the various fuel elements.

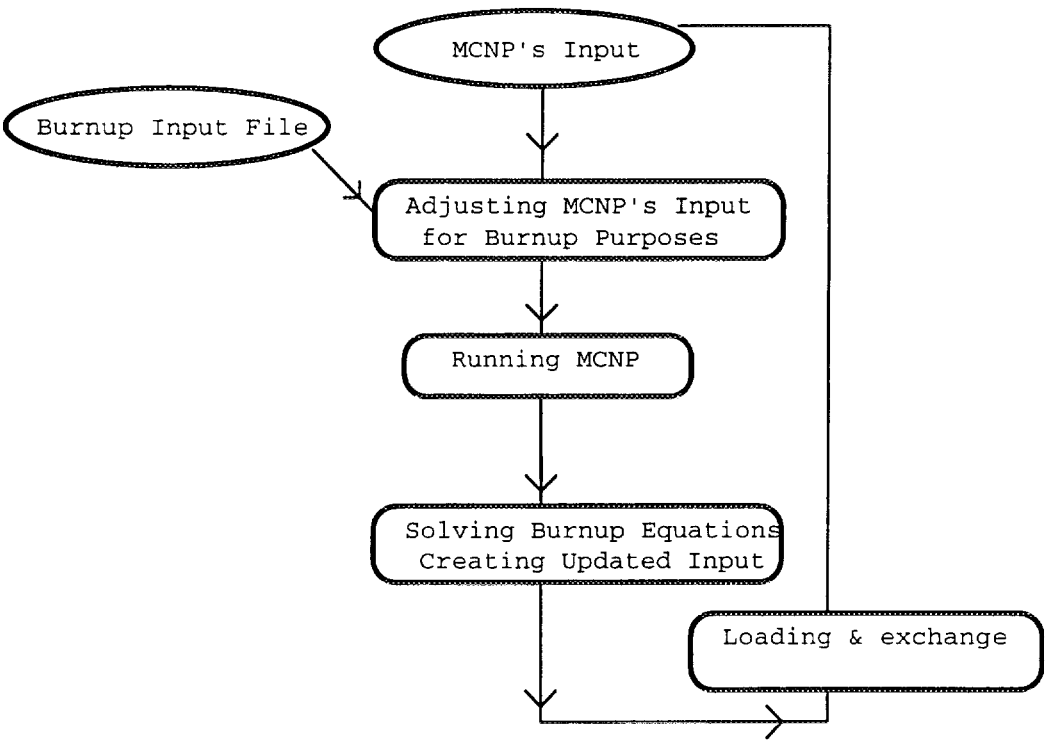

figure 1 - The BURNCORE Algorithm

Results: The validation of BURNCORE was investigated by comparison with burnup calculations carried out in the multigroup S_n code WIMS[3]. The compared parameters included the multiplication factor and the concentration of various important isotopes. Fig. 2 shows the multiplication factor (*K-Infinity*) evolution in an typical BWR[4] lattice cell as calculated by BURNCORE and WIMS. There is good agreement between the two calculations even though the MCNP and WIMS use different cross-section libraries.

The influence of the statistical nature of the MCNP on the depletion rates of the different isotopes, and the later's influence on global parameters such as the multiplication factor was examined. The calculations performed showed that the mistakes arising from the statistical inaccuracy tend to slightly 'fix' themselves, since a faster depletion in one step would lead to less material left and thus to slower depletion in the next step. In fig. 3 the influence of the statistics on the multiplication factor evolution is demonstrated. The graph includes accurate (1/3% statistical error in reaction rates) and inaccurate (1% statistical error) BURNCORE burnup results.

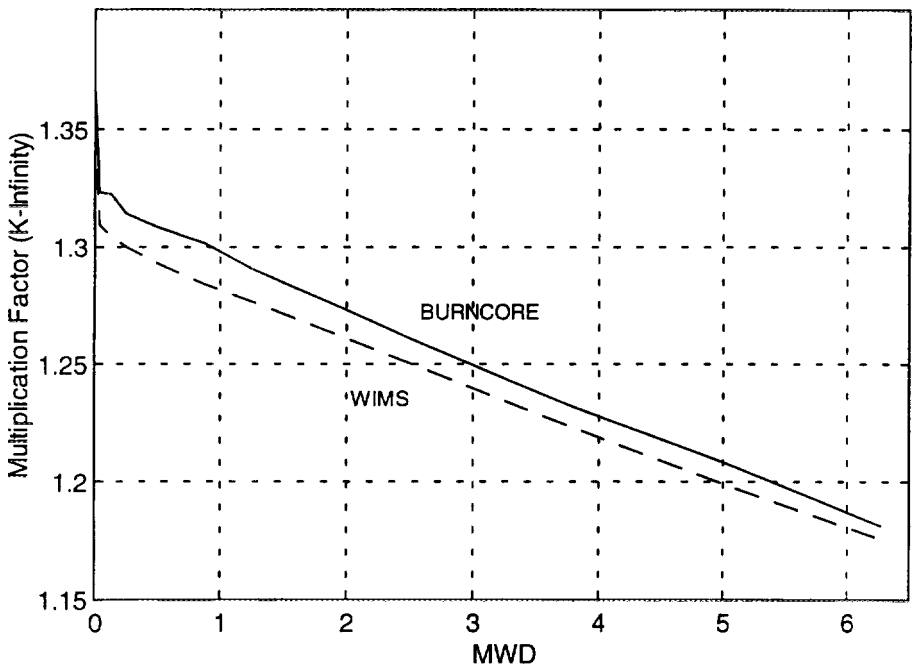

figure 2 - The multiplication factor evolution in an typical BWR lattice cell as calculated by BURNCORE (solid line) and WIMS (dashed line)

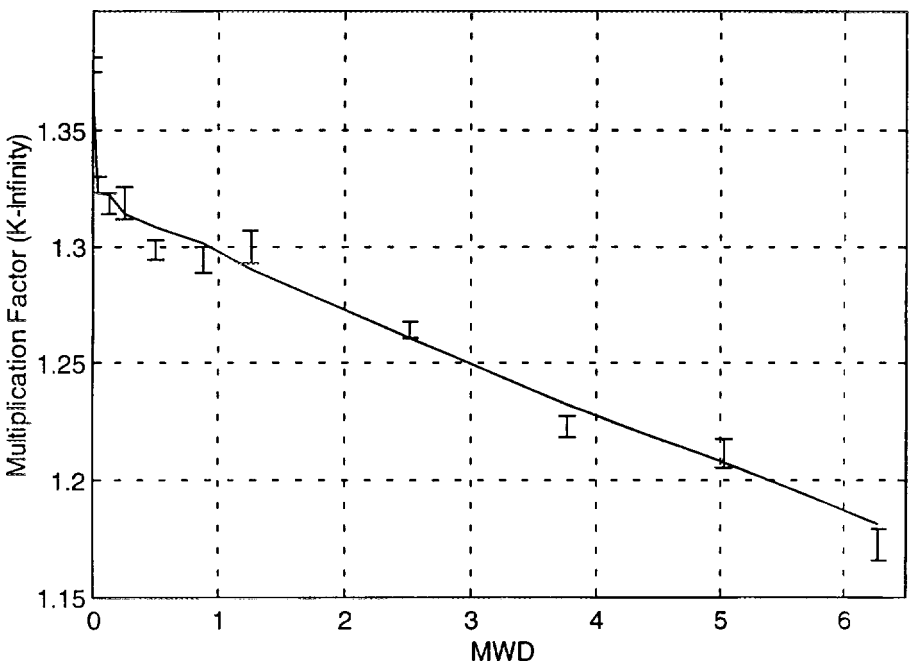

figure 3 - The multiplication factor evolution in a typical BWR lattice cell as calculated by BURNCORE accurately (lines, 1/3% statistical error in the reaction rates, error bars not shown) and inaccurately (error bars, 1% statistical error).

Conclusions: The use of the MCNP code for burnup purposes was validated. The major and only drawback of a burnup routine based on this code is the time required to achieve statistical precision in each of the static MCNP's calculations. Thus, we conclude that such a routine should be used as a checking tool to the results achieved from fast yet approximate burnup programs.

---

[1] J. Briestmeister, "*MCNP-A General Monte Carlo Code N-Particle Transport Code Version 4A*", LA-12625-M, Nov. 1993

[2] Abdul-Hamid S. A., Klein A. C., "*Monte Carlo burnup analysis code development and application to an incore thermionic space nuclear power system*", Anon.-29th intersociety energy conversion engineering conference: Technical papers. Part 1. Washington DC. American Inst. of Aerodynamics and Astronautics. 1994. 628 p. 457-462

[3] C. J. Taubman, J. H. Lawrence, "*WIMSD4 - Version 100 and Cataloged Procedure*", AEEW-M-1832, Feb. 1981

[4] V. Jagannathan, P. D. Krishnani, H.C. Gupta, "*Analysis of Benchmark on Interactive Effects of Gadolinium Pins in BWRs*", Proceedings of a Specialists Meeting held in Cadarache, France, 10-14 September 1990 and a Technical Committee Meeting and Workshop held in Rez, Czechoslovakia, 7-11 October 1991

High–Temperature Thermal–Chemical Analysis of Nuclear Fuel Channels

Y. Nekhamkin, V. Rosenband, D. Hasan, E. Elias, E. Wacholder and A. Gany
Technion – Israel Institute of Technology
Haifa, Israel 32000

1 Introduction

In a severe accident situation, e.g., a postulated loss of coolant accident with a coincident loss of emergency core cooling (LOCA/LOECC), the core may become partially uncovered and steam may become the only coolant available. The thermodynamic conditions in the core, in this case, depend on ability of the steam to effectively remove the fuel decay heat and the heat generated by the exothermic steam/Zircaloy reaction (Nekhamkin et al., 1994). Therefore, it is important to understand the high–temperature behavior of an oxidizing fuel channel.

The main objective of this work is to develop a methodology for calculating the clad temperature and rate of oxidation of a partially covered fuel pin. A criterion is derived to define the importance of the chemical reaction in the overall heat balance. The main parameters affecting the fuel thermal behavior are outlined.

2 Analysis

We consider a fuel channel consisting of a single fuel pin as shown in Fig. 1. The channel length is L and it is partially covered by water up to height $l = \mu L$. The fuel pellet radius is r_0 and the outer radius of the rod is R_0. The fuel is assumed to generate heat at a linear rate of:

$$q' = q'_0 \sin \frac{\pi x}{L} \tag{1}$$

Since the heat transfer coefficient in the wet zone is typically high, quasi steady–state conditions may be assumed there in which the decay heat is effectively removed by convection and boiling. A heat balance over the wet zone ($0 \leq x \leq \mu L$) yields:

$$\dot{m}_0 \left[C_f(T_s - T_0) + r\right] = q'_0 \int_0^{\mu L} \sin \frac{\pi x}{L} dx = \frac{q'_0 L}{\pi} \left[1 - \cos(\pi\mu)\right] \tag{2}$$

where $\dot{m}_0$ is the water inlet mass flow rate (equal to the rate of steam production), C_f is the water specific heat, r is the latent heat of vaporization and T_0 and T_s are the inlet and saturation temperatures of the water.

In the dry zone ($\mu L \leq x \leq L$) the clad is heated by the decay heat generated in the fuel and by the steam/metal reaction at the outer surface. Assuming a uniform clad temperature T_c in the dry zone, the heat balance is:

$$q_0' \int_{\mu L}^{L} \sin \frac{\pi x}{L} dx + Q' L(1-\mu) - \alpha_{cv} A_c (1-\mu) \Delta T_m =$$
$$= \rho_{Zr} C_{Zr} L(1-\mu)\pi(R_0^2 - r_0^2)\frac{dT_c}{dt} \tag{3}$$

Here α_{cv} is the convective heat transfer coefficient, and A_c is the total rods' surface area. C_{Zr} and ρ_{Zr} are the Zr specific heat and density. ΔT_m is the logarithmic mean temperature difference between the steam and cladding:

$$\Delta T_m = \frac{T_v - T_s}{\ln \frac{T_c - T_s}{T_c - T_v}} \tag{4}$$

where T_v is the steam outlet temperature.

Q' is the linear power generated by the steam/metal reaction:

$$Q' = Q_0 \rho_{Zr} 2\pi (R_0 - \delta)\frac{d\delta}{dt} \tag{5}$$

where δ is the thickness of the oxide layer, and Q_0 is the power generated by the steam/metal reaction per unit mass of Zr.

The chemical reaction between Zircaloy and steam is governed by the following equation of the oxide film kinetics:

$$\frac{d\delta}{dt} = \frac{k_r}{\delta} \exp\left(-\frac{B}{T_c}\right) \tag{6}$$

where k_r is the reaction constant (3.968×10^{-5} m^2/s) and $B = 22900$K.

A heat balance over the steam in the dry zone yields:

$$\dot{m}_0 C_s (T_v - T_s) = \alpha_{cv} A_c (1-\mu)\Delta T_m \tag{7}$$

where C_s is the steam specific heat. Equation (7) is solved as:

$$T_v = T_c - (T_c - T_s)e^{-\phi} \tag{8}$$

where ϕ is defined by:

$$\phi = \frac{\alpha_{cv} A_c (1-\mu)}{m_0 C_s} \tag{9}$$

Substituting $\dot{m}_0$ from eq. (2) and eqs. (5) - (8) into (3) yields for the dry zone:

$$\rho_{Z_r} C_{Z_r} L(1-\mu)\pi(R_0^2 - r_0^2)\frac{dT_c}{dt} = \frac{q_0' L\,[1+\cos(\pi\mu)]}{\pi} +$$

$$+ \quad Q_0 \frac{\rho_{Z_r} k_r R_0}{\delta} 2\pi L(1-\mu)\exp -\frac{B}{T_c} - \frac{q_0' L\,[1-\cos(\pi\mu)]\,C_s(T_c - T_s)(1-e^{-\phi})}{\pi\,[C_f(T_s - T_0) + r]} \tag{10}$$

Equations (6) and (10) constitute a complete system of differential equations which may be solved for δ and T_c. The initial conditions at $t = 0$ are: $\delta = \delta_0$ and $T_c = T_c(0)$. The equations can be non–dimensionalized by defining the following dimensionless parameters.

$$\beta = \frac{T_s}{B}\ , \quad \theta = \frac{T_c - T^*}{\beta T^*}\ , \quad \eta = \frac{\delta}{\delta^*}\ , \quad \tau = \frac{t}{t^*} \tag{11}$$

where the characteristic temperature T^* is defined as

$$T^* = T_s + \frac{[C_f(T_s - T_0) + r]\,[1+\cos(\pi\mu)]}{C_s(1-e^{-\phi})\,[1-\cos(\pi\mu)]}, \tag{12}$$

the characteristic oxide thickness δ^* is defined as

$$\delta^* = \frac{\beta T^* C_{Z_r}(R_0^2 - r_0^2)}{2Q_0 R_0} \tag{13}$$

and the characteristic time t^* is defined as

$$t^* = \left\{\frac{T^*\beta C_{Z_r}(R_0^2 - r_0^2)}{2Q_0 R_0}\right\}^2 \frac{\exp(1/\beta)}{k_r} \tag{14}$$

Using eqs. (11), (12), (13) and (14) the governing equations become:

$$\frac{d\theta}{d\tau} = \frac{\exp\left(\frac{\theta}{1+\beta\theta}\right)}{\eta} - \frac{\theta}{\omega} \tag{15}$$

and

$$\frac{d\eta}{d\tau} = \frac{\exp\left(\frac{\theta}{1+\beta\theta}\right)}{\eta} \tag{16}$$

where the following dimensionless group ω is defined:

$$\omega = \frac{\pi^2\,[C_f(T_s - T_0) + r]\,C_{Z_r}(1-\mu)\,[R_0^2 - r_0^2]\,\rho_{Z_r}}{q_0'\,[1-\cos(\pi\mu)]\,C_s(1-e^{-\phi})t^*} \tag{17}$$

Equations (15) and (16) were integrated numerically for a wide range of parameters covering the rage of conditions expected during a postulated LOCA/LOECC.

3 Results and Discussion

Figure 2 shows the cladding temperature for 2 different water levels, μ. The following typical data were used in the computations to define the cooling and heating rates: α_{cv}=100 W/m^2-K; $q_0^{'}$=318 W/m. It is shown that when the water level is low (μ=0.5) the steam generation rate is reduced and the clad temperature rises rapidly. The temperature reaches a critical value of about 2000K (melting) within 50s. At that level the temperature increases almost exponentially. At a higher water level (μ=0.8) the rate of heating is much slower, and no ignition temperature in this case is reached.

Figure 3 shows the oxide layer thickness for the same values of μ. For μ=0.5 the oxidation rate increases rapidly when the temperature reaches its critical value at less than 50s. Similarly, for μ=0.8 no critical conditions are reached.

The time at which oxidation becomes significant depends on many parameters, such as water level, μ, the rate of decay heat generation and the rate of heat transfer to the steam/water mixture in the dry zone. Following Khaikin et al. (1970) a complete oxidation or melting of the cladding will eventually take place if the following criterion is satisfied:

$$\omega > 2.45 \tag{18}$$

Otherwise, the clad temperature may never reach sufficiently high values to induce significant oxidation.

4 Conclusions

A combined process of nuclear heat generation and chemical reaction was considered. A set of differential equations was derived for predicting the cladding temperature and the rate of oxidation along a partially covered fuel pin. The importance of the oxidation process at elevated temperatures was demonstrated.

5 References

Khaikin, B. I., Bloshenko, V. N. and Merzhanov, A. G. 1970 On the ignition of metal particles, *Combustion, Explosion, and Shock Waves* **6**, 412.

Nekhamkin, Y., Hasan, D., Wacholder, E. and Elias, E. 1994 AP600 Post Blowdown Containment Transients, *Trans. Israel Nucl. Soc.* **18**, III-8.

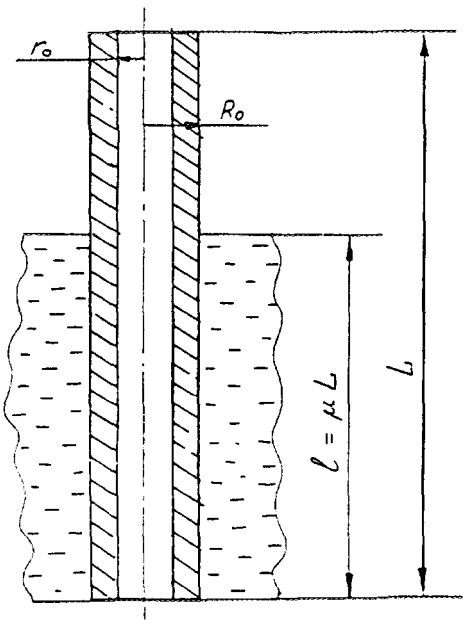

Figure 1: Schematics of a fuel channel

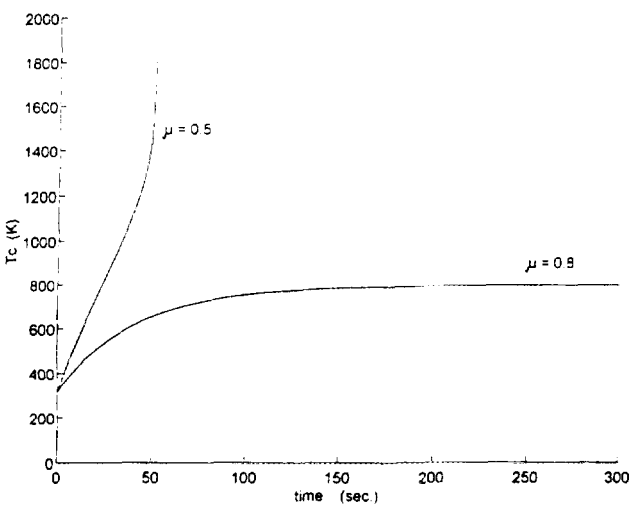

Figure 2: Cladding temperature vs. time for two water levels

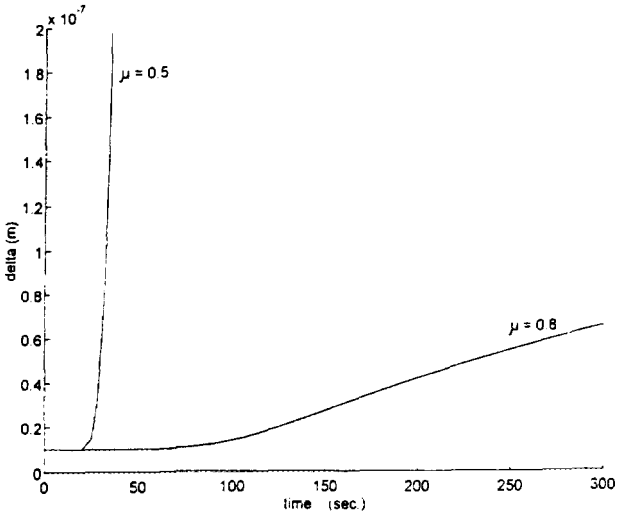

Figure 3: Oxide layer thickness vs. time for two water levels

Monitoring and Radiation Dose Estimation for Internal Contamination of Occupational Workers

R. Kol and Y.Laichter, Nuclear Research Center - Negev. P.o. Box 9001, Beer-Sheva.

The assessment of internal radiation doses due to intake of radionuclides differs totally from external dosimetry.
External dosimetry is relatively straight forward: Workers are equipped with appropriate dosimeters that give the dose upon direct reading.
Internal dosimetry is actually an assessment of the dose based on results of personnel and environmental monitoring.

Individual monitoring is achieved by direct measurements of body activity, excreta monitoring in-vitro and personal air samplers.
Monitoring of the working place is done by air samplers.

To complete internal dose evaluation additional data is required , such as:

- The radionuclide involved.
- The route of intake . (inhalation, ingestion atc..)
- Chemical / Physical characteristic of the contaminant.
- Type of intake .(Chronic or acute)
- The approximate time of intake for the acute intake or the period for chronic intake.

Data for every incident are being analyzed according to excretion / retention functions, for assessing the amount of activity taken up by the worker. The intake is than converted to internal dose.

Examples of dose calculations for acute intake by inhalation are given for ^{3}H and ^{125}I .
The theoretical curve graph for the excretion of tritiated water in urine is given in fig. 1.
The theoretical graphs for the retention of ^{125}I in the thyroid and the daily urine excretion are given in fig. 2 and 3 , respectively. The theoretical curves are according to ICRP-54.

All calculations are based on ICRP - 30 (1979) recommendations and are done with a computer code named CINDY. (Code for Internal Dosimetry software).

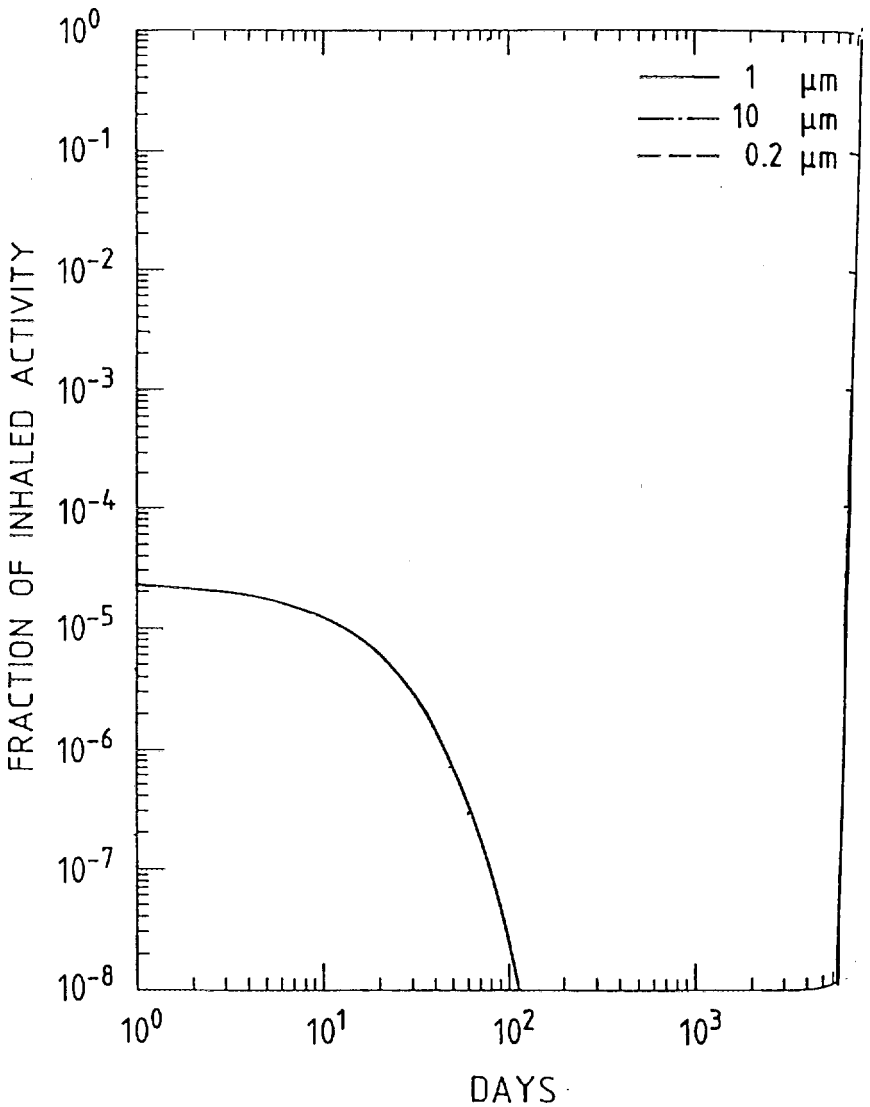

Fig. 1 : Tritiated water: Urinary concenrtation per ml., acute intake

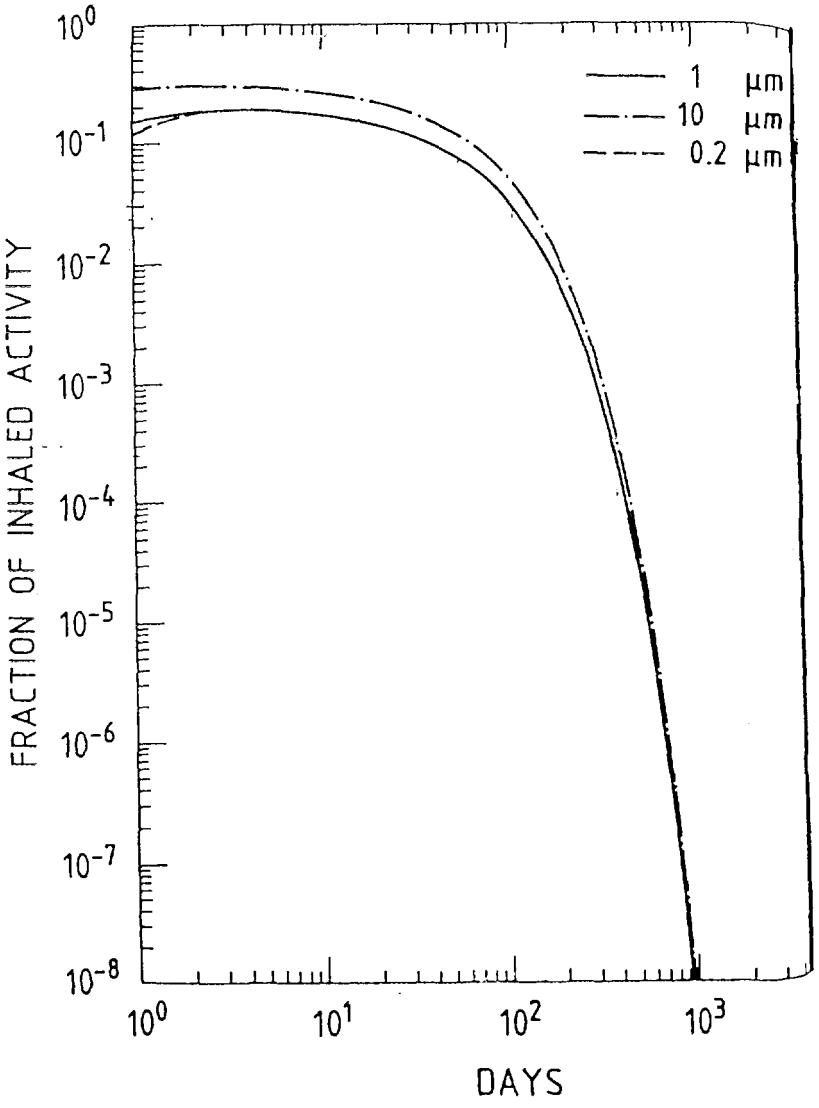

Fig. 2 : ^{125}I Class D : Retention in the thyroid after inhalation, acute intake

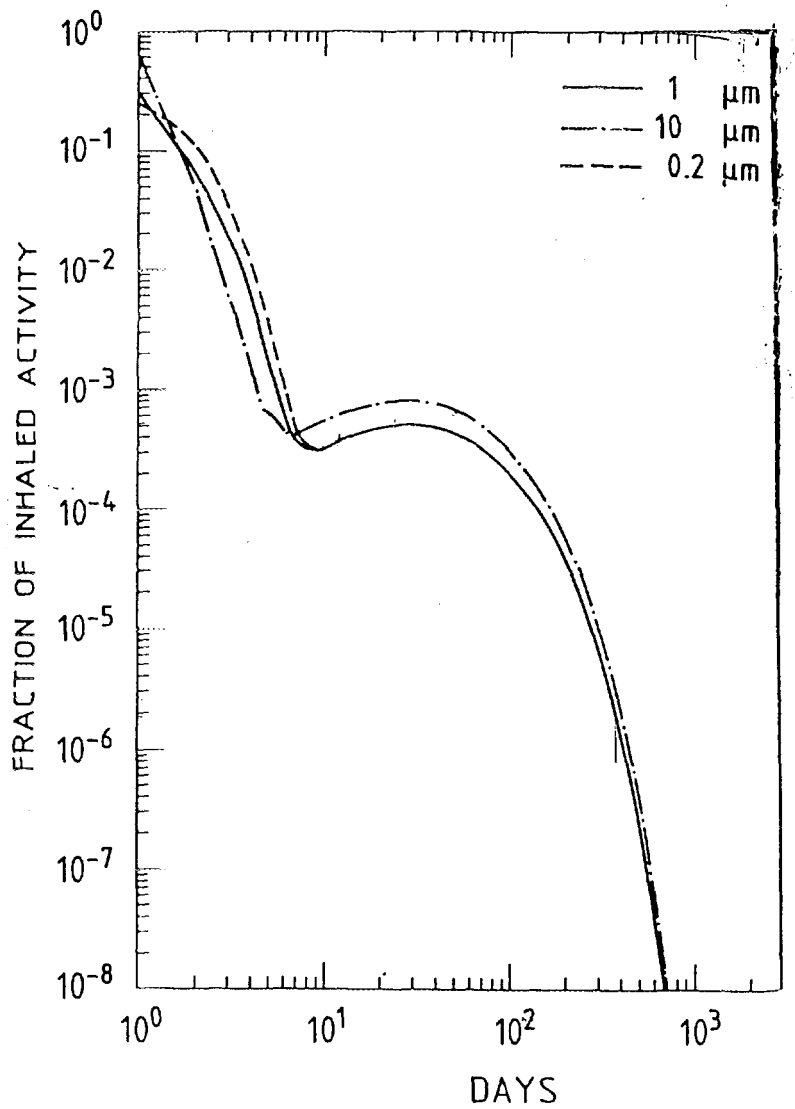

Fig. 3 : ^{125}I class D: Daily urinary excretion after inhalation, acute intake

ACUTE INTERNAL EXPOSURE TO IODINE-125: A CASE STUDY.

KOL R., CANFI A. N. DUKHAN., PELLED O., BRIKNER D., LAICHTER Y. AND GOLD B., NUCLEAR RESEARCH CENTER - NEGEV, POB 9001 BEER-SHEVA 84190 ISRAEL

Radioiodines I-125 and I-131 are extremely volatile even in the form of the relatively stable Iodine anion. This property renders frequent airborne contamination and sometimes accidental inhalation of the radioiodine by personnel heavily involved with it's handling.
In order to detect radioiodine contamination as early as possible, the laboratory and its surroundings are constantly air monitored, surfaces are monitored according to a predetermined regime and personnel is being checked upon completion of a job or upon leaving the laboratory.
Follow-up, routine or in special occasions, is performed by health-physics personnel who reports to the radiation medicine department.
We report here the measures and means used to monitor a case of an accidental inhalation of I-125 due to an externally contaminated NaI[I-125] commercial package.
The monitoring of the contamination is described, the dose to the thyroid and the Committed Effective Dose Equivalent (CEDE) are reported, and the medical evaluation is presented.

Methods: The contamination was found using a hand held detector (thin NaI(Tl) crystal) with Minimum Detectable Activity (MDA) of 2.7 Bq for one minute count. This detector was used for on-site semi-quantitative thyroid monitoring during the follow-up period. Measurements were taken once a week with the detector placed always in the same position - on the front of the neck touching the skin with no pressure.
Accurate quantitative measurements were performed using a Phoswich Detector calibrated with a Phantom and placed in a shielded room. The detector was calibrated daily and the background was constantly monitored.
Thyroid measurements were taken several times a week, during a period of three weeks after the exposure, than once a week and than monthly for almost one year.
During the first two weeks, 5 urine analyses were performed. For each analysis, urine was collected for 24 hours, 50 ml were than analyzed using x-ray spectrometry with a thin NaI(Tl) detector.
Skin contamination was ruled out thorough washing with warm water and soap and smear tests.

Constant reports of the laboratory tests were given to the Radiation Medicine physicians, for real time evaluation of medical status.
Internal exposure was calculated according to the ICRP 30 recommendations using CINDY® software.

Results: Fig. 1 shows the dose of I-125 in the thyroid as detected by the Phoswich detector .The curve coincides with the expected decay for I-125 in the thyroid. The semi-quantitative measurements taken by the hand held detector show lower activities.

The calculated internal Dose is presented in Table 1:

Table 1: Exposure doses (Sv) to the whole body and thyroid, calculated from measurements taken with Phoswich Detector during one year.

	Dose (Sv)
CEDE	4.7×10^{-3}
CDE to thyroid *	0.15
Internal Intake Activity**	777 kBq

* CDE = Committed Dose Equivalent
** Calculated to the day of exposure.

The results of the urine analyses were scattered and differed from the predicted decay pattern. The values obtained for internal exposure, were lower than those described above.
Medical monitoring and treatment: The contamination was discovered too late for KI treatment. The absorbed dose was lower than the Annual Limit of Intake (ALI) for I-125, which is 2MBq (27 μCi), therefore, no special steps were taken. However, TSH and T3 were measured 6 months later, for thyroid function determination, and found normal.

Discussion: Iodine is detectable in the thyroid 2 hours following an internal intake while KI blocking is most effective if given 30 minutes after it. Therefore, constant and reliable monitoring of the working area is of prime value while handling radioiodine, along with personnel monitoring.

The hand held monitors with the high sensitivity proved to be both reliable and accurate enough for an early detection and estimation of radioiodine contamination.
Direct measuring of I-125 in the thyroid, using a high sensitivity detector, is the method of choice for obtaining fast evaluation of exposure doses.
Due to incomplete urine collection and the individual nature of the physiology of each person which differs from "Standard Man", results obtain from urine analyses should be considered less quantitative and more as an indication for the presence of iodine internal contamination.

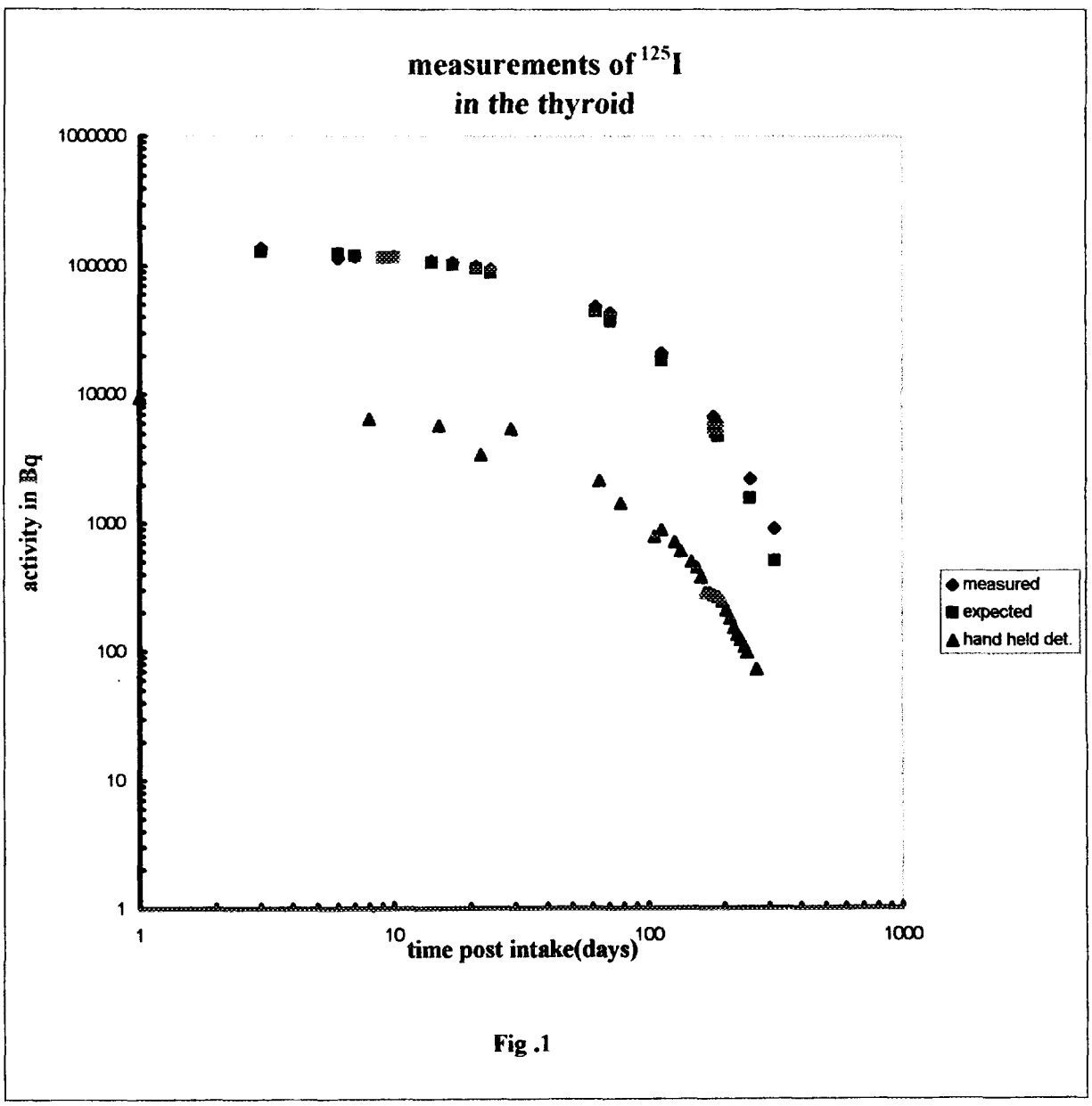

Fig .1

Limitations on the Concentration of Radioactive Substances (natural or enhanced by human activity) in Building Materials- A Draft Proposal for Israeli Regulations.

T. Schlesinger, R. Hareuveny and M. Margaliot
Radiation Safety Division, Soreq NRC, Yavneh, Israel 81800

Natural radioactive elements occurring in building materials constitute a major source of exposure of the public to ionizing radiation. Of the radionuclides that contribute to this exposure, members of the ^{238}U and ^{232}nd series and ^{40}K are of special interest, because usually they occur in building materials in the highest concentration (relative to other radionuclides).
^{40}K and part of the radionuclides of the two above mentioned series cause external exposure while the inhalation of and ^{222}Rn Thoron (^{220}Rn) , emitted from these radionuclides, and their short lived progeny lead to internal exposure of the respiratory tract to mainly alpha particles.

The exposure of humans to ionizing radiation can result in harmful health effects. For high doses these effects are acute and deterministic, with a dose threshold. For low doses the effects are delayed and of stochastic nature, whereby the risk of actual occurrence (and not the severity of harm) is proportional to the radiation dose. Of all delayed somatic effects, the most significant and prominent is the manifestation of malignant illnesses in the exposed individual 2-40 years following a single exposure or the onset of chronic exposure. The International Commission on Radiological protection (ICRP) evaluated in 1990 the fatal cancer risk of exposure to ionizing radiation to be 5%/Sv. This means that the chronic exposure of a population to an affective dose of 0.01 Sv (1 rem) per year will lead, eventually, to an excess of 500 cases of cancer deaths per year per 10^6 population. This risk factor was evaluated for

low doses of low LET radiation delivered at low dose rates. There is no dose threshold to this risk i.e. any radiation dose poses a risk.

The dose to members of the public attributed to natural radioactive elements in building materials, at their normal average concentrations, is usually low and does not exceed a few hundreds of μSv per year. The exact value of the dose depends on many parameters, e.g. the concentration of specific radionuclides in the material, the density and thickness of the walls, their geometrical configuration and the level ofthe emanation of Radon and Thoron from these walls.

In recent years there is a growing tendency to use new construction materials with naturally or technologically enhanced levels of radioactivity (e.g. phosphogypsum, fly ash exotic minerals, etc.). This trend causes a growing health concern. The result of this concern is legislation activity and publication of guidance notes by national authorities and international professional organizations related to the radiological implications of these novel technologies.

The ICRP considered, for many years, the problem of exposure to natural radiation as a chronic exposure situation which is subject only to "intervention" activities .

However in its recommendations published in 1990 the commission suggested to treat some natural sources causing public exposure as "practices". As such these sources are subject to all the three basic principles of radiation protection i.e. . Justification, Optimization and Dose Limitation.

The Ministry of the Environment in Israel is authorized by Israeli legislation to control the exposure of the public to ionizing radiation. The ministry asked in 1996 a professional group in the Radiation Protection Division of the Soreq NRC (the authors of this presentation) to study the radiological implications of the use of building materials with naturally or technologically enhanced concentrations of radioactive substances, and to submit draft regulations setting primary limits on excess exposure of the public to ionizing radiation from building materials and derived limits related to concentrations of specific radionuclides in these materials.

for presentation of the proposed draft proposal for the Israeli regulations we are using the following special notations:

The concentration index:

The concentration index for a set of concentration values ($C(A_1)$, $C(A_2)$, ... $C(A_n)$) of radionuclides A_1, A_2, ... A_n is defined as the sum of the quotients

$$\frac{C(A_1)}{C(A_1)_\ell} + \frac{C(A_2)}{C(A_2)_\ell} + \ldots \frac{C(A_n)}{C(A_n)_\ell}$$

Where $C(A_1)_\ell$, $C(A_2)_\ell$,.....,$C(A_n)_\ell$ are limiting values set on the concentration of the above radionudides for legislation purposes, as defined bellow.

Limiting Concentration Values

The limiting concentration value $C(A_i)_\ell$ is the concentration value for the radionuclide A_i that, if present in a building material, will cause, alone, a specified additional annual dose to the residents of a standard building built of this building material (e.g. for the "exempted level" specified bellow this annual dose is 0.5 mSv (50 mrem)).

Concentration Index Criteria

The "concentration index criteria" is the compliance of the set of concentrations ($C(A_1)$, $C(A_2)$ .... $C(A_n)$) with the requirement

$$\frac{C(A_1)}{C(A_1)_\ell} + \frac{C(A_2)}{C(A_2)_\ell} + \ldots \frac{C(A_n)}{C(A_n)_\ell} <= 1$$

The proposed draft for Israeli regulations related to limitations of the concentration of radioactive substances in building materials are based on the following principles and guidance values:

1. It is recommended to regard the exposure of the public to ionizing radiation from radioactive elements in building materials at their regular average levels as a chronic exposure situation.

2. There is no justification for intervention (taking remedy actions or setting limits on the concentration of radionuclides in building materials) as long as the additional exposure of members of the public (as compared to outdoor exposure) due to these materials does not exceed 0.5 mSv (50 mrem) per year due to external and internal exposure. This level will be called the "natural level" or "the exempted level".
   The derived "limiting concentration values" for the exempted level of ^{40}K, ^{226}Ra and ^{232}Th are (2500, 110, 135).

3. Exposure of the public to ionizing radiation due to naturally or technologically enhanced levels of radioactive elements in building materials should be regarded as exposure to sources within a practice (building methods and technology) and should be thus subject to dose limits and optimization. As part of the optimization process a dose constraint of 0.5 mSv (50 mrem) per year, in excess of the average 0.5 mSv caused by natural levels of radioactivity in building materials, is recommended. The derived "limiting concentration values" of ^{40}K, ^{226}R a nd ^{232}Th for this level are (5000, 220, 270).

The "limiting concentration values" specified in pa. 2) and 3) above were derived by calculating the external and internal exposure to residents in a standard building constructed from building materials with specified concentrations of ^{40}K, ^{226}Ra and ^{232}Th. This model assumes wall thickness- d of 0.24 m, density of the walls- ρ of $1.5x10^3$ kg/m^3 and an emanation coefficient- e (the fraction of radon that is emitted from the walls) of 0.05.

4. If the "concentration index" of a specific building material does not comply with the concentration index criteria, using the "limiting concentration values" specified in Pa 3 above, there is still an option to use the building material if it can be shown that it complies with the "concentration index criteria" using the "concentration limiting values" (5000, 400/(1+0.046 epd), 270) e, ρ and d being the actual values of the emanation coefficient, the wall density and the wall thickness respectively.

Example

To illustrate the use of the "concentration index criteria" and the "concentration limiting values" let us check the following actual case:

A request to allow the use of a building product (e.g. concrete based on the use of fly ash from coal fired power stations) with concentration values of 1000 Bq/kg, 100 Bq/kg and 80 Bq/kg for $^{4,0}K$, ^{226}Ra and ^{232}Th respectively.

to check compliance with the exemption level criteria we calculate the sum

$$\frac{1000}{5000}+\frac{100}{110}+\frac{80}{135}=1.90$$

obviously the building material does not comply with the exemption criteria.
However checking compliance with the "concentration index criteria" using the "concentration limiting values" (5000, 220, 270) specified in Pa.3 above, for ^{40}K, ^{226}Ra and ^{232}Th respectirely we, find that:

$$\frac{1000}{5000} + \frac{100}{220} + \frac{80}{270} = 0.946$$

i.e. the building material complies with the "concentration index criteria" for this optimized level and can be approved for use

Occupational radiation risks in conveyance of bulk Phosphate and Potash

Y. Grof, O. Even, T. Schlesinger and M. Margaliot
Radiation Safety Division, Soreq NRC, Yavne 81800, Israel.

abstract

The issue of occupational ionizing radiation risks encountered in the conveyance and storage of Phosphates and Potash as loose cargo got very minor attention from the national health and occupational safety authorities in the world. In Israel, the Phosphates include an average 100-150 ppm of Uranium in equilibrium with its daughters, while in Phosphates produced in most other countries the fraction reaches regularly only few ppm up to 50 ppm.

Because of the high content of the Uranium in the Phosphate in Israel we must take into consideration the radiological implications involved in the handling of this mineral. The radiological implications of handling Potash are less significant but can not be neglected as we demonstrate bellow.

In this presentation we will estimate the occupational radiological risks involved in the storing and transportation of Phosphate and Potash.

Note, that the main risk in working with Phosphate and Potash is the risk from the dust itself.

To the basic risk of external radiation from the Uranium and its daughters and from K-40 (natural potassium contents 0.0118% of ^{40}K which emits beta and high energy gamma radiation), we must add risks related to the ingestion and inhalation of the dust particles, basically, and by the inhalation of the Radon and its daughters. Therefore ,workers engaged in handling both Phosphates and Potash are potentially exposed both to external and internal radiation.

The results of actual measurements of external radiation dose rates and of radioactive contamination in the air, made by us recently in a Phosphate and Potash storage, are also will be presented. These measurements enabled the analysis related to the loose

cargo transportation, and discuss the potential radiation risks to the workers and to the people who live near by.

A preliminary work dealing with the same subject was published by us in 1987, but due to changes that will be discussed later, in the evaluation of ionizing radiation risks by the ICRP and in the international radiation protection standards, and because of the improvements in the measuring methods, we found it necessary to repeat the survey and the measurements and their analysis.

The presence of Uranium in the Phosphate has a double significance:

1.External radiation caused by the gamma rays from the Uranium chain.

2. Internal contamination from:

a. The Uranium itself and its long living daughters in the dust.

b. The short lived daughters of the Radon 222, causing radiation dose to the respiratory tract.

The Uranium and its long lived daughters appear as a component of Phosphate dust, airborne around Phosphate storage . This dust enter the respiratory tract, with the inhaled air.

All of the Uranium in Phosphate, appear as non soluble compounds, and is captured at the deeper parts of the respiratory tract, specially in the pulmonary region and the tracheobronchial lymph Nodes . The dose to a human inhaling this natural Uranium dust , is therefore caused mainly by the Uranium trapped in the lungs.

Radon is produced in the decay process of ^{226}Ra . It is a noble gas, and therefore it is not chemically connected to its surrounding media in the Phosphate and part of it can be emitted to the air. Radon decays radioactively in the air. The health risks of Radon and its daughters are well documented. National legislation in many countries require to limit Radon concentrations in homes and working premises. Remedy action levels of 200-600 Bq/m^3 in homes and 500-1500 Bq/m^3 on working premises has been set in these countries. In Israel the limit set by the ministry of the environment is 200 Bq/m^3 for homes. The national advisory committee on radiation protection recommended in 1994 to set a remedy level of 500 Bq/m^3 for Radon concentration in air in working premises in Israel. Note that such a level will lead to an effective dose of about 2.5 mSv during 2000 hours of stay on the premises (this estimation is based on an effective dose of 5 mSv/WLM).

Updated radiological data for internal contamination by members of the ^{238}U series are presented in table 1, e(g) is the effective dose per unit activity intake (Sv/Bq) for AMAD (Aerodynamic Median Activity Diameter) of 5 μm as presented in IAEA Safety Series No 115, 1995.

Also presented in the table are ALI values that we calculated from these e(g) values for an annual effective dose of 50 mSv (5 rem). For comparison we presented the ALI values for the same radionuclides as recommended in the earlier version of the International Basic Safety Standards for Radiation Protection, IAEA safety series -9, 1982.

Isotope	Inhalation			Ingestion		
	e(g) 5 μm	ALI		e(g) 5 μm	ALI	
		ss 115	old*		ss 115	old*
	Sv/Bq	(Bq)	(Bq)	Sv/Bq	(Bq)	(Bq)
^{238}U	5.70E-06	8.7E3	2E3	4.40E-08	1.1E6	5E5
^{234}Th	5.80E-09	8.6E6	6E6	3.40E-09	1.5E7	1E7
^{234}Pa	5.50E-10	9.1E7	2E8	5.10E-10	9.8E7	9E7
^{234}U	6.80E-06	7.3E3	1E3	4.90E-08	1.0E6	4E5
^{230}Th	2.80E-05	1.8E3	2E2	2.10E-07	2.4E5	1E5
^{226}Ra	2.20E-06	2.3E4	2E4	2.80E-07	1.8E5	7E4
^{222}Rn						
^{218}Po						
^{214}Pb	4.80E-09	1.0E7	3E7	1.40E-10	3.6E8	3E8
^{218}At						
^{214}Bi	2.10E-08	2.4E6	3E7	1.10E-10	4.5E8	6E8
^{210}Pb	1.10E-06	4.5E4	9E3	6.80E-07	7.4E4	2E4
^{210}Bi	6.00E-08	8.3E5	1E6	1.30E-09	3.8E7	3E7
^{210}Po	2.20E-06	2.3E4	2E4	2.40E-07	2.1E5	1E5
^{206}Tl						
^{206}Pb						

Table 1. ALI values for the ^{238}U series (most restricting values) e(g) values (Sv/Bq) are taken from IAEA Safety Series no 115.

Old* - values from IAEA Safety Series No. 9.

Based on these data, the effective updated ALI for inhalation of ^{238}U in equilibrium with its daughters is 1.1×10^3 Bq. The effective DAC for the same group is therefore 0.46 Bq/m^3 .

It can be seen from the table that for most of the radionuclides in the series the dose per unit intake is now considered to be lower than thought before (the ALI is higher). Also it can be seen that the ingestion risks are, in general, much lower than the inhalation risks.

We conducted preliminary measurements in a Phosphate and Potash storage , related to gamma dose rate levels and concentration of Radon and of Uranium dust in the air in several areas.

Results from the measurements made by us will be introduced in the meeting.

In conclusion we can see that particularly in Israel radiological risks in the handling of Phosphates and Potash is not negligible .

THE MINIMUM MEASURABLE DOSE (MMD) OF CaF_2:Dy MEASURED VIA AN IMPROVED HEATING PROFILE WITH AN AUTOMATIC 6600 THERMOLUMINESCENT DETECTOR

B. Ben-Shachar, M. Weinstein and U. German
NRC-Negev, P.O.B. 9001, Beer-Sheva, 84190, Israel.

ABSTRACT

One of the advantages of the thermoluminescent method is its ability to measure low doses,which is useful in environmental dosimetry, as well as in archeology. The CaF_2:Dy (known as TLD-200), has a sensitivity of 10-30 times greater than the sensitivity of TLD-100, when irradiated by Cs-137. In the present work we evaluated the TL-dose response of CaF_2:Dy, by using an improved heating profile which is giving the main glow peak alone. The relative standard deviations were fitted to a semiempirical expression, from which the minimum measurable doses (MMD) were derived. The MMD were calculated by taking 3 times the standard deviation of the unirradiated chips. The results of the TL-dose response, as well as the the calculated MMDs by taking 3 times the standard deviation of unirradiated chips, measured by the new 6600 automatic thermoluminescent detector, are presented in this work. We received a MMD of about 0.01 mGy (1 mrad), an improvement of a factor of 2.5 relatively to the integral light response evaluation using the standard heating profile.

INTRODUCTION

The most sensitive TLD phosphors are based on CaF_2 or $CaSO_4$. In the early days of dosimetry, the calcium fluoride was the most widely used material [1]. The natural CaF_2 was widely used by the Belgian company MBLE which developed an individual dosimetry system. Houtermans et al [2] and Schayes et al [3] showed that it has a high sensitivity and a good linearity and trap stability. However, its glow curve is complex and only limited amounts of adequate quality material were

available. Ginther [4] synthesised a manganese activated material (CaF_2:Mn), well suited to radiation dosimetry. This material exhibits a single peak at 280°C; however its sensitivity is lower than that of natural CaF_2. Binder et al [5] developed a dysprosium activated calcium fluoride (CaF_2:Dy), marketed by Harshaw as TLD-200 (chips, cards and powder form). Its sensitivity is about 10-30 times greater than the sensitivity of LiF:Mg,Ti (TLD-100), thus being the most sensitive CaF_2 TLD, but its glow curve is more complicated than that of CaF_2:Mn and it is more sensitive to light. The standard temperature profile is a preheat to 100°C and a linear heat of ~30°C /sec up to 220°C.

The aim of the present work was to check the TL-dose response of the CaF_2:Dy phosphor in the low dose range and to evaluate the minimum measurable dose (MMD) by applying an improved heating profile. The MMD was evaluated from the relative standard deviation (standard deviation divided by the mean) vs. the exposure curve, as described by Zarand and Polgar [6,7]. The MMD is defined as the dose level where the relative standard deviation is 0.2 (20%).

MATERIALS AND METHODS

The measurements were performed with the Bicron/Harshaw manufactured TLD-200 cards, each of them containing two chips of CaF_2:Dy (3mm X 3mm X 0.9mm). The cards were irradiated to several doses in the range 0.1 -10 mGy, by a calibrated source of Sr-90/Y-90, and evaluated immediately after the irradiation. The heating profile is a pre-heat to 150°C, and linear heat of ~25°C /sec up to 250°C. The TLD cards were read by the Bicron/Harshaw manufactured 6600 automatic thermoluminescent reader. All the TLD cards were calibrated individually by 5 repeated irradiations of each card to a dose level of 1.0 mGy and the standard deviation was found to be 1-2.5 % for each card.

EXPERIMENTAL RESULTS

In figure 1a we are presenting the glow curve of the CaF_2:Dy phosphor, evaluated after improved heating profile. This curve includes only the main glow peak of this phosphor. It is important to emphasize that the glow curve of CaF_2:Dy, evaluated by whole glow curve, includes several overlaping glow peaks (see figure 1 b).

Figure 1:The Glow Curve of CaF_2:Dy

(a) Main Peak

(b) Whole Glow Curve

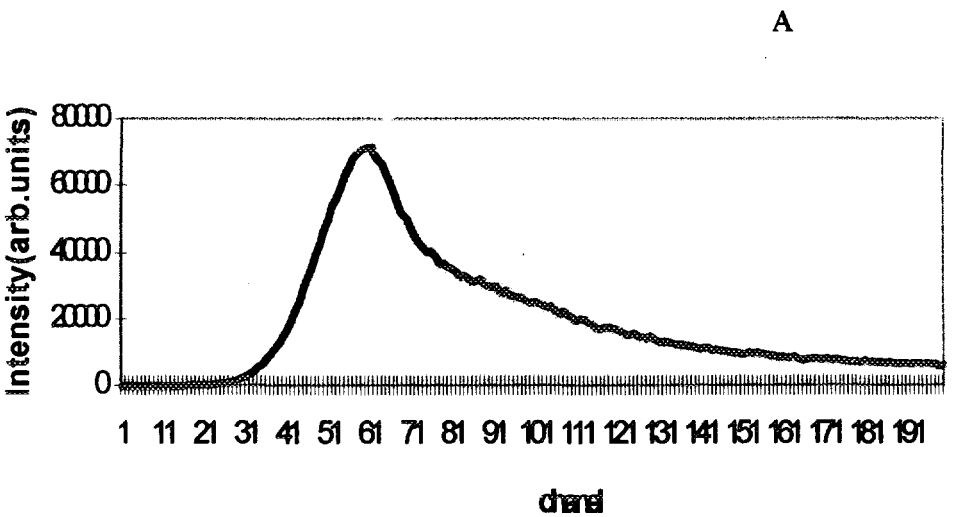

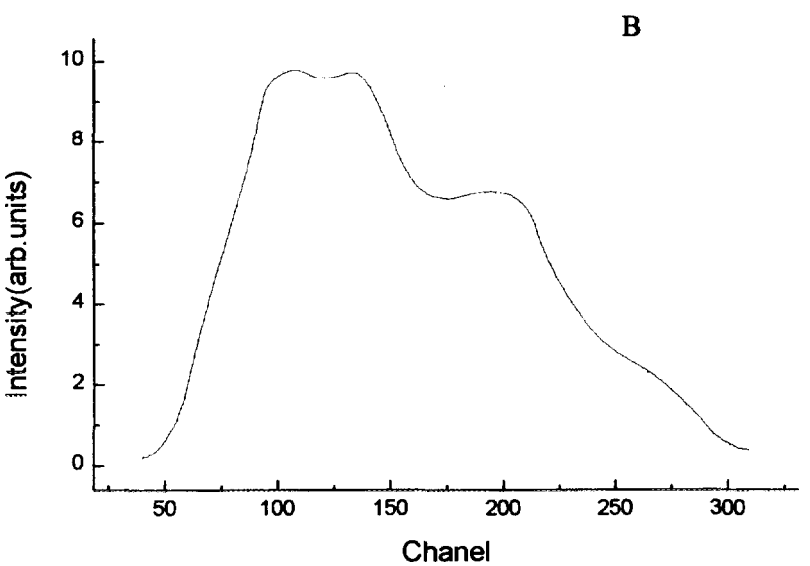

The TL-dose response was measured for five TLD-200 cards in the range of 0.1 - 100 mGy. All the TLD cards were irradiated 5 times to a

dose of 1.0 mGy for calibration. The results for each dose were calculated with individual calibration of each dosemeter. The dosemeters show a good linear response.

A semi-empirical expression following Zarand and Polgar [6,7] was fitted to the relative standard deviation for different exposures. These fits are useful in that they allow interpolation between the measured points so that the MMD can be more accurately estimated. The MMD is defined as the dose level where the relative standard deviation is 0.2 (20%). In figure 2 we are presenting the graph of the relative standard deviation versus the exposure for the CaF_2:Dy chips. The MMD was calculated from this graph. We received that the minimum measurable dose (MMD) is 0.013 mGy (see figure 2). In a previous work we presented the same results evaluated by whole glow curve integration when using the standard heating profile and received a MMD of 0.028 mGy [8].

Figure 2 : Relative Standard Deviation of the main peak area vs. the exposure for CaF_2:Dy

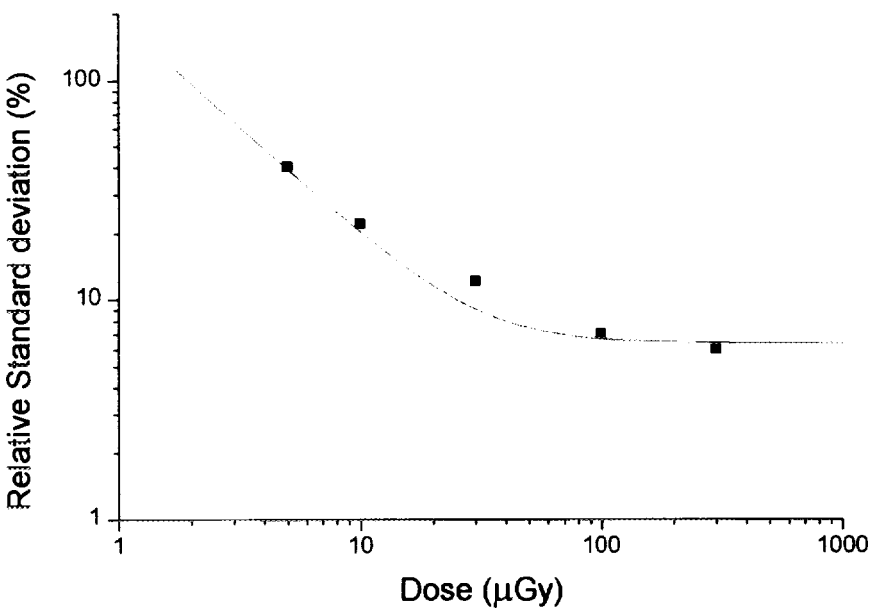

The MMD was also evaluated by reading the unirradiated chips of CaF_2:Dy and taking three times the standard deviation. We received a minimum measurable dose of 0.012 mGy, very close to the result obtained from figure 2.

CONCLUSIONS

A. A good fit was found between the MMD evaluated by the two methods (analytical fit or 3 times standard deviation of unirradiated chips) - the difference between the corresponding results is less than 10%.

B. When using the improved heating profile and the thermoluminescent reader type 6600, we received an improvement of a factor of 2.5 in the results of the MMD, compared to the results of whole glow curve integration (measured with the thermoluminescent detector 2271,and using the standard heating profile).

REFERENCES

1. G. Portal, Rad. Prot. Dosimetry., 1986, **13,** 351-357.
2. F. Houtermans et al., Ann. Phys., 1957, **20,** 283.
3. R. Schayes, CONF-650637, 1965, p.138.
4. R. J. Ginther, J. Electrochem. Soc., 1954, **101,** 248.
5. W. Binder, CONF-680920, 1968, p.43.
6. P. Zarand and I. Polgar, Nucl. Instrum. Meths., 1983, **205,** 525.
7. P. Zarand and I. Polgar, Nucl. Instrum. Meths., 1984, **222,** 567.
8. B. Ben-Shachar et al., ORNL/TM-11882, 1991, 31.

מדינת ישראל המשרד לאיכות הסביבה אגף בטיחות קרינה
אוניברסיטת ת"א, בית הספר לרפואה, ת"א 69978 טל 03-6414807, פקס 03-6429882

Radiocesium in the Soils of Jerusalem

E. Ne'eman[a], V. Butenko[a], S. Brenner[a], N. Lavi[a], J. Kronfeld[b], A. Gilat[c]

[a]Radiation Safety Department, Ministry of the Environment,
Sackler Medical Center, Tel Aviv University, Ramat Aviv 69978, Israel.

[b]Department of Geophysics and Planetary Sciences, Raymond and Beverly Sackler
Faculty of Exact Sciences, Tel Aviv University, Ramat Aviv 69978, Israel.

[c]Geological Survey of Israel, 30 Malkhei Yisrael St., Jerusalem 95501, Israel.

ABSTRACT

Surface (0-5 cm) soil samples taken from representative sites throughout Jerusalem, in the Fall-Winter 1993, were measured by high resolution γ-ray spectroscopy using an intrinsic Ge detector. ^{134}Cs and ^{137}Cs derived from Chernobyl accident were found in all samples, though the radiocesium activity varied widely (from 0.6 to 40 Bq/kg ^{137}Cs). Four depth profiles demonstrated that the cumulative ^{137}Cs concentration is at least twice the surface value. Mushrooms were collected at three sites during the same sampling period. These samples exhibited varying transfer coefficients among sites with a maximal radiocesium uptake of 100 Bq/kg fresh weight.

The radiocesium measurements are among the first reported for the Jerusalem region. Due to the rather high degree of mobility exhibited in these soils, it is not possible to perform any precise extrapolation in order to estimate the original activity of the radiocesium fallout.

INTRODUCTION

Approximately ten days after the explosion at the Chernobyl unit-4 reactor on April 26, 1986, the radioactive plume arrived over Israel, accompanied by a patchy drizzle. Measurements of air, soil, water and vegetation were taken by the authorities during and soon after the incident at certain sites in the country. The monitoring ceased after it was concluded that the situation was satisfactory from a public health stand point (Schlesinger et al., 1986). While the fallout from this accident has been intensely studied in Europe (Decort et al, 1990) it was generally considered that the contamination reaching the Levant was of little significance. However, there is virtually no published data to date on the long ranging effects of the chernobyl derived radioactive fallout over Israel and its neighbors. In the Fall-Winter of 1993, radio measurements of soils from central Israel were monitored. Though over $3^{1/2}$ half time periods had gone by, ^{134}Cs was readily detected along with the longer lived ^{137}Cs. In these samples, when the $^{134}Cs/^{137}Cs$ ratio was extrapolated back in time to April 26, 1986, a ratio of 0.5 was derived. This value is characteristic of the initial release from the Chernobyl exhalation (Papatesfanou et al, 1988). The present study was undertaken to examine the extent to which the Chernobyl derived radiocesium is distributed aerially within the boundaries of the Jerusalem region. It was anticipated that such a study would enable us to estimate the initial dose of the fallout over Jerusalem, seven and half years prior to the monitoring and to study the geochemical behavior of the radiocesium isotopes in the soil.

Study Area

Jerusalem is situated in the Judea Hills in the center of Israel. The city straddles the boundary between forest and desert. Despite intensive recent efforts of soil conservation and reforestation, the soils are young and generally thin. Soil formation barely keeps up with runoff and the base rock is exposed on many slopes. Rainfall is restricted to the winter months. Terra Rosa soils are thereby formed by the weathering of the Cenomanian-Turonian limestones and dolomites,

while the basic rendzina soils are formed from the weathering of the Senonian and Eocene chalks (Orni and Efrat, 1973).

Sampling and Methods

Samples of soils were collected from a representative geographical distribution Fig. 1). The samples were taken from the top 5 cm of the soil using a 12.3 cm diameter steel corer. At two sites a 10 cm depth profile was obtained. Two other sites yielded 15 cm depth profiles. The samples were air dried, weighted and placed in 470 ml sealed plastic containers. Measurements were carried out using a high resolution gamma-ray spectrometer (Canberra S-100), equipped with a 100 cm^3 intrinsic Ge crystal. The counting times were generally for one day. At three sites edible wide mushrooms, *Boletus luteus* were also collected and measured (fresh weight). A representative γ-ray spectrum from the mushrooms collected at Gilo (site 9) is presented in Fig. 3 to demonstrate the high degree of resolution of the energy spectrum.

RESULTS

The results of the soil analyses are presented in Table 1 as the activity of ^{137}Cs. ^{134}Cs isotope was encountered in all cases; however, after 3.5 half lives, most of this nuclide has already decayed away. The statical counting error reported in Table 1 is given at the 1σ level of confidence.

The radiocesium in the surface soils (0-5) ranged from 0.7 to 40.8 Bq/kg. The distribution of ^{137}Cs as a function of depth for the four radiometric profiles is presented in Fig. 3. ^{137}Cs was encountered in each of the mushroom samples. However, the radiocesium concentration as well as the transfer coefficient (TF) which is the ratio of the ^{137}Cs activity in the mushrooms (fresh wt)/ ^{137}Cs activity (dry weight) in the associated soils varied considerably. The ^{137}Cs activities and their associated transfer coefficients for the three sampling sites (identified in Table 1) are: Site 9 (100 Bq/kg, TF = 0.03), Site 17 (4.2 Bq/kg, TF = 0.01), and Site 24 (74 Bq/kg, TF = 0.06).

DISCUSSION

Radiocesium that was found in each sample that was analyzed had its source from the pollution released from the Chernobyl accident. This is demonstrated by the presence of the ^{134}Cs isotope. This nuclide of short half-life (2.08 y) is not produced in significant quantities by nuclear weapons testing (Gudiksen et al, 1989). Moreover, any bomb-derived ^{134} Cs that had been deposited would have decayed away since the last atmospheric nuclear tests. Still as over $3^{1/2}$ half-lives had elapsed since the Chernobyl accident and the time that these first measurements of Jerusalem soils were carried out, little of the original ^{134}Cs remained. In those samples where the ^{137}Cs concentrations were low, the ^{134}Cs activity was associated with poor counting statistics. However, using those samples where the statistics were sufficiently good, it was found that when the presently measured $^{134}Cs/^{137}Cs$ ratios were extrapolated backwards to April 1986, they yielded an initial ratio of 0.5 for most of the samples. This is the isotopic ratio that was characteristic of the radiocesium isotopes released from Chernobyl (e.g. Papastefanou et al, 1988). Unlike the ^{134}Cs isotope, most of the ^{137}Cs released globally was produced from the atmospheric bomb tests, and yet this component is not in evidence in the young soils of Jerusalem. It has been demonstrated (Cremers et al, 1988) that radiocesium in the soils is retained primarily in the finest grained size fraction, mostly by micaceous clays. Apparently part of the radiocesium that was introduced, is continually eroded away with the muddy fraction of the soil that is washed by seasonal rains to lower elevations or to the sea. It has been noted previously (Stiller et al, 1985 that radiocesium (pre-Chernobyl) is readily detected in the upper layers of sediment in the Dead Sea.

An appreciable amount of the Chernobyl-derived radiocesium has migrated downwards from the surface. In Fig. 2, it can be seen that only a little more than half of the total activity is currently found at the surface. During the last 8 years an amount almost equal to the extant surface value has migrated down to a depth of at least 10-15 cm. Plant uptake, as the analysis of the mushrooms demonstrate, also serve to deplete the radiocesium budget in the soil. The maximal activity of

^{137}Cs in the three (1993-94) mushroom samples collected was 100 Bq/Kg. This is well below the 600 Bq/Kg limit for the EEC public health standard (Heinrich, 1993). However, as collecting wild mushrooms in the Jerusalem area is an activity carried out annually by many citizens, it is more than just of speculative interest to estimate the initial range of concentrations that may have been encountered in earlier years. However, due to the redistribution of radiocesium in the soils (due dto mobility, erosion and plant up take) extrapolation back in time, using present surface values, would not be very accurate. Moreover, there is a very great variability at present among sample sites within the city. For example, even samples taken within 20 m of each other, such as sample #9 at Gilo (27.5 Bq/Kg) and #9a (6.0 Bq/Kg), exhibit very large differences. This variability may have been a characteristic of the primary deposition, related to particulate species washed out in the initial sporadic drizzle rainfall over the area. This variability in the spatial distribution of the ^{137}Cs activity has been noted in western Europe (Clark and Smith, 1988; Zombori et al, 1992; Lettner et al, 1992).

Considering that may factors may have acted upon and redistributed the Cs in the soils, it can be considered that the surface activity shortly after deposition may have ben twice or thrice that of today. To this should be added a 50% activity contribution of ^{134}Cs. If for example, the Gilo site exhibited the higher of the three transfer coefficients, it can be visualized that the initial radiocesium concentration in the mushrooms may have already approached or exceeded the 600 Bq/kg recommended safety limit. Likewise, if we consider the maximum value exhibited today of 40 Bq/kg ^{137}Cs, encountered in the soils by the Montefiori wind mill (site 6, Table 1), it may be estimated that at this particular spot the initial surface activity may have been as great as 10-12 KBq/m^2 immediately after it was deposited in May 1986.

The range of radiocesium values that are exhibited in the Jerusalem soils today are considerably lower and within a narrower range than values for Greece (0-150 KBq/m^2) (which received an earlier arrival of the Chernobyl plume) the nearest other Mediterranean country for which considerable data is available (Gerontindon et al, 1994). Using Fig. 2, it may be assumed that the initial average ^{137}Cs radiocesium deposition of between 2.5 to 3.5 KBq/m^2 may have approximated the

level of the average contamination for spring 1986 over Jerusalem. This would be similar in magnitude to that of a city like Padua in northern Italy (Battison et al, 1988) that received its radioactive contamination via the less efficient mode of dry deposition. A 2.5 KBq/m^2 would translate into a 1 year exposure of 0.008 m Sv. This calculated average external dose rate would not be harmful. However, as Cs is geochemically similar to the nutrient K, the internal dose rate - such as may have been incorporated through ingestion of wild mushrooms in the first year after the accident, should be considered as of importance. It is unfortunate that the soils in Jerusalem were not monitored soon after the Chernobyl contamination arrived. The present study tries to correct for this lack of information as best as possible; but, the high mobility of the radiocesium has led to its redistribution and the recreation of the initial conditions can be but a broad approximation at best.

LIST OF FIGURES

REFERENCES

Battiston, G.A., Degetto, S., Gerbasi, R., Sbrignadello, G. & Tositti, L. (1988). Fallout distribution in Padua and northeast Italy after the Chernobyl nuclear reactor accident. J. Environ. Radioactivity, 8, 183-91.

Clark, M.S. & Smith, F.B. (1988). Wet and dry deposition of Chernobyl releases. Nature, 332, 245-249.

Cremers, A., Elsen, A., DePreter, P. & Maes, A. (1988). Quantitative analysis of radiocesium retention in soils. Nature, 335, 247-9.

DeCort, M., Graziani, G., Raes, F., Stanners, D., Grippa, G. & Ricapito, I. (1990). Radioactivity measurements in Europe after the Chernobyl accident. Part II: Fallout and Deposition. EUR 12800 EM, WEC, Brussels.

Geronitidou, M.V., Hinis, E.P., Simopoulos, S.E., Louizi, A. & Proukakis, C. (1994). ^{137}Cs Chernobyl fallout in Greece and its associated radiological impact. 1st Mediterranean Congress on Radiation Protection. Athens, 5-7 April.

Gudiksen, P.H., Harvey, T.F. & Lange, R. (1989). Chernobyl source term, atmospheric dispersion and dose estimation. Health Physics, 57, 697-706.

Heinrich, G. (1993). Distribution of radiocesium in the different parts of mushrooms. J. Environ. Radioactivity, 18, 229-45.

Hilton, J., Cambray, R.S. & Green, N. (1992). Chemical fractionation of radioactive caesium in airborne particles containing bomb fallout, Chernobyl fallout and atmospheric material from the Sellafield site. J. Environ. Radioactivity, 15, 103-11.

Lettner, H., Zombori, P., Ghods-Esphabani, A., Girzilkowsky, R., La Rosa, G., Sitter, H., Schweiger, M. & Winkelman, I. (1992). Radiometric measurements in selected settlements in Byelorussia and the Ukraine. J. Environ. Radioacctivity, 17, 107-13.

Orni, E. & Efrat, E. (1973). Geography of Israel. 3rd Ed. Israel Universities Press, Jerusalem, 551 pp.

Papastefanou, C., Manolopoulou, M. & Charalambous, S. (1988). Radiation measurements and radioecological aspects of fallout from the Chernobyl reactor accident. J. Environ. Radioactivity, 7, 49-64.

Schlesinger, T., Biran, T., Even, D., Dunchan, R., Shami, Y., Koch, J., Tal, A, & Yisraeli, M. (1986). Environmental sampling in Israel, May-July, 1986 to study the influence of the Chernobyl nuclear accident upon the environmental radiation dose rate. Ministry of Health Report (in Hebrew) 49 pp.

Stiller, M., Yanaki, N.E. & Kronfeld, J. (1985). Comparative isotope study of two short sediment cores from the Dead Sea. Chem. Geology, 58: 107-20.

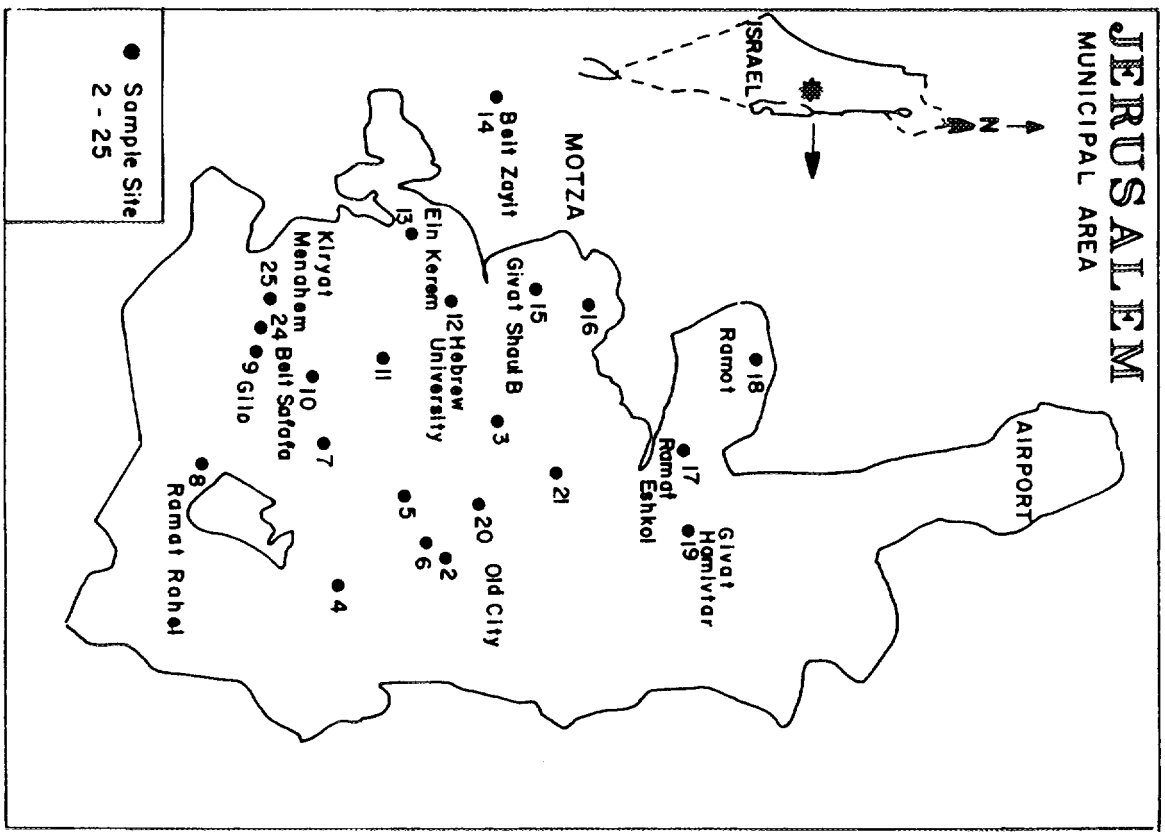
JERUSALEM
MUNICIPAL AREA
ISRAEL
N
Sample Site
2 - 25
MOTZA
Beit Zayit
14
Ein Kerem
13
Kiryat Menahem
25
24
Beit Safafa
9
Gilo
10
11
12 Hebrew University
Givat Shaul B
15
16
3
21
Ramot
18
17
Ramat Eshkol
19
Givat Hamivtar
AIRPORT
20
Old City
5
6
2
7
8
Ramat Rahel
4

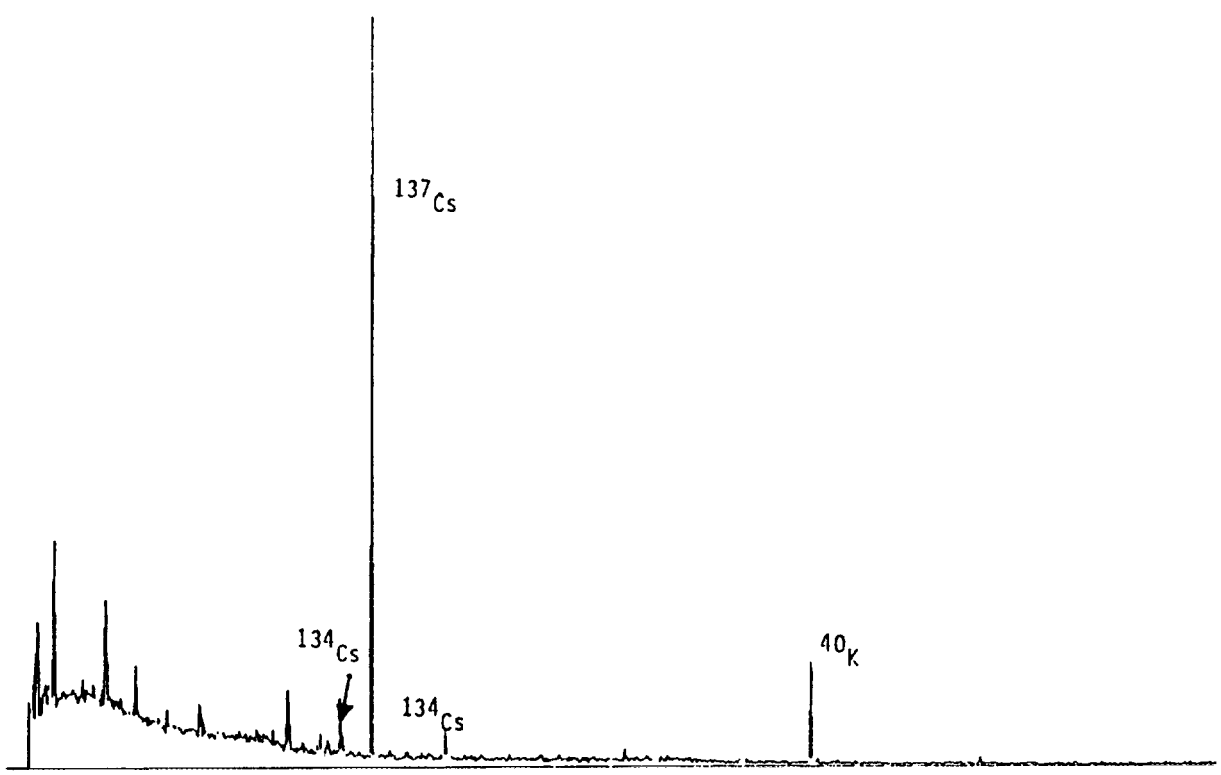
137Cs
134Cs
134Cs
40K

Table 1: Radiocesium in Jerusalem Soils (0 - 5 cm)

Sample Code Number	Location	^{137}Cs Bq/Kg
2.	City of David	29.6±0.7
3.	Rose Garden	10.1±0.5
4.	Silwan	4.1±0.3
5.	German Colony	18.4±0.6
6.	Montefiori Windmill	40.8±0.5
7.	Academy of Sciences	6.5±0.4
8.	Talbiye	17.5±0.5
9.	Gilo	27.5±0.7
9a	150m south of above 0-5 cm	6.0±0.2
	5-10 cm	2.1±0.1
	10-15 cm	0.9±0.1
10.	Gonen	0.9±0.3
11.	Independence Park	2.5±0.2
12.	Mount Scopus	17.4±0.5
13.	Hadassah Hospital(En Kerem)	0.7±0.2
14.	Beit Zayit	3.5±0.3
15.	Givat Shaul	16.1±0.5
16.	Biblical Zoo	15.0±0.5
17.	Ramat Eshkol 0-5 cm	14.3±0.2
	5-10 cm	9.0±0.2
18.	Ramot	2.8±0.4
19.	Givat Hamivtar	3.5±0.2
20.	Geological Survey	17.1±0.4
21.	Morasha	26.9±0.5
24.	West of Beit Safafa 0-5 cm	10.6±0.3
	5-10 cm	6.0±0.2
	10-15 cm	1.3±0.1
25.	Kiryat Menachem 0-5 cm	11.0±0.3
	5-10 cm	11.0±0.4

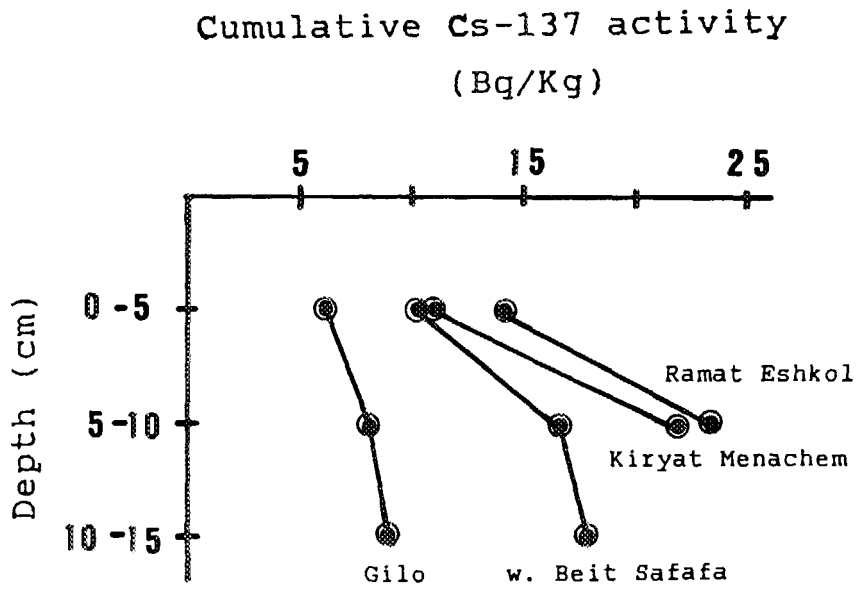
Cumulative Cs-137 activity
(Bq/Kg)
5
15
25
Depth (cm)
0 -5
5 -10
10 -15
Ramat Eshkol
Kiryat Menachem
Gilo
w. Beit Safafa

PORTAL IMAGING IMPROVEMENT WITH A LOW ENERGY UNFLATTENED BEAM IN HIGH ENERGY MEDICAL ACCELERATORS*

Yanai Krutman*‡, Sergio Faermann†‡ and Alex Tsechanski*‡

Ben-Gurion University of the Negev
‡Soroka Medical Center, Institute of Oncology
*Department of Nuclear Engineering,
†Faculty of Health Sciences,
P.O. Box 151, Be'er Sheva 84101, ISRAEL

1 Introduction

It is well known that portal image quality is poor. For x-rays in the energy range 1 - 15 MeV , as used in radiotherapy, Compton scattering is the main interaction of photons with tissue. Therefore x-ray attenuation is limited to small differences in bone and soft tissue [1]. Different techniques to improve the portal image quality have been proposed like : enhancing the response of the detector to the low energy part of the x-ray spectrum, the use of low-energy x-ray source [2].

Purdy et al., developed a portal image device in a Clinac 20 (Varian Assoc.) with an x-ray beam of 18 MV, based on a 6 MeV electron mode modified by inserting the x-ray target and removing the flattening filter from the beam path. [3]

Galbraith in 1989 used a low Z target (Be, graphite, Al)at the target slider, outside to the bend-magnet assembly of a Therac-20 AECL accelerator, obtainig the x-rays by means of a 6 MeV electron beam, resulting in an estimated 150 KeV diagnostic x-rays between 5%-18% for the 6 MeV energy range. [4]

Varian Associates made available a Portal Film Option, which consists of a low-energy x-rays portal unflattened beam, with nominal accelerating potential of 6 MV for the Clinacs high-energy line.[5]

*This work was partially supported by the Israel Cancer Association

In this work we present a further improvement of the portal film option, for a Clinac 18 accelerator with a 10 MV therapeutic x-ray beam. This is done by lowering the nominal photon energy to 4 MV, therefore increasing the relative contribution of the low energy portion of the x-ray spectrum. Improvement of the image quality is demonstrated with a portal film scale tray, and with an anthropomorphic phantom, a graphical analisis demonstrates the improvement on image.

2 Materials and Methods

.

The nominal accelerating potential of the new portal image option beam was lowered to 4 MV in order to increase the relative low energy contribution ($\leq$ 150 KeV)to the whole spectrum. Electron beam energy change was performed by decreasing the amount of RF power applied to the accelerating guide by means of the shunt tee drive assembly. Bending magnet DC current was matched (decreased) by 40% as compared to the routine 10 MV therapeutic mode.

Measurements of the PDD and profiles for the low energy beam, were performed with a Scanditronix RFA-300 Radiation Field Analyzer. Typical results for a 10x10 cm^2 field, SSD=100 cm, are presented in Fig. 1. A typical profile obtained for the unflattened beam, 20x20 cm^2 , depth=5 cm, is shown in Fig. 2. For a depth of 10 cm, a PDD of 62% was found, against the value of 67% specified by Varian.

Dose calibration was performed in water phantom (30x30x32 cm^3), with a Farmer 0.6 cc ion chamber (NE2571), coupled to a Keithley electrometer (model 35614), for a field size of 10x10 cm^2, at SSD = 100 cm, according to the NPL ion chamber certificate, Fig. 3.

The TPR_{10}^{20} ratio was measured for the low energy unflattened beam with the same set-up as used for the beam calibration.

After removing the target from the beam path, we measured the percentage ionization as a function of depth, for the low energy electron beam, by film dosimetry as seen in Fig. 4. X-Omat TL film, Nuclear Associates electron beam polystyrene cassette and polystyrene plates were used.

A portal film scale tray (Med-Tec, Inc) was adopted by us as a reference tool to analyze the image quality. The scale tray is made by plexiglass and is specialy designed for Varian medical accelerators; at both axes of the tray there are Pb pins which project reference dots equaly spaced 2 cm apart from the isocenter point. In order to analyze the portal image quality we selected a 10x10 cm^2 field size, source to film position 100 cm and used Kodak, X-Omat TL film with a build-up polystyrene plate to assure 5 cGy at the film position (OD = 1.2-1.5).

Portal films were taken with the Soroka Clinac 18, 10 MV therapeutic beam and the low

energy unflattened beam, and with the Rabin Clinac 1800, 6 MV therapeutic beam as shown in Fig. 5.

We have used a very simple test to quantify the sharpness of the portal image. It consists in measuring the optical density as function of the distance from the middle of the central dot, Fig. 6. The FWHM for each peak was normalized to the length of the scanning for comparison purposes.

Absorbed dose was measured as a function of field size, water thickness, and air-gap at the film-screen position with the 0.6 cc ion chamber. They were used for generation of a preliminary portal film chart for the low energy option in accordance with a methodology developed by two of us[2].

3 Results

The beam stability was checked, and a maximum 15% dose deviation was found, as specified by Varian[5].

Evaluation of the Nominal Accelerating Potential of the low energy unflattened beam was made by three methods: a) the TPR_{10}^{20} ratio, or the beam quality index. The measured quality index was 0.624, which agrees with a nominal accelerating potential of 4 MV, as shown in Fig. 3. b) the PDD measured at 10 *cm* depth. The value of 62% compares well with the data for a 4 MV Varian Clinac 4/100, PDD=64% [6]. c) a direct measurement of the electron beam with the x-rays target retracted, using film dosimetry. An average energy,E_0 = 4.7 MeV, and a most probable energy at the phantom entrance $E_{p,0}$ = 5.4 MeV, was obtained (Fig. 4).

The normalized FWHM was calculated for each portal beam as follows: 0.160 for 10 MV, 0.151 for 6 MV, and 0.138 for the low energy unflattened beam. The results clearly show the improvement of portal imaging when using the low energy unflattened beam.

Portal films of the head and neck region of an anthropomorphic phantom were taken with the three studied beams, and a remarkable improvement in anatomic details was achieved with the unflattened beam, Fig. 7.

4 Conclusion

A low energy unflattened beam for portal film option has been installed. A 15% maximum dose deviation and a PDD of 62% at 10 cm depth were obtained, matching the Varian specifications. The nominal accelerating potential was determined as being 4 MV, thus increasing the low energy part (up to 150 KeV) of the spectrum, as compared with the portal film option offered by Varian. Portal film images taken with a portal film scale tray and

anthropomorphic phantom show clear improvement obtained with the new beam. An useful method was developed for portal image quality evaluation. Further image improvement will be achieved by investigating the optimal energy for the average patient. For this purpose , electron beam, electronic and mechanical adjustements, and Monte Carlo calculations with the EGS4 code are now in progress. After optimization of the beam, portal film charts will be generated according to the best film-screen combination for use in routine operation.

References

[1] H I Amols, L E Reinstein, and Lagueux B. A quantitative assessment of portal film contrast as a function of beam energy. *Medical Physics*, 13:711–716, 1986.

[2] Sergio Faermann and Yanai Krutman. Generation of portal film charts for 10 MV x-rays. *Medical Physics*, 19:351–353, 1992.

[3] J. A. Purdy, R. L. Gerber, C. O. Granda, and P. A. Parrino. Improved localization films for a high energy linear accelerator. *Medical Physics*, 8:57, 1981. (Abstract).

[4] D. M. Galbraith. Low energy imaging with high energy bremsstrahlung beams. *Medical Physics*, 16:734–746, 1989.

[5] Varian Associates. catalog RAD 1933A 10/82.

[6] Shirish K. Jani. *Handbook of Dosimetry Data for Radiotherapy.* CRC Press, Boca Raton, Florida, 1993.

FIGURE CAPTIONS

Fig. 1: Low energy unflattened beam PDD measurement in water for field size 10x10 cm^2 and SSD = 100 cm. The upper curve corresponds to the thicker port at the copper target, the lower curve corresponds to the thinner port at the copper target.

Fig. 2: Typical beam profile (transversal axis) for a 20x20 cm^2, at 5 cm depth in water measured with the RFA300, for the low energy unflattened beam.

Fig 3. Nominal accelerating potential (NAP) as a function of beam quality index (TPR_{10}^{20}) extracted from the NPL (U.K.) calibration certificate for the ion chamber used in this work.

Fig 4. Central axis depth dose, for the electron low energy beam measured by film dosimetry.

Fig 5. Portal image obtained with a scale tray for portal films for a 10x10 cm^2 field size at SSD = 100 cm.

Fig 6. Graphical analisis by measuring the optical density at the scale tray central dots.

Fig 7. Example of Rando phantom portal film image, using portal film charts for Kodak X-Omat TL film and X-Omatic radiotherapy cassette, (4 MV unflattened beam).

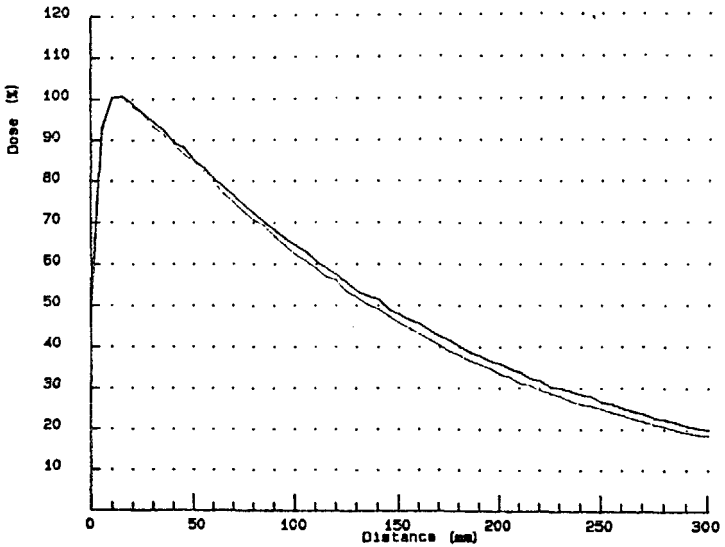

Fig 1

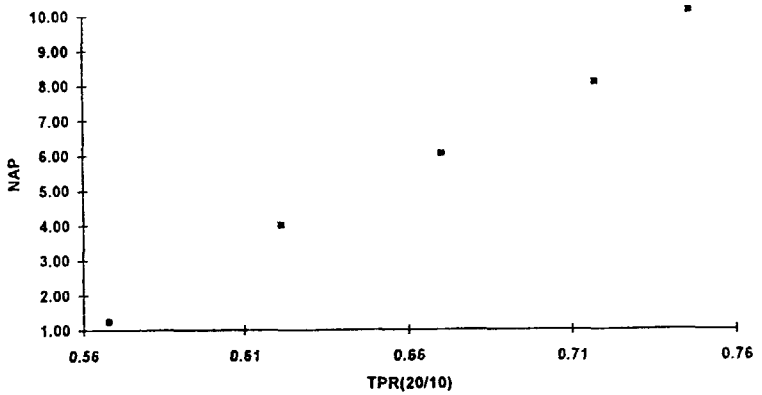

Fig. 3

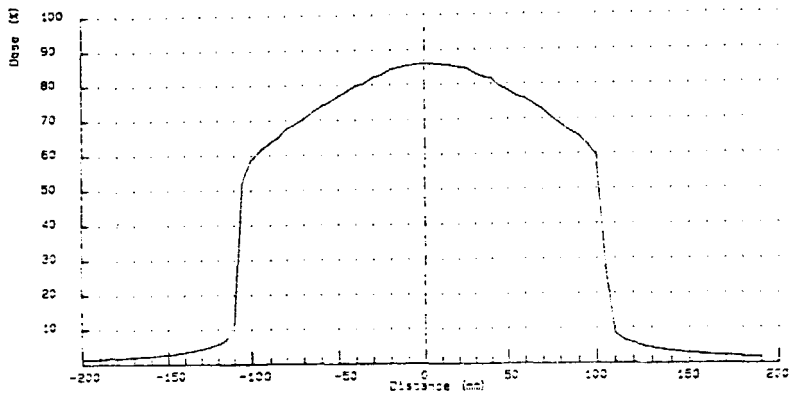

Fig 2

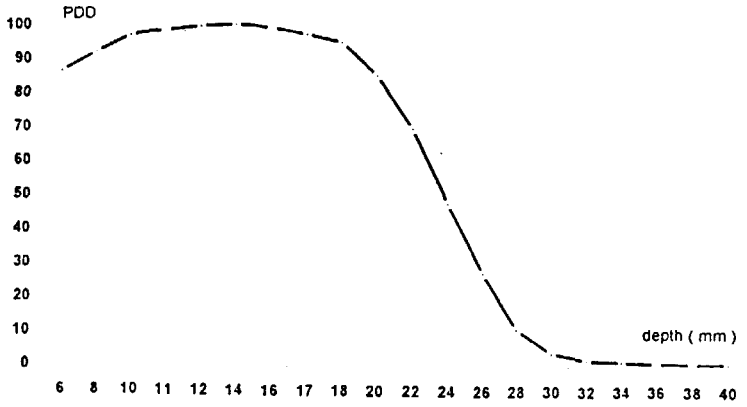

Fig. 4

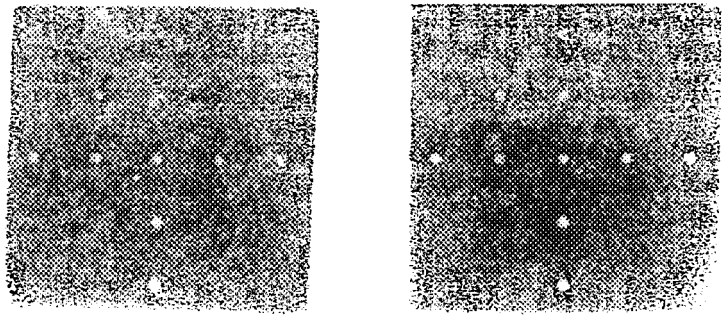

Fig. 5

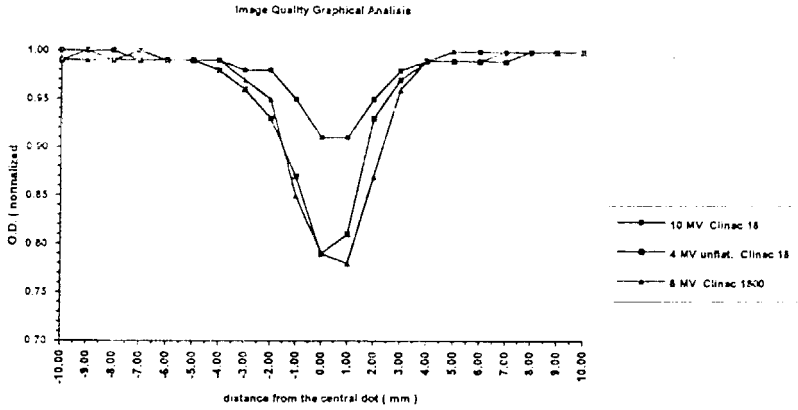

Fig. 6

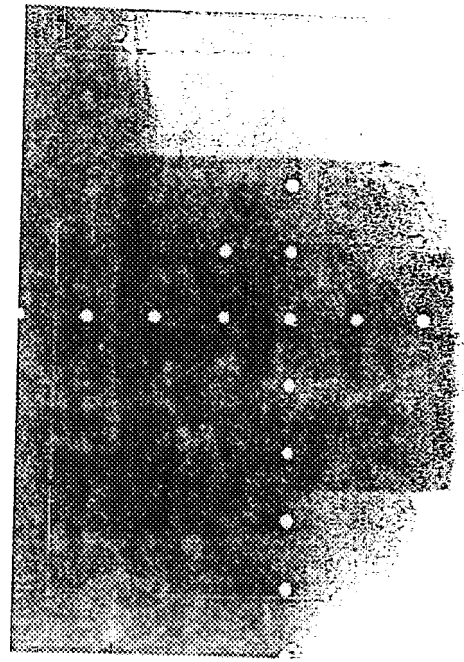

Fig. 7

THE ADJOINT MONTE CARLO - A VIABLE OPTION FOR EFFICIENT RADIOTHERAPY TREATMENT PLANNING.

M. Goldstein, Physics Department, Nuclear Research Center - Negev, P O Box 9001, Beer - Sheva, Israel

ABSTRACT

In cancer therapy using collimated beams of photons, the radiation oncologist must determine a set of beams that delivers the required dose to each point in the tumor and minimizes the risk of damage to the healthy tissue and vital organs. Currently, the oncologist determines these beams iteratively, by using a sequence of dose calculations using approximate numerical methods. In this paper, a more accurate and potentially faster approach, based on the Adjoint Monte Carlo method, is presented.

I. INTRODUCTION

During the past two decades, clinical procedures using highly collimated radiation beams, especially photons, have been used routinely [1]. The main idea in radiation cancer therapy has been to maximize the dose in each point of the tumor, without affecting the surrounding healthy tissue and especially the vital organs like the spine and the liver. The dose received by the healthy tissue and vital organs is usually lower than the dose received by the tumor, since multiple, individually non-lethal beams that intersect at the tumor, are used during treatment.

Currently, the selection of the best set of beams (or fields) for a particular patient, is determined by an iterative procedure, which includes in each step, a 3-D dose calculation for each beam configuration. The geometry is defined upon the information obtained from the patient's CT (Computed Tomography), or MRI (Magnetic Resonance Imaging) images. After assessing a previously chosen beam configuration, a modified (improved) configuration is devised. This process continues until the most promissing configuration is determined.

Current clinical dose calculation codes generally rely on semi-empirical methods that are fast and work well for geometrically simple problems, but are less accurate for practical, geometrically complex problems.

The best known method that can cope with that kind of physical and geometrical complexity, is the Monte Carlo method [2]. However, in order to solve dose calculation problems with reasonable statistical errors in individual voxels, the needed computation time is excessively large. As a result, Monte Carlo codes are not directly used for clinical treatment planning.

In this paper, we sketch a new approach for the 3-D dose computations aimed for radiotherapy treatment planning, based on the Adjoint Monte Carlo method [3]. The proposed approach is more accurate and have the promise to be faster than the current methods.

The contents of this paper are organized as follows:

In Sec.II we briefly describe the Adjoint Monte Carlo method. The proposed methodology for the selection of the best set of beams for a particular patient and the detailed 3-D dose computation, is described in Sec.III. In Sec.IV, preliminary results for a simple benchmark problem are illustrated. We conclude with a brief discussion in Sec.V.

II. THE ADJOINT MONTE CARLO METHOD.

The solution of the Adjoint Transport Equation [3] are widely used in perturbation theory and variational calculations related to the behaviour of nuclear reactors. The physical significance of the adjoint flux can be understood by considering a stationary system containing an external steady photon source, S. Suppose there is a dose detector, such as based on a response function $R(\mathbf{r},E)$, which is proportional to the flux-to-dose energy dependent conversion function. The photon flux in the system satisfies the stationary transport equation:

$$L\Phi = S \qquad (1)$$

where: L is the transport kernel, Φ is the photon flux and S is the external photon source

In addition, consider the adjoint equation with the adjoint source $R(\mathbf{r},E)$, that is:

$$L^*\Phi^* = R(\mathbf{r},E) \qquad (2)$$

Equation (1) is now multiplied by Φ^* and equation (2) by Φ; the resulting expressions are subtracted and the difference is integrated over all variables. By using the definition of the adjoint operators it is then found that:

$$\int S(r,\Omega,E)\Phi^*(r,\Omega,E)dVd\Omega dE = \int R(r,E)\Phi(r,\Omega,E)dVd\Omega dE \qquad (3)$$

The right hand side of this equation is the dose obtained at the detector of volume V, from the external source S. According to the left hand side of the equation, the adjoint flux $\Phi^*(\mathbf{r},\Omega,E)$ is the expected contribution to the dose at the detector, of a photon with position **r**, direction Ω and energy E.

III. RADIOTHERAPY TREATMENT PLANNING USING THE ADJOINT MONTE CARLO METHOD.

The radiotherapy treatment planning problem comprises of two steps:

1. The selection of the best set of beams for a particular patient, such that the dose in each point of the tumor is maximized, without affecting the surrounding healthy tissue and the vital organs,
2. The detailed dose calculation in each point (voxel) of the tumor.

Unlike the experience-based, trial-and error approach to treatment planning, the proposed method uses the adjoint Monte Carlo method for the selection of the best set of beams for a particular patient.

First, an adjoint transport calculation is made, starting from the tumor volume, with an isotropic adjoint source having a spatial and energetic distribution, given by the response function R(**r**,E), which is the flux-to-dose conversion function. The photon histories are followed to the external surface (skin) of the body and the adjoint flux $\Phi^*(r,\Omega,E)$ on the skin surface is calculated as a function of position, direction and energy. As we mentioned in the previous section, the adjoint flux is the expected contribution to the dose at the tumor, of a photon with position **r**,direction Ω and energy E.

Since we want to minimize the radiation effect on vital organs, an additional similar adjoint computation is made, starting this time from the vital organs. The resulted adjoint flux, $\Phi''(\mathbf{r},\Omega,E)$ is compared with the tumor's adjoint flux $\Phi^*(r,\Omega,E)$ for the selection of the best set of beams for a particular patient, that is choosing an external source $S(\mathbf{r},\Omega,E)$, such that the volumetric dose in the tumor, $\int S(r,\Omega,E)\ \Phi^*(r,\Omega,E)\ dV\ d\Omega\ dE$ is maximized.and the dose in the vital organs is minimized.

Finally, the detailed dose in each point (voxel) of the tumor is calculated, by solving the (forward) transport equation for photons emerging from the previously detemined external source, in acoupled photon-electron mode.

IV. PRELIMINARY RESULTS.

A very simple benchmark problem has been designed that will test the efficiency of the proposed method. This problem models a 30*30*30 cm^3 "human tissue" phantom which includes a 5*10*10 cm^3 "cancerous liver" and a 2*2*30 cm^3 "spine" (see Fig. 1.).

The "liver's" centroid is located 10 cm. off center, to the left (towards facet C), while the "spine" is located at the center of facet B.

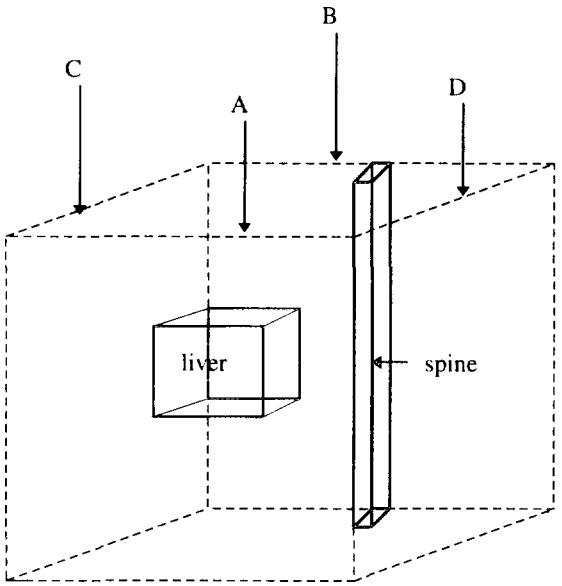

Fig. 1: The geometry of the benchmark problem.

The adjoint flux has been calculated on the external surface of the "body" (facets A,B,C and D, see Fig. 1), as a function of position and direction, for all energies between 0.01 to 20 Mev. Each facet has been divided into 9 equal square patches of 10*10 cm (see Fig. 2.). The angular variable domain, measuring the cosinus of the angle defined by the escaping adjoint photon and the positive normal to the external surface, has been divided into 14 angular bins. The adjoint flux was calculated for each patch on the external surface and each angular bin.
We compared the "liver" adjoint flux to the "spine" adjoint flux and found that the most promissing results, namely, the highest "liver" adjoint flux (6.56E-3) and the lowest "spine" adjoint flux (1.95E-4), have been obtained at the middle, left-hand side patch on facet B (see Fig. 2.), in a direction perpendicular to the patch. Therefore, the best source, providing the maximum dose at the "liver", without significantly affecting the "spine", is a source perpendicular to the middle, left-hand side patch on facet B (towards the "liver").

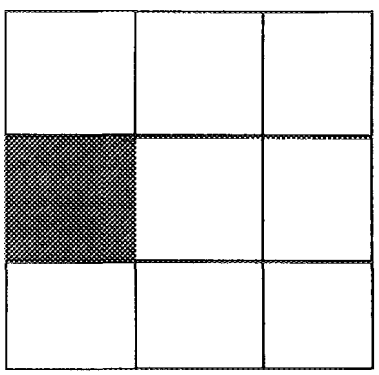

Fig. 2 : The optimal patch for the external photon source.

The adjoint computations have been executed by using the MCNP4A[4] Monte Carlo code, with a multigroup photon cross section library of 12 groups. MCNP4A is a generalized Monte Carlo code, capable of simulating coupled neutron-photon-electron problems, using a 3-D heterogeneous geometry system. It can solve the forward as well as the adjoint transport equation. MCNP4A provides for a detailed neutron, photon and electron physics treatment. The MCNP4A geometry package consists of first and second degree surfaces and supports nested (hexahedral or hexagonal) lattice features.
In the proposed method only the tumor region must be ddescribed in detail by voxels, to allow a "pointwise" dose calculation. During the adjoint computations for the external beams optimization, there is no need for a voxel representation of the geometry, since the adjoint flux is calculated on the external surface of the body. The geometry can be described accurately by using just the bondary surfaces of the different organs, or regions of the body with the same material composition. These surfaces can be identified during the segmentation of the CT or MRI images. Since MCNP4A (and other Monte Carlo codes) can handle just first and second degree surfaces, the bounding surfaces can be described by several first and second degree surfaces.
Finally, during the detailed dose calculation in the tumor, only the tumor region needed to be described by voxels, to allow the dose calculation in each voxel, while the rest of the geometry can bedescribed volumetrically, each organ (or homogeneous region) as a 3-D volume bounded by the previously identifyied surfaces, with its own density and composition.

V. CONCLUSIONS.

A new,accurate and potentially faster method for the radiotherapy treatment planning, based on the adjoint Monte Carlo method has been presented. The new method comprises of two steps:

1. Using the adjoint Monte Carlo method, the best set of beams for a particular patient are determined.
2. The "pointwise" dose in the tumor is calculated, using the conventional (forward) Monte Carlo method.

First, an adjoint transport calculation is made,starting from the tumor volume, with a source having a spatial and energetic distribution of the flux-to-dose conversion function. The resulted adjoint flux on on the external body surface is the distribution of the expected contribution to the dose at the tumor, of a source photon, as a function of position, direction and energy.
To minimize the radiation effect on vital organs, a similar adjoint computation, with a source defined in the vital organs, is made and the resulted adjoint flux is compared to the adjoint flux from the first calculation. A new adjoint flux distribution is defined, such that the radiation impact on the vital organs is minimized.
Using this adjoint flux distribution, the best set of beams for the particular patient is determined, such that the dose at the tumor is maximized.
Finally, the dose in each voxel of the tumor is computed by solving the (forward) transport equation of photons emerging from the previously determined photon beams.

The proposed method has been successfully used for a very simple benchmark problem. Currently we are assessing the feasibility of the proposed method for more realistic planning problems.

VI. REFERENCES.

1. F.M.Khan, "The Physics of Radiation Therapy", Williams and Wilkins, Baltimore (1994).
2. I. Lux and L. Koblinger, "Monte Carlo Particle Transport Methods: Neutron and Photon Calculations", CRC Press, Boca Raton, Florida (1990).
3. G. I. Bell and S. Glasstone, "Nuclear Reactor Theory", Van NostrandReinhold Company,New York, 1987.
4. J. F. Briesmeister, "MCNP- A General Monte Carlo N-Particle Transport Code, Version 4A", Los Alamos National Laboratory Report, LA-12625, (1993)
5. J. J. DeMarco, T. D. Solberg, R. E. Wallace, J. B. Smathers, "Performance Analysis of the Monte Carlo Code MCNP4A for Photon Based Radiotherapy Applications", Proc. of the Int. Conf. Mathematics and Computations, Reactor Physics and Environmental Analysis, Portland, Oregon, April 30- May 4, 1995.

A RETROSPECTIVE EVALUATION OF ONE YEAR OF CARDIAC PET IMAGING AT HADASSAH HOSPITAL USING RUBIDIUM-82 AND THE POSITRON CORPORATION HZL PET SCANNER

Chisin R., Freedman N., Marciano R., Taylor C., Schechter D.
Department of Medical Biophysics and Nuclear Medicine, Hebrew University
Hadassah Hospital, Jerusalem (Israel)

Aim

Falsely abnormal results in conventional nuclear cardiology using ^{201}Tl and even Tc-99m-MIBI for the detection of coronary artery disease (CAD) in well known. Artifactual abnormalities are caused by diaphragm overlap of the left ventricular inferior wall and breast overlap of the anterior wall. Falsely abnormal results often lead to unnecessery utilization of coronary catheterization and medical therapy.
With high resolution and sensitivity, as well as the ability to perform accurate attenuation correction, PET offers the potential for more accurate myocardial perfusion imaging, free from attenuation artifacts, particularly in large patients.
A retrospective study has been carried out to assess the diagnostic contribution of cardiac PET imaging with ^{82}Rb at the first Israeli PET center during its first 12 months of operation.

Methods

* A total of 243 successive patients (166 male and 77 female) referred for myocardial perfusion evaluation were scanned. 150 patients also had coronary angiograms and 97 patients had ^{201}Tl or Tc-99m-MIBI scans.
* All PET scans were obtained with the new Positron Corporation HZL PET scanner (axial field of view: 15 cm, transverse resolution: 6.2cm).

* An attenuation correction scan was first performed which collected 130-150 million counts in 30-45 minutes by scanning the patient with a rotating rod source of the positron emitter ^{68}Ge.
* Rest and dipyridamole stress emmision scans were obtained by infusing a bolus of 30-39 mCi of ^{82}Rb chloride, and after 70-80 sec. interval for clearance of tracer from arterial blood a static emission image was obtained over 6 minutes, giving a total of 25-30 minutes counts

Results

We were able to use a lower Rubidium-82 dose than the usual 50 mCi reported by most centers in view of the high sensitivity of the Positron HZL scanner. Our results showed a significant number of examples of inferior wall perfusion defects, and anterior wall defects, mostly in women, which were seen on ^{201}Tl scans and which were not present on PET. In those patients who also had coronary angiography it was possible to confirm that the coronary arteries were normal and that the apparent defects were attenuation artifacts. The presence of these breast attenuation artifacts in women and diaphragm artifacts was not confined to women with large breasts, or men with "beer-belly".

Conclusions

PET cardiac imaging has contributed to the assessment of myocardial perfusion in particular by identifying the existence of attenuation artifacts in stress ^{201}Tl SPECT. In our study these artifacts were found to occur not only in large patients where they might be expected, but also in small or average sized subjects where they were not anticipated.

^{99m}Tc High Resolusion Tomographic Imaging in the Thyroid Gland Diseases

Reitblat A. , Ben-Horin C. , Barzilai Medical Center , Ashkelon

In the experiments with the thyroid phantom and first studies of patients with hyperthyroidism it was proved that in combining SPECT imaging technique and high resolution ability of pinhole collimator (commonly used for conventional scintigraphy of the thyroid) it is possible to obtain quantitative information concerning the structure and unhomogenities of the thyroid tissue , not available from the planar imaging. The following applications of the the method are expected :

1) Estimation of the thyroid dimentions and volume for the accurate dosimetry of the following ^{131}I - therapy.
2) Determination of the location of the thyroid in the neck , occurances of the retrotracheal,retrolaryngeal and retrosternal extension of the goiter.
3) Estimation of the structure and unhomogenities of the thyroid gland .
4) Locations and dimentions of cold nodules in the thyroid tissue .

Some of these applications are illustrated in our studies of the patients with different thyroid gland diseases .

Materials and Methods

The APEX 409 AG ECT gamma camera system and the pinhole collimator APC-8 with accessible apertures of 2, 4.45 and 8 mm (Elscint , Israel) were used for acquisition of data , that was executed with a 180 arc of rotation RLAT-ANT-LLAT, because of the anterior position of the thyroid in the neck . Data was collected on 64 x 64 matrices , and filtered back projection reconstruction technique was used for obtaining one-pixel transaxial,coronal and sagittal sections of SPECT imaging. Three types of filters - Hanning,Butterworth,Shepp and Logan - were used for recon-

struction process , showing the necessity of selecting filter and its parameters for each individual case . The volumes of the thyroid phantom and the patients' thyroid were estimated from the break of the slope of the volume vs. the threshold curve, and the pixel scale was determined with the help of two ^{57}Co point sources.

Thyroid Phantom Experiments

The Picker thyroid phantom was used for determination of the optimal parameters of the thyroid SPECT imaging and its resolution ability. It contains tree cold points of 12 , 10 and 6 mm in diameter and one hot point of 12 mm . The phantom was filled with $^{99m}TcO_4^-$, supplying the same total counts that were tipical for our patients' SPECT imagings. The following parameters were found to be optimal for acquisition: zoom 2-4 ; the total counts - at least 300-350 Kcounts for the aperture 4.45 mm; The angular step of the aquisition in the 2 - 9 range does not visibly influence the quality of the image but the resolution ability considerably decreased with an 8-mm aperture. Apertures of 2 and 4.45 mm make it possible to distinquish the 12-mm hot point and the 9- and 12-mm cold points of the Picker phantom , but there is a significant decrease in the statistics of the image for the 2-mm aperture. The volume of the thyroid phantom was determined from its SPECT imaging according to the described method with ca. 10% accuracy.

Patient Studies and Results

The group of 42 patients (8 males and 34 females,age range 18-74 yr,mean age 47 yr) were examined between July 1992 and June 1996. The group encluded 8 patients with Grave's disease , 12 patients with multinodular goiter , 1 patient with autonomus adenoma , 1 patient with Hashimoto's thyroiditis , 13 patients with cold solitary nodule and 7 patients with normal thyroid. SPECT imaging was performed immediatly after intravenous injection of 259-370 MBq (7-10 mCi) of $^{99m}TcO_4^-$ and usual scintigraphic imaging of the thyroid with pinhole collimator (aperture 4.45 mm).

The usefulness of the described technique is illustrated here by the following cases:

1) Two patients that cold nodules were revealed in the SPECT imaging and were not seen in the planar pinhole thyroid scan (Fig. 1,2) .

2) Patient with Grave's disease that unhomogenities in the distribution of the thyroid tissue uptake were revealed in the SPECT imaging and the volume of the thyroid was estimated according to described method (Fig. 3) .

3) Patient with multinodular thyrotoxic goiter that Spect imaging helped to estimated the positions and dimentions of the nodules (Fig. 4) .

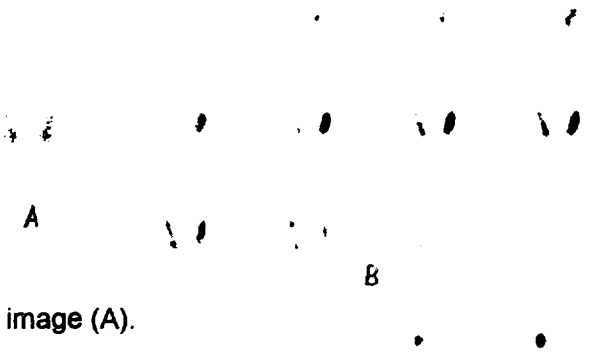

Fig.1 41 -year-old woman. The coronal slices (B) of of SPECT reveal large cold nodule in the anterior part of the right lobe not seen in the planar image (A).

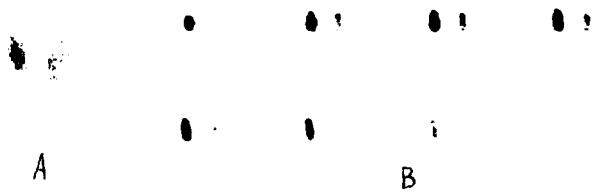

Fig.2 63 -year-old woman. The coronal slices (B) of SPECT reveal large cold nodule in the anterior part of the left lobe not seen in the planar image (A).

Fig.3 42-year-old woman with long-standing thyrotoxicosis complained of tremor and anxiety .Planar thyroid scan (A) showes an enlarged gland with comparatively homogeneous increased uptake of ^{99m}Tc.

In the coronal slices (B) two weak nodules are clearly seen in the right and left lobes surrounded by homogeneous tissue. The thyroid volume of 36 ml was estimated and it was in a good conformity with the estimation of experienced physician from palpation and planar pinhole image (40 ml) . The result was used for the following ^{131}I therapy.

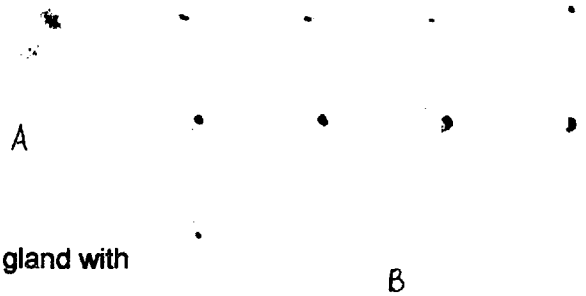

Fig.4 81-year-old woman with diabetes mellitus of 7 years' duration and thyrotoxicosis diagnosed earlier. Planar scan (A) shows an enlarged gland with nonhomogeneously increased uptake, compatible with multinodular thyrotoxic goiter.In the coronal slices of the SPECT (B) a hot large nodule and two small nodules are present in the left lobe.The right lobe is larger and has a more diffuse structure with the presence of small nodules along the whole lobe. One more hot nodule is present in the right part of the isthmus.

Conclusion

These studies have demonstrated that high-quality SPECT imaging of the thyroid can be achieved with the help of pinhole collimator. As compared to planar imaging, it can provide improved functional and anatomical information concerning the thyroid tissue,the anatomy of multinodular goiter,retrotracheal and retrolaryngeal extention of goiter,tracheal compression, and thyroid volume.

THE INVOLVEMENT OF OXYRADICALS IN BIOSTIMULATION

R. Lubart, H. Friedmann, H. Reuveni* and N. Grossman*
Bar-Ilan University, Soroka Medical Center, Israel

It was previously found that low energy lasers in the visible and near infra-red promote proliferation of fibroblasts and keratinocytes. The aim of the present work was to find out whether formation of oxyradical is involved in this phenomenon.

The proliferative response of cultured fibroblasts and keratinocytes to exposure of low energy doses of UVA, HeNe laser and 780 nm diode laser was studies. A single exposure to irradiation promoted a long-term effect on the mitotic activity of the cells. It simulated DNA synthesis beginning 6 hrs following exposure, and it increased division rate, resulting in a significant increased number of cells 48 to 72 hrs following irradiation. Addition of superoxide dismutase (SOD), vitamin E, azide and histidine suppressed the promoted cell division. Introducing very small amounts of photosensitizers (hematoporphyrin derivatives (HPD) for example) into the cells before irradiating enhanced the proliferation.

We therefore believe that biostimulation in the visible is a photosensitized process. Light probably starts the cascade of metabolic events by being absorbed by endogenous photosensitizers in the cell, generating small amounts of reactive oxygen species (ROS) which activate the cell.